

University of Alberta

Colloidal Particle Deposition onto Charge-Heterogeneous Substrates

by

Tania Rizwan

A thesis submitted to the Faculty of Graduate Studies and Research
in partial fulfillment of the requirements for the degree of

Doctor of Philosophy

Department of Mechanical Engineering

© Tania Rizwan

Fall 2009

Edmonton, Alberta

Permission is hereby granted to the University of Alberta Libraries to reproduce single copies of this thesis and to lend or sell such copies for private, scholarly or scientific research purposes only. Where the thesis is converted to, or otherwise made available in digital form, the University of Alberta will advise potential users of the thesis of these terms.

The author reserves all other publication and other rights in association with the copyright in the thesis and, except as herein before provided, neither the thesis nor any substantial portion thereof may be printed or otherwise reproduced in any material form whatsoever without the author's prior written permission.

EXAMINING COMMITTEE

Subir Bhattacharjee, Mechanical Engineering

Alidad Amirfazli, Mechanical Engineering

Don Raboud, Mechanical Engineering

Sushanta Mitra, Mechanical Engineering

Anthony Yeung, Chemical and Materials Engineering

Subhasis Ghoshal, Civil Engineering, McGill University

Dedicated To,

My Parents

Rehana and Rizwan; the source of my inspiration

And,

My Family

Rahat and Zayaan; the source of my strength

ABSTRACT

This dissertation investigates the influence of surface heterogeneities on colloid deposition. First, deposition of colloidal particles on a nanofiltration membrane during cross flow membrane filtration was studied under different operating pressures and solution chemistries. An atomic force microscope (AFM) was then used to observe the deposit morphology formed on the membrane. At the initial stages of fouling, more particles preferentially accumulate near the ‘peaks’ than in the ‘valleys’ of the rough nanofiltration membrane surface. This study demonstrates that it is difficult to isolate, correlate and assess the effects that physical (roughness) heterogeneity and chemical heterogeneity has on colloid deposition based on experiments involving surfaces where the physical and chemical heterogeneities are uncorrelated or ‘randomly distributed’.

In the second phase of the study, the deposition of model colloidal particles onto patterned charge-heterogeneous surfaces was studied both experimentally and theoretically. Controlled charge heterogeneity was created experimentally employing self assembled monolayers of alkanethiols patterned onto gold substrates using a soft lithographic technique. Model colloidal particles and fluorescent nanoparticles were sequentially deposited onto the patterned substrate under no flow (quiescent) conditions, and the deposited structures and the micro-patterns were imaged in situ using a combination of phase contrast and fluorescence microscopy. This study indicates that particles tend to preferentially deposit at the edges of the chemically favourable stripes.

The theoretical investigation involved the formulation of a mathematical model based on Random Sequential Adsorption (RSA). This study showed that a simple binary probability distribution assumed in the model is able to predict the experimental deposit morphology adequately, particularly the periodicity of the underlying patterns on the substrate. Furthermore, the effect of charge heterogeneity on the electrostatic double layer interaction between a particle and a charge heterogeneous planar surface was studied numerically employing a 3D finite element model. In this system, significant lateral forces at close separation distances were observed, and found to be appreciably higher when the particle is near the edge of a heterogeneous region of the substrate. From the above studies, it can be concluded that by altering/controlling the chemical heterogeneity of the substrate, it is possible to achieve significant control on the resulting deposit morphology.

ACKNOWLEDGEMENT

I have been fortunate to have received much help, advice, encouragement and support from a number of people during the years I have worked on this thesis. First I would like to thank my supervisor Dr. Subir Bhattacharjee for his encouragement, guidance and mentorship. His enthusiasm and passion for scientific research and his constant pursuit of a fundamental understanding of science will always be an inspiration to me. I especially like to thank him for allowing and encouraging me to work independently on challenging projects in which I learned how to design novel experiments and combine various analytical tools, but most importantly, I learned to trust in my abilities and hone my research skills making me into an independent thinker and a scientist.

I would like to thank the members of my supervisory committee Dr. Alidad Amirfazli and Dr. Don Raboud for their valuable advice and suggestions. I would also like to thank the members of my examining committee: Dr. Subhasis Ghoshal, Dr. Tony Yeung, and Dr. Sushanta Mitra, for reviewing my thesis.

Special thanks to the mechanical engineering department machine shop staff, office staff and IT personnel. It is because of their help in various aspects of my graduate life that has made my stay at University of Alberta smooth and uneventful. I am also grateful to Dr. Francis Nsiah (OSCIEF) for his assistance with FTIR measurements and to Dr. Anquang He (ACSES) for helping me with the TOF-SIMS analysis. The invaluable advice and guidance of Stephanie Bozic and Les Schowalter at the NanoFab facility is also acknowledged.

I would also like to express my gratitude to all my teachers from elementary school to graduate school for the part they played in forging my academic career.

I would like to acknowledge the financial support provided by Alberta Ingenuity through the Graduate Student Scholarship in Nanotechnology award that sustained me throughout the PhD program.

I would also like to thank all my past and present CCF lab mates. I am grateful to Neda, Shahnawaz and Farshid for their advice and friendship over the years. I would especially like to thank Noor, who allowed me to vent my frustrations on him when an experiment would not go my way and for the innumerable discussions on philosophy, religion and computer simulations. I am also grateful to Jeff for being a surrogate brother to me and for being a constant source of support.

I would like to extend my sincerest gratitude to my parents-Rizwan and Rehana and, brothers-Nadeem and Fahim. Their love and prayer always gives me comfort and inspiration. I would especially like to thank my parents who have supported me and my education in any and every possible way from grade school to graduate school and I do not think I would have ever gotten to this point without their unrelenting belief in my abilities. Last but not least, I would like to thank my husband Rahat and son Zayaan. I could have never completed my degree were it not for their love, understanding, and patience. My achievements and successes have more meaning simply because I have them to share it with. They remind me, always, of what is most important in life.

TABLE OF CONTENTS

CHAPTER 1 INTRODUCTION.....	1
1.1 Background and Overview.....	1
1.1.1 Significance of Colloid Deposition.....	1
1.1.2 The Deposition Process.....	2
1.1.3 Colloidal Forces Acting on a Particle Approaching a Collector Surface.....	3
1.2 Surface Heterogeneity Considerations in Deposition Studies	10
1.2.1 Physical Heterogeneity.....	10
1.2.2 Chemical Heterogeneity.....	12
1.3 Technological Significance of Chemically Patterned Substrates.....	15
1.4 Motivation and Research Needs.....	16
1.5 Objectives and Scope.....	19
1.6 Organization of the Thesis	22
CHAPTER 2 PARTICLE DEPOSITION ONTO ROUGH NANOFILTRATION MEMBRANES.....	28
2.1 Introduction.....	28
2.2 Materials and Methods.....	32
2.2.1 Nanofiltration (NF) Membrane.....	32
2.2.2 Colloidal Particle and Suspension	33
2.2.3 Quiescent (No Flow) Deposition	33
2.2.4 Cross Flow Membrane Filtration (CFMF) Setup	34
2.2.5 Atomic Force Microscopy (AFM) Imaging	35
2.2.6 Roughness Analysis	36

2.2.7	Bearing Analysis	36
2.3	Characterization of NF90 Membranes.....	39
2.3.1	Surface Morphology.....	39
2.3.2	Roughness of NF90 Membranes.....	40
2.3.3	Chemical Analysis of NF90 membranes.....	41
2.4	Deposition During No Flow Conditions	44
2.4.1	Deposit Morphology	44
2.4.2	Dry versus Wet AFM Imaging	45
2.5	Deposit Morphologies during Tangential Flow Conditions	47
2.5.1	Operating Pressure	47
2.5.2	Ionic Strength.....	48
2.5.3	Bearing Analysis	48
2.5.4	Long Term Deposition	49
2.6	Effect of Membrane Heterogeneity on Colloidal and Hydrodynamic Interactions	50
2.7	Conclusions	55

CHAPTER 3 PARTICLE DEPOSITION ONTO PATTERNED CHARGE-HETEROGENOUS SUBSTRATES..... 79

3.1	Introduction	79
3.1.1	Choice of Surface Modification-Self Assembled Monolayers of Thiols.....	80
3.1.2	Choice of Patterning Technique - Micro Contact Printing.....	81
3.2	Materials and Methods.....	82
3.2.1	Model Particles and Suspension	82
3.2.2	Patterned Model Substrates	82
3.2.3	Characterization of Patterned Substrates.....	85

3.2.4	The Deposition Process	87
3.2.5	Microscopic Imaging	88
3.2.6	Post processing and Analysis of Images	89
3.3	Results and Discussion	91
3.3.1	Characterization of Patterned Samples	91
3.3.2	Parameter Definitions.....	92
3.3.3	Deposition Morphology	94
3.4	Conclusions	99
CHAPTER 4 MODELING PARTICLE DEPOSITION ON CHARGE-HETEROGENEOU SUBSTRATES.....		114
4.1	Introduction	114
4.2	Simulation	115
4.2.1	Model Description.....	115
4.2.2	Procedure.....	116
4.2.3	Parameters Calculated	117
4.3	Results and Discussion	119
4.3.1	Variation of Size Ratio γ	119
4.3.2	Variation of Favourable Area Fraction λ	120
4.3.3	Fractional Surface Coverage	122
4.3.4	Comparison of Simulation Data with Experimental Results....	125
4.4	Conclusions	126
CHAPTER 5 ELECTROSTATIC INTERACTIONS BETWEEN A CHARGED PARTICLE AND A PLANAR CHARGE- HETEROGENEOUS SUBSTRATE.....		136
5.1	Introduction	136
5.2	Mathematical Modeling of Electrostatic Interactions.....	137

5.2.1	Governing Equation	137
5.2.2	Computational Geometry and Boundary Conditions.....	139
5.2.3	Calculation of Interaction Force	142
5.2.4	Trajectory Analysis	143
5.3	Numerical Solution Procedure	145
5.3.1	Finite Element Method.....	145
5.3.2	Mesh Generation.....	146
5.3.3	Validation of Numerical Model.....	148
5.3.4	Trajectory Analysis Procedure	149
5.4	Particle Interaction with Patterned Substrates.....	150
5.4.1	Potential Distribution	150
5.4.2	Interaction Forces.....	152
5.4.3	Trajectory Analysis-Particle Distribution	158
5.5	Conclusions	159
CHAPTER 6 SUMMARY AND RECOMMENDATIONS		175
6.1	Summary and Concluding Remarks	175
6.2	Recommendations	179
REFERENCES.....		180
APPENDIX A.....		207
APPENDIX B.....		215

LIST OF TABLES

Table 2.1 Nanofiltration (NF) membrane properties	59
Table 2.2 Colloidal particle and suspension properties	60
Table 2.3 Statistical roughness parameter definitions	61
Table 2.4 Typical result of a roughness analysis on a membrane area of $100 \mu\text{m}^2$	61
Table 2.5 Typical result of a bearing analysis on membrane sample obtained at operating conditions: Pressure = 60 psi, Ionic strength = 0.01 M.....	63
Table 3.1 Relevant properties of the model polystyrene sulfate particles used in the deposition experiments.....	101
Table 3.2 Stamp characterization results.....	102
Table 3.3 Experimental conditions under which the deposition experiments were performed for Figures 3.7, 3.8 and 3.9.....	103
Table 4.1 Physical and chemical properties of the system used in the simulations	162
Table 4.2 Comparison of the parameters of the system used in the experiment and trajectory analysis	163

LIST OF FIGURES

Figure 1.1: A schematic representation of the external forces acting on a colloidal particle of diameter d when it approaches a planar collector surface with velocity V_z under the influence of gravity g , in a no external flow condition.. 24

Figure 1.2: (a) Illustration of the electrostatic double layer around a charged particle (according to the Stern model) in an electrolyte solution and corresponding plot of the electric potential versus distance through the double layer showing the surface potential ψ_0 , stern plane potential ψ_s and zeta potential ζ . (b) Sections of two surfaces with the electric double layer interacting between them when both surfaces are likely charged (repulsion) and oppositely charged (attraction) respectively. 25

Figure 1.3: A typical potential energy U as a function of separation distance (of closest approach) h , for a particle-plate interaction. The attractive van der Waals energy is denoted by U_{vdw} , the electric double layer repulsion as U_{edl} and the total energy as U_T . The U_T curve shows three distinct features: the primary minimum (PM), the energy barrier (EB) and the secondary minimum (SM). 26

Figure 1.4: Flow diagram depicting the evolution of the research highlighting the relevant sequence of tasks. 27

Figure 2.1: Schematic representation of deposition of colloidal particles of different sizes relative to the roughness features of a macroscopically flat surface. (a) Particle size much larger than roughness; (b) particle size comparable to the roughness, and (c) particle size much smaller than the roughness features..... 64

Figure 2.2: Schematic drawing illustrating a typical cross sectional structure of a thin film composite (TFC) nanofiltration NF90 membrane..... 65

Figure 2.3: (a) Schematic of the cross flow membrane setup and (b) a photograph of the membrane module..... 66

Figure 2.4: Bearing analysis of the AFM topographic image. The image in (a) is a colour reproduction of the topographic image taken in tapping mode and (b) shows the results of a bearing analysis performed for a bearing plane height of 400 nm above the lowest scanned point on the image. (c) A composite bearing analysis image obtained by overlaying the bearing image (b) on the topographic image (a). The red regions in (c) indicate the areas above the bearing plane. The percentage of area calculated above this bearing plane (red regions) was 12.9%. (d) A schematic representation of the bearing analysis. The image shows the cross section of the membrane plan view. The area above the bearing height Z_b is rendered red and covers the particles in that region. The particles visible below Z_b can now be counted.. 67

Figure 2.5: SEM micrographs of a clean NF90 membrane at two magnifications. In (a) the bar scale in the micrograph is 30 μm . At this scale the membrane appears relatively smooth. In (b) the bar scale is 2 μm . The roughness is more apparent at this scale and the membrane structure shows an intertwining fibrous network. 68

Figure 2.6: (a) Topographic AFM images of two different 10 $\mu\text{m} \times 10 \mu\text{m}$ areas of a clean NF90 polymeric membrane in tapping mode. The colour variation illustrates the vertical profile of the membrane surface; light colour represents high lying regions and the darker regions being the pores. (b) The 3D orthographic images have the vertical scale enhanced to amplify the surface morphology of the membranes (500 nm/division for Z-scale compared to 2 μm per division for X and Y). CM1: Average roughness, $R_a = 67.37 \text{ nm}$ and CM2: Average roughness, $R_a = 59.40 \text{ nm}$ 69

Figure 2.7: FTIR IRRAS spectrum collected for the NF90 membrane shown over the range of 3800 cm^{-1} to 750 cm^{-1} . Peak centered at 3300 cm^{-1} is due to overlapping of stretching vibration of N–H and carboxylic groups in the polyamide layer. Peaks in the range of 2800–3000 cm^{-1} is assigned C–H stretching. Peaks around 1660 cm^{-1} and 1541 cm^{-1} are assigned to amide I (C=O stretch) and amide II respectively. Peaks at 1610 cm^{-1} and in between 1480 cm^{-1} , 1350 cm^{-1} indicate NH_2 deformation and COOH deformation respectively. Finally, the peaks near 1584 cm^{-1} , 1503 cm^{-1} , 1487 cm^{-1} , and 1151 cm^{-1} , all correspond to the polysulfone support. 70

Figure 2.8: An AFM image of 100 nm diameter polystyrene sulfate particles adsorbed on the NF90 membrane surface during the quiescent deposition experiments. The deposition lasted for 3 days at room temperature (25°C) in the colloidal suspension of ionic strength $I = 0.01$ M NaCl, particle concentration $N_p = 10^{16} \text{ m}^{-3}$ and pH = 6.4. 71

Figure 2.9: Wet mode AFM images of (a) a clean NF90 membrane and (b) of 100 nm diameter polystyrene sulfate particles adsorbed on the NF90 membrane surface during the quiescent deposition experiments. The deposition lasted for 3 days at room temperature (25°C) in the colloidal suspension of ionic strength $I = 0.001$ M NaCl, particle concentration $N_p = 10^{16} \text{ m}^{-3}$ and pH = 6.4..... 72

Figure 2.10: AFM image of polystyrene particles deposited on NF90 membrane surface under different operating pressures. Deposition test lasted for 10 min in each case. Ionic strength $I = 0.01$ M NaCl, Temperature = 27°C and pH = 6.4 The applied pressure: (a) 40 psi; (b) 60 psi; and (c) 80 psi. 73

Figure 2.11: Comparison of the particle deposition on NF90 membranes at different pH and salt concentrations. Deposition lasted for 10 min at a pressure 60 psi. Particle concentration in feed was 10^{16} m^{-3} . The following salt concentrations were used: (a) pH = 6.03, ionic strength, $I = 0.001$ M and, (b) pH = 6.4, ionic strength, $I = 0.01$ M..... 74

Figure 2.12: AFM tapping mode images of particles deposited at 60 psi and 0.01 M NaCl concentration 10 min used for the bearing analysis. In (a) membrane section (labelled 41) represents an area in the downstream portion of the membrane coupon. Samples shown in (b) to (e) (labelled 42 to 45) represent sections progressively moving upstream of the membrane coupon. Changes in height across the area are denoted in the colour scale bar where highest region is lightest in colour. Visual inspection of the images shows that the spherical shapes of the colloidal particles are discernable from the structure of the membrane. 75

Figure 2.13: Bar graphs of the particle distribution obtained from the bearing analysis in the deposition images shown in Fig 2.12. The bars represent the

percentage of particles tallied above each of the threshold or bearing height, Z_b . The percentage area present above the bearing plane at Z_b (the bearing ratio) is cited above the bar for the corresponding Z_b . Majority of the particles have deposited between 400 to 600 nm with almost no particles depositing below 300 nm. 76

Figure 2.14: Particle deposit morphologies at later stages of filtration at 80 psi: (a) deposit morphology after 30 min; (b) deposition after 1 h. In (a) large clusters of particles are seen to aggregated around the initial seeding locations on the asperity peaks, with several valleys remaining vacant; (b) illustrates the complete coverage of membrane surface signifying that at this point the surface appears homogeneous and equally favourable for deposition; this phenomenon is observed for all salt concentrations used in the study. 77

Figure 2.15: Schematic representation of the additional colloidal force experienced by a tracer particle due to the presence of asperities. Techniques like surface element integration cannot account for this additional force, since these techniques only consider the interaction between the particle and the vertically projected area of the particle on the membrane..... 78

Figure 3.1: Schematic representation of a highly ordered monolayer of alkane thiolate formed on a gold substrate. The most ordered structures are formed from organic compounds of $\text{HS}(\text{CH}_2)_n\text{X}$ with $n = 10-18$ and $\text{X} =$ a small functional group. The chain tilt varies from $\sim 27^\circ-50^\circ$ relative to the surface normal and the thickness of the monolayer varies between 20-30 Å 104

Figure 3.2: Flow diagrams summarizing the steps in micro contact printing of SAM of thiol on an Au coated glass surface. The stamp was inked by exposure to a 10^{-4} M ethanolic solution of $\text{HS}(\text{CH}_2)_{10}\text{COOH}$ (negative terminus), brought into contact with the gold substrate, and removed. The substrate was then soaked for 30 min in a 10^{-4} M ethanolic solution of $\text{C}_{11}\text{H}_{25}\text{NS-HCl}$ (positive terminus). The substrate was finally washed with anhydrous ethanol and dried in a stream of N_2 105

Figure 3.3: (a) Diagram depicts an exploded view of the closed cell assembly. (b) Photograph of the assembled closed cell..... 106

Figure 3.4: Images showing the results of the various techniques used to characterize the created patterned charge heterogeneous substrate. The substrates shown in all the images have 4 μm (positive) by 3 μm (negative) stripes. (a) AFM Tapping mode image of the patterned substrate showing no visible physical variation in the topology of the surface due to the similarity in chain length of the two thiols used. (b) Friction Force Microscopy (FFM) image of the same area as scanned in (a). This image shows the low friction areas as dark (corresponding to the negatively charged stripes) and the high friction areas as light (corresponding to the positively charged stripes). (c) Scanning Surface Potential Microscopy (SSPM) image showing the relative surface potential difference between the adjacent patterned thiols groups. The more positive surface potential (light) is associated with the NH_2 terminated thiol monolayer. (d) ToF-SIMS image showing the presence of the amine thiol (bright) as evident by the contrast obtained from the C^+ signal. 107

Figure 3.5: Fluorescence microscopy image of a patterned charge heterogeneous substrate. The patterns are 2 μm (positive) by 2 μm (negative) and image was taken at a magnification of 10X (scale bar is 10 μm and view area is approx. 251 $\mu\text{m} \times 251 \mu\text{m}$). The negatively charged patterns appear as dark coloured stripes while the positively charged bands fluoresce (red) due to the negatively charged 100 nm Nile Red polystyrene sulfate particles depositing on the oppositely charged stripes. 108

Figure 3.6: Diagrammatic representation of the patterned substrate showing the key dimensional parameters and the radial distribution calculation scheme. The square collector of length L consists of rectangular stripes with alternate regions that are favourable (gray) and unfavourable (white) to deposition of widths w and b respectively. The total width of a favourable and unfavourable stripe gives the pitch, p . The deposited spherical particles are of diameter d . Each particle is placed at the origin of a circular shell that sweeps out radially from the center of the particle in question. Each shell forms one particular circular bin of radius r and width Δr . Any particle that is found within the area covered by the circular bin is counted as being a part of that bin. This procedure is then repeated for all the particles in the image area.. 109

Figure 3.7: Results of the deposition on the control substrates. Part (a) and (c) are optical pictographs of 0.96 μm diameter negatively charged polystyrene particles (bright spots) depositing on a negatively chemically homogenous

negatively charged substrate and positively charged substrate respectively. The deposition conditions are: KCl concentration = 0.1 mM with a pH ~ 5.15 and deposition lasted for 24 h. The view region corresponds to a 256 μm by 192 μm area. Parts (b) and (d) are radial distribution functions obtained for the deposition images shown in (a) and (c) respectively. 110

Figure 3.8: Fluorescence microscopy images displaying the deposition of 2 μm negatively charged polystyrene sulfate particles on a 2 μm (positive) by 2 μm (negative) striped pattern ($\lambda = 0.5$, $\gamma = 1$) (a) Phase image showing the 2 μm particles deposit in an apparently random fashion on the substrate (b) Fluorescent image of the exact same area in (a) obtained by depositing 100 nm negatively charged Nile Red particles onto the remaining regions of the positively charged stripe. The model 2 μm sized particles appear as dark circular shapes on the fluorescent positively charged stripe while the negatively charged patterns appear as dark coloured stripes. (c) Image of a larger area on the same substrate obtained by superimposing images like those obtained in (a) on (b), such that the model particles and the underlying pattern are now visible, simultaneously. 111

Figure 3.9: (a) Optical micrographs of polystyrene sulfate particles (bright spots) deposited on chemically patterned planar substrates for three different γ values (from left to right) of 1, 2 and 4. View area represents 160 $\mu\text{m} \times 160 \mu\text{m}$ on the substrates. The surface coverage calculated was $\Theta_{(\gamma=1)} = 0.27$, $\Theta_{(\gamma=2)} = 0.26$ and $\Theta_{(\gamma=4)} = 0.1$. (b) Plots of the radial distribution function (c) and x -directional distribution functions obtained for the corresponding deposition images. All distances are scaled with respect to particle diameter. The locations within the deposition image that are likely particle positions are indicated by the peaks in the distribution functions. Table 3.3 contains other information relevant to the deposition images obtained in part (a). .. 112

Figure 3.10: Optical microscope images of polystyrene particles (bright spots) deposited on chemically patterned planar substrate when $\gamma = 1$ and $\lambda = 0.5$. (a) Same image as shown in Fig. 3.8a. The two shaded areas (in green) highlight the order observed in the macroscopic scale. (b) A zoomed image of the region marked out within the red square as shown in (a). This region represents an area of roughly 39 $\mu\text{m} \times 39 \mu\text{m}$. At this scale, one observes a lack of colloidal order observed in (a). 113

Figure 4.1: Schematic representation of the modeled surface charge heterogeneity. The square collector of height L consists of rectangular stripes with alternate regions that are favourable (gray) and unfavourable (white) to deposition and of widths w and b respectively. The sum of the width of a favourable and unfavourable stripe gives the pitch, p . The deposited spherical particles of diameter $d = 2a_p$ have their centers constrained to lie within the favourable stripes. 129

Figure 4.2: A schematic representation of the standard RSA method of simulation: (a) A random virtual particle fails to deposit due to overlapping with previously deposited particle. (b) A successful deposition has occurred at a vacant site..... 130

Figure 4.3: Particle distribution histograms for simulation results obtained by varying width to diameter ratios (a) $\gamma = 0.25$, (b) $\gamma = 0.5$, (c) $\gamma = 1.0$ and (d) $\gamma = 2.0$. Particles of diameter d (varying from 0.05 to 0.00625) were deposited on a scaled square area of 1.0 with $\lambda = w/p = 0.5$ (where, $w = b = 0.0125$). Each stripe pair (composed of half favourable and half unfavourable region) has been divided up into 16 bins. The dotted line represents the boundary between the favourable and unfavourable stripes. The inset diagrams show the relative magnitude of the particle size to the stripe widths and are drawn to scale. The particles (centers) present in each bin are counted and a distribution of deposited particles is obtained over a single pair of stripe. This is repeated over the entire area and the particle count is normalized with the average particle number in each bin and averaged for the total number of stripe pairs (in this case 40 pairs)..... 131

Figure 4.4: Particle density distribution charts obtained for the simulations results by varying favourable width to pitch ratios (a) $\lambda = 0.25$, (b) $\lambda = 0.5$, (c) $\lambda = 0.8$ and (d) $\lambda = 1.0$. Particles of diameter $d = 0.0125$ were deposited on a scaled square area of 1.0 with $\gamma = w/d = 1.0$ (where, $w = 0.0125$ and b is varying). Each stripe pair has been divided up into 20 bins. The dotted line represents the boundary between the favourable and unfavourable stripe. The inset diagrams show the relative magnitude of the particle to the stripes and are drawn to scale. The analysis procedure is the same as described in Fig. 4.3..... 132

Figure 4.5: Near-blocking surface coverage calculated over the total favourable available area (θ_{fmax} in square “■”) and the total collector area (θ_{max} in circles “o”) for varying (a) γ values and (b) λ values. 133

Figure 4.6: (a) Distribution of adsorbed particles generated in the RSA simulation by depositing on a striped surface with a 50% favourable area ($\lambda = 0.5$) by spheres (disks) of diameter that is twice the size of the width of a favourable stripe ($\gamma = 0.5$) and coverage is $\theta = 0.551$. (b) Distribution of same sized particles as in (a) deposited onto a homogeneously favourable collector ($\lambda = 1.0$) with $\theta = 0.527$. (c) Radial pair distribution functions and (d) directional distribution functions plotted for the cases shown in (a) and (b). Both the plots are shown over a scaled distance of 5 particle diameters with the dotted line representing the data for the striped surface ($\lambda = 0.5$) and the solid line representing the homogenous surface ($\lambda = 1.0$). 134

Figure 4.7: (a) Comparison of the radial distribution functions obtained for $\gamma = 1.0$ and $\lambda = 0.5$ with a total coverage of $\theta \approx 0.3$; the continuous line shows the simulation results for a 2D hard sphere and the dots shows the experimental results. (b) Comparison of the x -directional distribution function for the same parameters as in (a). All distances are scaled with respect to the particle diameter, d 135

Figure 5.1: (a) Pictorial and (b) schematic representation of the numerical model showing the substrate as a planar surface consists of rectangular stripes of alternating negative (white) and positive (gray) surface potentials with width of b and w , respectively. The particle of radius a , is negatively charged and approaches the substrate from a vertical distance h . In these simulations, the width of the stripes are held equal, *i.e.* $b = w$ 164

Figure 5.2: Illustration of the smoothing sigmoidal function to represent the variation (with y) of a scaled striped surface potential $\psi_s = (+1, -1)$ along the width of a heterogeneous substrate (a) by employing Eq. (5.11) with the following parameter values: $\Psi_{sn} = -1$, $\Psi_{sp} = 1$, $a = 80$, $y_1 = 1$ and $y_2 = 2$, and (b) extended over a substrate with three pairs of oppositely charged stripes of width $2 \mu\text{m}$ each. 165

Figure 5.3: Schematics showing mesh generation (a) in the entire computational domain (b) on the $y - z$ plane of the box and (c) on the particle surface. 166

Figure 5.4: Comparison of the electrostatic double layer interaction forces between a charged spherical particle and a planar substrate obtained from the finite element 3D-NLPB model (open symbol, \circ) with the corresponding estimates from Carnie model (solid symbol, \blacktriangle) and the analytical HHF equation (solid line). The variations of the scaled electrostatic force f_z with scaled (surface to surface) separation distances κh are depicted for a scaled surface potential of $\Psi_p = \Psi_s = 1.0$ at constant potential (CP) condition for $\kappa a = 1$ and $\kappa a = 5$ 167

Figure 5.5: Flowchart outlining the scheme used for the trajectory analysis. ... 168

Figure 5.6: Comparison of the potential maps near a negatively charged particle and the charge heterogeneous surface at a separation height of $h/a = 0.03$ and $\kappa a = 1$ for 4 different size ratios γ . Schematic showing the rectangular stripes of alternating negative (white) and positive (gray) surface potentials also accompany each potential map. The particle, in all cases, is positioned above the boundary between a negative and positive stripe. The colour blue represents the negative potential while red represents the positive potential (as shown by the colour bar). A sharp change in colour denotes a higher electric field implying a larger electrostatic force. The scaled surface potential of the particle is $\Psi_p = -1$ and the negative and positive stripes have a scaled potential of $\Psi_{sn} = -1$ and $\Psi_{sp} = 1$, respectively. 169

Figure 5.7: Variation of the scaled (a) normal force f_n , (b) lateral force f_l and, (c) force ratio f_l/f_n with different size ratios γ (stripe width to particle diameter ratio) at $\kappa a = 1$ and a scaled separation distance of $h/a = 0.03$. The x axis represents the relative position of the particle above the stripe. The scaled particle potential is $\Psi_p = -1$ and the negative and positive stripes have a constant potential of $\Psi_{sn} = -1$ and $\Psi_{sp} = +1$, respectively. The boundary between the negative and positive stripe is located at $2y/w = 0$ and is indicated by the dotted line. 170

Figure 5.8: Variation of the scaled (a) normal force f_n , and (b) lateral force f_l acting on the particle placed at different scaled y/a positions along the heterogeneous surface for $\kappa a = 5$ and $\gamma = 1.0$. The various scaled separation distances h/a are represented by the different symbols. The particle has a constant surface potential, $\Psi_p = -1$ and the negative and positive stripes have a constant potential of $\Psi_{sn} = -1$ and $\Psi_{sp} = 1$, respectively. The boundary

between the negative and positive stripe is located at $y/a = 0$ as indicated by the dotted line. 171

Figure 5.9: Vector plot of the net EDL force acting on the particle at $\kappa a = 5$ when particle center is placed at above different scaled y positions along the width of the charge heterogeneous surface for different scaled separation distances h/a under the same conditions as stated for Fig. 5.8. The ratio of the stripe width to particle diameter γ is 1.0. The direction in which the force is acting is indicated by the arrowhead and the relative magnitude by the arrow body. The boundary between the negative and positive stripe is located at $y/a = 0$ as indicated by the dotted line. 172

Figure 5.10: Comparison of the (a) normal and (b) lateral forces experienced by the particle for three different κa values (shown with symbols) at two representative scaled separation distances, $h/a = 0.1$ (solid lines) and $h/a = 0.03$ (dotted lines) for $\gamma = 2$. The scaled particle potential is $\Psi_p = -1$ and the negative and positive stripes have a constant potential of $\Psi_{sn} = -1$ and $\Psi_{sp} = 1$, respectively. The boundary between the negative and positive stripe is located at $y/a = 0$ as indicated by the dotted line. 173

Figure 5.11: Particle distribution histograms for $\gamma = 2.0$ and $\kappa a = 15$ obtained by depositing particles of radius $1 \mu\text{m}$ on a pair of striped surface with $\lambda = w/p = 0.5$ (where, $w = b = 4 \mu\text{m}$). The stripe pair composed of half favourable and half unfavourable region which was divided up into 40 bins. The particles (centers) present in each bin are counted and a distribution of deposited particles obtained over the width of the pair of stripes. The solid columns represent the particles whose initial positions were chosen at random and the hatched columns represent the particles that were released consecutively in an ordered manner along the stripe width. The boundary of the two stripes is indicated by the dashed line. 174

CHAPTER 1

INTRODUCTION

1.1 Background and Overview

1.1.1 Significance of Colloid Deposition

Colloidal particles are small entities with a size range from 1 nm to 10 μm and have been employed in many industries such as foods, emulsions, paints, coatings, ceramics, photonic crystals, and novel electronic devices [1], to name a few. Deposition of these colloids, proteins and other biomaterials on solid/liquid interfaces is of major significance for many engineered and natural processes. For example, deposition of colloidal and bio-particles is vital for processes such as filtration [2-4], coating formation, and colloid lithography [5]; here deposition is desired. In other applications deposition needs to be prevented as much as possible, such as, in bio fouling of membranes [6-8], transplants and artificial organs, fouling of heat exchanger surfaces and in detergency [9]. From an engineer's point of view, whether deposition is desirable or not, the challenge is to control the extent of deposition, deposit morphologies *etc.* to attain the desired functionality. This may be done by harnessing naturally occurring deposition processes or by engineering new ones. A good example of the former are the studies directed at better understanding membrane fouling [10-12], whereas the creation of new structures ranging from photonic crystals [13] to chemical sensors [14] exemplifies the latter. Besides these practical applications, the study of colloid deposition has a major significance for colloids science as it can furnish fundamental information regarding the interactions between particles and interfaces [15].

1.1.2 The Deposition Process

The deposition process is usually described as the mechanism by which particles dispersed in a suspension are transported to a surface, where they become attached. Deposition depends on essentially two distinct steps: (1) Transport step - which involves the transport of colloidal particles to the surface of the stationary collector and (2) Attachment step - which involves the colloidal particles from a bulk solution attaching to the collector surface. The transport step at the initial stages depends on physical factors like particle size and particle velocity, while the attachment step is primarily controlled by solution chemistry and chemical characteristics of the particle and the collector surface [15, 16]. In most practical cases, these two processes can be treated independently [15], the reason being that the transport step brings the particle and substrate in close proximity from comparatively large distances, over most of which colloidal interactions play no role. On the other hand, the attachment step involves particle–substrate interactions that are of short range (usually much less than the particle size), so that the particles have to approach close to the substrate before any significant interaction is felt. Thus the study of particle deposition is of inherent interest in colloid science since its dependence on the physicochemical conditions can reveal the fundamental nature of forces acting between various interacting surfaces.

The deposition of particles is strongly governed by the magnitudes of the various particle/particle and particle/substrate colloidal interactions. Typically, in deposition of particles from stable colloidal suspensions (no coagulation of the colloids in the bulk suspension), a strong attraction between the particles and the oppositely charged collector surface leads to deposited particles, maintaining fixed positions on the surface. This is called ‘irreversible deposition’, when the deposited particles are unable to return to the bulk suspension (desorption) or sample other regions of the surface (surface diffusion) [15]. On the other hand, in many systems the particle-surface attraction may be relatively weak, and consequently the deposited particles may diffuse on the surface or desorb into the bulk suspension. This scenario is referred to as ‘reversible deposition’ [15]. As deposi-

tion proceeds, the deposition rate slows down as the deposited particles occlude the collector surface from subsequent depositions due to the electrostatic repulsions between the free particles and deposited particles [17-19]. This surface exclusion is termed ‘blocking’ and it restricts the particle density on the collector surface to a single monolayer in thickness. This study focuses on the *irreversible, monolayer* deposition of colloidal particles in a *quiescent* system (*i.e.* in absence of fluid flow). The behaviour of solid-liquid interfaces and solid particles in several natural and engineered processes reflects the interplay of the interactions between them. A brief description on the origins and characteristics of the two basic interactions, dispersive and electrostatic, is contained in the next section.

1.1.3 Colloidal Forces Acting on a Particle Approaching a Collector Surface

As seen from the previous section, particle transfer from the bulk to the substrate surface is affected by a variety of interactions differing widely in magnitude and characteristic length scale. Figure 1.1 depicts the forces acting on a particle when approaching a planar substrate in the absence of fluid flow (quiescent system). In a quiescent system, for distances exceeding the particle dimensions, transfer of particles over these macroscopic distances can be induced by external field forces such as gravitational, electrical and magnetic. Due to the absence of any external electric/magnetic field in the present study, gravitational force F_g is considered to be the only field force that the particle experiences. The particles also experience a frictional resistance or hydrodynamic drag force, F_d while moving through the viscous fluid medium, and a buoyancy force F_b . At a closest approach distance of 100 nm or so, absorbing particles become influenced by the force fields generated by the interacting interfaces. When the particles approach the collector surface within this separation distance, for the types of systems that this study pertains to, primarily two types of colloidal interactions dominate the particle motion: van der Waals forces F_{vdw} , and electric double layer forces F_{edl} . These two types of colloidal forces are widely recognized and well documented in the literature. In this section, a general description of these colloidal forces is provided. The

section also introduces the DLVO theory [20, 21] and its limitations which lead to the discussion of the effects of surface heterogeneity on these sorts of interactions.

van der Waals Forces: The van der Waals (vdW) forces have their origin in atomic- and molecular-level interactions due to permanent and induced polarities created in molecules. These interactions are usually attractive and they dominate over a separation range of 0.2-10 nm [22]. More detailed description of van der Waals forces can be found in textbooks by Israelachvili [22] and by Masliyah & Bhattacharjee [1].

There are two well-known approaches in calculating the vdW interaction. One is the Hamaker approach based on the assumption of pair wise additivity of all the intermolecular interactions. The second is the Lifshitz theory based on quantum electrodynamics, which provides a more rigorous expression for van der Waals interaction [1]. The vdW interaction between a depositing particle and a planar substrate can be represented by the interaction between a sphere and a flat plate. An approximate expression for the non-retarded van der Waals force between a sphere and an infinite planar surface based on Hamaker's approach and Derjaguin's approximation is as follows [1, 22]:

$$U_{vdw}(h) = -\frac{aA_H}{6h} \quad (1.1)$$

where U_{vdw} is the interaction energy, A_H is the Hamaker constant, a is the radius of the spherical particle, and h is the distance of closest approach between the spherical particle and the flat surface.

The vdW interaction force is simply equal to the negative value of the first derivative of the interaction energy U_{vdw} with respect to the separation distance h . The vdW force between a particle and collector surface acts along the normal direction to the collector surface. It is dependent on the geometric characteristics and properties of the material of the surfaces and the media, and on the separation distance (as shown by Eq. (1.1)). The Hamaker constant between the spherical particles and the collector surface inside the aqueous solution is considered to be a positive number. This means that vdW interaction between the particle and the collector surface in such a case is attractive and acts favourably in the particle

deposition process.

Electric Double Layer Forces: Solid surfaces and colloidal particles develop surface charge in aqueous media due to different charging mechanisms. Some of those mechanisms include the dissociation of surface groups (such as COO^- , NH_3^+), the adsorption of ions or charged molecules onto the surfaces and substitution of surface atoms [23, 24]. Whatever the origin of the surface charge, due to the electro-neutrality of the whole system, the surface charge of the immersed body should be exactly balanced by an equal and opposite charge in solution. This balancing of charge is accounted for by an excess number of oppositely charged ions (counter-ions) in the solution adjacent to the charged surface and a deficit of similarly charged ions (co-ions). This redistribution of the ions in the solution together with the surface ions give rise to what is referred to as electric double layer (EDL) [23, 24].

One of the accepted models for the electric double layer is the Stern model [24]. According to this model, due to electrostatic attraction, some immobile counter-ions are located adjacent to the surface and form the ‘Stern layer’ as shown in Figure 1.2a. Outside the Stern layer, the mobile counter-ions are distributed such that the motion of these ions is balanced by both electrostatic attraction and the diffusion due to thermal effects. This layer is called the ‘diffuse layer’. The shear plane is the boundary of the mobile inner part of the EDL located one or two radii away from the surface where the no slip fluid flow boundary condition is assumed to apply. The potential at this shear plane is called zeta potential ζ , which can be determined with electrophoresis or electro-osmosis measurements [1, 23]. When two charged surfaces in an aqueous solution come into close proximity, their diffuse layers projecting from each surface overlap (Fig. 1.2b). As a result the ionic and potential distribution around the particle when brought near a surface is no longer symmetrical. This causes asymmetrical stresses of an electrical nature on the particle resulting in the electrostatic double layer (EDL) interaction and the particle experiences a force.

The expression for the interaction potential energy between a sphere and a flat plate is derived from the well-known Hogg, Healy, and Fuerstenau (HHF) expres-

sion [25] for the electric double layer interaction energy per unit area between two infinite planar surfaces:

$$\frac{U_{edl}(h)}{A} = \frac{\varepsilon\kappa}{2} \{ (\psi_1^2 + \psi_2^2) [1 - \coth(\kappa h)] + 2\psi_1\psi_2 \operatorname{cosech}(\kappa h) \} \quad (1.2)$$

Here ψ_1 and ψ_2 are the surface potentials of the two plates, $\varepsilon (= \varepsilon_r \varepsilon_0)$ is the permittivity of the medium where ε_r is the solvent dielectric constant (or relative permittivity of the medium) and ε_0 is the permittivity of vacuum, and κ is the inverse Debye length, given by:

$$\kappa = \sqrt{\frac{2e^2 z^2 n_\infty}{\varepsilon k_B T}} \quad (1.3)$$

where n_∞ is the bulk ionic number concentration of the electrolyte, k_B is the Boltzmann constant, z is the absolute valence of the ($z:z$) electrolyte, e is the elementary charge and T is the absolute temperature. The HHF expression applies to constant surface potential and is valid for low surface potentials.

Next, one applies the Derjaguin's approximation [23] to Eq. (1.2) to obtain the expression for the interaction energy between two spheres. Derjaguin's technique remains the same whether one calculates the vdW interaction energy or EDL interaction energy for curved surfaces. This process yields the following expression for the interaction potential between two unequal sized spheres of radii a_1 and a_2 and having surface potentials ψ_1 and ψ_2 [1]:

$$U_{edl} = \frac{\pi a_1 a_2 \varepsilon}{a_1 + a_2} \left\{ 2\psi_1 \psi_2 \ln \left[\frac{1 + \exp(-\kappa h)}{1 - \exp(-\kappa h)} \right] + (\psi_1^2 + \psi_2^2) \ln[1 - \exp(-2\kappa h)] \right\} \quad (1.4)$$

Finally, the expression for the interaction potential energy between a sphere of radius a and a flat plate is obtained by letting $a_1 = a$ and $a_2 = \infty$ in Eq. (1.4) [1]:

$$U_{edl} = \pi a \varepsilon \left\{ 2\psi_1 \psi_2 \ln \left[\frac{1 + \exp(-\kappa h)}{1 - \exp(-\kappa h)} \right] + (\psi_1^2 + \psi_2^2) \ln[1 - \exp(-2\kappa h)] \right\} \quad (1.5)$$

where ψ_1 and ψ_2 are the surface potential of the particle and plate respectively. A more detailed discussion of the mathematical description for the EDL interaction between a sphere and a plate is given in Chapter 5. Depending on the strength and sign of the charge (potential) of the particle and the substrate surface, the EDL interaction can be either attractive or repulsive. Additionally, the range and magnitude of these interactions can be varied within broad limits by adjusting the

electrolyte concentration, change of pH and adsorption of surfactants or charged polymers on the surfaces [24].

DLVO Description of Colloid Deposition: Once the electrostatic and van der Waals interactions for the particle interface are known, one can attempt to construct the overall interaction energy profile which is a prerequisite for estimating colloidal particle deposition phenomenon. The Derjaguin-Landau-Verwey-Overbeek (DLVO) theory [20, 21] plays an essential role in providing a quantitative interpretation of the colloidal interactions in particle deposition [15]. The application of the principles of this theory enables, at least qualitatively, the study and interpretation of a large amount of experimental data regarding aggregation, deposition, membrane separations *etc.* Neglecting other possible forces (all other interactions except these two are referred to as non-DLVO interactions), one can predict whether a colloidal dispersion will deposit or not by adding the attractive and repulsive forces approximated by Eqs. (1.1) and (1.5). This is the basis of the DLVO theory. Essentially, van der Waals attraction U_{vdw} and electric double layer interaction (EDL) U_{edl} are assumed to be additive and combined to give the total energy of interaction or the DLVO potential U_T between surfaces as a function of separation distance:

$$U_T = U_{vdw} + U_{edl} \quad (1.6)$$

A typical profile of the net interaction energy predicted by the DLVO theory is presented in Figure 1.3. The attractive energy U_{vdw} is inversely proportional to the distance and hence increases rapidly as the particle approaches the plate while the repulsive energy U_{edl} changes relatively slowly. The U_T curve has three distinct features: the primary minimum, an energy barrier and the secondary minimum.

The shape of the interaction profile has a profound influence on the kinetics of colloid deposition. The nature of the interaction profile is governed by the interplay between the vdW and EDL interactions which depend on various physicochemical parameters such as particle size, potentials, electrolyte composition and Hamaker constant, as seen from Eqs. (1.1) and (1.5). For example, at low ionic strengths, the EDL repulsion outweighs the vdW attraction, because the diffuse layer is thick and so electrostatic forces tend to dominate particle-plate

interactions over a wide range of separation distances. In such a case, there exists a potential energy barrier (see Fig. 1.3) which typically prevents the colloidal particles from closely approaching the collector surfaces, and so prevents deposition. For particles to experience deposition in the primary minimum, which is often irreversible, they have to surmount this repulsive energy barrier. At intermediate ionic strengths, the EDL repulsion is lowered causing the energy barrier to become lower, and contact of the particles with the substrate can occur more readily. In such cases there exists a shallow attractive well in the total potential profile, which is referred to as the secondary minimum, where the vdW attraction dominates over the electrostatic repulsion. This secondary minimum can be responsible for the reversible deposition of particles where the particles can attach to the collector but can be easily detached due to the relatively low attraction energy. At high ionic strength, the diffuse layer is compressed to such an extent that the energy barrier can essentially disappear, causing the vdW attraction to dominate over all separation distances. In this situation, colloidal particles can readily approach and attach to collector surfaces.

Limitations of the DLVO theory: The DLVO theory tends to capture the underlying physics of colloidal interactions quite well for some clearly defined model systems [26]. For example, the experiments Israelachvili performed to determine the interaction forces between two molecularly-smooth freshly cleaved mica surfaces have shown remarkable agreement with the DLVO model [22]. While direct measurements of the force between molecularly smooth and homogenous surfaces generally show good agreement with the traditional models, experiments performed with practical surfaces frequently show substantial discrepancy. The inability of the DLVO theory in successfully predicting the behaviour of such colloidal systems might be an artefact of either the oversimplified nature of the DLVO potential (manifested via the key assumptions of the DLVO theory on which it is based) such that it fails to account for the complexities inherent in these real systems, or due to the inaccurate usage of the theory itself. Some of the key assumptions upon which the DLVO theory is based are as follows [1]:

- The solvent is treated as a continuum.
- The ions in the solvent are treated as point masses and are from indifferent electrolytes.
- The interacting surfaces are assumed to be geometrically smooth and uniformly charged.
- The DLVO potential is an approximate potential of the mean force between two charged bodies suspended in an infinite medium where many body effects are not considered.

Some researchers have sought to bridge the gap between theory and experiment by adding new forces to compensate [22, 27-31] leading to an extended DLVO interaction model. However, looking back at the tremendous developments in the general subject of colloidal interactions, one is faced with a fundamental question: When interactions between atoms are primarily dictated by dispersion and columbic forces, how can other types of forces manifest themselves in colloidal systems? Most other types of forces invoked to describe colloidal phenomena (such as hydration forces [32-36], steric interactions [32], depletion forces [6, 32], acid–base interactions [37-39], and specific ion effects [40] could be manifestations of the simplifications or assumptions made in the DLVO model.

The discrepancy between theoretical predictions and experimental results is perhaps not more pronounced in any other situation than in the case of particle deposition [41]. The deposition of particles onto a collector surface has been studied using a number of different experimental geometries such as rotating disk technique, parallel-plate flow cell, packed bed technique, stagnation flow cell *etc.* (a thorough review of the works can be found in the text book by Elimelech *et al.* [15]). Traditionally, one would model such a colloidal system by assuming ideal surfaces (meaning important physical and chemical properties of the interacting surfaces are uniform everywhere) and apply the DLVO interaction model to this simplified system, thereby ignoring the heterogeneity present in the system. Regardless of the method used, the experiments have invariably shown that when the depositing particles must overcome a significant energy barrier prior to

deposition (unfavourable condition), the measured deposition rates are substantially higher than predicted by standard DLVO theory in the deposition models. By comparison, deposition under favourable conditions (no significant energy barrier) has showed reasonable agreement between experimental results and theoretical predictions [41]. In nearly all such studies, researchers have suggested that the cause of such discrepancies to be the heterogeneities on the interacting surfaces either in the form of surface roughness or non uniform charge density [41]. In the next section, a closer look is cast upon the effect of heterogeneity on deposition studies.

1.2 Surface Heterogeneity Considerations in Deposition Studies

As mentioned in Section 1.1.3, most studies on particle deposition that have employed the DLVO interaction model have treated the particle and the planar surface as homogeneous bodies, having perfectly smooth surfaces and being composed of pure substances. However, such homogeneous systems (as assumed by the DLVO theory) are rare in nature as real surfaces are typically rough and varied in composition on various scales (otherwise referred to as *heterogeneous*). Most of the deposition surfaces in these studies therefore possess a certain degree of heterogeneity in their chemical and/or topographical features that are often randomly positioned on the surfaces. A number of different classifications of surface heterogeneities are possible. A simple distinction, which is pertaining to this dissertation, would be to divide them into *two* broad categories, namely *physical* (or topographic) heterogeneities and *chemical* heterogeneities.

1.2.1 Physical Heterogeneity

Physical heterogeneities are due to the surface roughness or due to artificially created topographic features. All natural solid surfaces are rough to some extent, on a sufficiently small scale. The roughness can be an intrinsic property of the material itself or the result of manufacturing or some preparation process. Periodic roughness or artificial topographic features have been created in textured

substrates that are composed of regular features at the nano/micro scale (such as in super hydrophobic surfaces) [42, 43]. Many studies on deposition of particles on collector surfaces cite roughness and chemical heterogeneity as the possible causes for discrepancy between predicted and experimental results. For example, Hull and Kitchner [44] used a rotating disc technique to measure deposition rates of polystyrene latex particles onto smooth plastic films and found that under unfavourable deposition conditions the measured deposition rate was several orders of magnitude higher than predicted. Similar discrepancy was observed by Bowen and Epestein [45] who measured deposition rates using silica particles and by Elimelech and O'Melia [46] using polystyrene sulfate particles. Both studies were conducted in a parallel plate arrangement on glass plates, and cited roughness and chemical heterogeneity of the glass substrate as probable causes for the discrepancy. Deposition studies on commercial membranes have also shown that surface morphology and structure influence the performance characteristics (like colloidal fouling) of the membrane [47-50]. For example, atomic force microscopy (AFM) images of fouled membranes show that the initial colloid deposition rate is higher and deposited particles were not evenly distributed on a rough nanofiltration membrane compared to a smooth membrane [49]. Furthermore, recent experimental work using the AFM colloid-probe technique indicates that DLVO interactions between silica particles and rough polymeric membrane surfaces can be strongly influenced by membrane surface roughness [51, 52].

With intentions to produce more sophisticated and realistic models, there have been both theoretical and experimental studies in the past two decades that have included some type of physical heterogeneity in their system. Extensive work has been done to model the effect of surface topography on DLVO forces on surfaces with well defined, usually periodic topographic structures (such as in textured surfaces) [41, 53-56]. In some works, attempts have been made to model 'real' deposition surfaces by introducing the randomness of distribution of the heterogeneity using statistical estimates of the surface topology obtained from atomic force microscopy investigation of real surfaces (like nanofiltration membranes [47, 57]).

Although roughness considerations in the models in all the aforementioned studies have shown improvement when compared with experiment, including those that emulate a ‘real’ deposition surface, discrepancy still remains. This is because many of these models developed have usually been specific to one type of geometry (*e.g.* the roughness is in the form of cones or hemispheres). Thus more general models that could simulate a variety of surface morphology would be even more valuable. Another possible cause for deviation of theory from experiment is that most of these models only account for the effect of surface roughness, while ‘real’ surfaces contain *both* morphological and chemical heterogeneities.

1.2.2 Chemical Heterogeneity

Chemical heterogeneities are related to the variations in the chemical properties of the surface such as surface charge, chemical composition, *etc.* As seen from the previous section, discrepancies between theory and experiments studies on deposition still remain despite accounting for the effect of physical heterogeneities in the models. In those studies, often the chemical heterogeneities of the interacting surfaces, which are present in conjunction with the roughness, have been cited as another possible cause for the deviation [52]. Chemical heterogeneities manifest on surfaces as variation in surface charge density (or surface potential) along the surface. For example, in minerals, variations in charge density arise because of different functional groups on the adjacent facets of the mineral surface while in crystalline materials, microscopic charge heterogeneities can arise from defects in the arrangement of ions within the crystal lattice [58]. Such chemical variability results in uneven or heterogeneous surface charge that are randomly distributed, of arbitrary geometrical shapes, and various length scales. Most of the homogenous surface that were used in the deposition experiments as depositing surfaces, can be assumed to be chemically ‘homogenous’ substrates (such as high quality glass slides or glass beads used in many deposition studies), in a macroscopic sense. However, studies have shown that these surfaces are known to contain some nano- or even micro-scale chemical heterogeneity that can

arise due to the intrinsic property of the material itself or as a result of manufacturing or some preparation process. For example, surfaces of high quality soda-lime silicate glass have been found to be chemically inhomogeneous at the nanoscale [59].

The role of surface charge heterogeneity in the study of particle deposition kinetics has been noted for a while now. Hull & Kitchener [44], Bowen & Epstein [45] and Gregory & Wishart [60] reported the results of controlled colloid deposition experiments under unfavourable (chemical) conditions. They observed that experimental deposition rates were many orders of magnitude higher than theoretical predictions based on the classic DLVO theory. The discrepancy was attributed to inherent physical and chemical heterogeneities of collector surfaces. These investigators further suggested that particle deposition occurs preferentially onto chemically favourable sites, resulting in initial deposition rates much higher than those predicted based on the average collector surface potential. Additional studies relating the anomalous particle deposition rates observed in experiments under unfavourable chemical conditions to surface charge heterogeneity have been reported for deposition in packed beds [46, 61] stagnation-point flow [33, 62] and parallel plate channels [63]. In fact, bacterial adhesion and subsequent cell growth that leads to biofouling is a common problem faced by various engineered systems (like water treatment plants [64], marine surfaces [65] and medical devices [66] to name a few) and has been attributed to the presence of charge heterogeneities on the surface [67].

A commonly adopted technique to model surfaces with macroscopic charge heterogeneity is to define at least two types of charge locations on a given collector (for instance, positive and negative), assigning the surface area fraction occupied by one type of charge and using a two-site averaging process generally referred to as the '*patchwise heterogeneity model*' [58, 68]. These patches are assumed to be much larger than the depositing colloidal particles such that the interactions between patch boundaries have a negligible effect on particle deposition. For such surfaces, the overall particle deposition rate is considered to be a linear combination of deposition rates on the various surface patches and regions.

While the patchwise heterogeneity models provide an accurate description of macroscopic charge heterogeneity (*i.e.* when the patches are much larger than the depositing particles), they may not be well-suited for microscopic charge-heterogeneous patches that have a comparable length scale to the particle size [69-71]. For such systems, it was theoretically demonstrated that the initial particle deposition rates on a 50% favourable surface may resemble that of a completely favourable surface [70, 71]. It is therefore of great importance from both a theoretical and a practical point of view to fundamentally explore the effects of micro-scale charge heterogeneity on governing mechanisms of the particle deposition process.

Particle deposition processes have a stochastic nature [72]. Therefore, traditionally to study deposit structures, one employs Monte Carlo simulations based on Random Sequential Adsorption (RSA) theory [73] for irreversible deposition. Monte Carlo simulation is one of the most efficient ways of obtaining structural data and predicting structures of deposits but these studies do not quantitatively predict the evolution of the physical system due to the absence of physical time-scale *i.e.* the dynamics of the deposition process is not the focus of the study. In studies of RSA, one is usually interested in characterizing the jammed state morphology at large times, *i.e.* when a dense deposit is formed and no available particle landing sites are left, as well as the approach to the jammed-state coverage. These RSA type models can have increasingly complexity by incorporating other effects such as electrostatic interactions [74-77], gravity [78-81] or Brownian motion [82-85].

Several theoretical works have examined the irreversible particle adsorption kinetics involving the heterogeneity of the substrates, which are commonly portrayed as discrete point-like adsorption sites (quasi-continuous, random or lattice) within an otherwise non-adsorbing substrate [56, 86-96]. These models provide a good understanding of deposition of larger colloid particles at macroscopically uniform surfaces (like mica, quartz, glass or other polymeric surfaces) bearing adsorption centers such surface charges or ionic species (like polyelectrolytes or proteins) and are representation of the nanoscale heterogeneity. There are

several experimental deposition studies that focus on deposition on such macroscopically homogeneously charged surfaces created by modification of the natural surfaces using appropriate chemicals. To ensure a similar chemical interface, the substrates are usually modified using chemical units that cover the surface more or less homogeneously such as by modifications of surfaces by polymers [44, 97], surfactants [98], or chemical coupling agents (silanes) to change the natural surface charge of substrate surfaces [16, 74]. The range of applicability of the above theoretical approaches and numerical results have been compared with experimental results obtained mostly by the direct optical microscope observation or the by indirect methods like reflectometry, electron microscopy, atomic force microscopy, and streaming potential [17, 18, 34, 94, 99-106].

Some theoretical studies have modeled the situation when adsorption sites are in patches having finite dimensions (patterned substrates) when compared to the adsorbing particle size [96, 107-113]. Because this field of research is under development [96], there have been very few systematic experimental measurements of particle deposition conducted on substrates bearing patterned linear and curvilinear surface features. With the recent advancement of microfabrication technology, some experimental measurements have been performed in the past few years for deposition on surface features having the form of circles and dots [114-116], squares [117, 118] and rectangles or stripes [69, 119-123]. However all of these studies involve the heterogeneity pattern being much larger than the depositing particles. Furthermore, little attention has been given toward understanding deposit morphologies formed on the patterned charge heterogeneous substrates, correlated with the particle size and the size and shape of the underlying heterogeneity. Experimental quantification of the surface coverage and deposit morphology on large-scale the patterned areas of substrates is also lacking.

1.2.3 Technological Significance of Chemically Patterned Substrates

One of the properties exhibited by chemically heterogeneous surfaces as a result of their heterogeneity is that of ‘selectivity’ during deposition. When colloidal

particles suspended in solution come in contact and interact with heterogeneously patterned surfaces, they exhibit specific dynamic signatures and adhesion characteristics based on their shape, size, charge, topography, chemical properties, *etc.* Thus, the synthesis of such novel materials bearing tailored properties will involve the formation of surface bound micro/nanostructures through controlled deposition processes on these heterogeneous surfaces.

The enormous potential of such ‘selective’ surfaces has led to the development of advanced fabrication techniques to design artificially patterned surfaces [124, 125]. While these artificially prepared surfaces are less complex than the naturally occurring surfaces, some heterogeneity, either induced or natural, still exists in them. The selective nature of artificially patterned surfaces makes them important components of tissue scaffolds, sensors, smart adhesives, separation media, and related applications. Engineered patterned surfaces are used as biosensor mediated optical devices, electrodes, field effect transistors, and piezoelectric devices to increase the response speed and sensitivity of current electrochemical devices [55].

Pattern recognition based on selective particle-surface interactions is observed in many biological systems. For example, for some biomedical applications, special proteins (antibodies) are attached to a surface to promote selective binding of a desired component from protein mixtures such as in affinity chromatography [126] and recognition processes (biosensors) [127], immunological assays [128], *etc.* The adsorption and subsequent self assembly of colloidal particles on a template of chemically patterned solid substrate has also been proposed as the basis for several nano-technological devices such as nanowires [129] quantum memory and photonic devices [13, 130, 131] and chemical sensors [132-134].

1.3 Motivation and Research Needs

The immense potential of the usefulness of (naturally existing or patterned) heterogeneous surfaces in real world applications certainly prompts the need for an in-depth understanding of the physics that govern selective behaviour exhibited

by them [125]. Integrating colloidal particles into more complex structures is now a key challenge for modern technology in creating nano- and micro-scaled devices. Recent advances in the cutting edge fabrication technologies have shown promising ability to precisely control surface patterns in the order of a few nanometres [135-137]. Understanding of the fundamental mechanisms that drive the assembly of particles on such patterned surfaces will provide strategies to create the desired colloidal microstructures or control the deposition process by identifying and subsequent modification of the key controlling parameters.

Notwithstanding the technological importance of such patterned heterogeneous substrates and the ability of current micro/nanofabrication technology to create them, there still seems to be some deficiency in the fundamental understanding of the phenomenon occurring at these microscopic length scales. Despite the attention the scientific world has conferred upon the issue of heterogeneity effects on particle deposition, there are fundamental questions to which the answers still remain incomplete, unsatisfactory or debatable. Some questions that have been posed regarding such a system include: How can one modify the chemical (and/or physical) properties of the system to encourage the deposition of a particle on the surface? Does size and shape (of particle and heterogeneity) matter in such instances? Can the location of where a particle contacts the heterogeneous surface be predicted with a high certainty? The lack of systematic experimental investigation and the scarcity of information in the literature regarding the effect of heterogeneity on the deposition structures in such systems provide the motivation for this research.

The effect of patterned chemical heterogeneity on deposition systems has been much less in focus in comparison to physical heterogeneities or roughness [41, 96]. Although there are several theoretical studies reported on patterned surface charge heterogeneity and its effect on deposition, there have been fewer experimental studies available involving patterned heterogeneity. Some experimental studies during the past years report deposition of particles on select types of patterned substrates (such as circles, lines, or a checkerboard structure) (see Section 1.2.3). However, most of these studies involve the pattern sizes that are

larger than the depositing particles. As such, little consideration has been given to the effect microscopic-sized heterogeneities, particularly when the heterogeneities are of the same scale as the particles, on deposition. Furthermore, systematic experimental studies employing large periodic arrays of a repeated pattern, where the pattern features are varied relative to particle size, are also not available in literature. Nor are there much information regarding the decoration of particles on the substrates, correlated with the particle size and the size and shape of the underlying heterogeneity [111, 112.]. Experimental quantification of the surface coverage and deposit morphology on large-scale patterned areas of substrates is also lacking.

The structure of the colloidal deposits near these surfaces is particularly important, specifically where a given micro-structure is desired on the surface. For example, deposit structure is especially important in monolayer colloidal films used in devices, such as heterogeneous catalysts which usually require specific deposition sites to function adequately [5]. Thus, often with these deposition studies, what matters is not solely the dynamics of deposition process or the amount of deposited material (which are often the main focus of the study), but also where and in what fashion the material is organized in the deposit, *i.e.* the deposit structure. However, in the few available experimental studies available involving patterned heterogeneity and deposition studies, the experimental methodologies used to observe the deposition structure has almost always involved a drying step which lead to significant alteration of the structure of the deposit (particle monolayer) and thus loss of important information.

Thus, based on the above discussion, the following needs can be identified in the research field of patterned chemical heterogeneity and its effect on deposition:

- Systematic investigations into the effect of chemical heterogeneity on particle deposition using patterned substrates (particularly when patterns are of the same scale length scale as the particles).
- Formulation of experimental methodology to allow *in situ* observation of the deposit morphology (without drying or any other structure modifying effects).

- Investigation of the deposition distribution and the morphology of particles on the patterns and identification of relevant variables (such as particle size, patch size *etc.*) that will correlate the deposited structure with the underlying heterogeneity.

The lack of systematic experimental studies in this area can be attributed to the difficulties in fabricating microscopic-scale surface charge heterogeneity in well-controlled patterns [96]. With the advent of technological advancement in the field of micro fabrication in the past decade, it is now possible to create micro patterns with relative ease in large scales. For segregated or patterned areas on a substrate, this is generally achieved by chemically modifying the substrate topography by patterning the substrate in a controlled way using lithographic printing or other etching technique such as photo lithography [117, 138, 139], laser ablation [140-142], or by soft lithographic processes [69, 117, 121, 138, 143-151]. Not only are these patterns created with nanometre precision, they can also be characterized accurately and non-intrusively with tools like Atomic Force Microscope (AFM) and related techniques which have proved to be promising candidates for morphological, physical, electrical and chemical characterization of such surfaces on the sub-micrometer scale [152-156].

With the possibility of facile fabrication of such surfaces in a larger scale (reproducibly) and having access to state of the art characterization tools such as the AFM, experimental procedures involving the creation of controlled surface charge heterogeneity and consequent *in-situ* deposition study are feasible. Such studies will enable a more in depth look at the role of surface charge heterogeneity on deposition (and colloidal interaction) in aqueous systems. This provides the impetus in pursuing this work in studying the effect of heterogeneity on colloidal deposition while focussing primarily on chemically patterned substrates.

1.4 Objectives and Scope

As seen from the discussion in Section 1.2, physical and chemical heterogeneity have often been used as ‘scapegoats’ to justify the breakdown of the DLVO

theory when tested for and used in experimental observations using natural or ‘real’ surfaces. In view of this, the aim of this research was to investigate the effects of chemical heterogeneity on colloidal interactions in context of how it influences particle deposition dynamics and deposit morphology on chemically heterogeneous surfaces.

Initially, an investigation of the initial stages of deposition in a macroscopically planar ‘real’ surface (commercial nanofiltration membranes) was conducted. These surfaces are known to inherently possess physical heterogeneities (or roughness) distributed in a random fashion throughout the membrane surface and were assumed to be otherwise chemically homogenous. The goal of this phase of the research was to understand the effect of the more dominant physical heterogeneity on deposition in this system and determine whether such a system would be ideal to study the effects of artificially created chemical heterogeneity on deposition in such a system. As will be evident from Chapter 2, the following observation was made from this phase of the study: A systematic experimental study of chemical heterogeneity employing naturally occurring substrates becomes non-trivial owing to the randomness in the distribution of chemical properties of substrates, and presence of physical heterogeneity (roughness) in conjunction with chemical heterogeneity in most practical deposition systems.

In this context, it seems pertinent that to systematically study effect of chemical heterogeneity on particle deposition, model substrates should be used where the heterogeneity is created by patterning chemically heterogeneous patches of regular geometries on smooth substrates. Since the distribution and nature of these chemical heterogeneous patches are known *a priori*, and the physical heterogeneity has been taken out of the picture, studying deposition onto these ideal systems can lead to considerable insight into how the deposition behaviour is influenced by the presence of surface charge heterogeneity. This will render comparison of experiments with theory more tractable and can provide systematic and quantitative information that can contribute to a greater practical understanding of deposition processes. The influence of certain parameters, such as particle size, dimensions of the heterogeneity, *etc.*, can be thoroughly investigated and the

results will often enable, at least, a qualitative interpretation to be made of similar phenomena in real systems. This phase of the research will include both experimental and numerical modeling studies performed on ideal systems. The emphasis of the work was on those deposition processes in which:

- The particles are comparable to the scale of underlying heterogeneous structure of the substrate, and are large compared to the range of the particle–particle and particle–substrate interactions.
- An irreversible deposition (*i.e.* no particle motion on the surface and no detachment) of a monolayer of the particles occurs.

Thus, in its most general formulation, the aim of this work is to understand how the irreversible deposition of micron-sized colloidal particles onto a well-defined chemically heterogeneous substrate in a quiescent system is modified with respect to a homogenous substrate. Based on the research needs identified in Section 1.2.4., the more specific objectives of this work were:

1. Experimental studies aimed at directly visualizing the influence of surface heterogeneity of a nanofiltration membrane on the colloidal deposit morphology during initial deposition of model particles.
2. Creation of large scale chemically heterogeneous patterned areas on macroscopically smooth substrates, reproducibly, and development of characterization techniques to quantify them.
3. Formulation of a method for direct experimental assessment of the deposition on these model substrates that will allow *in situ* observation of the created deposition structure simultaneously with the underlying patterned heterogeneity.
4. Identification of some key parameters that will dictate the variations in the deposit pattern during deposition in these model heterogeneous systems under no-flow conditions (also referred to as quiescent deposition).
5. Develop a theoretical model for particle deposition onto these patterned surfaces and compare predictions obtained from the simulations with the experimental results.

The results of this study will provide a better fundamental understanding of

particle deposition in patterned/heterogeneous substrates and at least provide a qualitative interpretation of similar phenomena in real systems.

1.5 Organization of the Thesis

The research plan is outlined in the flow diagram in Figure 1.4 and depicts the evolution of this research highlighting the relevant sequence of tasks. It is broken down into several stages which translate into various chapters of this dissertation. Based on Fig. 1.4, the proposed study is divided into two major phases. In the first phase, the study focuses on the deposition of colloidal particles in heterogeneous substrates in a representative practical system. In the second phase, the experimental and numerical work is done with model chemically heterogeneous substrates.

A general introduction and pertinent facts relating to colloidal deposition is presented in this chapter. A literature review pertaining to the effects of heterogeneity (chemical and physical) on deposition is included, as well as an overview of experimental and theoretical work done involving chemically patterned substrates. The overall objectives and scope of the study have been delineated in this chapter and the motivation behind this research has been also been laid out.

Chapter 2 investigates particle deposition in a real system by conducting an experimental study on the initial stages of membrane fouling of commercial NF90 nanofiltration membranes by submicron spherical polystyrene sulphate particles in a cross flow membrane filtration setup. The structure of the particle deposits were studied using an atomic force microscope by scanning the fouled membrane surfaces containing deposits of colloidal particles obtained during the filtration experiments under different pressures and electrolyte concentrations.

In Chapter 3, an experimental study of the deposition on chemically patterned substrates is presented, which was performed with model colloidal particles depositing onto rectangular striped model charge-heterogeneous surfaces to analyze the influence of surface charge heterogeneity on the subsequent deposit morphology. The charge heterogeneity was created using a soft lithographic

technique and alkanethiols to produce patterned self assembled monolayers on gold coated microscopically planar substrates. The procedure allowed the creation of large periodic arrays of a repeated pattern, where the pattern features were varied relative to particle size. Polystyrene sulfate microspheres and fluorescent polystyrene nanoparticles were sequentially deposited onto these patterned substrates under no flow (quiescent) conditions and the deposited structures and the micro-patterns were imaged *in situ* using a combination of phase contrast and fluorescence microscopy.

Chapter 4 deals with the formulation of a simple mathematical description of particle deposition on rectangular (striped) surface features (similar to those experimentally created in Chapter 3) employing a Monte-Carlo type simulation technique based on Random Sequential Adsorption (RSA). Predictions obtained from the simulations for different particle sizes and stripe dimensions were then compared with the experimental results.

In Chapter 5, a 3-dimensional (3D) model of the electric double layer interaction between a spherical particle approaching a patterned planar surface is presented along with numerical techniques, solution methodology, and numerical results. The interaction forces calculated are finally incorporated in a simple trajectory analysis to understand the particle distribution results obtained in Chapter 3.

Finally in Chapter 6, a summary of this work is presented providing the major conclusions drawn from the research and the possible directions for future work are outlined.

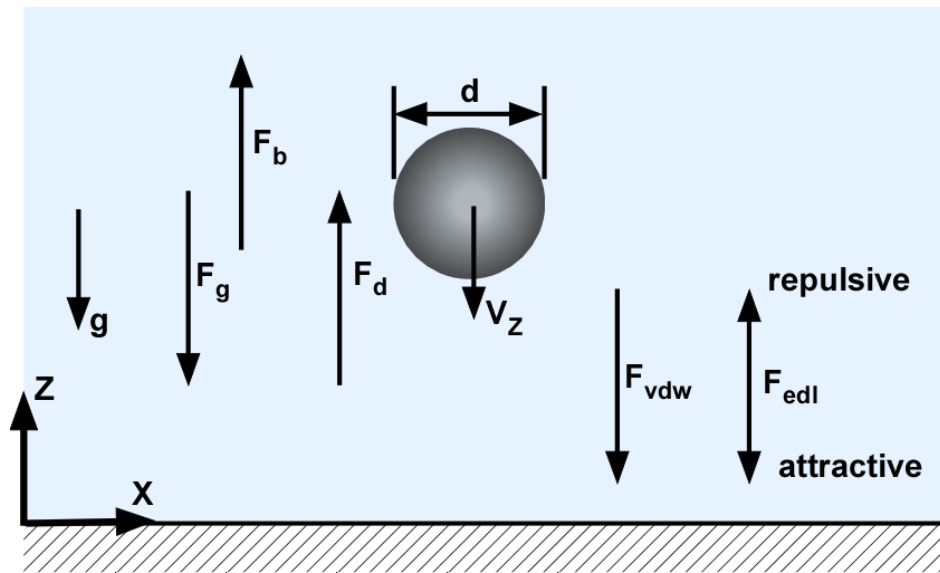


Figure 1.1: A schematic representation of the external forces acting on a colloidal particle of diameter d when it approaches a planar collector surface with velocity V_z under the influence of gravity g in a no external flow condition.

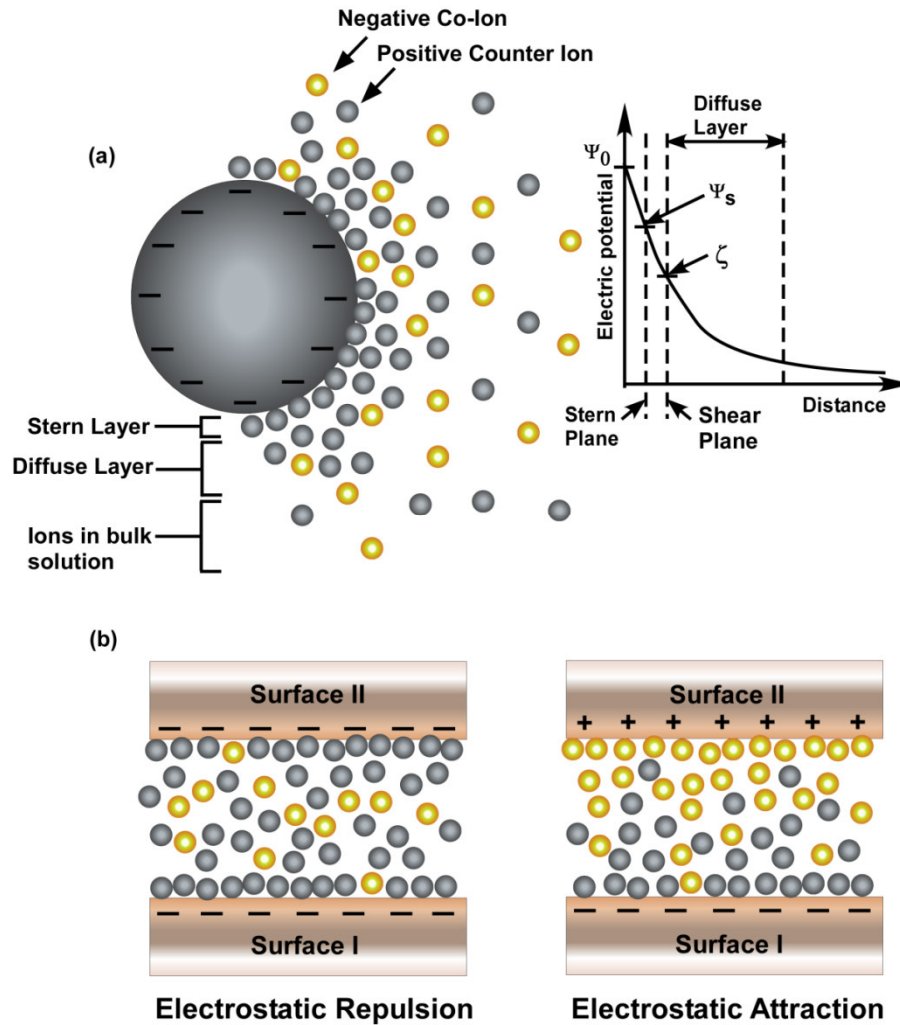


Figure 1.2: (a) Illustration of the electrostatic double layer around a charged particle (according to the Stern model) in an electrolyte solution and corresponding plot of the electric potential versus distance through the double layer showing the surface potential ψ_0 , stern plane potential ψ_s and zeta potential ζ . (b) Sections of two surfaces with the electric double layer interacting between them when both surfaces are likely charged (repulsion) and oppositely charged (attraction) respectively.

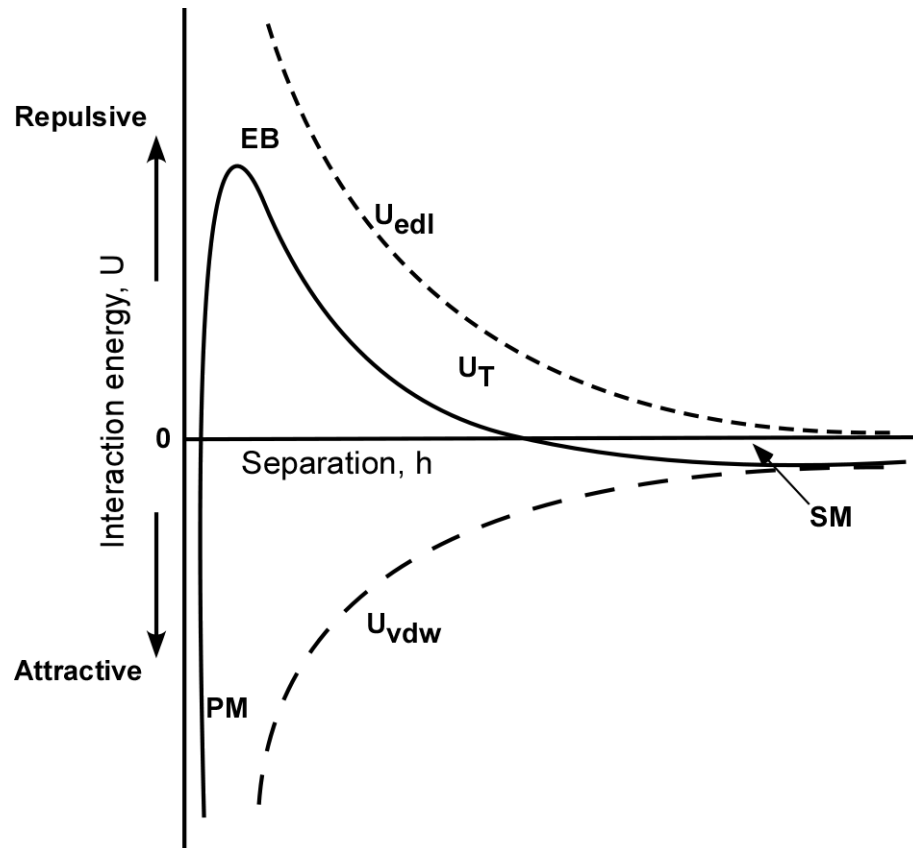


Figure 1.3: A typical potential energy U as a function of separation distance (of closest approach) h , for a particle-plate interaction. The attractive van der Waals energy is denoted by U_{vdw} , the electric double layer repulsion as U_{edl} and the total energy as U_T . The U_T curve shows three distinct features: the primary minimum (PM), the energy barrier (EB) and the secondary minimum (SM).

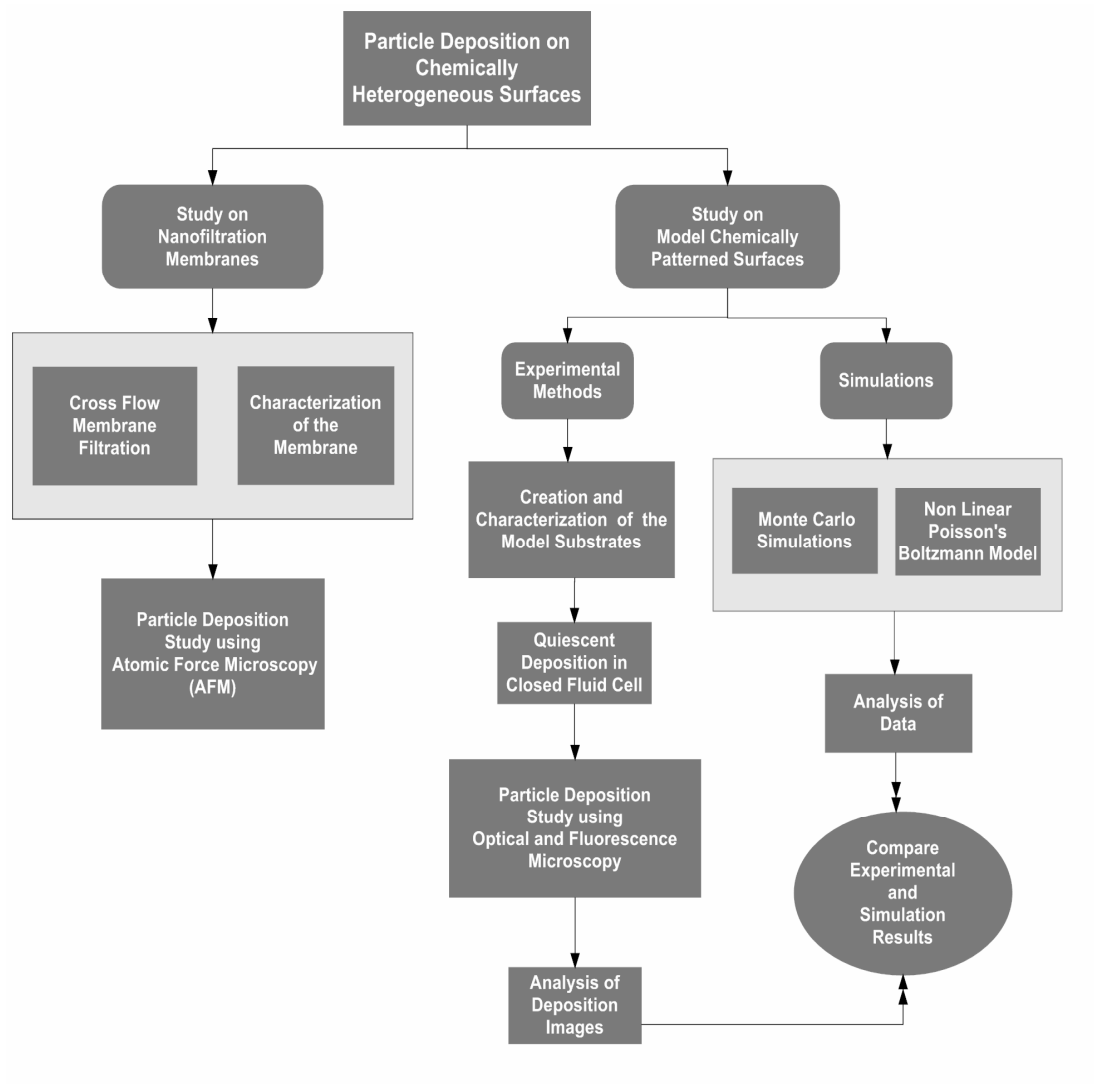


Figure 1.4: Flow diagram depicting the evolution of the research highlighting the relevant sequence of tasks.

CHAPTER 2

PARTICLE DEPOSITION ON ROUGH NANOFILTRATION MEMBRANES

2.1 Introduction

Homogeneous systems (as assumed by the DLVO theory) are rare in nature as real surfaces are typically rough and varied in composition on various scales. Most of the deposition surfaces therefore possess a certain degree of heterogeneity in their chemical and/or topographical features that are often randomly positioned on the surfaces. The aim of this study[†] was to investigate the effect of chemical heterogeneity on deposition in a real system. In this context, studying deposition of submicron sized particles onto a commercially available semi-permeable nanofiltration membrane (NF) serves as a suitable premise for studying particle deposition phenomena in a practical system where the deposition is affected by the heterogeneities inherently present in the system. The goal was to understand the effect of physical heterogeneity on deposition in this system and then impose artificially created chemical heterogeneity on to the membrane to observe the effect this has on particle deposition.

The nanofiltration membrane was primarily chosen because it is known to be rough substrate with a more or less chemically homogenous surface. Morphological investigations by means of Scanning Electron Microscopy (SEM), Transmission Electron Microscopy (TEM), and Atomic Force Microscopy (AFM)

[†] Parts of this chapter are related to the published work of “Tania Rizwan and Subir Bhattacharjee” in the Canadian Journal of Chemical Engineering, v.85, pp 570-579, 2007.

have routinely shown the substrate topography to possess a typical rough terrain [49, 51, 52, 157-159]. The membrane in general is considered to be chemically homogenous in the micro-scale by the scientific community (as suggested by zeta potential measurements and other characterization techniques) [47, 49, 157-159]. However, the membrane top layer is also known to have some chemical variations; but quantifying the chemical heterogeneity that arises due to the chemical structure of the active layer is much less commonly reported partly due to the difficulty in chemically characterizing this extremely thin barrier layer [160, 161].

These membranes are used for nanofiltration of aqueous feed suspensions using a convenient membrane filtration technique that allows simultaneous rejection of large colloidal particles, macromolecules, divalent ions, and considerable amounts of monovalent ions with application of reasonable pressure drops of <100 psi in a single operation [162]. This has led to widespread proliferation of the technique in treatment of aqueous streams in a diverse range of industrial treatment applications. A common problem encountered in this technique, however, is membrane fouling, particularly by deposition of particulate solids and colloidal matter [163-166]. Considerable attention has been devoted to understand the mechanism of membrane fouling, and its abatement. Yet, some concerns remain regarding the true mechanisms and nature of colloidal fouling of nanofiltration membranes (NF).

Conventionally, deposition of colloidal particles on various collectors is addressed by modeling the fluid (solvent) flow using the Navier-Stokes and continuity equations, followed by evaluation of the particle deposition rates from the forces acting on the particles due to fluid drag and long-range particle-collector interactions [1, 15]. The initial stage of membrane fouling is predominantly ascribed to the particle–membrane interactions that favour attachment of the particles to the membrane surface [47, 158]. The interactions between a colloidal particle and the membrane can be due to van der Waals attraction, as well as electric double layer interactions when the particle and membrane are charged [158] and are usually represented using the DLVO theory which is generally based on the assumption of ideally smooth surfaces with uniform

chemical properties of the interacting entities.

Experimental observation of particle deposits on various types of impermeable substrates is fairly common [18, 146, 167]. In contrast imaging of colloidal deposits on a semi-permeable membrane surface is relatively scarce [49]. In particular, experimental studies aimed at directly visualizing the influence of surface heterogeneity of a nanofiltration membrane on the colloidal deposit morphology are rare. Typically, experimental studies involving direct visualization of particle deposits are limited to at least micrometer-sized colloids with fewer experiments conducted to study deposition of sub-micrometer sized colloid on nanofiltration membranes. Observations of particle deposits on smooth impermeable surfaces, particularly at low particle concentrations, seem to be in conformity with the classical continuum models based on DLVO theory [18, 167]. Even colloidal deposits on smooth membranes appear to be fairly homogeneous and qualitatively conform to the classical continuum models [49]. However, on rough membrane surfaces, particularly when the roughness is comparable to or larger than the particles, the deposits appear to be highly localized [49] and cannot be predicted by DLVO based models in which the interactions are commonly modeled assuming the particle to be a sphere, and the membrane to be an infinite smooth planar surface having uniform chemical properties. Thus such modeling approaches have led to considerable discrepancy between theoretical predictions and experimental observations. This is particularly the case for most NF membranes, where the membrane surface is extremely heterogeneous [49, 158].

In this context, (i) morphological heterogeneity or roughness of the interacting surfaces [39, 47, 52, 158], (ii) chemical heterogeneity of the membranes, and (iii) other types of interactions, such as acid-base interactions [158], have been identified as possible sources of the discrepancy between predictions based on DLVO theory and experimental observations of particle deposition onto membranes. Among these alternatives, roughness of membranes seems to offer a reasonably acceptable explanation for the discrepancy between the DLVO model and experimental observations of colloidal membrane fouling. It has been proposed that the interaction energy between a colloidal particle and a rough membrane has

considerable lateral variations, giving rise to localized energy minima where the particles will have a greater tendency to accumulate [49, 168]. Furthermore, during membrane filtration, the enhanced particle concentration at the membrane surface owing to the retained particles may lead to many-body interactions [169] that, even considering ballistic deposition of hard spheres, may result in varied morphologies of the deposit layer [170].

The influence of membrane surface roughness on the particle-membrane interaction energy can be qualitatively assessed from the schematic representations of Figure 2.1. If a particle is much larger than the roughness features of the membrane (Fig. 2.1a), the contact between the particle and the membrane will be at a few isolated points near the peaks [158]. This can generally lead to a lower interaction between the particle and the rough membrane compared to that between the particle and a smooth planar surface. In this case, steric effects will prevent the particle from sampling configurations where it can increase its contact with the membrane surface. When the particle size is comparable to the membrane roughness (Fig. 2.1b), the particles can find locations on the membrane where the contact area between the particle and the membrane are much larger than the corresponding contact area between a particle and a smooth planar surface [47]. In this case, there is decidedly a greater probability of the particles finding a spot in the valleys of the rough membranes to deposit. Finally, when the particle is considerably smaller than the roughness features of the membrane (Fig. 2.1c), there ceases to be a clear interaction energy based distinction between which part of the rough membrane surface is more favourable for deposition. In this case, the particle membrane interaction will tend to approach sphere-flat plate interaction, and there will be no relative preference between the particle adhering to the peak or trough of the rough membrane. In such cases, a question arises as to which regions of the rough membrane the particles will deposit on to. Will deposition occur predominantly at the peaks or in the troughs of the rough surface?

In this context studying particle deposition on NF membranes provides a unique platform for studying the effects of roughness on deposition where the

membrane roughness is comparable or larger than the fouling particles. The fluid velocity field in such a cross flow system is also considerably different from conventional deposition systems. In most conventional deposition systems, the collector (the surface on which particles deposit) is impermeable [15, 171]. In membrane filtration, due to permeation of the solvent through the membrane under an applied transmembrane pressure difference, the fluid velocity normal to the membrane (collector) surface is finite. This finite normally directed flow results in a higher than normal convective force on the particles approaching the membrane. This convective force coupled with other long-range particle-membrane interactions, can lead to several interesting morphological characteristics of the deposited particle layers.

To this end, an experimental study was performed on the initial stages of membrane fouling of commercial NF90 membranes by submicron spherical polystyrene sulphate (PS) particles in a cross flow membrane filtration (CFMF) setup. The structure of the particle deposits were studied using an atomic force microscope (AFM). Because AFM can image surfaces in air or liquid with minimal surface preparation, this has made it the technique of choice in the study of surface morphology and characterization of membranes [172-181]. AFM scans were performed on the fouled membrane surfaces containing deposits of colloidal particles obtained during filtration experiments under different pressures and electrolyte concentrations.

2.2 Materials and Methods

2.2.1 Nanofiltration (NF) Membrane

Commercial polyamide thin film composite (TFC) NF90 membranes supplied by the Dow Chemical Company (Midland, USA) were used in this study. The basic structure of a NF90 membrane is illustrated in Figure 2.2. The membrane structure has a thin dense active barrier layer (thickness $\sim 0.2 \mu\text{m}$) supported by porous sub layers. The actual selectivity of the membrane is determined by this top layer

[162] and such membranes are capable of rejecting over 90% of monovalent ions like sodium (Na^+) [162, 182].

The membranes were stored in deionized water (DI) (Direct Q™, Millipore Corporation, USA) at 5°C with the water replaced regularly. Table 2.1 lists some of the pertinent properties of these commercial membranes. The membranes are reported to be moderately negatively charged (−15 to −25 mV) at typical solution chemistries based on streaming potential analyses performed on similar membranes as reported elsewhere [49, 157-159].

2.2.2 Colloidal Particle and Suspension

An aqueous suspension of polystyrene sulfate (PS) particles (Interfacial Dynamics Corporation, USA) was used as the feed in the membrane fouling experiments. The mean particle diameter as reported by the manufacturer was 100 nm with a coefficient of variation of 4.1%. The electrolyte concentration of the suspension was adjusted to 0.01 M and 0.001 M using ACS grade NaCl (Fisher Scientific, USA). All solutions were freshly prepared using DI water that was collected the day before the experiment and refrigerated at 5°C. The pH measured for the feed solution in the cross flow filtration test was in the range of 6.0-6.4. Pertinent properties of the colloidal particles and the suspension are given in Table 2.2.

2.2.3 Quiescent (No Flow) Deposition

Membrane samples containing adsorbed PS particles were prepared for AFM analysis by carefully immersing clean membrane coupons in the same diluted PS suspensions as used for the deposition study ($N_p = 10^{16}$ particles/m³ in 0.01 M NaCl solution) with minimal agitation or mixing of the fluid. The membrane coupons were handled using clean stainless-steel forceps to prevent contamination of the suspension. Particles were allowed to adsorb from the fluid to the membrane surfaces for a controlled period of time (3 days). The membrane coupons were then withdrawn from the suspensions and dried thoroughly in air prior to imaging.

2.2.4 Cross Flow Membrane Filtration (CFMF) Setup

A schematic diagram of the laboratory-scale membrane test unit used in the cross flow membrane filtration (CFMF) experiments is shown in Figure 2.3. The colloidal suspension, held in a 15 L polypropylene feed tank, was fed to the inlet port of the membrane module by a pump. The flow rate of the feed suspension was measured by a floating disc rotameter connected between the outlet to the membrane module and the reservoir inlet. The transmembrane pressure was controlled by a needle valve installed on the outlet side of the membrane module. Pressure gauges connected to the inlet and outlet side of the membrane module measured the transmembrane pressure.

Initially the CFMF test unit was flushed with DI water for about 3 to 4 h to remove any build up of organic contaminants in the system. At the start of each run, membrane coupons of roughly the size of 29 cm by 5.5 cm were cut from a rolled sheet of membrane and washed with copious amounts of DI water. The membrane coupon was immediately loaded onto the CFMF test unit. The membrane was equilibrated before the experiment in order to dissociate any flux decline due to compaction. Membrane equilibration was carried out at about 60 psi pressure by filtering of DI water through the system (permeate and retentate are both recycled) until a satisfactory steady state is achieved. Once equilibrium was reached, an electrolyte (NaCl) solution was added to the feed tank to provide the appropriate background electrolyte concentration. The pressure was adjusted to the desired level to obtain the initial permeation rate and the solution was recirculated through the system until a satisfactory steady state was achieved. The duration of the initial equilibration stage was about 60 min for each membrane sample, but typical electrolyte solution equilibration time was about 30 min. Finally, a measured dose of PS particles (model foulant) was added to the feed tank to provide a colloidal concentration $N_p = 10^{16}$ particles/m³. The flow rate was kept constant at 6.33×10^{-5} m³/s (1 gallon per minute). Once the PS particles were added, the system was allowed to run for 10 min to allow particle deposition on the membrane. Following this, the system was depressurized, dismantled, and the

membrane was promptly removed and prepared for AFM imaging. Several such runs were performed consecutively for different samples of the membrane at ionic strengths of 0.001 and 0.01 M NaCl under pressures of 275, 415, and 550 kPa (40, 60 and 80 psi, respectively). A sample of the feed solution was collected for pH measurements at the end of each experiment. The feed solution pH was found to range within 6.03 to 6.40 in all the experiments. A few filtration experiments were conducted for longer durations (up to about 1 h) to observe how the cake deposits appear after a continuous filtration over a longer duration. No measurable permeate flux decline was observed during any of the 10 minute fouling experiments.

The experimental conditions used in terms of applied pressure, flow rates, and feed suspension conditions are similar to those as reported in other lab-scale membrane filtration studies [49, 158, 159, 183]. The particle concentration used in the filtration experiments (10^{16} m^{-3}) might be slightly higher than encountered in a practical nanofiltration operation, approximately 200 mg/L (compared to 100 mg/L in Boussu *et al.* [159]). However, the particle concentration is still sufficiently low to ensure that particle-particle interactions are not manifested strongly in the bulk suspension.

2.2.5 Atomic Force Microscopy (AFM) Imaging

AFM imaging of the dried samples was performed with a Bioscope™ Atomic Force Microscope (Digital Instruments, USA) using the technique of Tapping Mode™ (TM) in air [184]. A brief description of the working principle of an AFM and the Tapping Mode is given in Appendix A. In this mode, the lateral forces and shearing forces that are necessarily applied to the sample in contact mode AFM [185] where the tip maintains continuous contact with the sample, are avoided through the intermittent contact of the probe, making this a preferable mode for the imaging of adsorbed particles. In the absence of the lateral forces, particles that are held weakly to the surface can be imaged without altering the positions of the particles on the surface. Etched silicon probes (TESP, Digital Instruments, USA) were used which consisted of a single-crystal silicon tip with a

nominal tip radius of 5-10 nm, mounted on a single-beam cantilever of length 160 μm . The TESP probes had a spring constant of 20-100 N/m and resonant frequency of 200-400 kHz.

Prior to imaging, the membrane was cut roughly into 2 cm^2 sections and allowed to air dry. The coupons were then mounted on glass slides using epoxy resin and allowed to set overnight in a covered Petri dish. A scan rate of 0.5 Hz was used with a 512×512 pixel resolution. All post-processing operations were performed using the NanoscopeTM IIIa imaging software Version: 5.12b36 (Digital Instruments, USA). Edge and contrast enhancement were performed on all images to improve the resolution.

The membrane samples were cut from different axial positions of the original fouled membrane. The sample images for AFM analysis presented in the following sections were obtained from a specific location at 6.3 cm downstream from the leading edge of the active filtration area of the membrane, unless noted otherwise. All samples were subjected to a minimum of two scans on the same area, and different areas on the same coupon were also scanned.

2.2.6 Roughness Analysis

Membrane surface roughness was determined by the AFM imaging and post analysis using the NanoscopeTM IIIa imaging software. Imaging was performed in the tapping mode as described in the above section. Clean membrane coupons were removed from storage in deionized water and allowed to dry before AFM scans were performed. Several statistical parameters that have been used to quantitatively describe the roughness of the membrane surface are summarized in Table 2.3. These parameters were recorded for $10 \mu\text{m} \times 10 \mu\text{m}$ sections for clean membrane and $8 \mu\text{m} \times 8 \mu\text{m}$ sections for fouled ones.

2.2.7 Bearing Analysis

Bearing analysis of the AFM images were used to infer the height information pertinent to this study, and this section briefly describes the methodology em-

ployed. The word bearing refers to the relative roughness of a surface in terms of high and low areas [186]. A bearing analysis reveals how much of a surface lies above or below a given height. This measurement provides additional information beyond standard roughness measurements. Surface roughness is generally represented in terms of statistical deviation from average height; however, this gives little indication of height distribution over the surface. By using bearing analysis, it is possible to determine what percentage of the surface (the bearing ratio) lies above or below any arbitrarily chosen height. The bearing height Z_b is the height where the bearing plane is located, and is defined relative to the lowest scanned height (deepest point in the valley) of an AFM image. In this study, the bearing analysis was used to obtain the following information: percentage of area present (the bearing ratio) above a specified bearing height, Z_b , and, the amount of particles deposited below Z_b .

For a clean membrane, the bearing analysis was used to determine what percentage of the membrane surface is located above different bearing planes. For fouled membrane samples, since the foulant particles were model spherical colloids, their topographies were uniquely visible on the membrane in the AFM images. In this case, the bearing analysis provides quantitative information about what fraction of the deposited particles are located below (or above) specific bearing planes. Figure 2.4 depicts the methodology employed for this analysis. In Fig. 2.4a, a typical scan of a fouled membrane is shown, which depicts the particle deposits on the membrane after about 10 minutes of filtration. The 100 nm diameter particles are clearly identified in the image. Fig. 2.4b shows a bearing analysis image of the same membrane, where the white regions indicate the areas located *above* a bearing plane of 400 nm (measured from the *lowest* scanned point of the image). In this image, the area rendered in white was approximately 12.9% of the total image area. When the bearing image is overlaid on the topographic image (Fig. 2.4c), the red shade (bearing area) covers the membrane areas that are above 400 nm. The regions lying lower than 400 nm remain visible. One can now count the particles exposed in this image, or change the bearing plane height until no particles are visible in the composite image. For

instance, it becomes evident from Fig. 2.4c that all the particles deposited on the membrane are covered by the red highlighted area, and hence, have deposited above a height of 400 nm. Fig. 2.4d shows a schematic presentation of the bearing analysis. The image shows the cross sectional view of a membrane showing the rough terrain of the surface. The area above a chosen Z_b is rendered red and covers all the particles present in this region. The particles below Z_b remain visible and can be counted.

The above process is summarized as follows:

Step 1: Obtain a topographic image of a representative area on the membrane in the tapping mode. The model particles are clearly visible against the membrane structure in these images (Fig. 2.4a).

Step 2: Select a bearing plane height, Z_b heights (relative to the lowest scanned point) based on the maximum roughness of the sample. The bearing height Z_b is measured from the lowest scanned point of the image area. Thus for example, if roughness analysis reveals $R_{max} = 600$ nm, then a bearing height of 500 nm can be chosen as the starting point for analysis. Regions lying above the chosen bearing plane are rendered white and quantified in percentage of the total area. This constitutes the bearing image (Fig. 2.4b).

Step 3: The bearing image is overlaid on top of the topographic one to obtain a composite bearing image. This is done for better visualization and for obtaining a quantitative measure of the number of particles residing in regions below the bearing plane. In this composite image (Fig. 2.4c) the fouling 100 nm diameter particles are clearly identifiable. The red shade covers the membrane areas (and any particles lying in that area) above the chosen bearing height Z_b while the regions lying below Z_b remain visible. The particles detectable in these regions in the composite image can now be counted.

Based on the results of the roughness analysis, a few bearing heights were selected that are progressively decreasing in value. For each of these, the above steps are repeated. Bearing heights of 500 nm, 400 nm, 300 nm, 200 nm *etc.* would be chosen until a height value is reached at which no particles are visible in the composite image. The results of each bearing analysis are then compiled in

the form of a histogram that plots the percentage of the particles seen above the chosen set of bearing heights. The bearing ratio (or percentage area present above the corresponding bearing height) is also recorded on the histogram.

2.3 Characterization of NF90 Membranes

2.3.1 Surface Morphology

Figure 2.5 shows Scanning Electron Microscopy (SEM) images of a typical area on a clean NF90 membrane in two different scan sizes to illustrate the dramatic differences in the morphology between them. Fig. 2.5a represents a membrane area of roughly $120\ \mu\text{m}$ by $90\ \mu\text{m}$. At this scale, the membrane appears to be quite smooth and dense because the pores are not visible at this magnification. Fig. 2.5b is a magnified image of a smaller area in the previous image. The $6.25\ \mu\text{m} \times 5.5\ \mu\text{m}$ (approximately) image provides a better view of the membrane terrain. At this magnification, the membrane surface appears rough with numerous pores. However, since the height information is not recorded in these 2D images, it becomes difficult to perceive the height variations (roughness) from these images alone.

Figure 2.6a show tapping mode images obtained from the AFM for two $10\ \mu\text{m} \times 10\ \mu\text{m}$ sample areas on the membrane surface and Fig. 2.6b show the corresponding rendered 3D topographical image of the same membrane area. Although, the AFM images lack the resolution of the SEM images of Fig. 2.5 and cannot capture the exact shape of surface roughness features, the magnitude and periodicity of roughness features are retained in these images. The topographic images represent the membrane surface with information on the depth of the samples (z -direction) coded in colour intensity where the light regions are the highest points and the darker regions the pores. The images show a topographic relief having a fine network-like fibrous structure, similar to the ones observed in Fig. 2.5b. The rendered 3D orthographic image (Fig. 2.6b) shows the occurrence of peaks and valleys. It should be emphasized that the z -axis is expanded relative to the x - y plane; therefore, the surfaces are not as ‘bumpy’ as they appear on the images.

2.3.2 Roughness of NF90 Membranes

The morphological features in the AFM images are defined by x , y , and z coordinates, which indicate the relative height (z) of the cantilever tip at each x and y planar location. Quantitatively, the differences in the membrane surface morphology can be expressed in terms of the following AFM “roughness analysis” parameters: mean (Z_{mean}), average roughness (R_a), root-mean-square (RMS) roughness (R_q), surface area difference (SAD), and maximum roughness (R_{max}) as defined in Table 2.3. These parameters were calculated for all studied surfaces. Table 2.4 shows the results for roughness analysis performed on the two representative samples CM1 and CM2 as shown in Figure 2.5. The table also includes roughness analysis data obtained for NF70 membranes [47] for comparison. Qualitatively, the surface roughness appears consistent with the high degrees of roughness reported for NF70 and NF90 membranes [47, 159].

The mean value, Z_{mean} is defined as the arithmetic mean of all height data obtained from an AFM surface scan. The mean value represents the absolute z -value of the mean-plane that is drawn through the cross section of peaks and valleys for a rough surface. The calculated Z_{mean} is typically nonzero because all data points are measured with respect to the starting elevation of the AFM probe tip, which is arbitrary. For the surface areas analyzed in this study the mean value was found to be quite small (approximately 0.1 nm).

The average roughness (R_a) measured by AFM is the average deviation of the measured z -values from the mean plane. While R_a is useful as a general guideline of surface texture, it typically proves too general to describe the surface’s functional nature. R_a makes no distinction between peaks and valleys, nor does it provide information about spatial structure. Thus a surface with sharp spikes, deep pits or general isotropy could all yield the same average roughness value. However, R_a used in conjunction with the parameters discussed below provides an adequate description of the membrane profile for the analysis. Based on the R_a values obtained for the NF90 membranes, it can be said that the membranes are quite rough and are rougher than the NF70 membrane.

Root-mean-square roughness (R_q) effectively describes the standard deviation of an entire distribution of z -values for a large sample size. In Table 2.4, for the membranes tested the R_q values increase in the same order as the average roughness and are larger in magnitude than the average roughness value. This high value of standard deviation indicates that the height data are spread out over a large range of values around the mean.

Maximum roughness (R_{max}) indicates the difference between the largest positive and negative z -values. This does not indicate that any peak-to-valley depth of this magnitude exists, but more accurately provides quantification of the spread of the distribution of measured asperity heights. This value also helped provide a starting point for the bearing analysis. The range of R_{max} was found to range from 800 to 600 nm for the membrane samples tested.

The average roughness parameters by the AFM statistics indicate that the roughness is limited to about 100 nm around a mean plane. This led to the selection of the 100 nm particles for the experiments so that the particle dimensions were made comparable to the statistical roughness of the membrane. Although most of the surface will have a roughness of the order of 100 nm, a closer look at the bearing analysis results in Table 2.4 indicates that relative to the lowest scanned depth of the membrane, there are peak regions that extend to over 500 nm. The analysis indicates, for example, for the membrane sample CM1 there is approximately 19% of the area that projects beyond 300 nm, about 6% above 400 nm and about 1.3% above 500 nm. Thus the membrane surface has a small percentage of area that protrudes to a considerable distance above the lowest scanned depth that can extend well beyond 4 to 5 times the particle diameter (100 nm) used in the fouling experiments from the lowest points in the valleys.

2.3.3 Chemical Analysis of NF90 membranes

The FilmTec NF90 membranes are thin film composite cross linked aromatic polyamide (PA) membranes produced by interfacial polymerization [187, 188] and having amide bonds (-CONH-) (see Table 2.1). For a fully aromatic polyamide, aromatic amine monomers (such as 1,3-phenylenediamine) in an aqueous

solution are brought into contact with aromatic acid chloride monomers (such as 1,3,5-benzentricarbonyl chloride) in an organic solvent [182, 189, 190] to form the PA layer that is typically rough, (due to the ridge-and-valley structures) and is less than a few 100 nm thick [160]. This thin top layer acts as the active layer and because it is formed by interfacial polymerization process, the structure and composition of the top layer is highly inhomogeneous [160, 162, 191]. Even such basic physical and chemical properties of the membrane as the atomic density, swelling in water, distribution of charged species, and the mobility of water and ions, are poorly understood [192]. The extreme thinness of the skin, which is the key to the success of NF membranes, also constitutes a major obstacle to understanding their structure and functioning [160, 192].

Some of the most widely used in membrane chemical composition and surface charge characterization techniques include methods such as X-ray Photoelectron Spectroscopy (XPS) [181, 193, 194], Attenuated Total Reflection Fourier Transform Infrared Spectroscopy (ATR-FTIR) [195-198], Nuclear Magnetic Resonance Spectroscopy (NMR) [181, 193], and streaming potential analysis [190, 199, 200]. Some of the microscopic tools used that are mostly for investigating membrane morphology at a length scale spanning from a several nanometres to hundreds of micrometers, have also been used to investigate the chemical and charge characteristics of NF membranes, such as Scanning Electron Microscopy (SEM) [160], Transmission Electron Microscopy (TEM) [160, 195, 201, 202] and Atomic Force Microscopy (AFM) [51, 52, 161, 203].

Of all the above methodologies, the Fourier Transform Infra Red (FTIR) was opted as the method of choice for analyzing the chemistry of the top layer. FTIR spectroscopy is a most powerful tool for identifying types of chemical bonds (functional groups) by detecting the vibration characteristics of the chemical functional groups in a sample. While being less quantitative than XPS, which measures elemental composition (except H), and chemical bonding information for the top 1-5 nm depth of the surface region, FTIR is able to provide significant qualitative detail about the types of functional groups present in both the polyamide and polysulfone layers. In the FTIR instrument, when an infrared light

interacts with the sample, chemical bonds stretch, contract and bend. As a result, a chemical functional group tends to adsorb infrared radiation in a specific wave number range and the wave number positions, despite the effect of temperature, pressure, sampling, or regardless of the structure of the rest of the molecule [204]. For example, the C=O stretch of a carbonyl group appears at around 1700 cm^{-1} in a variety of molecules. The wavelength of light absorbed is characteristic of the chemical bond and by interpreting the infrared absorption spectrum, the chemical bonds in a molecule can be determined. Hence, the correlation of the band wave number position with the chemical structure is used to identify a functional group in a sample. FTIR spectra of pure compounds are generally so unique that they are like a molecular "fingerprint". For most common materials, the spectrum of an unknown can be identified by comparison to a library of known compounds. A brief description of the working of a FTIR spectrometer is given in Appendix A.

To analyze the chemical composition of NF90 membranes, samples were cut and dried in air and were placed in a Nexus 670 FTIR spectrometer (Thermo Electron Corporation, USA) equipped with Nicolet Continuum FTIR microscope and a low-noise mercury-cadmium-tellurium (MCT) detector cooled with liquid nitrogen to about 77 K . A PIKE Technologies Variable Angle Accessory was employed. Infrared Reflection Absorption Spectroscopy (IRRAS) spectra were collected at 4 cm^{-1} resolution with a glancing angle of 72° . Several samples were scanned and three replicate FTIR spectra were obtained for each membrane sample, with each spectrum averaged from 500 scans collected from 650 to 4000 cm^{-1} at 4 cm^{-1} resolution. These spectra were subsequently corrected for background. The reverse side of the membrane was used as the background. Both samples and background spectra were collected with the same instrument parameters and under similar conditions.

Figure 2.7 is an IRRAS spectrum collected for the NF90 membrane shown over the range of 3800 cm^{-1} to 750 cm^{-1} and is similar to those obtained in previous studies [190, 205-207]. The broad peak centered at 3300 cm^{-1} is due to overlapping of stretching vibration of N-H and carboxylic groups in the polyam-

ide layer. The peaks in the range of 2800-3000 cm^{-1} may be assigned C–H stretching [190, 204]. The presence of the amide I (C=O stretch) peak at 1660 cm^{-1} and the presence of the amide II peak near 1541 cm^{-1} show that the active layer was made from a primary amine (1,3 benzene diamine) [205, 206]. Peaks at 1610 cm^{-1} and in between 1480 cm^{-1} , 1350 cm^{-1} indicate NH_2 deformation and carboxylate deformation respectively [204]. Finally, the peaks near 1584 cm^{-1} , 1503 cm^{-1} , 1487 cm^{-1} , and 1151 cm^{-1} , all correspond to the polysulfone support [196, 205, 207].

This chemical analysis shows that over the scan areas studied (a few micrometers in dimension), the basic membrane chemical composition is consistent with what has been reported by the manufacturer. In addition to having a complex aromatic polyamide structure, there are presences of the amine and carboxylate functional groups within the polymer structure. A complete chemical mapping of the membrane surface would be useful to provide information regarding the spatial location of the heterogeneity with respect to the morphology of the membrane surface. This was however not performed due to the lack of spatial resolution of the FTIR instrumentation (minimum resolution 2 μm).

2.4 Deposition during No Flow Conditions

2.4.1 Deposit Morphology

Figure 2.8 depicts the result of the quiescent deposition experiment where the membrane was immersed in a quiescent colloidal (100 nm PS particle) suspension of 0.01 M ionic strength for 3 days. The images represent an 8 $\mu\text{m} \times 8 \mu\text{m}$ area on the membrane surface captured using the AFM in the tapping mode in air.

The prominent feature that differentiates this image from that of the clean membrane (as seen in Fig. 2.6a) is the presence of the nano-particles which are identifiable owing to their distinct spherical shape. The particle deposits are clearly visible on the membrane, with a greater accumulation of particles at the peaks or ridges of the rough membrane. These quiescent deposition experiments

reveal that the particles are indeed captured by the membrane under the chemical conditions used in the experiments, even in absence of hydrodynamic forces. Furthermore, the capture predominantly occurs at the peaks or ridges of the membrane. Virtually no deposition could be observed in the valleys.

2.4.2 Dry versus Wet AFM Imaging

One aspect of these experiments that could potentially alter the particle deposit structure was the air drying of the membrane for AFM imaging. It is understood that such concerns regarding the modification of the deposit structure will inevitably arise with any ‘post mortem’ technique employed for characterization of particle deposits on a membrane. The drying process employed in these experiments was adopted after several attempts to minimize the effect of drying on the deposit structure. Notably, the membranes being porous hydrophilic structures, some moisture is retained in the interior of the membrane even after the overnight drying process in a closed Petri dish.

To investigate the effect of drying on the membrane samples, two sets of clean and fouled membranes samples were imaged under deionized water (DI) using a fluid cell in the tapping mode and compared with AFM images obtained in the dry mode (in air). The clean membrane sample (which is normally stored under DI water) was cut into a small piece and immediately prepared for imaging. For the fouled sample, the wet scanning was done immediately after the end of the deposition experiment. In each case, the membrane piece was glued to a glass slide and mounted on the imaging platform, and a drop of deionized water placed on it to maintain an aqueous environment and to prevent further drying. Generally, several trials were conducted to indicate what happens to the membrane/deposit structure as the membrane progressively dries.

Figure 2.9 depicts results of the wet mode scans. In Fig. 2.9a, the AFM image shows a topographic view of a clean membrane surface scanned in the wet mode. Comparing this wet mode image with the ones taken in air (dry mode) in Fig. 2.5, it is seen that the AFM images shows the structure of the membrane to be the same under both operations with no significant differences between them. The

images obtained in air are however, sharper than those obtained under liquid. The primary reason for this is the difficulty in gluing the underside of the wet sample to the slide so that it remains immobile during scanning.

Fig. 2.9b depicts the wet mode image of a membrane sample in quiescent deposition. The deposition lasted for 3 days at room temperature (25°C) in the colloidal suspension of ionic strength, $I = 0.001$ M NaCl, particle concentration $N_p = 10^{16} \text{m}^{-3}$ and pH = 6.4. Comparing Fig. 2.6 with Fig. 2.9b, despite the difference in the scanning methodology (dry vs. wet respectively), the deposit structures show remarkable similarities. Both images show particles to be distributed along the higher regions of the membrane surface. A slightly larger proportion of the particles appear to remain more randomly distributed over the scanned surface in Fig. 2.9b. The difference in the two deposit morphologies can be due to repositioning of the particles during drying, as well as due to the influence of ionic strength on the deposit structure. Notwithstanding the possibility of alterations in the deposit morphology owing to drying, the wet and dry imaging results indicate that a majority of the particles deposit at the higher elevations of the membrane.

It, therefore, can be concluded that although drying induced restructuring may not have been completely avoided in these experiments, the essential trend of the deposition, namely, depositions of particles on the elevated regions of the membrane are shown in both dry and wet mode scans. The drying process may have contributed to enhanced clustering of the particles as the water recedes, due to drying, from the top to the bottom of the membrane causing the particle clusters to become more closely packed (capillary action is dominant when particles are closer together and would result in some rearrangement in the particle deposit structure [208]). This implies that those particles that have deposited on the peaks (or valleys) will have neighbouring particles close enough for the clustering to occur. Also as an effect of drying, one would expect the particles around the peaks to be pulled down to the valleys as the water recedes resulting in more particles near the valleys rather than on the peaks. However this was not the case as can be seen in all the dried membrane images. This observation counters the possibility of particles reordering from the peaks to valleys or vice versa during

the air drying of the membrane samples. Based on these observations, the dry mode technique was adopted as the method for imaging over the wet mode.

2.5 Deposit Morphologies during Tangential Flow Conditions

2.5.1 Operating Pressure

Figure 2.10 depicts AFM images of the particles deposited onto the membrane surfaces under different operating pressures keeping the ionic strength of the colloidal suspension fixed at 0.01 M. All the membrane samples were obtained after 10 min of filtration, and had been cut from roughly the same location of the membrane (same axial position) in the filtration experiment. Each image represents an $8\ \mu\text{m} \times 8\ \mu\text{m}$ area on the membrane surface. Changes in height across the area are denoted in the colour scale bars accompanying the images, higher regions being represented by lighter colours. The AFM images of the fouled membranes reveal clusters of densely packed polystyrene PS particles adsorbed onto the membrane. The clusters appear to be predominantly present at the higher elevations (peaks or ridges) of the membrane rather than in the valleys. Note that the numbers of particles deposited on the membrane in these filtration experiments are comparable to or larger than the corresponding number in the quiescent deposition experiment, even though the filtration experiments were conducted for only 10 min (as opposed to three days for the quiescent deposition experiments). Counting the number of particles deposited in each AFM image of Fig. 2.10, it was observed that with increase in operating pressure, there is a corresponding increase in the number of particles deposited on the membrane. However, all three images in Fig. 2.10 show the colloidal particles to cluster around the crests of the rough membranes, rather than in the crevasses. The AFM imaging was repeated with different samples of the membrane cut from different axial locations. In all cases, the increase in deposition with increase in operating pressure was observed.

2.5.2 Ionic Strength

Figure 2.11 depicts the particle deposits on the membrane obtained for two different suspension ionic strengths (0.001 M and 0.01 M) corresponding to a fixed applied pressure of 415 kPa (60 psi). For the low ionic strength suspension, more particles deposit on the membrane (Fig. 2.11a) compared to the higher ionic strength (Fig. 2.11b). It is also evident that the deposition at the lower ionic strength is somewhat more scattered, with particles depositing even on the depressed regions of the membrane. However, there is a distinct tendency of the particles to deposit on the ridges and peaks as opposed to the valleys. The deposition at the higher ionic strength, on the other hand, is predominantly confined to the highest peaks and ridges.

Thus, a visual inspection of all the above AFM deposition images indicates that the number of adsorbed particles on or near the peaks and ridges clearly outweighs the number of particles in the valleys for each of the experimental conditions investigated.

2.5.3 Bearing Analysis

To obtain a quantitative verification of the distribution of particles observed in all the images shown above, a bearing analysis as described in Section 2.2.7 (Fig. 2.3) was systematically conducted on all the images obtained. Figure 2.12 represents one such set of AFM images on which a bearing analysis was performed. In the figure, the AFM images are labelled 41 to 45 and denote that the samples have been taken from upstream (41) to downstream (45). Based on the roughness analysis of these membranes, the maximum height, R_{max} , of the membranes are found to be in the order of 700 nm. The mid plane located at a height of around 350 nm from the lowest scanned elevation of the corresponding image. Table 2.5 and Figure 2.13 represent the bearing analysis performed on the images in Fig. 2.12. All these images were subjected to bearing analysis using bearing heights between 600 nm to 0 nm at 100 nm intervals.

The bar charts in Fig. 2.13 represent the particle distribution obtained from the

bearing analysis. In all cases, it was observed that over 80% of the particles (nearly 100% in case of membranes labelled 41 and 45) were deposited above 300 nm. The plane located at 300 nm represents the mean plane position of the rough membrane. It is evident from the analysis that the particle deposition locations coincide with the higher regions of the membrane, with none depositing below the mean plane in the valleys. The average deviation (above or below) the mean plane of the scanned surface, hence, the average roughness feature size is about 120 to 140 nm, roughly the same size as the particles. The RMS roughness value mathematically represents the standard deviation of roughness features. Statistically, approximately two-thirds of all surface roughness features are smaller than about 150-180 nm. Only a small number of surface features sampled by the AFM probe tip are in the order of 400-700 nm. These small regions of the membrane that are significantly rougher are the locations where the particle deposition was found to initiate. The propensity of the particles to deposit above this mean plane clearly indicates that during initial stages of colloidal fouling, valley clogging is virtually non-existent in these experiments. Using bearing analysis, quantitatively it was shown that the percentage of the surface that constitutes these high peak regions (beyond heights of 400 nm and 500 nm) are not more than 20% on average. The interesting fact of these measurements is that in virtually every experiment it was observed that most of the particles deposit in these highest regions above 300 nm measured from the base. Thus the deposition does not correlate well with the statistical roughness characteristics of the membrane, since they are predominantly triggered by the outliers of the roughness distribution.

2.5.4 Long Term Deposition

Some additional experiments were conducted to observe the deposit structures after a longer duration of filtration. Figure 2.14 depicts two AFM images obtained after filtration of polystyrene PS suspensions for (a) 30 min, and (b) over 1 h under a pressure of 80 psi. It is evident that the uniform coverage of the rough membrane by a particle deposit requires considerable time during filtration at the bulk colloid concentrations used in the experiments. From Fig. 2.14a, it is evident

that even after 30 min the valleys in the membrane are still vacant. It appears that the initially deposited particles on the ridges and peaks of the membrane act as seeds for capture of more colloidal particles in this case. It is only at very late stages of the filtration that the cake deposit appears uniform (Fig. 2.14b), and covers the entire surface of the membrane.

2.6 Effect of Membrane Heterogeneity on Colloidal and Hydrodynamic Interactions

To summarize, the system investigated in this study involved the interactions of 100 nm diameter particles with a surface that has a few scattered asperities protruding as much as 600 nm from the lowest point of the membrane. The study revealed that a large number of particles are adsorbed to the elevated regions of the membrane. The tendency of the particles to deposit at the peaks ridges of the membrane, and form increasingly larger aggregates as filtration progresses cannot be explained readily. This observation is in contrast to what is normally observed for particle deposition on smoother membranes as well as speculations regarding deposit structures based on purely interaction energy considerations [47]. Even a visual and purely qualitative appraisal of these images suggests that the deposition process is highly localized around the peaks of the rough membranes which are corroborated by the quantification made using the bearing analysis.

When the solvent permeates through a rough membrane, the bottom of a valley (pore) presents the path of least resistance to solvent permeation. Hence, the permeation of solvent through the rough membrane would be confined to these regions while the normal convective force on the particles will tend to draw these into the valleys. Yet, the experimental observations from this study seem to refute the notion that initial deposition on rough surfaces is localized within the valleys of the rough substrate. It is also discernable that the peaks of the rough membrane will have a small radius of curvature, which may significantly alter the magnitude of the electrostatic energy barrier. However, even when such peaks and ridges are covered by particles (*cf.* Fig. 2.8, Fig. 2.9, and Fig. 2.10) more particles tend to

cluster around them, forming aggregates. The colloidal particles have a substantial negative charge. For the given particle size and range of ionic strengths, the repulsive energy barrier based on DLVO theory will be about 30-50 $k_B T$ (k_B being the Boltzmann constant and T , the temperature). Thus, the deposition process should be unfavourable for such surfaces.

From a purely qualitative appraisal of the images, one of two conclusions can be drawn regarding the position of the particle deposits:

- *The particles were seen to have deposited in valleys and stacked up on each other to form columnar structures.* This is highly improbable because such free standing structure would be very unstable as AFM imaging was done on dried samples. The average thickness of the barrier layer of the TFC membrane is 200 nm [182] and the maximum peak to valley height is within 1 μm . The maximum vertical distance (Z) that the AFM probe can sample is around 6 μm which implies that the entire depth of the membrane could be scanned. Within these limits, very few particles were seen at the deepest valleys.
- *Particles are depositing initially on the peaks.* The peaks are possibly acting as precursors for deposition. Drying of the membrane during sample preparation cannot be responsible for the particles depositing on the peaks because it would cause the particles to be pulled down into the valleys as the water recedes. Thus observation that the peaks act as “particle collectors” is the most probable interpretation of the images.

Another observation made was that particle deposition is more pronounced at higher pressures and lower ionic strengths, which can be readily explained by considering the convective and colloidal forces. At higher operating pressures, the convective force on the particles owing to permeation drag of the solvent will be higher, thereby increasing particle deposition. Based on the DLVO theory, the total colloidal force between the particle and the membrane is obtained by adding the van der Waals attraction and the electric double layer (or screened Coulomb) repulsion. At higher ionic strengths, the electric double layer interaction is screened substantially, which gives rise to a sharply increasing repulsive force

barrier at close separations between the particle and the collector. In contrast, at lower ionic strengths, the longer range of the electric double layer interaction results in a more gradual rise in the repulsive force over a larger separation distance. In other words, the repulsive energy barrier is pushed further away from the collector surface at lower ionic strengths. The hydrodynamic force on the particle, which increases with separation distance from the collector surface, may easily overcome the repulsive energy barrier formed at a larger separation at lower ionic strengths. This inverse dependence of deposition rate on suspension ionic strength is relatively well understood [209] and the results seem to be in conformity with this picture.

The system studied in these experiments involves colloidal interactions between flowing particles of radius 50 nm with asperities that are generally 400-700 nm. Thus, these systems represent the case described in Fig. 2.1c. Based on the surface properties of the particles and the membranes, the colloidal interactions (in a DLVO context) will consist of short-range electric double layer repulsion and a long-range van der Waals attraction between the membrane and the particles. The ionic strength of the bulk suspension used in the experiments, and the fact that ion rejection by the membrane can potentially increase the local ionic strength in the vicinity of the membrane [15], render the screening length of the electric double layer (κa_p) $\gg 1$. Thus, the electric double layer interaction between the particle and the membrane is extremely short-ranged in this system compared to the range of the van der Waals attraction and particularly the hydrodynamic interaction.

Hoek *et al.* [157] obtained the interaction energy distribution on rough membranes employing a technique called Surface Element Integration (SEI) [210] that provided the interaction energy between a test particle and a small region of the rough substrate in the vicinity of the point of closest approach between the particle and the membrane. A later study [211] showed that the lateral and normal forces experienced by a colloidal particle as it approaches a surface containing spherical asperities undergoes considerable modifications. In particular, when the test particle is smaller than the asperity, repulsion between multiple asperities and

the test particle can result in a net normal force that decelerates the approach of the particle to the valley of the membrane.

Figure 2.15 depicts a sketch of this phenomenon, where $F_{v,asp}$ is the additional vertical force arising from the collective repulsion between the test particle and the asperities. Note that techniques like Derjaguin approximation or SEI will not account for this additional force due to the asperities since these techniques calculate the interaction based on the projected area of the test particle perpendicular to the substrate, and hence, will miss the additional contribution of asperities. To summarize, repulsive interaction between the asperities and the depositing particle can alter the normally directed colloidal forces. Furthermore, due to the presence of roughness on the membrane, the repulsive energy barrier will be considerably diminished, thus making it easier for the hydrodynamic forces to bring the particles in contact with the surfaces. The long-range part of the DLVO interaction is attractive, and hence, the asperities generally attract the depositing particles from the flowing suspension. This long-range attraction (primarily due to van der Waals forces) aids the capture of the flowing particles by the asperities. The attractive force, in conjunction with the permeation drag, can draw the flowing particles toward the asperities. Since the tangential velocity of the particle diminishes as it approaches the no-slip surfaces of the asperity, it is clearly discernable that the long-range DLVO attraction aids the deceleration and eventual capture of the particles by the asperities. A closer inspection of this coupling between the mildly attractive DLVO interaction and the hydrodynamic interactions is necessary for assessment of particle deposition on rough surfaces.

From a surface energy viewpoint, it might seem that membrane surface is chemically heterogeneous, thereby providing the peaks as attractive sites where the particles can favourably deposit. The NF membranes acquire electrical charge by a number of mechanisms. When they get in contact with an electrolyte solution, the functional groups of a membrane dissociate depending on the pH of the solution. The carboxylic groups ($-\text{COOH}$) present on polyamide membranes are weakly acidic and do not dissociate at a low pH while the amines ($-\text{NH}_2$) protonate at a low pH. Other mechanisms are adsorption of ions from solution,

adsorption of polyelectrolytes, ionic surfactants, and charged macromolecules [199]. Surface roughness (resulting in a variation in charge density) and charge distribution (arising due to variation in chemical functionality) are both identified as the principle sources of variability in surface charge [52].

Measurements of the streaming potential [49, 51, 190, 199, 212, 213] along the membrane surface indicate that the polyamide TFC NF membranes possess negative charge in the working pH range 5-7 which is supported by XPS data [181, 193, 194]. Out of these experimental investigations, a comprehensive investigation of zeta potential measurements was made by Artuğ *et al.* [199] and Teixeira *et al.* [200] on NF90 membranes performed for KCl salt concentration of 0.005 M and 0.001 M respectively. Measurements were conducted from acidic to alkaline pH (3–11). Both results show that the NF 90 membrane surface has a slightly positive zeta potential at the lowest pH, passes through an isoelectric point (IEP) at pH 4.2 and is negatively charged above this pH. Zeta potential variations of this nature are characteristic of amphoteric surfaces or surfaces with *both* acidic and basic functional groups, carboxylic and amine groups, respectively. This observation is also in agreement with the FTIR analysis performed on NF90 membrane (Section 2.3.3). Thus although the membranes have a homogeneous chemical composition in the micrometer scale (as seen from FTIR measurements), these membrane surfaces can be called ‘chemically heterogeneous’ (at the same scale as the roughness) because they possess both the amine and carboxylic groups (changes in functionality) that can contribute to the local variation in surface charge [15, 52].

Thus for rough or chemically heterogeneous surfaces, surface potential calculated from streaming potential measurements provides an incomplete description of the surface’s charge characteristics [15]. Streaming potential measurements cannot account for nor describe any charge distribution across a surface as it only provides an average zeta potential value for the whole surface. A study performed by Brant *et al.* [214] using the AFM to calculate the zeta potential of the membrane surface, was successful in quantifying the variation in charge distribution along the NF membrane surface. Although the contributions of physical and

chemical heterogeneity could not be distinguished in AFM analysis, their study indicate that despite roughness features being present on the membrane surface, they were sparsely distributed which suggest that factors other than roughness (*e.g.* chemical heterogeneity) could also contribute to the measured variation in charge.

It is not possible, however, to extrapolate some of the conclusions derived from the above studies in the analysis of the observation pertaining to the deposition particles on the peaks of the membrane. This is partly because most of the chemical characterizations techniques are performed on mostly dry membrane samples while the charging reaction occurs in the aqueous phase so the information obtained from these methods are incomplete. The other reason is that the resolution of most current commercial instrument that analyze the membrane surface is not fine enough to provide information (*e.g.* streaming potential measurements cannot distinguish the potential variation of membrane peaks from valleys) that would help assess the effect of chemical heterogeneity on deposition. However what can be concluded is that the chemical heterogeneity that is inherently present in the membrane can manifest itself as charge variations on the surface of the membrane and may have a coupled effect along with roughness in determining the deposition structure of the foulant particles on these membrane surfaces. Furthermore the simultaneous presence of both type of heterogeneities on the membrane surface, would result in a combined effect on the interactions between the particles and the membrane surface that cannot be isolated from one another to assess how each of these component would independently affect the deposition of the particles.

2.7 Conclusions

The initial stages of fouling of a rough nanofiltration membrane (NF90) by spherical polystyrene PS particles of 100 nm diameter were studied in a tangential flow filtration system. The methodology involved a ‘post mortem’ analysis of fouled membrane morphologies employing AFM imaging. The images indicate a

deposit morphology characterized by clusters of particles deposited around the peaks or ridges of the rough membrane. These deposits were generally localized above the mean plane of the rough membrane surface. At very late stages of the filtration the cake deposit appears uniform, and covers the entire surface of the membrane. The following conclusions can be drawn from this study:

- The enhanced propensity of the particles to deposit on the peaks of the rough membranes as opposed to the valleys is ascribed to a coupled interplay between the colloidal and near field hydrodynamic interactions between the depositing particles and the protruding asperities. The hydrodynamics of the CFMF system simply assist in increasing the rate of collision of the suspended particles with these peaks, thereby stimulating rapid formation of larger aggregates.
- Additionally it seems that the asperities can act as highly efficient particle capture sites under the combined influence of hydrodynamics and colloidal interactions, particularly when the particles are smaller than the asperities. However, the morphology of these deposits clearly indicates the necessity of re-evaluating the present theoretical picture of particle deposition onto rough semi permeable surfaces, particularly when the overall magnitude of the roughness is larger than or comparable to the particle dimensions. An interesting observation regarding these deposit structures is that they leave the pores of the membrane vacant, thereby rendering the permeation velocity relatively unaffected. This might be construed as an advantage of using rough membranes as filters.
- Physical and chemical heterogeneities are concurrently present on the membrane surfaces; the chemical heterogeneities being of the same length scale as the roughness. Current characterization techniques lack the necessary resolution, and thus, cannot account for, nor describe, any charge distribution across a surface as it only provides an average value for the surface. It, therefore, becomes hard to describe this complex system in sufficient detail to enable a complete analysis to be undertaken or to determine conclusively what effect the presence of chemical heterogeneity

will have on the deposition process.

- The coexistence of the chemical and physical heterogeneities possibly creates a combined and rather convoluted interaction scenario and the arbitrary shape/size and random distribution of the heterogeneities renders the task of quantifying these heterogeneities difficult. Therefore, one cannot study the effect of chemical heterogeneity alone if it is present along with physical heterogeneity because it becomes a challenging task to isolate, correlate and assess the effects that each heterogeneous component has on the deposition phenomenon, separately.

The aim of the study was to assess whether the membrane surfaces would serve as a suitable premise to study the effects of chemical heterogeneity on deposition process in context of a practical engineering problem like fouling of nanofiltration membrane. From the above it can be concluded that although particle depositions on ‘real’ heterogeneous substrates such as filtration membranes are useful, using them to assess the specific roles of surface heterogeneity is not optimal owing to the randomness in the distribution of chemical properties of substrates, and the presence of physical heterogeneity (roughness) in conjunction with chemical heterogeneity. Furthermore, properly characterizing these heterogeneities and correlating them with the deposition studies can become a formidable task. Moreover, the fluid velocity field in such a cross flow system (which considerably differs with conventional deposition systems where the surface is impermeable) coupled with colloidal interactions further complicates the scenario and does not provide a suitable premise for studying the effects of heterogeneity in a simplified and tractable form. Thus in an effort to fundamentally understand how colloidal particles interact with heterogeneous (specifically chemical inhomogeneous) substrates, a complete analysis would require accurate knowledge about the nature and interaction of the surfaces, which means:

- Being able to characterize and quantify the different sources of heterogeneities (which are often microscopic) [41] on the surface;
- Being able to identify the individual contribution of the different types of heterogeneities and decouple the effect each has on the particle–surface in-

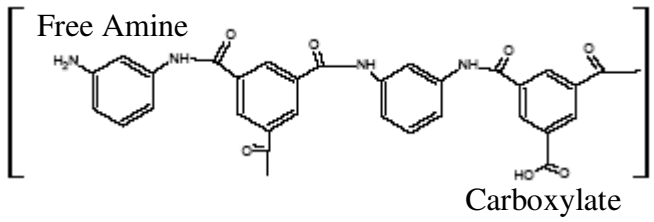
teractions;

- Being able to correlate the contribution of the different types of heterogeneity to the effect each has on the deposition phenomenon.

In this context it would be ideal to study how the irreversible deposition of micron-sized particles is modified on synthetic substitutes that are geometrically smooth and containing well defined and characterized chemical patterns.

In the next chapter, particle deposition onto model patterned charge heterogeneous substrates is studied and the deposition structure analyzed to help quantify the effects of these heterogeneities on deposition. Since the heterogeneities are artificially created and their nature is known *a priori* and accurately, elucidation of their influence on particle deposition becomes more tractable. Observations made on such well-defined systems can thus provide systematic and quantitative information that can contribute to a greater practical understanding of real processes.

Table 2.1 Nanofiltration (NF) membrane properties

NF90 Filmtec® membrane	
Properties	Description
Membrane material (barrier layer)	<p>An aromatic polyamide made from 1,3 phenylene diamine and the tri acid chloride of benzene.</p>  <p>Figure: Approximate structure of the barrier layer of a NF90 membrane[†]</p>
Thickness of barrier layer [†]	Average ~ 2000 Å, not exceeding 1 µm
pH range, continuous operation [†]	3 - 10
Maximum operating temperature [†]	113°F (45°C)
Maximum operating pressure [†]	600 psi (41 bar)
Stabilized salt rejection [†]	NaCl : 85-95%; MgSO ₄ : > 97%
Zeta potential [‡]	-15mV to -25mV (within the pH range 5 - 7)

[†] [182]

[‡] [47, 49, 157-159]

Table 2.2 Colloidal particle and suspension properties

Polystyrene sulfate particles		
Parameters	Units	Value
Mean diameter	μm	0.10
Standard deviation of diameter	%	4.1
Percent Solids	g/100 ml	2.2
Density of polystyrene at 20°C	g/cm^3	1.055
Particle number concentration	particles/ m^3	3.9×10^{13}
Surface charge density	$\mu\text{C}/\text{cm}^2$	1.0
Surface (zeta) potential, ζ	mV	-25

Suspension		
Parameters	Units	Value
pH		6.03 - 6.40
Particle concentration, N_p	particles/ m^3	10^{16}
Ionic strength (NaCl)	M	0.001 - 0.10

Table 2.3 Statistical roughness parameter definitions

Parameters	Definition	Calculation
Z_{mean}	Average of all Z values within the enclosed area	$Z_{mean} = \frac{1}{n} \sum_{i=1}^n Z_i$ where, n = data points, Z = height deviation
R_a	Average of the absolute Z values	$R_a = \frac{1}{n} \sum_{i=1}^n Z_i - Z_{mean} $
R_q	Standard deviation of the Z values	$R_q = \sqrt{\frac{1}{n} \sum_{i=1}^n (Z_i - Z_{mean})^2}$
R_p, R_v	Maximum peak & valley depth; distances from the mean plane to the highest/lowest point in the evaluation area	Measured
R_{max}	Maximum vertical distance between the highest and lowest point in the data	$R_{max} = R_p + R_v$
SAD	Surface area difference in percentage, where the surface area is the 3D surface obtained by the sum of the triangles formed by three adjacent points, and the projected area is the 2D surface produced by projecting the surface onto the threshold plane	$SAD = \left[\frac{\sum (\text{surface area})}{\sum (\text{projected area})} - 1 \right] \times 100 \%$

Diagrammatic representation of the roughness parameters

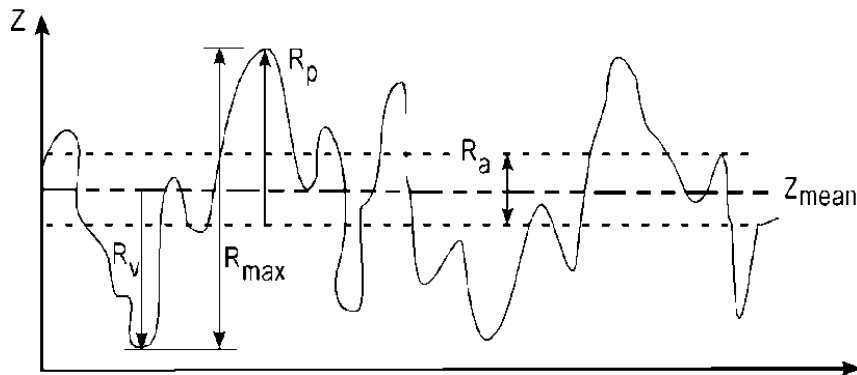


Table 2.4 Typical result of a roughness analysis on a membrane area of 100 μm^2

Morphological parameters	NF90-CM1	NF90-CM2	NF70[†]
Mean, Z_{mean} (nm)	0.141	0.139	0.147
Average roughness, R_a (nm)	67.37	59.40	43.30
RMS roughness, R_q (nm)	88.95	75.65	56.50
Maximum peak, R_p (nm)	395.89	374.26	-----
Maximum valley height, R_v (nm)	-239.74	-223.26	-----
Maximum roughness, R_{max} (nm)	635.63	597.68	577
Surface area difference, SAD (%)	40.186	41.195	20.7
Bearing Ratio (%) at threshold height, Z_b			
300 nm	19.04	12.51	-----
400 nm	5.81	1.26	-----
500 nm	1.268	0.07	-----

[†]From [47]

Table 2.5 Typical result of a bearing analysis on membrane sample obtained at operating conditions: Pressure = 60 psi, Ionic strength = 0.01 M

Membrane section	Total no. of particles visible in the section N_t	Roughness Parameters (nm)	Bearing plane height Z_b (nm)	Bearing ratio (% area above bearing plane)	Particles seen below Z_b (% of N_t)
Mem 41	$N_t = 265$	$R_a = 66.424$ $R_q = 86.978$ $R_{max} = 676.57$	600	1.43	89.81
			500	8.71	67.17
			400	38.3	11.7
			300	84.14	0
Mem 42	$N_t = 230$	$R_a = 57.554$ $R_q = 74.167$ $R_{max} = 637.39$	600	0.63	93.04
			500	2.5	79.13
			400	10.91	31.74
			300	42.91	3.043
			200	87.11	0
Mem 43	$N_t = 105$	$R_a = 68.952$ $R_q = 86.543$ $R_{max} = 761.31$	600	0.33	100
			500	1.53	86.67
			400	11.4	48.57
			300	45.97	10.47
			200	87.98	0
Mem 44	$N_t = 183$	$R_a = 68.333$ $R_q = 89.550$ $R_{max} = 683.05$	600	0.037	98.90
			500	0.68	97.26
			400	5.36	13.15
			300	37.38	1.09
			200	87.49	0
Mem 45	$N_t = 153$	$R_a = 87.428$ $R_q = 67.990$ $R_{max} = 792.09$	600	0.035	100
			500	3.28	89.29
			400	12.34	40.18
			300	49.72	0

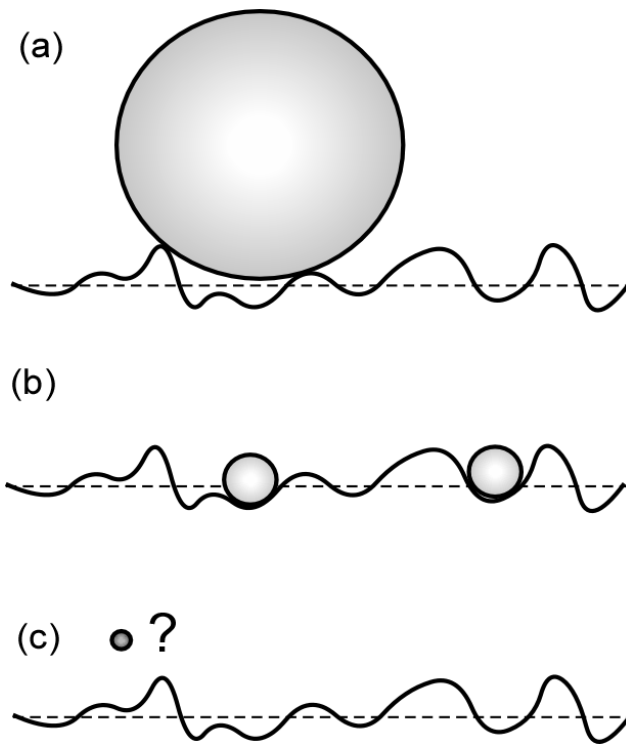


Figure 2.1: Schematic representation of deposition of colloidal particles of different sizes relative to the roughness features of a macroscopically flat surface. (a) Particle size much larger than roughness; (b) particle size comparable to the roughness, and (c) particle size much smaller than the roughness features.

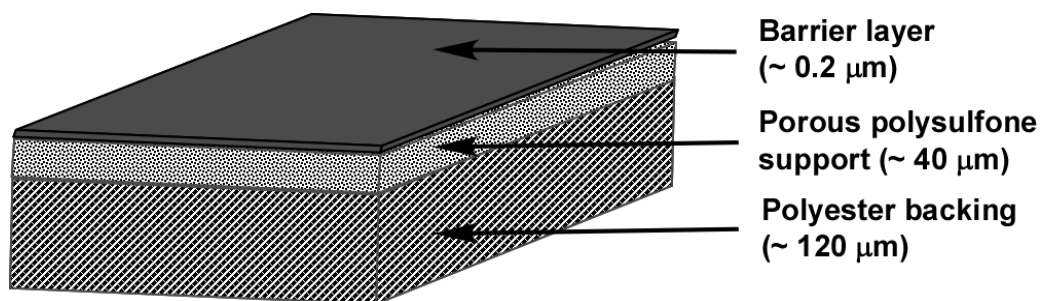


Figure 2.2: Schematic drawing illustrating a typical cross sectional structure of a thin film composite (TFC) nanofiltration NF90 membrane [162].

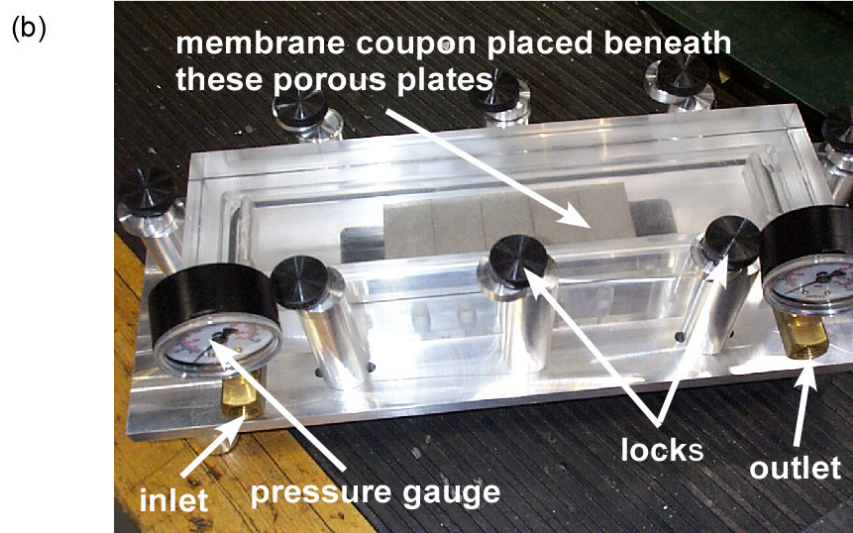
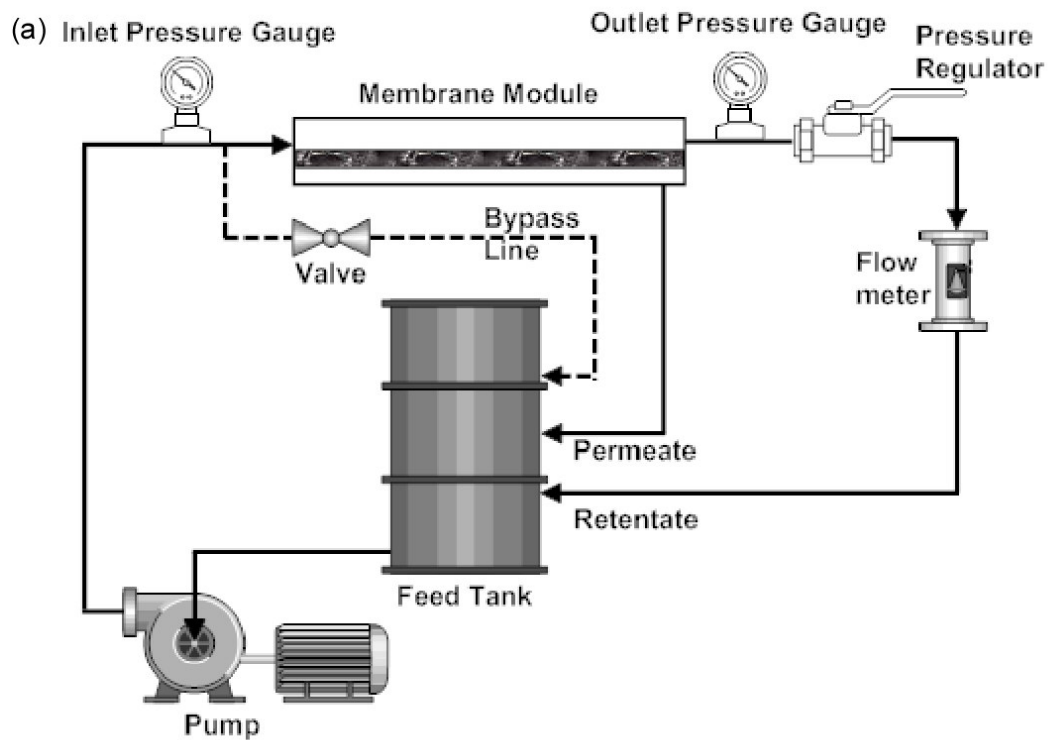


Figure 2.3: (a) Schematic of the cross flow membrane setup and (b) a photograph of the membrane module.

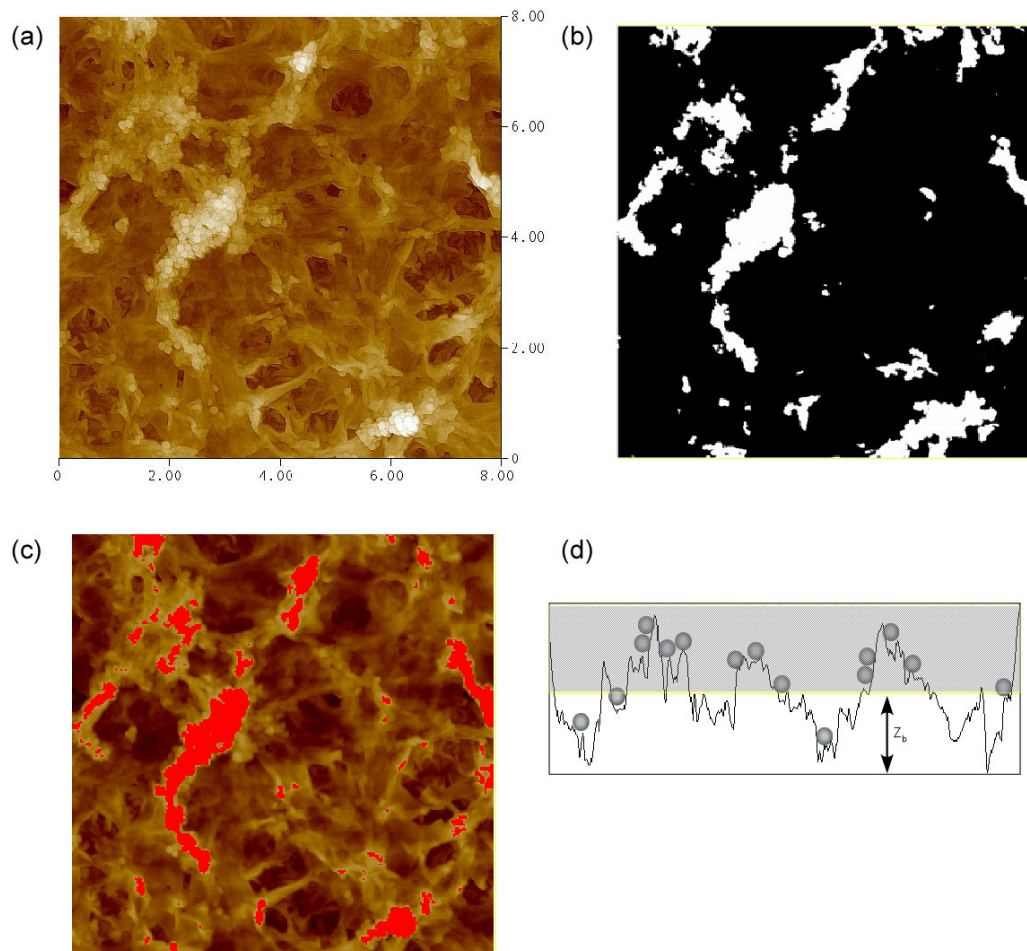


Figure 2.4: Bearing analysis of the AFM topographic image. The image in (a) is a colour reproduction of the topographic image taken in tapping mode and (b) shows the results of a bearing analysis performed for a bearing plane height of 400 nm above the lowest scanned point on the image. (c) A composite bearing analysis image obtained by overlaying the bearing image (b) on the topographic image (a). The red regions in (c) indicate the areas above the bearing plane. The percentage of area calculated above this bearing plane (red regions) was 12.9%. (d) A schematic representation of the bearing analysis. The image shows the cross section of the membrane plan view. The area above the bearing height Z_b is rendered red and covers the particles in that region. The particles visible below Z_b can now be counted.

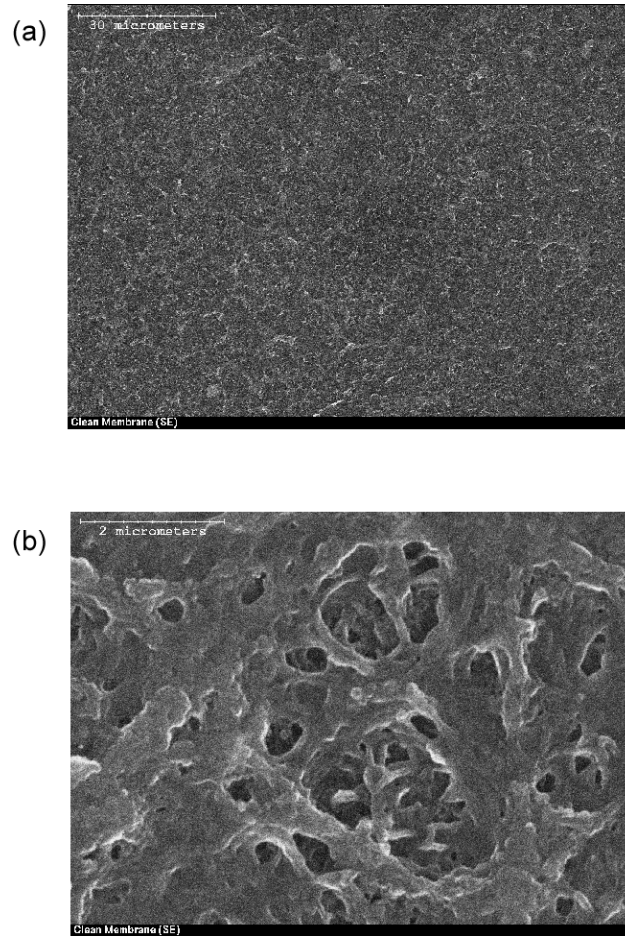


Figure 2.5: SEM micrographs of a clean NF90 membrane at two magnifications. In (a) the bar scale in the micrograph is 30 μm . At this scale the membrane appears relatively smooth. In (b) the bar scale is 2 μm . The roughness is more apparent at this scale and the membrane structure shows an intertwining fibrous network.

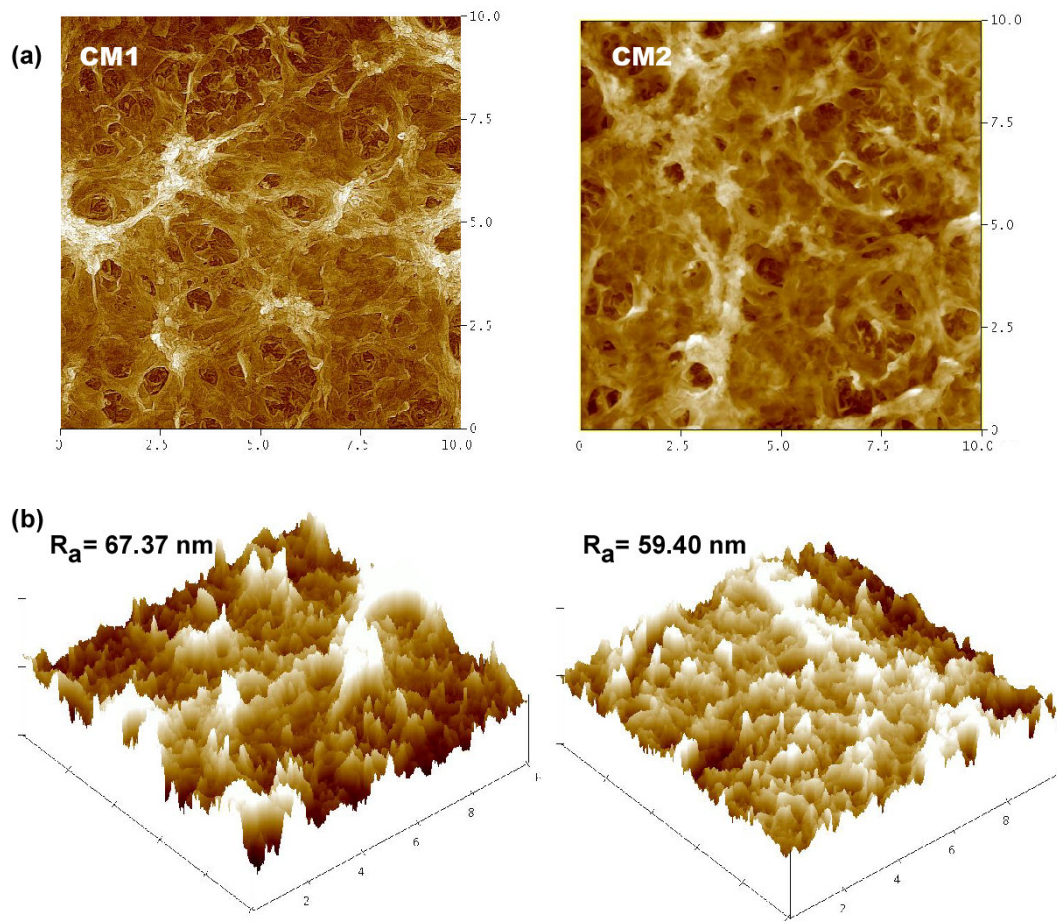


Figure 2.6: (a) Topographic AFM images of two different $10\ \mu\text{m} \times 10\ \mu\text{m}$ areas of a clean NF90 polymeric membrane in tapping mode. The colour variation illustrates the vertical profile of the membrane surface; light colour represents high lying regions and the darker regions being the pores. (b) The 3D orthographic images have the vertical scale enhanced to amplify the surface morphology of the membranes (500 nm/division for Z-scale compared to $2\ \mu\text{m}$ per division for X and Y). CM1: Average roughness, $R_a = 67.37\ \text{nm}$ and CM2: Average roughness, $R_a = 59.40\ \text{nm}$.

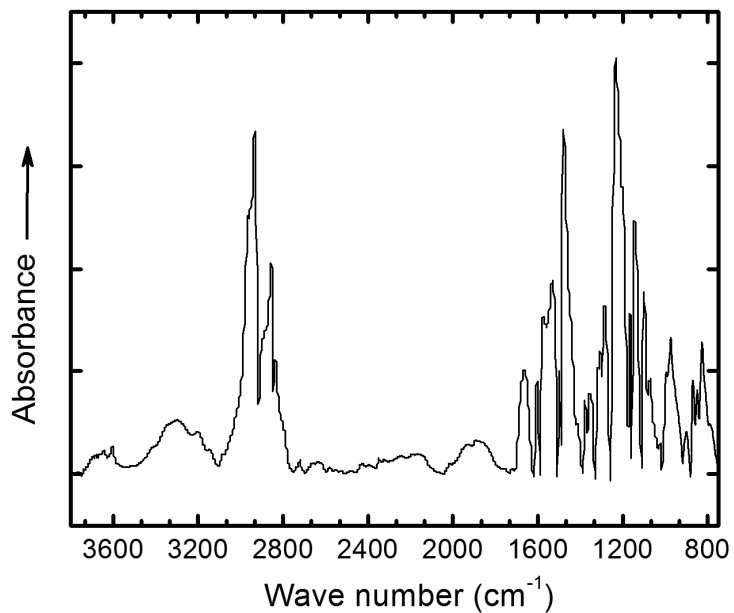


Figure 2.7: FTIR IRRAS spectrum collected for the NF90 membrane shown over the range of 3800 cm^{-1} to 750 cm^{-1} . Peak centered at 3300 cm^{-1} is due to overlapping of stretching vibration of N–H and carboxylic groups in the polyamide layer. Peaks in the range of $2800\text{--}3000\text{ cm}^{-1}$ is assigned C–H stretching. Peaks around 1660 cm^{-1} and 1541 cm^{-1} are assigned to amide I (C=O stretch) and amide II respectively. Peaks at 1610 cm^{-1} and in between 1480 cm^{-1} , 1350 cm^{-1} indicate NH_2 deformation and COOH deformation respectively. Finally, the peaks near 1584 cm^{-1} , 1503 cm^{-1} , 1487 cm^{-1} , and 1151 cm^{-1} , all correspond to the polysulfone support.

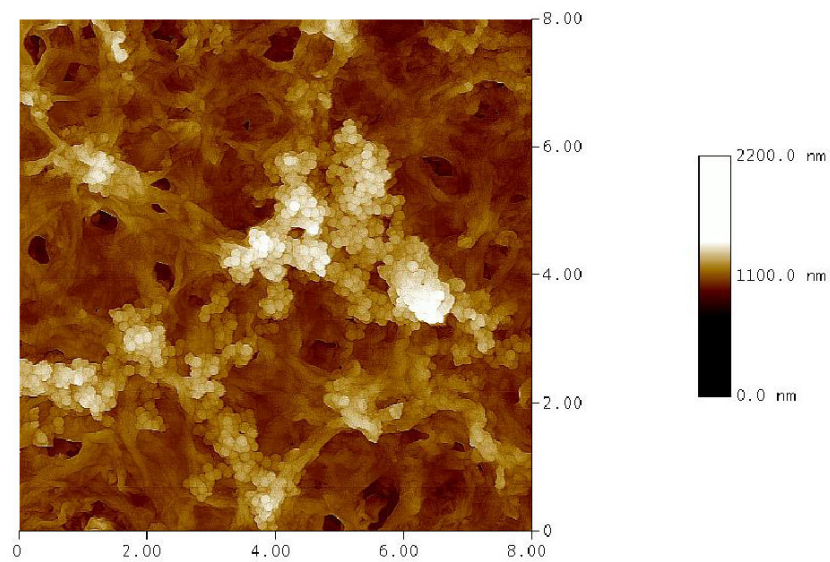


Figure 2.8: An AFM image of 100 nm diameter polystyrene sulfate particles adsorbed on the NF90 membrane surface during the quiescent deposition experiments. The deposition lasted for 3 days at room temperature (25°C) in the colloidal suspension of ionic strength $I = 0.01$ M NaCl, particle concentration $N_p = 10^{16} \text{ m}^{-3}$ and pH = 6.4.

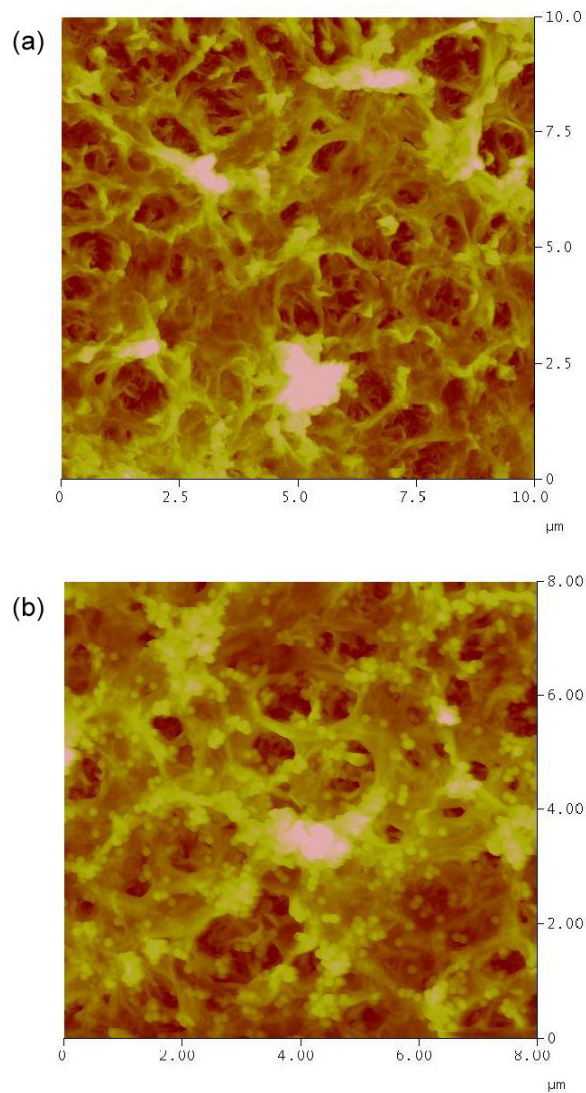


Figure 2.9: Wet mode AFM images of (a) a clean NF90 membrane and (b) of 100 nm diameter polystyrene sulfate particles adsorbed on the NF90 membrane surface during the quiescent deposition experiments. The deposition lasted for 3 days at room temperature (25°C) in the colloidal suspension of ionic strength $I = 0.001$ M NaCl, particle concentration $N_p = 10^{16} \text{ m}^{-3}$ and pH = 6.4.

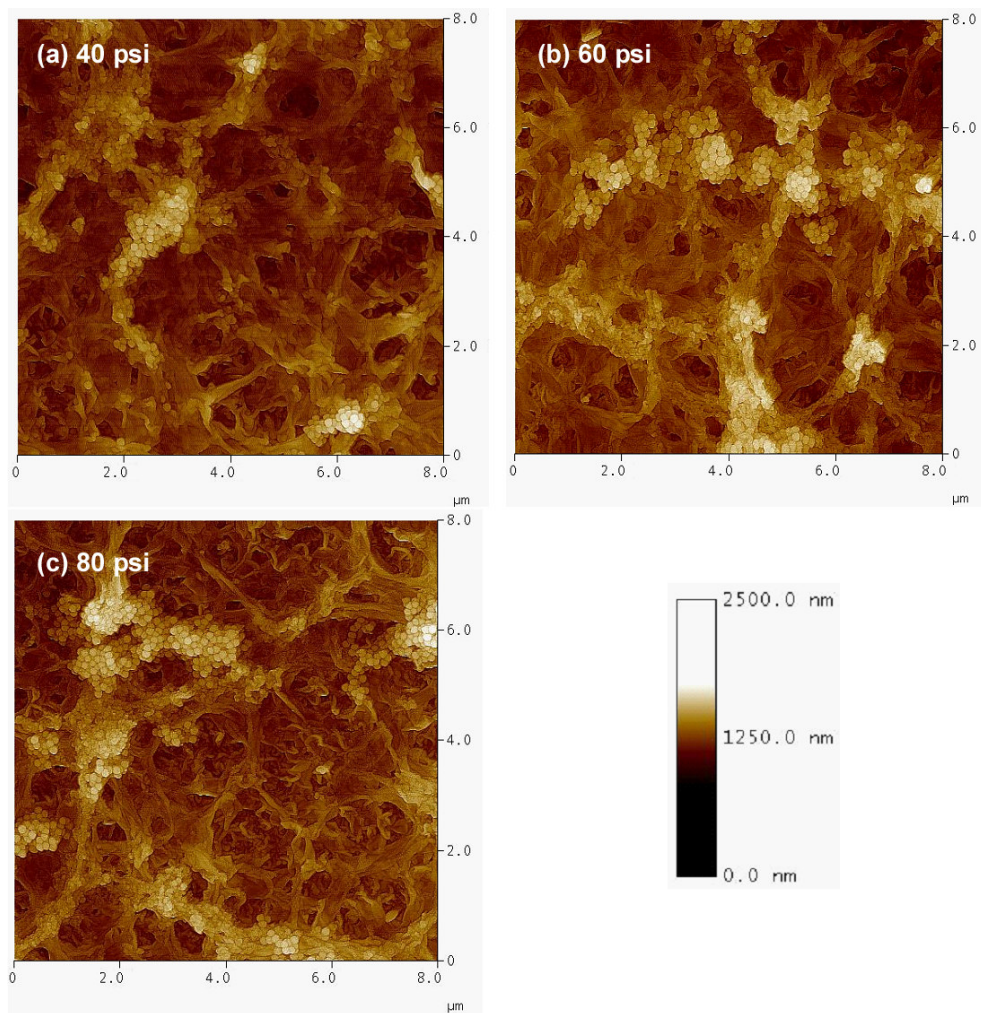


Figure 2.10: AFM image of PS particles deposited on NF90 membrane surface under different operating pressures. Deposition test lasted for 10 min in each case. Ionic strength $I = 0.01$ M NaCl, Temperature = 27°C and pH = 6.4. The applied pressure: (a) 40 psi; (b) 60 psi; and (c) 80 psi.

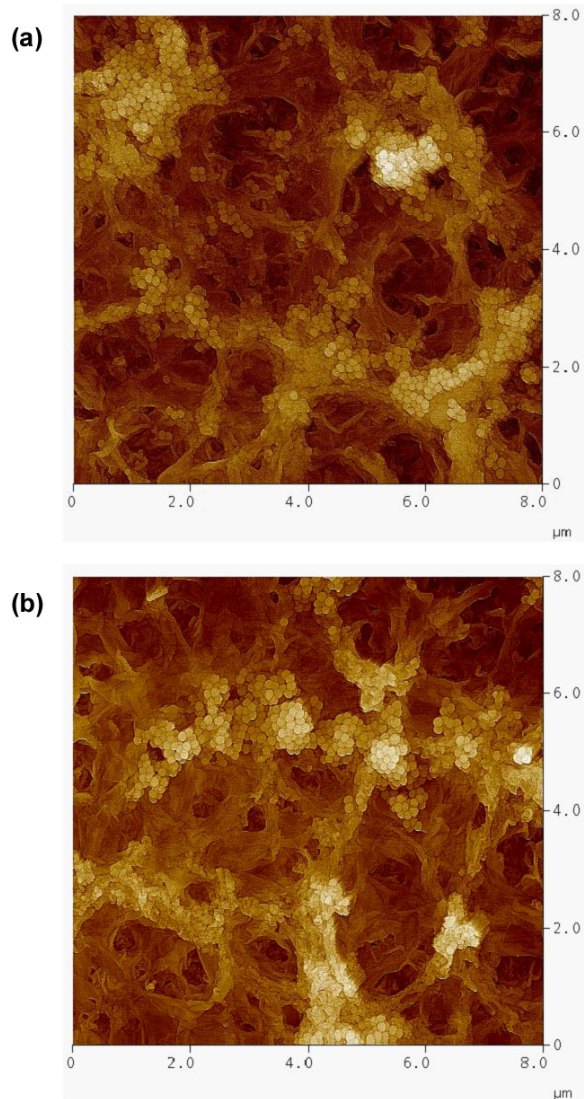


Figure 2.11: Comparison of the particle deposition on NF90 membranes at different pH and salt concentrations. Deposition lasted for 10 min at a pressure 60 psi. Particle concentration in feed was 10^{16} m^{-3} . The following salt concentrations were used: (a) pH = 6.03, ionic strength $I = 0.001 \text{ M}$ and, (b) pH = 6.4, ionic strength $I = 0.01 \text{ M}$.

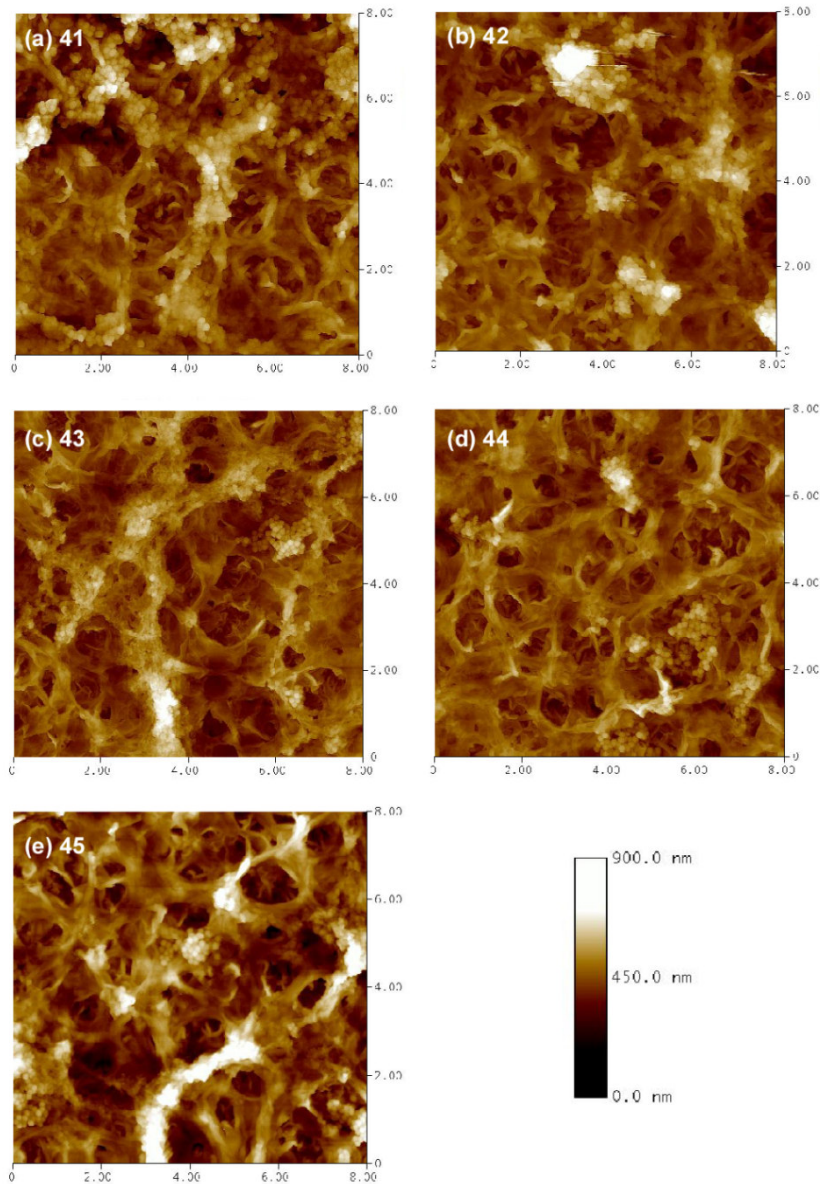


Figure 2.12: AFM tapping mode images of particles deposited at 60 psi and 0.01 M NaCl concentration 10 min used for the bearing analysis. In (a) membrane section (labelled 41) represents an area in the downstream portion of the membrane coupon. Samples shown in (b) to (e) (labelled 42 to 45) represent sections progressively moving upstream of the membrane coupon. Changes in height across the area are denoted in the colour scale bar where highest region is lightest in colour. Visual inspection of the images shows that the spherical shapes of the colloidal particles are discernable from the structure of the membrane.

Pressure = 60 psi, Ionic Strength of NaCl = 0.01M

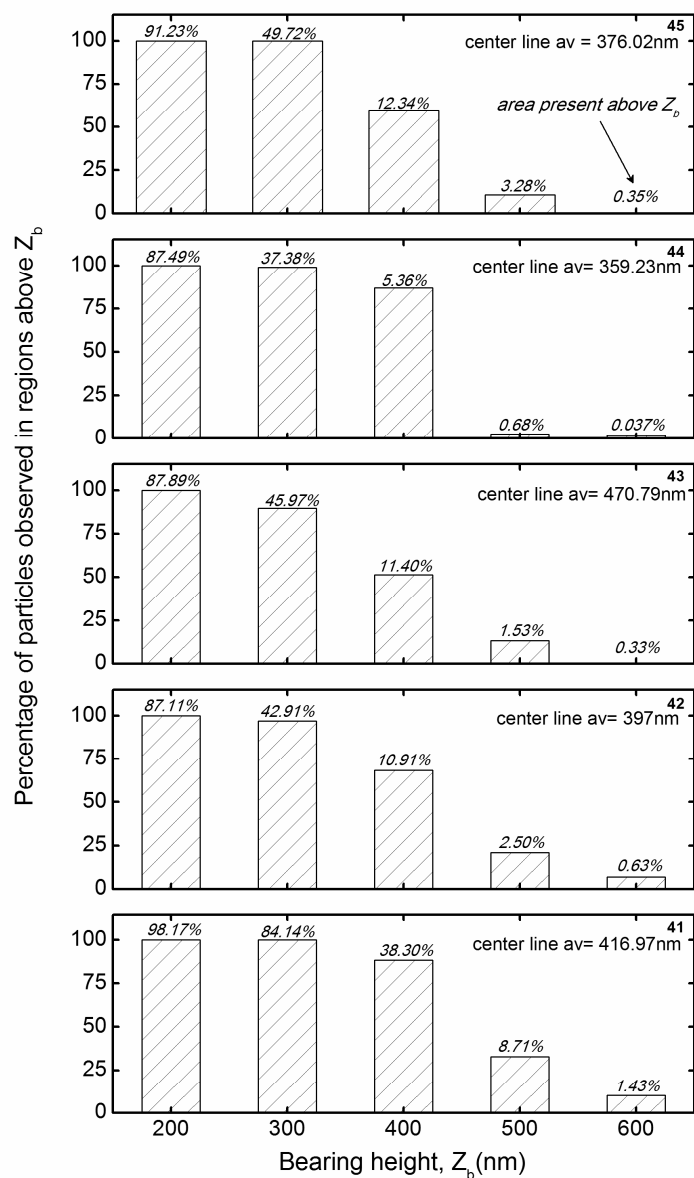


Figure 2.13: Bar graphs of the particle distribution obtained from the bearing analysis in the deposition images shown in Fig. 2.12. The bars represent the percentage of particles tallied above each of the threshold or bearing height, Z_b . The percentage area present above the bearing plane at Z_b (the bearing ratio) is cited above the bar for the corresponding Z_b . Majority of the particles have deposited between 400 to 600 nm with almost no particles depositing below 300 nm.

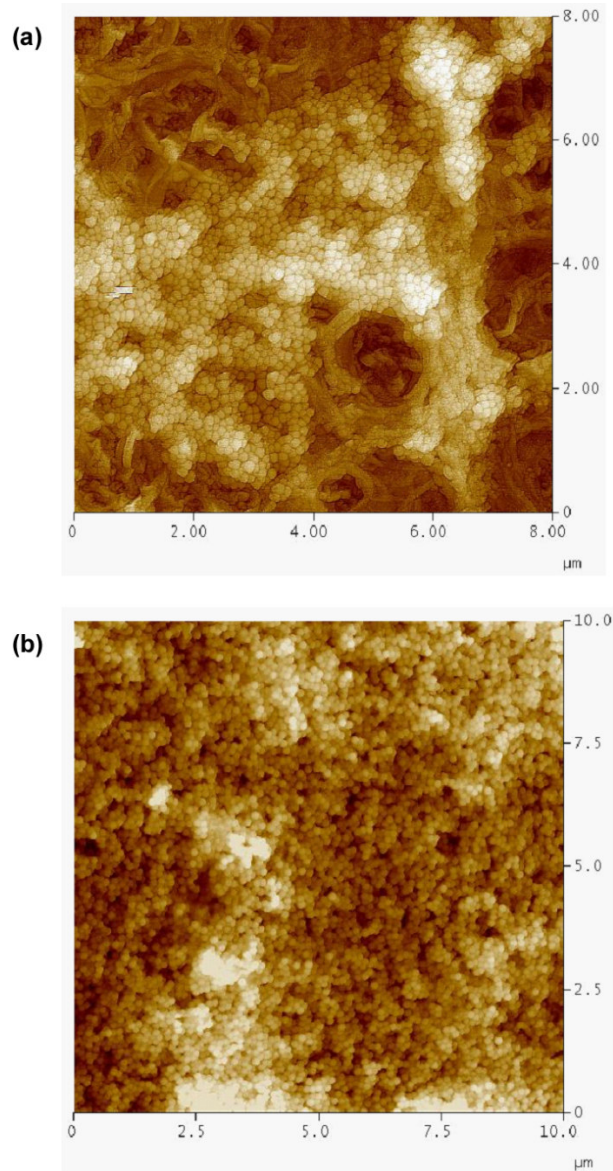


Figure 2.14: Particle deposit morphologies at later stages of filtration at 80psi: (a) deposit morphology after 30 min; (b) deposition after 1 h. In (a) large clusters of particles are seen to aggregated around the initial seeding locations on the asperity peaks, with several valleys remaining vacant; (b) illustrates the complete coverage of membrane surface signifying that at this point the surface appears homogeneous and equally favourable for deposition; this phenomenon is observed for all salt concentrations used in the study.

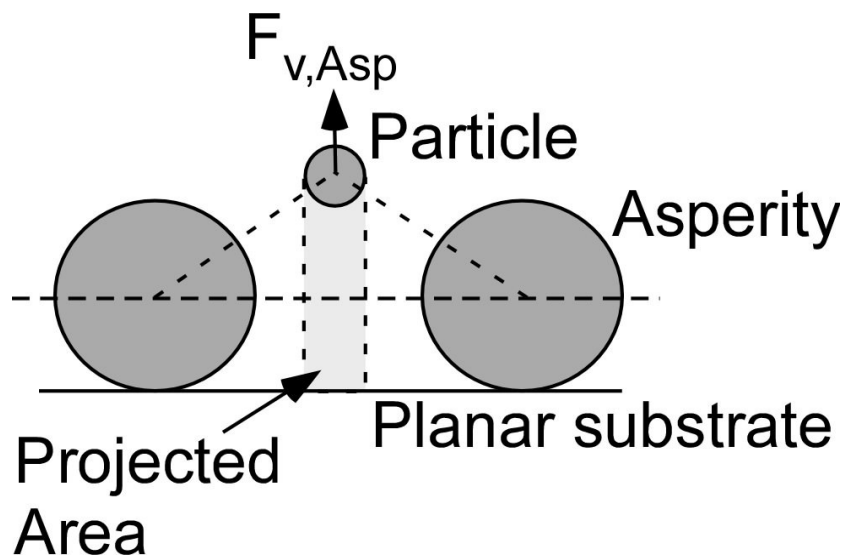


Figure 2.15: Schematic representation of the additional colloidal force experienced by a tracer particle due to the presence of asperities. Techniques like surface element integration cannot account for this additional force, since these techniques only consider the interaction between the particle and the vertically projected area of the particle on the membrane [47].

CHAPTER 3

PARTICLE DEPOSITION ONTO PATTERNED CHARGE HETEROGENEOUS SUBSTRATES

3.1 Introduction

In this chapter[†], an experimental study of colloid deposition on patterned substrates is presented, which was performed with model colloidal particles onto created striped charge-heterogeneous surfaces to analyze the influence of surface chemical heterogeneity on the subsequent deposit morphology. From a theoretical perspective, deposition on such patterned substrates poses interesting challenges by itself, including the identification of the parameters that control the properties of the resulting deposit [70]. Such studies employing patterned heterogeneity have mostly been limited to elucidation of the initial deposition rates on a clean surface. There has been little attention given towards understanding the long term kinetics of deposition and the ensuing deposit morphologies formed on patterned charge-heterogeneous substrates. Several experimental studies during the past years report deposition of particles on select types of patterned substrates (such as circles, lines, or a checkerboard structure) [114, 119, 143]. Systematic experimental studies employing large periodic arrays of a repeated pattern, where the pattern features are varied relative to particle size, are not available in the literature (see Chapter 1, Section 1.2.2). Experimental quantification of the surface coverage and deposit morphology on large-scale patterned areas of substrates is also lacking.

Thus, the aim of this work is to experimentally create well-defined charge-heterogeneous surfaces and investigate the deposition of model particles on these substrates. The charge heterogeneity was created using a soft lithographic tech-

[†] Parts of this chapter are related to the published work of “Tania Rizwan and Subir Bhattacharjee” in *Langmuir*, v. 25(9), pp 4907-4918, 2009.

nique called microcontact printing (μ CP) and alkanethiols and their derivatives (like carboxyl and amine terminated alkanethiols) were used as the 'ink' for the μ CP to produce the patterned SAMs on Au coated substrates. The procedure allowed the creation of large periodic arrays of a repeated pattern, where the pattern features were varied relative to particle size. Polystyrene sulfate microspheres and fluorescent polystyrene nanoparticles were sequentially deposited onto these patterned substrates under no flow (quiescent) condition and the deposited structures and the micro-patterns were imaged using a combination of phase contrast and fluorescence microscopy. Throughout this study, the particles used were negatively charged, so the negatively-charged regions were unfavourable to particle deposition and the positively-charged regions were favourable to deposition.

3.1.1 Choice of Surface Modification-Self Assembled Monolayers of Thiols

Molecular self-assembly has emerged as a key route to create and to manipulate functional surfaces. Self assembled monolayers (SAMs) provide an easy and reliable way to create functional substrates. They form spontaneously by chemisorptions and self organization of functionalized long chain organic molecules onto appropriate substrates. In particular, fundamental research focusing on alkanethiolate SAMs on Au has gained considerable attention due to the spontaneous formation of the versatile Au-S bond, resulting in highly ordered molecular films that can be fabricated over large areas. Because of their ease of preparation and handling, ordered SAMs formed by long chain alkanethiols when adsorbed from solution onto noble metal substrates (such as gold and silver) are often chosen as the means to modify the surface functionality of substrates.

Thus, in this study long chain alkanethiols adsorbed onto gold surfaces from ethanolic solutions were used to create the patterned substrates for deposition. The most ordered structures are formed from compounds $\text{HS}(\text{CH}_2)_n\text{X}$ with $n = 10-18$ and X is a small functional group (like $-\text{CH}_3$, $-\text{COOH}$, $-\text{NH}_2$, $-\text{OH}$, *etc.*) [148, 215] (as shown in Figure 3.1). The self assembly process is not completely understood, but it probably involves oxidation addition of thiols to gold, resulting in a gold-

thiolate linkage [215]. In general, the resulting SAMs are densely packed, well ordered films with a tilt angle varying from 27°~50° relative to the surface normal. The interfacial properties of the surface can vary from hydrophobic to hydrophilic, non-polar to polar or non ionic to ionic by varying the terminal functional group X. This flexibility of changing the chemistry of X terminal group provides an easy control of the surface functionality.

3.1.2 Choice of Patterning Technique-Micro Contact Printing

With advances in microfabrication, there are now several methods available to a researcher for creating chemical patterns on a smooth planar surface (as discussed in Section 1.2.2 in Chapter 1). Amongst all the processes, soft lithography [144] is a widely used technique for ‘printing’ and attaching self assembling molecules. Control of surface chemistry and corresponding patterns of chemical functional units can be achieved by using SAMs [216] of organic molecules that have good adhesion to the substrates (for example, thiols to gold [119, 121, 145, 149, 216, 217], silanes to silica substrates [147, 150, 216], and polyelectrolytes [119, 149, 216]).

Of all the soft lithographic techniques, development of charge heterogeneity on substrates employing microcontact printing (μ CP) is well established [148, 151, 218]. Recently, substrates bearing patterned surface features of regular shapes such as circles (dots) [114, 116, 145], squares [143, 146], and rectangles (stripes) [119, 121, 219] have been created on homogeneous surfaces by μ CP. Microcontact printing involves the transfer of molecules of SAM from an elastomeric stamp to a metallic thin film (usually Au). It can be used to reproducibly produce patterned surfaces with feature dimensions ranging down to 500 nm laterally [148]. A master template is prepared by photolithography consisting of a relief structure of the appropriate pattern. Stamps are cast with an elastomeric polymer usually polydimethyl siloxane (PDMS). Multiple stamps can be cast from the same master template and each stamp can be used several times without loss in the quality of the printed stamps. Stamps are ‘inked’ in a solution of alkanethiol in ethanol, dried and brought into contact with the gold substrate. The elastomeric

stamp permits conformal contact between the surface and the relief structure of the stamp resulting in transfer of the alkanethiol in the regions where the surface and the stamp come into contact.

3.2 Materials and Methods

3.2.1 Model Particles and Suspension

As model colloids in the deposition experiments, two different diameters of white polystyrene sulfate (PS) particles (Interfacial Dynamics Co., USA) were used. The properties of the particles are shown in Table 3.1. Size and charge data are as reported by the manufacturer. The zeta potential of these particles was determined using a Brookhaven ZetaPals (Brookhaven Instruments Co., USA). The colloidal suspensions were made using ACS grade KCl (Fisher Scientific, USA) with ionic concentration of 10^{-4} M and the pH was held between 5.1 and 5.2 by adding appropriate amount of 0.01 N HCl solution. The particles are negatively charged at these pH levels. The concentrations of the PS particles in these solutions were typically between 1.7×10^{13} to $1.8 \times 10^{14} \text{ m}^{-3}$.

3.2.2 Patterned Model Substrates

To create the patterned chemical heterogeneities, microcontact printing (μ CP) and solution deposition [144, 148, 218, 220] was employed in which the micron-sized features of self-assembled monolayer (SAM) are patterned on gold coated glass substrates. The following describes the steps leading to the creation of the patterned surfaces:

Stamp Fabrication: The first step in creation of a patterned substrate is the fabrication of the stamps. The stamps for micro-contact printing were created by casting an elastomeric material polydimethyl siloxane (PDMS) (Sylgard 184, Dow Corning, USA) against a silicon master containing the pattern complementary to that to be reproduced. For accurate reproduction of the pattern on to the substrates, it is required that the stamp material be: i) Rigid enough to support a topographic microstructure at its surface; ii) Porous enough to incorporate a

sufficient amount of active solution, and iii) Soft enough to enable a smooth conformal contact with the solid surface onto which printing is desired. In this context, PDMS is a popular choice as a stamp material. Such elastomer-based stamps have several advantages: i) Elastomers based on PDMS come from an extensively studied family of polymers that are largely inert and commercially available in a wide range of molecular weights with many combinations of other polymers possible ii) The stamp accommodates the substrate topography by deformation. Nanoscale asperities are readily subsumed by the μ CP process [144, 218] causing little or no macroscopic alteration of the printed pattern. iii) μ CP provides the best results when the stamps acts as a dense sponge, taking up liquid in a region largely limited to the surface of the polymer. PDMS can take up the alkanethiols, for example, with no apparent change in dimension on scales greater than 20 nm [144], so that pattern transfer remains faithful to the features present on the original master. The pattern transfer occurs only in areas of conformal contact by chemical diffusion of the contacting ink on the surface of the stamp, resulting in a highly controllable chemical modification of the substrate [144, 218].

The stamps were formed by cast molding technique [218] in which a master is used to mold the stamps by pouring PDMS on them. The master mold was made from 4 inch diameter standard silicon wafers with the pattern formed on them using conventional photolithography and etching procedures. For details on the photolithography, etching and molding procedures please refer to Appendix B. The cast stamps were peeled and cut into individual pieces with each stamp having a thickness of approximately 2.5 mm and a patterned area of 1 mm². Prior to use, the stamps were cleaned using 100% anhydrous ethanol and dried in a stream of N₂. Each stamp was placed on a glass cover slip (with pattern side facing upwards) to provide a firm backing, as well as provide a means of manually holding the stamp during the printing process. The stamps created were then characterized using the AFM in the Tapping mode. Table 3.2 shows a typical result of the measurement done on stamps created from a Si master having 4 rows of patterns of different dimensions. Each dimensional value represents an average

of 9 readings taken from different areas on each stamp. This analysis shows that the created stamps are within $\pm 0.3 \mu\text{m}$ of the designed dimension.

Substrate Preparation: The substrates were prepared from 26 mm \times 76 mm glass slides (Fisher Scientific, USA) coated with 1-3 nm of Cr (at 300 W, 372 V at a pressure of 7×10^{-3} Torr) and 200 nm of Au (at 75 W, 444 V, at a pressure of 7×10^{-3} Torr) using a sputtering technique (Lesker, Germany). The Au coated slides were then diced into 1 mm by 1 mm pieces utilizing a dicing saw. Plastic tweezers were used to handle the substrates so as not to scratch the Au surface. Each substrate piece was then cleaned in a cold Piranha solution for about 10 min followed by a thorough wash using DI water and drying in N_2 . (*Caution:* Piranha solution reacts violently with many organic materials and should be handled with care).

Thiol Solution Preparation: High molecular weight thiols are usually preferred to create the SAMS because long chains ($n > 11$) form densely packed highly-ordered monolayers [215]. In this study, the patterned surfaces were made using 11-mercaptoundecanoic acid, $\text{HS}(\text{CH}_2)_{10}\text{-COOH}$ of 98% purity (Sigma Aldrich, USA) and 11-amino 1-undecane thiol-HCl of 99% purity (Asemblon, USA). To make a 10^{-4} M ink solution, the thiols were added in measured amounts to anhydrous ethanol (Fisher Scientific, USA) and agitated in a vortex mixture until all the thiol had visibly dissolved. The solutions were stored in amber bottles; back filled with dry N_2 . Solutions were prepared fresh on the day stamping was scheduled and discarded after 3 days from the day of preparation.

Microcontact Printing (μCP) and Solution Deposition: Patterned self assembled monolayers (SAMs) were formed on the substrates using μCP . The steps involved in this process (as illustrated in the flow diagram in Figure 3.2) are described below:

- The PDMS stamp with the imprinted microstructures was inked by placing a drop of the 10^{-3} M solution ethanolic solution of carboxyl thiol onto the engraved surface of the stamp for 15 s.

- The ink solution was then quickly (>30 s) removed under a stream of N₂ to ensure the drop has evaporated, leaving the carboxyl thiol molecules on the stamp surface.
- Immediately following inking, the stamp was brought into contact with the gold surface for 15 s. Only gentle pressure was required to ensure complete contact. During the printing step, care was taken to ensure the stamp was kept parallel to the Au surface.
- Next the stamp was gently peeled off from the surface. On removal of the stamp, care was taken to avoid ‘double printing’ by carefully detaching the stamp from the substrate surface so that it did not slip. The Au surface was now printed with the carboxylic acid terminated SAM containing discrete areas of negatively charged domains. The substrate was then rinsed with anhydrous ethanol.
- The substrates were subsequently immersed in a 10⁻³ M solution (*i.e.* solution deposition) of amine thiol in ethanol for 1 h to cover the remainder of the substrate surface with the positively charged domains. A final rinse of the substrate surface with ethanol completed the process.

A pair of control samples was also created. For the control samples, cleaned Au substrates were soaked in separate solutions of 10⁻³ M amine thiol and carboxyl thiol for 24 h. This resulted in coverage of the Au surface with one particular thiol monolayer giving either a positively charged or a negatively charged surface.

3.2.3 Characterization of Patterned Substrates

The stamped patterns contained rectangular stripes ranging from 2 μm to 4 μm in width which are not visible optically. To characterize these patterns, the chemical property variations in the pattern features were detected using Atomic Force microscopy (AFM) in the Lateral Force Microscopy [186] mode, (LFM; also known as Friction Force Microscopy, FFM) and the Scanning Surface Potential Microscopy (SSPM) [221] mode; both performed in air and under ambient conditions. The measurements were performed on a Bioscope equipped with a Nanoscope IIIa controller and Extender Module (Digital Instruments, USA).

In LFM, the AFM was operated in the contact mode with the cantilever scanning the surface laterally (perpendicular to its length) and it twists as it transits past high-friction sites; low friction sites tend to twist the cantilever less. The relative measure of these lateral forces encountered along a surface yields a map of high- and low-friction sites. A brief description of the LFM is given in Appendix A. LFM was performed using 200 μm long DNP (Veeco Metrology, USA) V-shaped silicon nitride (SiN) cantilevers with a nominal spring constant $k = 0.12$ N/m and resonant frequency of 20 kHz.

Surface potential (SP) mapping was performed using a two-pass interleaved technique (Lift Mode) [221]. In this configuration, the tip operating in tapping mode, scans over one line of topography then it lifts up to a selected height and measures the surface potential difference over the same line at a constant distance from the sample (see Appendix A for details on this mode). Magnetic Force Etched Silicon Probes (MESP, Veeco, USA) coated with a thin conductive layer with a nominal spring constant of 2.8 N/m and resonant frequency of 75 kHz was the probe used for the experiment. The initial conditions used for SP mapping were-AC drive amplitude: 5 V, AC drive frequency: 130 kHz, lift height: 100 nm, and scan rate: 0.5 Hz.

To further substantiate the presence of chemical segregation on the substrate, Time of Flight Secondary Ion Mass Spectrometry (ToF-SIMS) [222] was performed on the patterned substrates. ToF-SIMS is a surface-sensitive spectroscopy that uses a focused, pulsed particle beam (typically Cs or Ga) to dislodge chemical species on a materials surface. Particles produced closer to the site of impact tend to be dissociated ions (positive or negative). Secondary particles generated farther from the impact site tend to be molecular compounds, typically fragments of much larger organic macromolecules. These particles are then accelerated into a "flight tube" and their mass is determined by measuring the exact time at which they reach the detector (*i.e.* time-of-flight). ToF-SIMS spectra were acquired in an ION-TOF TOF SIMS IV spectrometer (ION-TOF GmbH, Germany) using a 15 keV Ga^+ ion source. Spectra were acquired for the negative secondary ions over a mass range of $m/z = 0-1000$ using an analysis area of 30 μm by 30 μm . In general,

the results obtained from the ToF-SIMS analysis corroborated with the findings in the AFM characterization.

3.2.4 The Deposition Process

Particle deposition experiments under quiescent conditions were carried out using the optical microscopic observation method in a closed rectangular cell. The cell consisted of two glass slides of dimension of 2 cm × 6 cm separated by a PDMS spacer about 3 mm thick. The patterned substrate was attached to one of the glass slides, and remained immersed in the liquid throughout the experiment. The glass slides and spacer were enclosed in an aluminum holder provided with a rectangular opening on its top surface for visualization (Figure 3.3). The top glass slide was also provided with two ports for addition or removal of solutions from the cell.

For model colloids in the deposition experiment, two different diameters (1 μm, 2 μm) of white PS particles were used; relevant properties of these particles are listed in Table 3.1. The stock suspension concentration of the negative PS particles used in experiments was typically within 1.7×10^{16} to $1.8 \times 10^{16} \text{ m}^{-3}$. The zeta potentials of carboxylate SAMs are reported to be near neutral at pH 3 to 4 and become more negative with increasing pH, consistent with the weak acidity of -COOH groups [222-224]. The amine SAMs exhibit positive zeta potential at low pH, decreasing with increasing pH and becoming negative above pH 7 [222, 224]. Based on this information, the pH of the suspension of particles of different volume fractions was kept within the range of 5.1 to 5.2 in order to encourage disassociation of both the carboxylic acid and the amine head groups on the patterned SAM. The colloidal solutions were made using KCl (ACS grade, Fisher Scientific) with ionic concentration of 10^{-4} M and the pH was controlled by adding appropriate amount of 0.01 N HCl acid solution. Approximately 2 mL of the suspension was introduced into the closed cell with the patterned substrate in place.

All experiments were performed at 25°C and deposition was allowed to occur for 24 h under quiescent condition. After deposition, the cell was flushed to

remove the excess suspended particles using 10^{-4} M KCl solution modified to have the same pH as the particle suspension used, thereby preserving the final deposition structure in solution. It was observed that this rinsing process did not dislodge any of the deposited particles from the substrate surface, implying the particles were irreversibly deposited on the surface.

3.2.5 Microscopic Imaging

The deposition structures formed by the particles were investigated *in situ* with an optical microscope. The closed deposition cell was placed under an upright microscope (Zeiss, Germany) coupled with a CCD camera (Basler A 311f, Basler Vision Technologies, USA). Images were captured at two magnifications (10X and 25X) and the image sizes were 640 by 480 pixels. Post processing of the images (see Section 3.2.6) was conducted using NI Vision 8.0 (National Instruments, USA) to determine the position of the centers of the deposited particles and count the total number of particles deposited.

Fluorescence microscopy: As noted in Section 3.2.3, the chemical patterns imprinted on the substrates are not visible under an optical microscope. In order to capture the patterns optically both before and after deposition of the model particles, a fluorescence microscopy method [225] was used employing negatively charged Nile Red fluorescent polystyrene particles of 100 nm diameter (excitation/ emission wavelength of dye: 520 nm/580 nm; Interfacial Dynamics, USA). Other relevant properties of these particles are listed in Table 3.1. These particles preferentially deposit on the positively charged stripes. The images were captured using a fluorescence microscope (Axiovert 200M, Zeiss, Germany) fitted with a FITC filter set (FS10, Zeiss, Germany) having an excitation band pass filter of range (450-490 nm) and emission band pass filter of range (515-565 nm) and coupled with a colour CCD camera (Basler A 102fc, Basler Vision Technologies, USA). Images were captured at 10X, 20X and 40X magnifications using the NI Vision 8.0 frame grabber.

To capture the image of the bare patterned substrate, 100 μ L of the fluorescent particle laden stock suspension was added to the closed cell containing the sample

immersed in 10^{-4} M KCl solution. The particles were allowed to deposit over a 24 h period after which the suspension was flushed and replaced again with fresh KCl solution. The captured images reveal the negatively charged patterns as dark coloured stripes while the positively charged stripes fluoresce due to the deposition of the 100 nm particles.

To image the underlining pattern concomitantly with the deposited structures, first the larger model particles were allowed to deposit (using the deposition procedure mentioned earlier) in the closed cell. At the end of the deposition cycle, the model particle suspension was flushed out, and a second suspension containing the 100 nm fluorescent particles was added. The deposition of the fluorescent particles was allowed to continue for 24 h, after which the second suspension was removed and replaced by fresh KCl solution. Next, the substrates were imaged under a microscope to acquire two types of images under identical magnification, and on the same region of the substrates. The first image was captured in the phase contrast mode (no fluorescence), showing only the deposited structure of the larger model particles. The second image was captured in the fluorescence mode. The fluorescent regions correspond to locations on the substrate which are positively charged and do not contain any large model particle.

3.2.6 Post processing and Analysis of Images

The images were captured as 8 bit grayscale images using the frame grabber option in the image processing software (NI Vision Assistant 8.0, National Instruments, USA). For each experimental condition studied, at least 4 images were taken from each sample at different locations on the sample. From each of these 640 by 480 pixels sized images, 5 smaller windows (images of size 200 by 200 pixels) were randomly chosen for analysis. The images were also corrected for angular tilt where necessary.

Next a particle analysis was performed on each of images. Particle analysis consists of a series of processing operations and analysis functions that produce information about particles in an image. A typical particle analysis process first involves a series of modifications to enhance the image quality for better recogni-

tion of the particle. Then the process scans through the entire image, detects all the particles in the image, and provides statistical information on each particle—such as the presence of particles, their number and size, and location. The following briefly describes the steps involved in the process [226]:

a. Edge detection: Edge detection refers to the process of identifying and locating sharp discontinuities in an image. The discontinuities are abrupt changes in pixel intensity which characterize boundaries of particle in the image. For our analysis, the Laplacian method [227] of edge detection was used using a 3x3 kernel.

b. Thresholding: Next a binary image was created using a thresholding process. Particles are characterized by an intensity range. They are composed of pixels with gray level values belonging to a given threshold interval (overall luminosity or gray shade). All other pixels are considered to be part of the background. Thresholding sets all pixels that belong to a range of pixel values, called the threshold interval, to a user-defined value, and it sets all other pixels in the image to 0. The threshold interval has two user-defined parameters: lower threshold and upper threshold. All pixels that have gray level values equal to, or greater than, the lower threshold and equal to, or smaller than, the upper threshold are selected as pixels belonging to particles in the image. Pixels outside the interval constitute a part of the background.

c. Particle filter: Particle filters isolate and keep the ‘circular’ particles while removing the remaining non-circular objects from the image. Multiple user-defined parameters such as perimeter, angle, area, and center of mass can be used to identify and classify these particles. For our analysis, the filter criterion chosen was the particle area. Any particle that did not fit in the range bounded by the minimum and maximum values for the area was removed and the particles that fit in the range were kept.

d. Measurements: The pixel measurements were calibrated against real-world measurement and was found that for the magnification studied, 1 pixel = 0.3922 μm for 25X and 1 pixel = 0.9709 μm for 10X magnification. Next the image is

scanned and all the particles present within the image are detected while recording the positional information for each particle.

All the above steps were incorporated in a script form and run in a batch process for each image analysis. Once the data file was generated for each image, the file contained the following information: total number of particles in the image, length and width of image (in pixels and real units), and the x and y coordinate information of the center for each particle (in pixels and real units).

3.3 Results and Discussion

3.3.1 Characterization of Patterned Samples

Images of the amine ($-\text{NH}_2$) and carboxylic terminated ($-\text{COOH}$) thiol SAM patterns, produced by μCP using a PDMS stamp containing alternate $4\ \mu\text{m}$ (positive or $-\text{NH}_2$ terminated) by $3\ \mu\text{m}$ (negative or $-\text{COOH}$ terminated) wide stripes, are shown in Figure 3.4. In the first topographic image (Fig. 3.4a), as obtained in the tapping mode, no pattern is evident because the chain lengths of the $-\text{NH}_2$ and $-\text{COOH}$ terminated thiols are similar (both C11), and consequently no perceptible height variations are observed. However, in the friction mode, it is possible to detect the pattern because of the difference in adhesion properties between the tip and the chemically patterned substrate. As seen from the $30\ \mu\text{m} \times 30\ \mu\text{m}$ FFM image in Fig. 3.3b, contrast between regions of patterned SAMs terminated by NH_2 and COOH groups are visible in the friction mode as the technique detects changes in the lateral forces between the tip and the substrate due to the change in chemical functionality in adjacent regions. This image shows the relative variation in the frictional property of the two regions; the bright region (higher friction) of approximately $4\ \mu\text{m}$ widths corresponds to the stripe patterned with the $-\text{NH}_2$ terminated thiol, and the darker region (lower friction) of approximately $3\ \mu\text{m}$ corresponds to the $-\text{COOH}$ terminated region. Fig. 3.3c is the surface potential map of a section of the same patterned substrate obtained in the SSPM mode. This image shows the relative variation in surface potential of the two regions; the bright region (higher surface potential) corresponds to the stripe

patterned with the -NH_2 terminated thiol, and the darker region (lower surface potential) corresponds to the -COOH terminated region. ToF-SIMS was used to confirm the presence of the thiols in the pattern. In Fig. 3.3d, the contrast obtained from the Cl^- signal (for the amine-HCl thiol) in the figure shows the stamped $4\ \mu\text{m}$ pattern, but with less definition than that seen in the FFM or SSPM images. In summary, a variety of surface characterization modes were used to indicate that the pattern has been successfully reproduced over the gold substrate.

A second set of experiments was used to validate the formation of the patterned SAM. In this case, the patterned substrate was immersed in a concentrated dispersion of the fluorescent Nile Red 100 nm polystyrene particles. The negatively charged particles deposited on the oppositely charged (positive) stripes of the substrate. A high concentration of the fluorescent particles used in the deposition ensured that the favourable stripes would be almost entirely covered by the particles, thus making them visible for imaging. Figure 3.5 depicts the fluorescence microscopy image obtained for $2\ \mu\text{m}$ (positive) and $2\ \mu\text{m}$ (negative) patterns on the substrate. The negatively charged patterns appear as dark stripes whereas the positively charged bands fluoresce due to the deposited particles. This method of imaging the patterns allowed us to capture larger view areas (a maximum of approximately $800\ \mu\text{m} \times 600\ \mu\text{m}$ area for a 1280×960 pixel image) on the substrate, which was not possible in the other modes of characterization used. This shows the modest uniformity of the SAM patterns over relatively large areas of the substrate.

3.3.2 Parameter Definitions

In this section, some of the parameters and mathematical functions used to analyze the deposition images are introduced. Figure 3.6 is a geometric representation of the square image of a patterned substrate. The substrate consists of striped chemical heterogeneity with particles of diameter d , depositing on the surface. The width of the favourable or attractive stripes (shown in gray in the figure) is w , whereas the width of the unfavourable stripes is b . The structure thereby created has a periodicity along the horizontal direction, which is aligned

perpendicular to the stripes with the periodicity length or pitch, $p = w + b$. The ratio of the width of the favourable stripe to the particle diameter, or the *size ratio*, γ is a non-dimensional measure of the size of the particle with respect to the width of the favourable region and is given by:

$$\gamma = \frac{w}{d} \quad (3.2)$$

The ratio of the favourable stripe width to pitch or the *favourable (area) fraction* λ specifies the fraction of the surface favourable for deposition and is given by:

$$\lambda = \frac{w}{p} \quad (3.3)$$

The total surface coverage of particles is calculated as:

$$\theta = \frac{\text{Total surface area covered by the deposited particles}}{\text{Collector surface area}} = \frac{N_p S_p}{S} = \frac{\pi N_p d^2}{4L^2} \quad (3.4)$$

where N_p is the number of adsorbed particles over the collector, $\pi d^2/4$ ($= S_p$) is the projected cross-sectional area of the particle, and L^2 ($= S$) is the surface area of the substrate.

Radial distribution function or pair correlation, $g(r)$ is a mathematical function that is used to describe a cluster or aggregation of objects. Conceptually, the radial distribution function $g(r)$ is defined as the probability of finding a particle at a radial distance r from another particle (placed at $r = 0$) normalized with respect to a uniform distribution. To obtain $g(r)$, the images were first processed by the particle analysis procedure described in Section 3.2.6 to locate the coordinates of the centers of the particles. The $g(r)$ was then determined by sweeping an annular ring of fixed width radially outward from the center of the particle in question (Figure 3.6). This ring or circular bin forms one particular sub-region. Many sub-regions are formed as the ring is swept outward. Any particle that is found within the area covered by the circular bin would be counted as being a part of that bin. This procedure is then repeated for all the particles in the image area under study and the particles in each bin counted. After the occupation number of all of the bins has been determined, the result is then averaged over all the particles in the system. A $g(r)$ curve for the distribution of the particles is then constructed using the definition,

$$\begin{aligned}
g(r) &= \frac{\text{Local particle density}}{\text{Average particle density}} \\
&= \frac{\text{Total number of particle pairs in each bin, } \Delta N_p}{\text{Average number of particle pairs in each bin, } \Delta N_{av}} \\
&= \frac{\Delta N_p}{\text{Area of bin} \times \rho_{av}} = \frac{\Delta N_p}{2\pi r \Delta r \times \frac{4\theta}{\pi d^2}}
\end{aligned} \tag{3.5}$$

where ΔN_p is the number of particles adsorbed within the annular bin of area $2\pi r \Delta r$ drawn around the central particle. The value obtained in Eq. (3.5) is evaluated for N_p particles and averaged to give the desired radial distribution function.

The directional distribution function is calculated following a scheme similar to the radial distribution function; the primary difference is that the radially scanned annular shell used for the $g(r)$ calculation is replaced by a rectangular bin of area $L\Delta x$ and scanned along the x -direction:

$$g(x) = \frac{\Delta N_p}{\text{Area of bin} \times \rho_{av}} = \frac{\Delta N_p}{L\Delta x \times \frac{4\theta}{\pi d^2}} \tag{3.6}$$

Similarly, the direction distribution function in the y direction can be calculated. For convenience both distances r and x have been normalized using the particle diameter d as the scaling variable.

3.3.3 Deposition Morphology

Figure 3.7 show the optical images obtained for the two control experiments performed where the substrates were made chemically homogenous *i.e.* each substrate is completely positively charged and negatively charged individually. The bright spots in the images represent the spherical model particles against the dark background of the sample substrate. In Fig. 3.7a, as expected, little or no particles are seen to deposit on the negative control substrate (as both particle and substrate bear the same charge). What little deposition was observed on the negative control was attributed to experimental error (*e.g.* caused by presence of dirt or scratches on the Au surface). The $g(r)$ function (the radial distance r is scaled with respect to the particle diameter, d shown in Fig. 3.7b for this case shows that there is very little probability of finding particles (as $g(r)$ tends to zero). The high peak reflects that should a particle deposit, the chances of finding

another particle close to the deposited one is very high as the remaining area is not favourable to deposition.

In Fig. 3.7c, the negatively-charged particles are seen to deposit in a random fashion on the positively charged substrate. The deposition on the positive control represents a random system, in which all spatial locations are equally likely, implying no certain positional information in the long range. Indeed, Fig. 3.7d demonstrates a nearly featureless radial distribution function implying the distribution of the particles to be rather homogeneous (as $g(r)$ value approaches the value of 1). The main peak of the curve is located at a distance ($r > d$) at about 1.55 times the particle diameter. The distance of the first peak in the radial distribution function stands for the nearest neighbour distance. For hard spheres (with no charge), the first peak would appear at $r = d$. This is referred to as the steric exclusion effect, *i.e.* the particles in the first nearest neighbour ring cannot get closer to the origin than by a diameter of the particle because of the presence of the hard spherical particle already present there. The shift in the distance observed from the steric position is related to the strength of the inter particle repulsion arising from electrostatic interactions. At long distances, the $g(r)$ value approaches 1 which indicates the absence of long-range order.

Figure 3.8 depicts the deposit morphologies obtained after deposition of model 2 μm diameter PS particles on the patterned substrate consisting of alternate negative and positive stripes that are both 2 μm in width ($\gamma = w/d = 1$). The favourable area fraction λ of the substrate is 50%. The images were obtained by initially depositing the model 2 μm particles followed by the deposition of the 100 nm fluorescent particles (procedure as discussed in Section 3.3.1). Table 3.3 contains the other pertinent experimental conditions.

Figure 3.8a depicts the phase contrast image of the model particles depositing onto the heterogeneous substrate. The particles (bright spots) appear to be depositing in an apparently random fashion on the substrate; the pattern underneath cannot be discerned readily by merely looking at this deposition image.

Figure 3.8b is the fluorescence image of the exact same area shown in Fig. 3.8a. In this image, the positively charged stripes appear as bright coloured

regions due to the 100 nm negatively charged fluorescent particles depositing on them while the model 2 μm particles appear as dark circular shapes (being non-fluorescent) against the bright positive charged stripes. The negatively charged stripes are the dark lines present in between the bright positive stripes.

Figure 3.8c is an image obtained by superimposing the images obtained in Figs. 3.8a and 3.8b, such that the (2 μm) model particles and the underlying pattern are now visible simultaneously. This unique imaging method provides insight regarding the deposit morphology on a patterned heterogeneity. From the image, it is apparent that majority of the particles (around 95%) have deposited on the positively charged stripes. Furthermore, there seems to be a propensity of these particles to deposit near the edges of the favourable stripes. Finally, the image reveals that the negatively charged stripes are not completely devoid of particles.

In Figure 3.9, the results of the particle deposition experiments on patterned substrates conducted for three different ratios γ ($= w/d$) are presented. In each experiment, the deposition was performed for the same overall duration (24 h) following which the samples were directly imaged without drying (see Table 3.3 for other pertinent information on the experimental conditions). Figure 3.9a shows the three microscopic images of the deposition structure created on the charge modified substrate (area shown is approximately $160 \mu\text{m} \times 160 \mu\text{m}$ at a magnification of 25X). In each image, the positive and negative lines are vertically oriented. Three combinations of stripe width and particle size were investigated. The images (from left to right) represent the case of $\gamma \approx 1$ (*i.e.*, when the favourable stripe width is about the same as the particle size; particle diameter is 2 μm and pitch is 4 μm), $\gamma \approx 2$ (favourable stripe width is roughly twice the particle size; the particle diameter is 0.96 μm and pitch is 4 μm) and $\gamma \approx 4$ (favourable stripe width is about four times the particle size; particle diameter is 0.96 μm and pitch is 7 μm) respectively. All the images show bright specks against a dark background (the substrate), the bright regions being the model particles. In the first image ($\gamma \approx 1$), at first glance, the particles appear to have deposited randomly with no apparent pattern. For this case, the favourable area fraction of the sub-

strate is $\lambda = 0.5$. In the subsequent two images representing the cases $\gamma = 2$ (with $\lambda = 0.5$) and $\gamma = 4$ (with $\lambda = 0.57$), the deposition pattern appears much more ordered than observed for the case of $\gamma = 1$. In both these images, the particle size (or diameter) is smaller than the stripe (one half of the width and a quarter of the width of the stripe, respectively).

Comparing all three images, it appears that the underlying heterogeneity pattern cannot be discerned readily when the particle diameter and the width of the favourable stripes are comparable, with the unfavourable gap between two consecutive favourable stripes being smaller. In other words, for $\lambda \geq 0.5$, the large scale particle ordering due to chemical patterning of the substrate becomes less pronounced as γ approaches 1.

Figures 3.9b and 3.9c are plots of the pair correlation functions (radial and directional, respectively) of the corresponding deposition images underneath which they are placed. In Fig. 3.9b the value of the radial distribution function $g(r)$ reflects the density of pairs separated by distance r averaged over the entire population and normalized to the uniform bulk density. The radial distance r is scaled with respect to the particle diameter, d . All the three radial distribution profiles show a series of well developed peaks, varying periodically with r . This oscillatory behaviour of the plot implies that there is an alternation between enhanced and reduced probability of finding a particle at a certain distance r from the central particle relative to that for uniformly distributed particles. In each panel, the locations of the favourable (positively charged) areas are indicated by the regions of enhanced probability ($g(r) > 1$) while locations where $g(r)$ is less than unity represent the unfavourable (negatively charged) deposition sites.

This emergence of the order is a correlation effect that develops during the deposition stage, due to the pre-patterning of the substrate. The presence of the periodic heterogeneity in the system significantly affects the shape of the distribution functions for the particles as indicated by the value of the frequency of the plots (distance from one peak to the next peak) which coincides with the pitch of the underlying pattern. For example, the frequency of the graphs for the first two images ($\gamma = 1$ and $\gamma = 2$) is approximately $4 \mu\text{m}$ and is around $7 \mu\text{m}$ for $\gamma = 4$,

which are also the pitch values for the underlying stripes in these figures (Table 3.3). Although the distribution profiles all closely emulate the periodic nature of the underlying heterogeneity, the correlation becomes weaker at large distances.

The distance of the first peak in the radial distribution function represents the nearest neighbour distance. For the first graph, this distance is $r \approx 2.6 \mu\text{m}$ for the $2 \mu\text{m}$ particles, whilst the first peak distance corresponds to $r \approx 1.6 \mu\text{m}$ for the $0.96 \mu\text{m}$ particles in the subsequent two images. This shift in the distance from the steric position ($r = d$) is similar to that observed in the case of the deposition on the positive control (where, $r \approx 1.55d$) which was said to be related to the strength of the inter particle repulsion arising from electrostatic interactions between the like charged particles. The relative value of the first peak value for the case $\gamma = 1$ is lower than compared to those for $\gamma = 2$ and $\gamma = 4$. This implies that for the case when the particle size is the same width of the stripe, the probability of finding particles in the immediate neighbour of the central particle is less than that of those when the particle is smaller in size than the stripe. This is a reasonable observation because when $\gamma = 1$, the particles being roughly the same size as the favourable stripe and furthermore since their centers are constrained to remain within the favourable stripe, the particles cannot position themselves side by side (*i.e.* laterally) but they have positions available to them above (and/or) below the particle in question (in the vertical direction).

In Fig. 3.9c are plots showing the directional probability in the horizontal direction (x) of the patterned substrate (the patterns lie vertically along the y axis, as in Fig. 3.6). The directional probability $g(x)$ is defined as the probability of finding a given particle at x scaled distance (scaled with respect to the particle diameter d) from the center of another particle, normalized to unity at large distance. The correlation effect is more pronounced in these plots; the periodicity does not die out at larger distances. The directional probability plots in the y direction (not shown) showed no such correlation and the plots were similar to that shown in Fig. 3.9d for a homogeneously attractive surface. This implied that the patterns were positioned perpendicular to the x -axis (causing a certain order in the deposition structure in that direction) whilst deposition in the y -direction

resembled random deposition. The frequencies of the plots were in sync with the pitch of the underlying pattern (as seen for the radial distribution).

In summary, comparing all three images, it appears that the underlying heterogeneity pattern cannot be as easily identified when $\gamma \approx 1$, particularly if the favourable stripes are very closely spaced. The close spacing of the favourable stripes is ensured when the favourable area fraction, $\lambda \geq 0.5$. When $\gamma \approx 1$ and $\lambda = 0.5$, one can detect some organization order of the particles on very close inspection in the macroscopic level over the large patterned region as shown by the green shaded area in Fig. 3.10a. However, in comparison, in Fig. 3.10b, the deposition seen in the smaller view area (about 1/15th the size of Fig. 3.10a) appears to be random at that small scale. The randomness observed in the small scale in the images implies that the deposition process can be described by the 2D random sequential adsorption (RSA) process [72]. In the basic RSA model (more details in Chapter 4), a particle in proximity to the surface can either adsorb or bounce away from the surface depending upon the availability of the adsorption sites. Recalling the definition of the dimensionless coverage (2D density) as $\theta = \frac{N_p S_p}{S}$ (Section 3.3.2), the maximum (or jamming) surface coverage for hard spheres in on a homogeneously favourable surface derived from the RSA process is $\theta_{\max} \approx 0.546$ [73]. The surface coverage calculated for the deposition images (where the surface area S considered is the entire collector surface, including both favourable and unfavourable areas) in Fig. 3.9a is $\theta_{(\gamma=1)} = 0.27$, $\theta_{(\gamma=2)} = 0.26$ and $\theta_{(\gamma=4)} = 0.097$.

3.4 Conclusions

Deposition of model colloidal particles onto striped charge heterogeneous planar substrates in a quiescent aqueous medium was studied. The striped patterns were developed using microcontact printing of carboxyl and amine terminated thiols on a gold substrate and characterized using the different modes in the AFM. Deposit morphologies were observed using a unique combination of phase contrast and

fluorescence microscopy on a bi-disperse particle deposit. The primary conclusions from the study are:

- The majority of the particles are deposited on the positively charged stripes and the negatively charged stripes are not completely devoid of particles.
- Particles tend to preferentially deposit at the edges of the favourable stripes.
- The extent of this bias to deposit at the edge is controlled by the proximity of consecutive favourable stripes (or width of the intervening unfavourable stripes) as well as the particle size relative to the stripe width.
- In the deposition images, the underlying heterogeneity pattern cannot be discerned readily when the particle diameter and the width of the favourable stripes are comparable, with the unfavourable gap between two consecutive favourable stripes being smaller. In other words, for $\lambda \geq 0.5$, the large scale particle ordering due to chemical patterning of the substrate becomes less pronounced as γ approaches 1.
- Radial distributions functions and x -directional distribution functions prove to be a useful tool in investigating the deposition structure on these heterogeneous substrates and the profiles closely emulate the periodic nature of the underlying heterogeneity.

In the next chapter, a Random Sequential Adsorption (RSA) deposition model based on a Monte Carlo procedure and employing a simple binary probability distribution is formulated to try and predict the deposit morphology obtained in these experiments.

Table 3.1 Relevant properties of the model polystyrene sulfate particles used in the deposition experiments

Property	1 μm model particles	2 μm model particles	100 nm fluorescent Nile Red particles
Mean diameter [†] , μm	0.96	2	0.10
Standard deviation of diameter [†] , %	9.4	2.6	4.1
Percent Solids in stock [†] (gm/100 ml)	8.4	8.1	2.2
Particle number concentration [†] , m^{-3}	1.7×10^{16}	1.8×10^{16}	3.9×10^{19}
Surface charge density [†] , $\mu\text{C} \cdot \text{cm}^{-2}$	-6.4	-7.1	-1.0
Zeta Potential [‡] , mV	-83.57 ± 0.50	-104.80 ± 1.03	-----

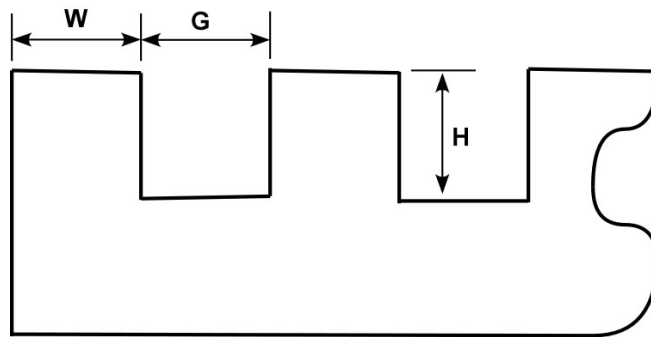
[†]As reported by manufacturer

[‡]As measured using a Brookhaven ZetaPals, 10 runs taken in a 0.01mM KCl solution of pH 5.12

Table 3.2 Stamp characterization results

Design Dimensions			
Stamp number	G μm	W μm	H nm
1	2	2	500
2	3	2	500
3	4	3	500

Created Mean Dimensions			
Stamp number	G μm	W μm	H nm
1	2.1 ± 0.05	1.8 ± 0.2	459.3 ± 11.1
2	3.3 ± 0.1	1.6 ± 0.07	449.5 ± 13.6
3	4.1 ± 0.03	2.9 ± 0.07	457.3 ± 7.1



Schematic diagram of a cross-section of a stamp

Table 3.3 Experimental conditions under which the deposition experiments were performed for Figures 3.7, 3.8 and 3.9.

Properties	$\gamma = w/d$		
	1	2	4
Mean diameter of particle, d (μm)	2	0.96	0.96
Width of favourable stripe, w (μm)	2	2	4
Pitch, p (μm)	4	4	7
Favourable area fraction, λ ($= w/p$)	0.5	0.5	0.57
Particle concentration, N_p (particles/ m^{-3})	1.8×10^{13}	1.7×10^{14}	1.7×10^{14}
KCl solution molartiy, M/pH	$10^{-4} / 5.12$	$10^{-4} / 5.11$	$10^{-4} / 5.13$

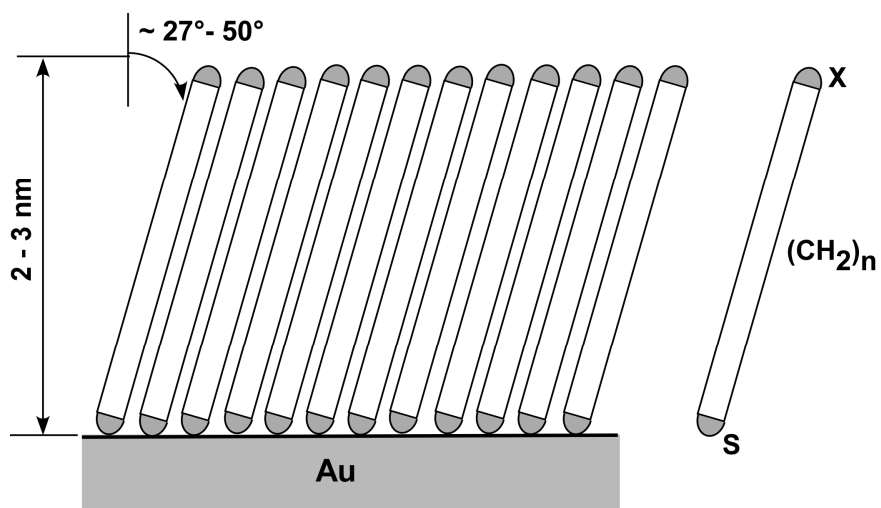
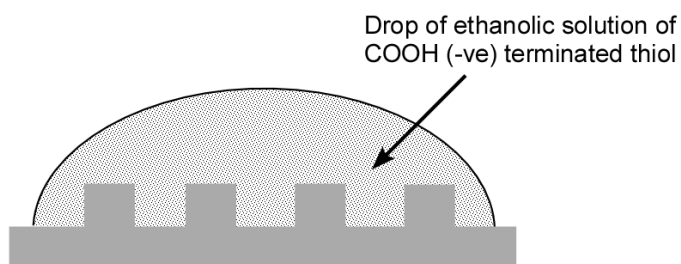


Figure 3.1: Schematic representation of a highly ordered monolayer of alkane thiolate formed on a gold substrate. The most ordered structures are formed from organic compounds of $\text{HS}(\text{CH}_2)_n\text{X}$ with $n = 10-18$ and X = a small functional group. The chain tilt varies from $\sim 27^\circ$ - 50° relative to the surface normal and the thickness of the monolayer varies between 20-30 Å [215].

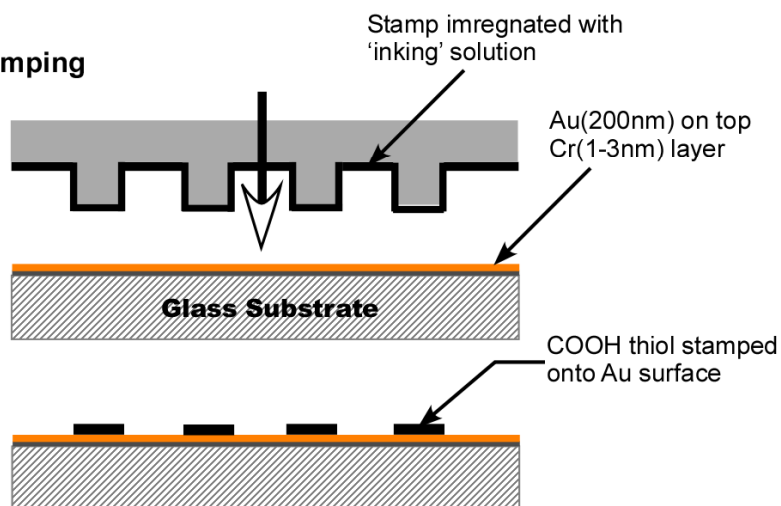
1. PDMS stamp



2. Inking



3. Printing/Stamping



4. Patterned substrate

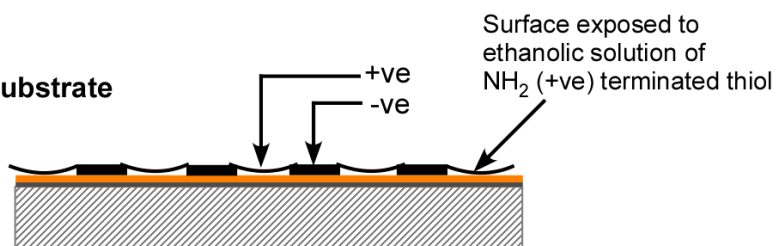


Figure 3.2: Flow diagram summarizing the steps in micro contact printing of SAM of thiol on an Au coated glass surface. The stamp was inked by exposure to a 10^{-4} M ethanolic solution of HS $(\text{CH}_2)_{10}\text{COOH}$ (negative terminus), brought into contact with the gold substrate, and removed. The substrate was then soaked for 30 min in a 10^{-4} M ethanolic solution of $\text{C}_{11}\text{H}_{25}\text{NS-HCl}$ (positive terminus). The substrate was finally washed with anhydrous ethanol and dried in a stream of N_2 .

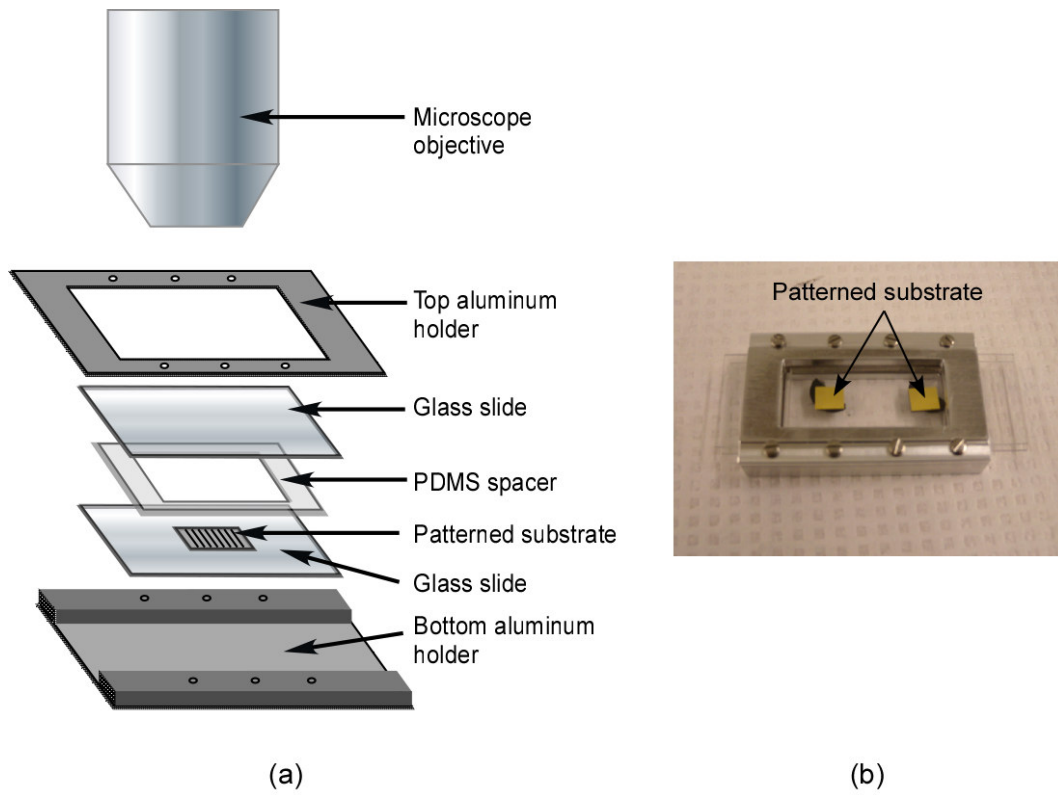


Figure 3.3: (a) Diagram depicts an exploded view of the closed cell assembly. (b) Photograph showing the assembled closed cell.

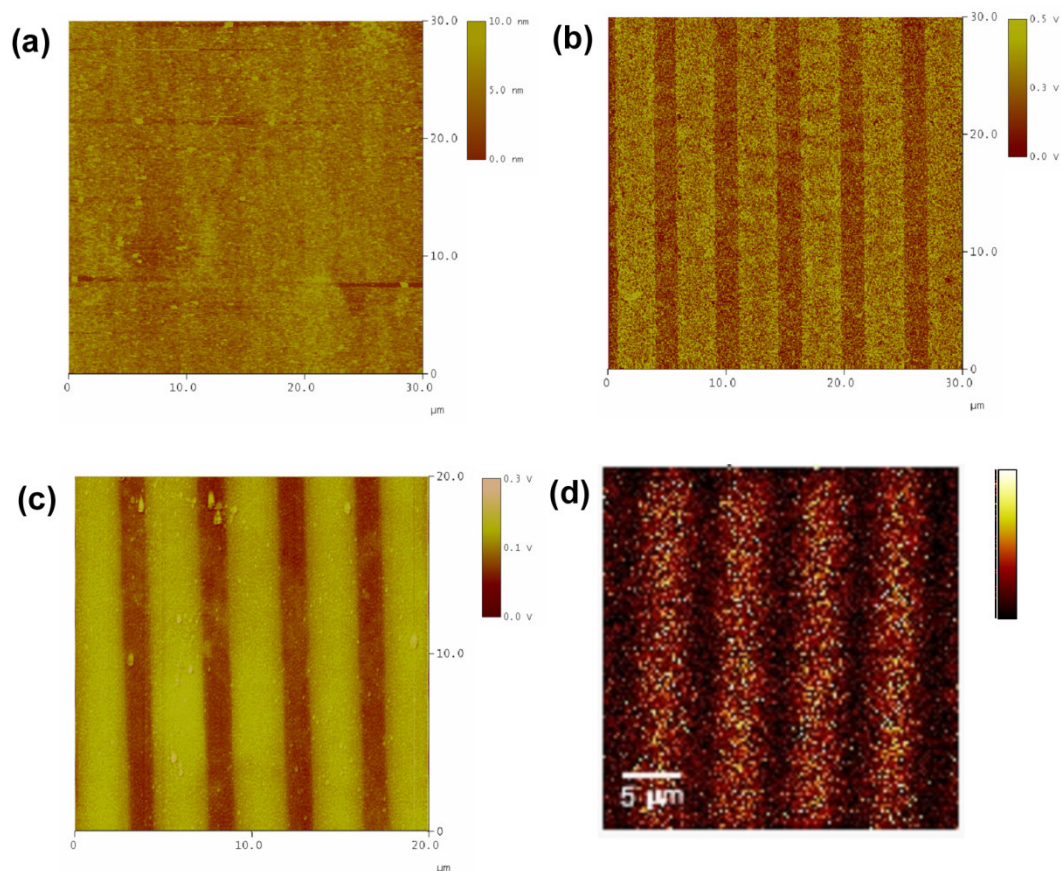


Figure 3.4: Images showing the results of the various techniques used to characterize the created patterned charge heterogeneous substrate. The substrates shown in all the images have 4 μm (positive) by 3 μm (negative) stripes. (a) AFM Tapping mode image of the patterned substrate showing no visible physical variation in the topology of the surface due to the similarity in chain length of the two thiols used. (b) Friction Force Microscopy (FFM) image of the same area as scanned in (a). This image shows the low friction areas as dark (corresponding to the negatively charged stripes) and the high friction areas as light (corresponding to the positively charged stripes). (c) Scanning Surface Potential Microscopy (SSPM) image showing the relative surface potential difference between the adjacent patterned thiols groups. The more positive surface potential (light) is associated with the NH_2 terminated thiol monolayer. (d) ToF-SIMS image showing the presence of the amine thiol (bright) as evident by the contrast obtained from the Cl^- signal.

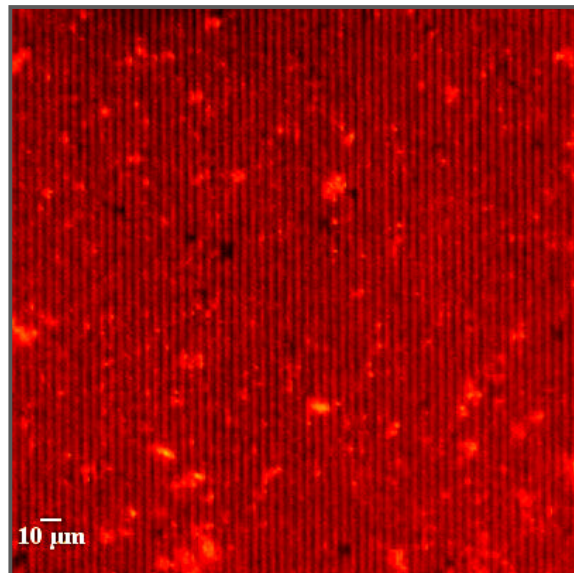


Figure 3.5: Fluorescence microscopy image of a patterned charge heterogeneous substrate. The patterns are 2 μm (positive) by 2 μm (negative) and image was taken at a magnification of 10X (scale bar is 10 μm and view area is approx. 251 μm × 251 μm). The negatively charged patterns appear as dark coloured stripes while the positively charged bands fluoresce (red) due to the negatively charged 100 nm Nile Red polystyrene sulfate particles depositing on the oppositely charged stripes.

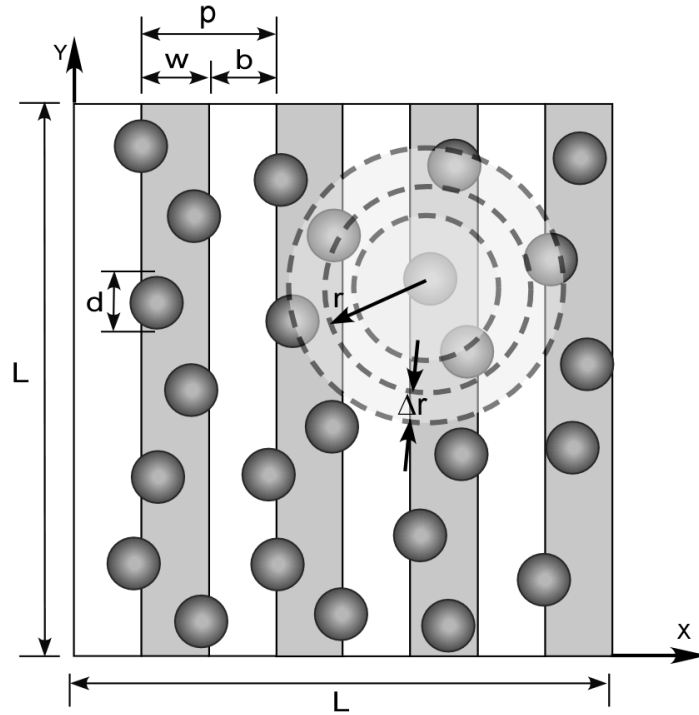


Figure 3.6: Diagrammatic representation of the patterned substrate showing the key dimensional parameters and the radial distribution calculation scheme. The square collector of length L consists of rectangular stripes with alternate regions that are favourable (gray) and unfavourable (white) to deposition of widths w and b respectively. The total width of a favourable and unfavourable stripe gives the pitch, p . The deposited spherical particles are of diameter d . Each particle is placed at the origin of a circular shell that sweeps out radially from the center of the particle in question. Each shell forms one particular circular bin of radius r and width Δr . Any particle that is found within the area covered by the circular bin is counted as being a part of that bin. This procedure is then repeated for all the particles in the image area.

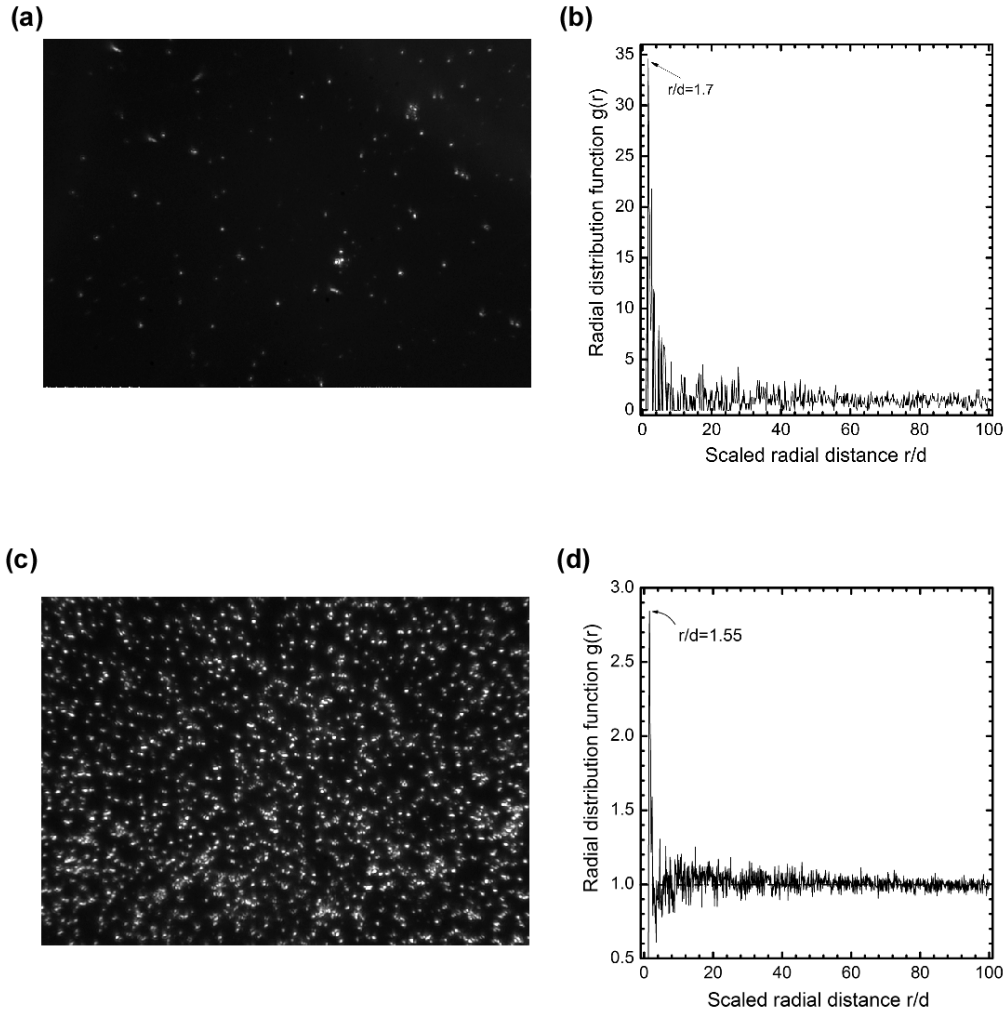


Figure 3.7: Results of the deposition on the control substrates. Part (a) and (c) are optical pictographs of $0.96 \mu\text{m}$ diameter negatively charged PS particles (bright spots) depositing on a negatively chemically homogenous negatively charged substrate and positively charged substrate respectively. The deposition conditions are: KCl concentration = 0.1 mM with a $\text{pH} \sim 5.15$ and deposition lasted for 24 h. The view region corresponds to a $256 \mu\text{m}$ by $192 \mu\text{m}$ area. Parts (b) and (d) are radial distribution functions obtained for the deposition images shown in (a) and (c) respectively.

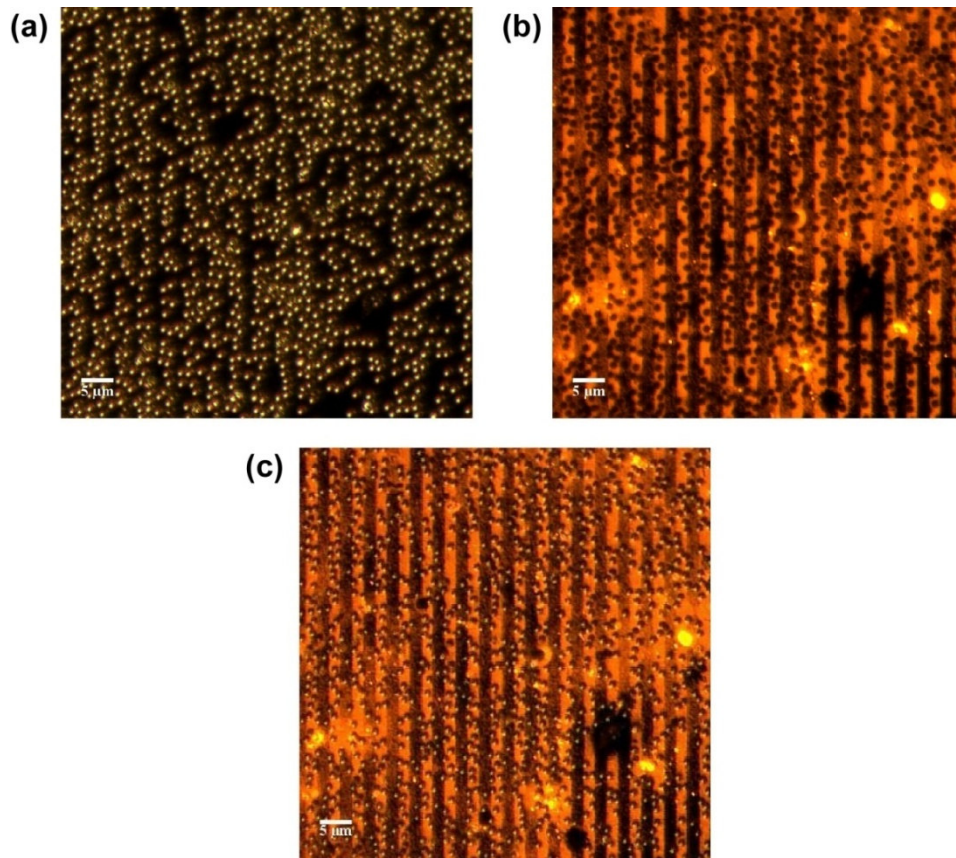


Figure 3.8: Fluorescence microscopy images displaying the deposition of 2 μm negatively charged polystyrene sulfate particles on a 2 μm (positive) by 2 μm (negative) striped pattern ($\lambda = 0.5$, $\gamma = 1$) (a) Phase image showing the 2 μm particles depositing in an apparently random fashion on the substrate (b) Fluorescent image of the exact same area in (a) obtained by depositing 100 nm negatively charged Nile Red particles onto the remaining regions of the positively charged stripe. The model 2 μm sized particles appear as dark circular shapes on the fluorescent positively charged stripe while the negatively charged patterns appear as dark coloured stripes. (c) Image of a larger area on the same substrate obtained by superimposing images like those obtained in (a) on (b), such that the model particles and the underlying pattern are now visible, simultaneously.

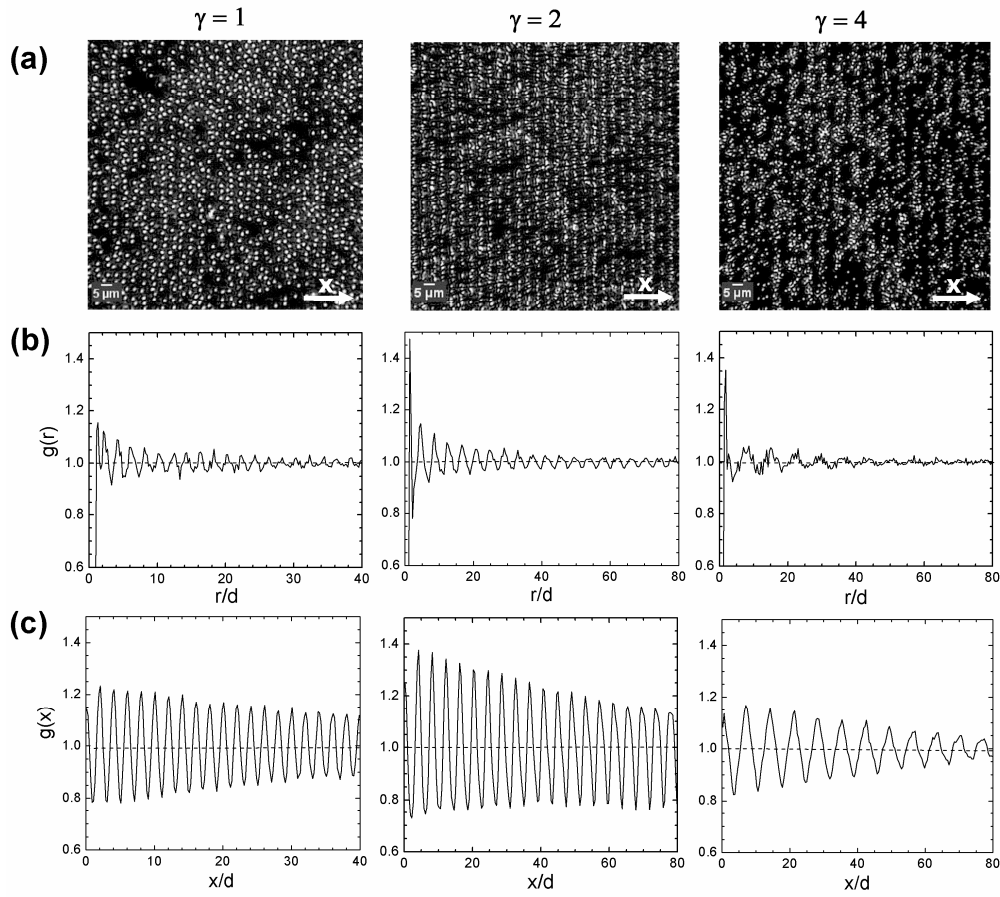


Figure 3.9: (a) Optical micrographs of polystyrene particles (bright spots) deposited on chemically patterned planar substrates for three different γ values (from left to right) of 1, 2 and 4. View area represents $160 \mu\text{m} \times 160 \mu\text{m}$ on the substrates. The surface coverage calculated was $\Theta_{(\gamma=1)} = 0.27$, $\Theta_{(\gamma=2)} = 0.26$ and $\Theta_{(\gamma=4)} = 0.1$. (b) Plots of the radial distribution function (c) and x -directional distribution functions obtained for the corresponding deposition images. All distances are scaled with respect to particle diameter. The locations within the deposition image that are likely particle positions are indicated by the peaks in the distribution functions. Table 3.3 contains other information relevant to the deposition images obtained in part (a).

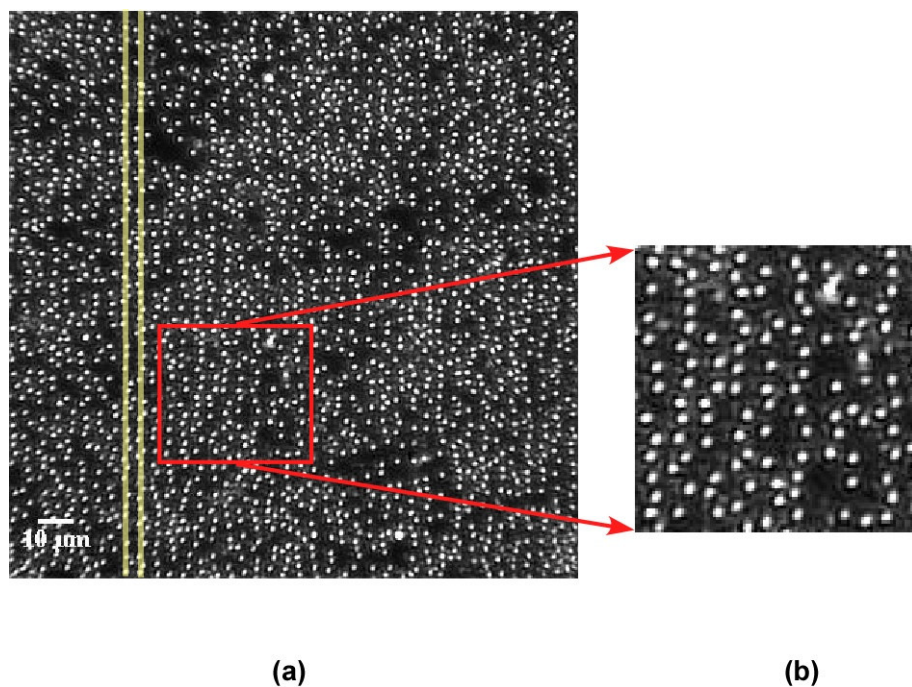


Figure 3.10: Optical microscope images of polystyrene particles (bright spots) deposited on chemically patterned planar substrate when $\gamma = 1$ and $\lambda = 0.5$. (a) Same image as shown in Fig. 3.8a. The two shaded areas (in green) highlight the order observed in the macroscopic scale. (b) A zoomed image of the region marked out within the red square as shown in (a). This region represents an area of roughly $39 \mu\text{m} \times 39 \mu\text{m}$. At this scale, one observes a lack of colloidal order observed in (a).

CHAPTER 4

MODELING PARTICLE DEPOSITION ON CHARGE-HETEROGENEOUS SUBSTRATES

4.1 Introduction

In the previous chapter, an experimental investigation was undertaken to study the deposition structure of micron sized colloidal particles on model heterogeneous substrates containing patterned charge heterogeneity. In this chapter[†] a simple mathematical description of particle deposition on such chemically patterned surfaces employing a Monte-Carlo [228] type simulation technique is presented. Predictions obtained from the simulations for different particle sizes and stripe dimensions are then compared against the experimental results presented in Chapter 3.

Adsorption of colloidal particles onto solid surfaces is often an irreversible process [229]. This was also observed for the deposition conditions investigated in Chapter 3. For strong attractive interactions between the particle and the surface, the energy barrier for desorption can be much higher than the corresponding barrier for adsorption with little or no diffusion of the particles on the solid surface [229]. As a consequence, once the particle is deposited, it appears to be irreversibly attached to the surface on the time scale of the experiment. In such limiting cases of monolayer deposition, the process can be suitably described by the random sequential adsorption (RSA) model [73, 103, 230]. The standard RSA model considers a sequence of trials of particle adsorption on a homogenous interface and is defined by the following three rules: (a) the particles are adsorbed sequentially and randomly on the surface (b) two adsorbed particles cannot

[†] Parts of this chapter are related to the published work of “Tania Rizwan and Subir Bhattacharjee” in *Langmuir*, v.25 (9), pp 4907-4918, 2009.

overlap, and (c) an adsorbed particle cannot move along the surface (no diffusion), nor can it move away from the surface (no desorption) once it is deposited. Once an available empty surface site is found, the particle is adsorbed, otherwise the particle is rejected and a next addition attempt is undertaken. Adsorption can be continued until no further particles can be placed, and this situation is called the jamming limit θ_∞ . At this limit approximately 54.6% of the surface covered by the monodispersed hard spheres.

The classical RSA model accounts only for steric effects, and omits all consideration of energetics which limits the capability to model real systems accurately. Nonetheless, the conceptual simplicity of the classical RSA model still makes it an attractive basis for development of more realistic descriptions. For example, there have been a number of extended RSA models developed that include the effects of particle shape [231-234], Brownian motion [82-85], external forces (like gravity) [78-81], particle-particle [74-76] and particle-interface electrostatic interaction [77], colloid-particle polydispersity [235-237], and surface heterogeneity [56, 109, 238, 239] to name a few. The Monte Carlo method is usually used to select the coordinate of the particle on the substrate. A Monte Carlo method is a stochastic technique, meaning that it is based on using random numbers and probability to investigate problems [228]. The defining characteristic of the Monte Carlo method is its use of random numbers in its simulations. Although the Monte Carlo simulation technique has formally existed since the early 1940s', only with the increase in computer technology and power in recent times has the technique become more widely used.

The following section describes in some detail the model created and the simulation procedure employed.

4.2 Simulation

4.2.1 Model Description

A smooth planar collector is considered that is represented as a square lattice of edge, L , as shown schematically in Figure 4.1. The substrate consists of striped

chemical heterogeneity. The adsorbing particles are assumed to be spheres (with a disk shaped projected area) of diameter $d = 2a_p$. The width of the favourable (attractive) stripes is w , whereas the width of the unfavourable stripes is b . The stripes are arranged perpendicular to the length of the substrate, the structure thereby created is periodic along the x -direction, which is aligned perpendicular to the stripes with the periodicity length or pitch, $p (= w + b)$. The number of favourable (or unfavourable) stripes on the square lattice is $n_{pair} = L/p$, although their relative contribution to the total surface area will vary depending on the ratio w/p . The total surface area of the favourable stripes is given by $S_f = n_{pair}wL$, and the corresponding favourable area fraction is:

$$\lambda = \frac{S_f}{S} = \frac{n_{pair}w}{L} = \frac{w}{p} \quad (4.1)$$

where S is the total surface area of the collector. The ratio of the width of the favourable stripe to the particle diameter is given by the size ratio, $\gamma (= w/d)$. Both these ratios have been previously defined in Section 3.3.2.

4.2.2 Procedure

A simple probabilistic method was employed to derive information on the distribution of particles deposited on the patterned surface. These simulations were conducted according to the aforementioned random sequential adsorption (RSA) model. In other words, once a particle is deposited on the substrate, its projected area is considered to be inaccessible for deposition of subsequent particles. The basic rules of the RSA simulation scheme (as shown schematically in Figure 4.2) for spherical particles depositing on a planar surface are summarized below [103]:

- (i) An adsorbing particle is created whose position and orientation is described by the set of coordinates selected at random within prescribed limits defining the adsorption domain.
- (ii) If the particle fulfils the adsorption criteria, it is adsorbed with unit probability and its position remains unchanged during the entire process, *i.e.* the particle is adsorbed irreversibly.

(iii) If the adsorption criteria are violated, a new adsorption attempt is made that is uncorrelated with previous attempts.

For these simulations, the probability of a particle attaching to a site, $p(x,y)$, is defined as

$$\begin{aligned} p(x, y) &= p_f & \theta \in \theta_{f,a} \\ &= p_u & \theta \in (1 - \theta_{f,a}) \end{aligned} \quad (4.2)$$

When the particle is located on a region of the collector that is completely favourable and is accessible to the particle (or a vacant favourable site), $\theta_{f,a}$, a probability of $p_f = 1$ is assigned. Elsewhere on the substrate, the probability is assumed to be $p_u = 0$. More complex distribution functions can be proposed, but in this study the investigation is primarily based on the above simple representation of the deposition probabilities.

The deposition algorithm starts by randomly selecting an (x, y) location on the substrate as a possible attachment point. Following this, the probability of the attachment at this point is determined. If the surface is favourable and vacant, the probability of deposition is 1, and the particle position is accepted (deposition on a vacant favourable site). Otherwise, if the randomly selected position overlaps with the projected area of a previously deposited particle, the probability is chosen to be zero. Finally, if the particle position is on the unfavourable region, the probability of deposition is again chosen to be zero. When the jamming configuration is about to be reached, much of the area on the surface is blocked by previously deposited particles. Only tiny disconnected regions are available for further deposition. Since the sites are chosen at random, these available sites are hard to find. Thus to minimize the simulation time spent at this stage of the deposition, in all the simulations the deposition attempt was stopped when 2000 consecutive attempts failed to result in deposition. The scheme was coded using Fortran 77 and simulations performed on a PC.

4.2.3 Parameters Calculated

In this section, the parameters that are calculated for analysis are defined.

The total fractional surface coverage of particles is calculated as,

$$\theta = \frac{\text{Total surface area covered by the deposited particles}}{\text{Collector surface area}} = \frac{N_p S_p}{S} = \frac{\pi N_p d^2}{4L^2} \quad (4.3)$$

where N_p is the number of adsorbed particles over the collector, $S_p = \frac{\pi d^2}{4}$ is the projected cross-sectional area of the particle and $S = L^2$ is the surface area of the collector. Alternatively, the fractional surface coverage of only the favourable fraction of the heterogeneous substrate can also be calculated by replacing the total area of the collector, S , with the surface area of the favourable fraction, $S_f = \lambda S$, yielding

$$\theta_f = \frac{\text{Total surface area covered by the deposited particles}}{\text{Favourable surface area}} = \frac{\pi N_p d^2}{4\lambda L^2} \quad (4.4)$$

The local particle density distribution $\rho^*(x)$ is defined as the probability of finding a particle at a given location of the substrate relative to a uniform distribution. The uniform particle distribution is computed as $\rho_{av} = N_p/S$, where N_p is the total number of particles, and S is the area of the region of interest of the substrate. Assuming the region of interest to be a square of edge L , it is noted that $S = L^2$. In this study, $\rho^*(x)$ is calculated by first generating a deposited particle population according to the RSA scheme described previously. Then the substrate is divided into n_{bin} number of rectangular bins along the x axis, where the area of each bin is given by $A_{bin} = L^2/n_{bin}$. After counting the number of particles in each bin, ΔN_p , the local particle density at the mid-point of each bin is given by $\rho(x) = \Delta N_p n_{bin}/L^2$. The normalized particle density can now be determined as,

$$\rho^*(x) = \frac{\rho(x)}{\rho_{av}} = \frac{\Delta N_p n_{bin} S}{L^2 N_p} = \frac{\Delta N_p n_{bin}}{N_p} \quad (4.5)$$

In subsequent sections of this chapter, the density distributions are reported over a single heterogeneous stripe pair. This quantity is denoted as $\rho_n^*(x)$. Since the entire substrate consists of $n_{pair} = L/p$ pairs of stripes, $\rho_n^*(x)$ can be computed as follows: Each stripe pair is divided into Δn bins and the particle density distributions were calculated on them. Let the particle density distribution evaluated over the i th stripe pair be denoted as $\rho_i^*(x)$. This process is repeated over each stripe pair, and the accumulated results averaged over the n_{pair} stripe pairs. The resulting expression of the distribution function is:

$$\rho_n^*(x) = \frac{\sum_{i=1}^{n_{pair}} \rho_{i^*}(x)}{n_{pair}} \quad (4.6)$$

Note that Eqs. (4.5) and (4.6) yield identical results in the limit of an infinitely large surface or a large number of samples. For finite sized samples and small surface areas, though, Eq. (4.6) provides smoother variation of the density with position.

The radial distribution (pair correlation) function $g(r)$ and directional distribution functions have already been defined in Section 3.3.2 and are calculated invoking Eqs. (3.5) and (3.6). For convenience both distances r and x have been normalized using the particle diameter d as the scaling variable. All particle centers located outside the perimeter of the simulation area were discarded for all the above calculations.

4.3 Results and Discussion

In this section some results of the simulations performed are presented. The effect of the variation in size ratio and favourable area fraction on particle distribution was investigated. Size ratios were varied from $\gamma = 0.25$ to 2, while the favourable area fraction varied from $\lambda = 0.25$ to 1.0 (where $\lambda = 1.0$ corresponds to a completely homogenous substrate). Radial distribution functions were also determined and compared with those found experimentally.

4.3.1 Variation of Size Ratio γ

Figure 4.3 depicts the particle density distribution on the substrate for different combinations of size ratio γ , corresponding to a fixed favourable area fraction λ . The distribution is shown over a rectangular region of the substrate having an area of pL (*i.e.* distribution is shown over a pair of favourable and unfavourable stripes). The normalized single particle density distribution on the surface is shown as histograms in Figure 4.3. Clearly, all the particles deposit on the favourable fraction of the surface. When $\gamma = 0.25$ and 0.5, *i.e.*, when the particle diameter is 4 and 2 times the favourable stripe width, respectively, the distribution

is fairly even on the favourable stripe, with the probability density $\cong 2$ on every segment of the favourable stripe (Figs. 4.3a and 4.3b). When $\gamma = 1$ (particle diameter equal to the favourable stripe width), there is a greater probability of finding the particles at the edges of the favourable stripes (Fig. 4.3c). This behaviour is also apparent when $\gamma = 2$ in Fig. 4.3d. Therefore, as $\gamma \leq 1$ (or, $d \leq w$), the particle distribution appears to be considerably biased toward the edges of the favourable stripes.

4.3.2 Variation of Favourable Area Fraction λ

Figure 4.4 depicts the particle density distributions for a fixed value of $\gamma = 1$ (particle diameter equal to the favourable stripe width) corresponding to different favourable area fraction λ , ranging between 0.25 to 1.0 (fully favourable). In Figs. 4.4a ($\lambda = 0.25$) and 4.4b ($\lambda = 0.5$), the density distributions depict a considerable bias toward a greater particle density at the edges of the favourable stripes. However, for $\lambda = 0.8$ and $\lambda = 1$ (Figs. 4.4c and 4.4d), the density distribution becomes more uniform over the entire favourable surface.

It might be of interest to note that although a uniform probability, $p_f = 1$ was used to deposit the particles on the favourable stripe; the particles develop a distinct bias toward depositing at the stripe boundaries during the random sequential adsorption. Recently, this trend has also been reported by Adamczyk *et al.* [240]. They observed from their theoretical study of deposition of particles on a collector with a single favourable stripe that there is a definite tendency of particles to concentrate preferentially at the perimeters of these stripes. In these studies, however, a single boundary of a favourable stripe was considered. Consequently, the probability of a particle depositing at the edge of a favourable stripe remained unchanged as particle deposition progressed. These results indicate that the deposition probability at the favourable stripe boundary is subject to modification depending on the width of the adjoining unfavourable stripes. In particular, if the widths of the unfavourable stripes become comparable to the particle diameter, then the particles deposited on two consecutive favourable stripes can

influence the deposition probabilities at the stripe edges.

The tendency for particles to deposit on the edge of the favourable stripe due to the effect of heterogeneity on deposition can be explained qualitatively in light of the *entropic principle* [240]. Entropy may be seen as a measure of a system's disorder. Maximum entropy is the most probable (equilibrium) state within a system subject to constraints, since everything tends to disorder [241]. Consider the deposition of particles onto a homogeneously favourable substrate. The chances of a particle depositing on a given point on the surface of this substrate is the same as anywhere else on the surface, i.e., the particles have equal probability of deposition on a homogenous substrate resulting in a 'disordered' or random distribution (higher entropy) of the particles. Now, consider the striped surface where the applied constraints limits the choices the particles now have for deposition, thus confining the particles in some specific configurations. Within this system, the particles will seek to maximize the entropy (or the disorder) and show preferential deposition in certain locations on the striped surface. A configuration which requires particular constraints of order (such as no particles can overlap with another particle or no deposition in a particular region of surface) is clearly less likely to occur spontaneously than one in which the conditions are less stringent. Sites near the center being energetically favourable will tend to have more particles. However, at the sites near the edge, a particle adsorbing here does not overlap from 'outside' with other particles (as no particles are depositing in the unfavourable stripe, and so no crowding occurs), so it can 'overhang' from the contour of the collector. The sites near the edge provide more leeway for the particles to arrange themselves in a more disordered manner rather than the sites at the center of the stripe. This is particularly true if the neighbouring favourable stripes are positioned far enough away that there is no crowding of the particles of the neighbouring stripes (as seen in Figs. 4.4a and 4.4b) or the particle is sufficiently small compared to the width of the unfavourable stripe (as seen in Figs. 4.4c and 4.4d). Thus, adsorption to a favourable patch is maximized when the particles can aggregate near the edge without overlapping particles at neighbouring edges. This suggests that under these circumstances, even though

energetically the central region of the favourable stripe is more conducive to deposition, the particles will tend to show a bias towards depositing at the edge of the favourable region.

The above parametric study indicates that there is a considerable variation in the deposit morphology corresponding to different ratios of particle size to favourable stripe width, and the favourable area fraction of the charge heterogeneous substrate. It is particularly interesting that the deposit morphology can be systematically altered by judiciously changing these ratios. In the next section, how these distributions influence the fractional surface coverage of the deposited particles on the patterned surface and the ensuing blocking effects are explored.

4.3.3 Fractional Surface Coverage

It is straightforward to calculate the fractional coverage of the spherical particles on the substrate. Two types of fractional coverage were defined in Eqs. (4.3) and (4.4), namely θ and θ_f , where the former is based on the entire area of the substrate, and the latter is based on only the favourable area of the collector. Notably, when $\lambda = 1$, $\theta_f = \theta$. In fact, in this limiting situation, the maximum theoretical coverage attained by hard spherical particles (also called jamming limit) is $\theta_{\infty} \sim 54.6\%$ [73]. In all cases, the maximum coverage on homogeneous surfaces after a large number of attempted particle placements approached 54.6%.

Figure 4.5 depicts the maximum surface coverage attained on the charge heterogeneous surfaces for different combinations of λ and γ . The primary calculated variable shown in the figures is the maximum surface coverage based on the entire surface area, θ_{max} . The filled symbols are the fractional surface coverage on the favourable area fraction, $\theta_{fmax} = \theta_{max}/\lambda$. The maximum coverage was determined approximately after depositing a large number of particles, when 2000 consecutive attempts failed to result in deposition of a new particle on the substrate. In Fig. 4.5a, the variation of the fractional surface coverage with γ is depicted for a fixed favourable area fraction of 0.5 (50% of the surface is favourable). In this case, the fractional surface coverage approaches the hard-sphere

jamming limit, *i.e.* $\theta_{max} \rightarrow \theta_{\infty}$ for small values of $\gamma \leq 0.5$ (*i.e.* particle diameter is larger than the width of the favourable stripe). For larger values of γ , the maximum coverage is lower. The corresponding maximum coverage evaluated on the basis of the favourable surface area is higher. Clearly, values greater than 1 are unreasonable (the two values of θ_{fmax} enclosed in the dotted box in Fig. 4.5a for $\gamma \leq 0.5$). This apparently anomalous result can be explained in light of the particle size compared to the stripe width. For $\gamma < 0.5$ values (that is when particles are larger than the width of the favourable stripes), particles depositing onto such a surface not only covers the favourable regions, but also a portion of the particle encroach onto the neighbouring unfavourable stripes thereby covering a certain area on those stripes. This extra region that the particle covers on the unfavourable stripe has not been taken into consideration while calculating the favourable coverage, thus resulting in the favourable coverage values being greater than 1. However, all these results show that on these heterogeneous surfaces, the deposition on the favourable fraction of the substrate is enhanced. Also this implies that in particular, when the particle diameter is larger than the width of the favourable stripe, the overall surface coverage attains values that are similar to the coverage attainable on a completely favourable surface (54.6%). In other words, only a 50% favourable surface can act as completely favourable to particle deposition. This interesting observation was pointed out in other earlier studies [70, 71] and shows how the deposit morphology leads to such a behaviour.

Figure 4.5b depicts the maximum coverage corresponding to different favourable area fractions for a fixed value of $\gamma = 1$ (particle diameter = favourable stripe width). The hard-sphere jamming limit is attained ($\theta_{max} = \theta_{fmax} = \theta_{\infty} = 0.546$) when $\lambda = 1$ (entire surface is favourable). When λ is reduced, the overall surface coverage, θ_{max} , decreases monotonically, but the coverage based on favourable surface of the collector, θ_{fmax} increases. This observation indicates that small favourable patches on an otherwise unfavourable site are highly amenable to particle deposition. A closer look is now cast at this scenario.

In Figure 4.6, the deposition distributions obtained on two surfaces is explored;

one surface is made 50% favourable ($\lambda = 0.5$) and the other is a homogeneously favourable surface (no stripes, $\lambda = 1.0$). Deposition patterns on both surfaces were obtained by depositing particles that are twice as large as the width of the favourable stripe on the heterogeneous surface (*i.e.* $\gamma = 0.50$). Fig. 4.6a shows the configuration of the deposited particles generated on the 50% favourable surface while Fig. 4.6b shows the deposited particles on the homogenous surface. The distributions are shown over a square region of the substrate having an area of L^2 and drawn to scale. The total coverage (which is near the maximum limit for both) was calculated to be $\theta = 0.551$ for the striped surface and $\theta = 0.527$ for the homogenous one. In both the distribution maps, it appears as though the particles have adsorbed randomly on the surface of the collectors. It is difficult to determine by a cursory observation of the map and state which substrate has an underlying pattern. It appears that for this combination of particle size and favourable surface fraction (50% favourable), the deposition morphology on the striped surface appears to be similar to Fig. 4.6b (homogenous surface). Fig. 4.6c is a comparison of the plots of the radial distribution or pair correlation function versus the normalized radial distance for the two cases. The $g(r)$ obtained for the homogenous substrate is typical of those obtained by using the 2D hard sphere RSA model [73]. For the striped (dashed line) and homogenous surfaces (solid line), the primary peak (nearest neighbour particle probability) occurs at a distance of $r = d$ and the peak value is only slightly higher for the striped surface. This could be due to the pattern present in the striped surface imparting some ordering by increasing the probability of finding more nearest neighbour particles in the striped substrate than in the homogenous substrate. Compared to the striped surface, the oscillations of the $g(r)$ around the uncorrelated value of 1 are more strongly suppressed for the homogenous substrate. The oscillatory behaviour of the $g(r)$ curve for the striped surface is not as strongly suppressed implying a long range order and a periodicity (the peaks appear at an interval of d) which matches with the pitch of the underlying heterogeneity (pitch, $p = d$).

The salient difference between the two cases is observable in Fig. 4.6d. These

are the plots of the directional distribution function for the two cases. The striking feature is that there is no correlation observed for the homogenous surface in the x direction (as expected), since the particles have an equal probability of depositing anywhere on the substrate along that direction. This is not the case for the striped surface, which has both favourable (deposition probability of 1) and unfavourable (zero probability for deposition) regions. Thus, a strong oscillatory behaviour is seen here (which is also present but less apparent in Fig. 4.6c) with an alternation between enhanced (representing the favourable locations) and reduced probability (unfavourable regions) of finding a particle. The favourable particle locations, as seen in the $g(r)$ plot, coincide with the pitch of the pattern.

4.3.4 Comparison of Simulation Data with Experimental Results

The distribution of particles on the charge patterned surface was computed theoretically, and in this section, these theoretical results are compared against the experimentally observed deposit morphologies from the previous chapter. As mentioned earlier, the theoretical calculations were performed assuming $p_f = 1$ and $p_u = 0$. With this simple binary deposition probability, the resulting deposit morphologies obtained on the substrate depends on the favourable surface area fraction, λ and the size ratio, γ . In Figure 4.7 the experimental data is compared with the simulation results for the case of $\gamma = 1.0$ (particle is the same size as the favourable stripe width) and $\lambda = 0.50$ (surface is 50% favourable) and plot the $g(r)$ and x -directional distribution functions. The experiment was performed using 2 μm polystyrene particles with a solution concentration of 0.1 mM and pH 5.15 on a substrate having 2 μm positive and negative stripes giving the same γ and λ values as investigated in the simulation. In Fig. 4.7, there is a fairly good agreement of experimental data (dashed line) and the numerical results (solid line). Both the $g(r)$ and $g(x)$ plots show that the numerical model predicts the nature of the plots satisfactorily. The oscillatory nature of the $g(r)$ (and $g(x)$) plots that are characteristic of deposition structures on these striped surfaces (and have become a signature of the presence of a pattern), is nicely captured by this simple model.

The position of the peaks of the numerically obtained $g(r)$ and $g(x)$ plots coincide with those of the experiment. However there is a shift observed in the position of the primary (first) peak for the experiment. The position of the peak for the numerical result is at $r = d$, while the peak position as obtained from the experimental data is $r = 1.3d$. At this point it is pertinent to mention that an important feature which was ignored in the theoretical RSA model is the effect of colloidal interactions (*e.g.* electrostatic interaction). The shift in the primary peak observed signifies that the minimum separation distance between the central particle and its nearest neighbour is larger than predicted by the hard sphere model and points toward the presence of electrostatic repulsion between the particles in the experiment, which has been ignored in the model.

The other discrepancy is the magnitude of the peaks; the numerical results show consistently higher values (for the enhanced probability) and lower values (for the reduced probability) than the experimental results. The higher (and lower) peak values seen in the plots for the numerical result are also a consequence of the simplification of the model. The lower values in the experiment imply that there will be fewer particles (than the numerical prediction) available at the favourable sites. When the particles are assumed to be hard spheres in the numerical simulations, they are allowed to deposit right next to each other (if there is a favourable site available). The excluded area is thus just the projected surface area of the previously deposited particle on the surface. However, with electrostatic repulsion acting between them, the exclusion zone for the next particle to come and deposit near the previously deposited particle will be increased. This will affect the short range order of the particles which is singled out by the $g(r)$ and $g(x)$ plots.

4.4 Conclusions

In this chapter, the deposition of model colloidal particles onto striped charge heterogeneous planar substrates was simulated using a simple Random Sequential Adsorption (RSA) model employing a Monte-Carlo technique. The following conclusions can be drawn from the above study:

- RSA process alone cannot impose long-range ordering. Indeed, the particle correlations in RSA are usually rather short range (as seen in deposition on a uniformly charged substrate). It is found that the patterning of the surface can induce ordering over many particle diameter spacing, which reflects the symmetry of the underlying pattern (as seen in the experimental investigations). Thus, the pattern does influence the creation of ordered structures in an otherwise uniform deposition process.
- Particles tend to preferentially deposit at the edges of the favourable stripes, depending on the geometric parameters discussed in this chapter. This is similar to what was observed in the experimental results in Chapter 3. Moreover, the results indicate that this entropic maximization of the deposition probability at the favourable stripe boundary is subject to modification depending on the width of the adjoining unfavourable stripes. In particular, if the widths of the unfavourable stripes become comparable to the particle diameter, then the particles deposited on two consecutive favourable stripes can influence the deposition probabilities at the stripe edges. This also corroborates with the findings in Chapter 3.
- There is a considerable variation in the deposit morphology corresponding to different values of size ratio γ , and the favourable area fraction λ of the charge heterogeneous substrate. It is particularly interesting that the deposit morphology can be systematically altered by judiciously changing these ratios.
- When the particle diameter is larger than the width of the favourable stripe, the overall surface coverage attains values that are similar to the coverage attainable on a completely favourable surface (54.6%). In other words, only a 50% favourable surface can act as a substrate that is completely favourable to particle deposition.
- Deposit morphologies near jamming limits formed on 50% favourable patterned surfaces can be visually indistinguishable to those formed on fully favourable surfaces. Under such circumstances, the underlying patterns can-

not be readily discerned, except by investigating subtle differences between particle radial distributions.

- A simple binary probability distribution based Monte Carlo RSA deposition model adequately predicts the deposit structure. The radial and directional distribution plots obtained from the experimental data and simulation results coincide fairly well, particularly the observed periodicity of the deposition corresponding to the underlying patterns on the substrate.
- There is a discrepancy in the magnitudes of the peaks of the distribution functions; the numerical results show consistently larger oscillations compared to the experimental results. This discrepancy can be attributed to the simplification of the model where electrostatic interactions between the particles have been ignored.

In the next chapter, the goal is to try and understand deposition behaviour on these patterned substrates in light of the interaction forces that occur between a charged particle placed near a chemically heterogeneous substrate.

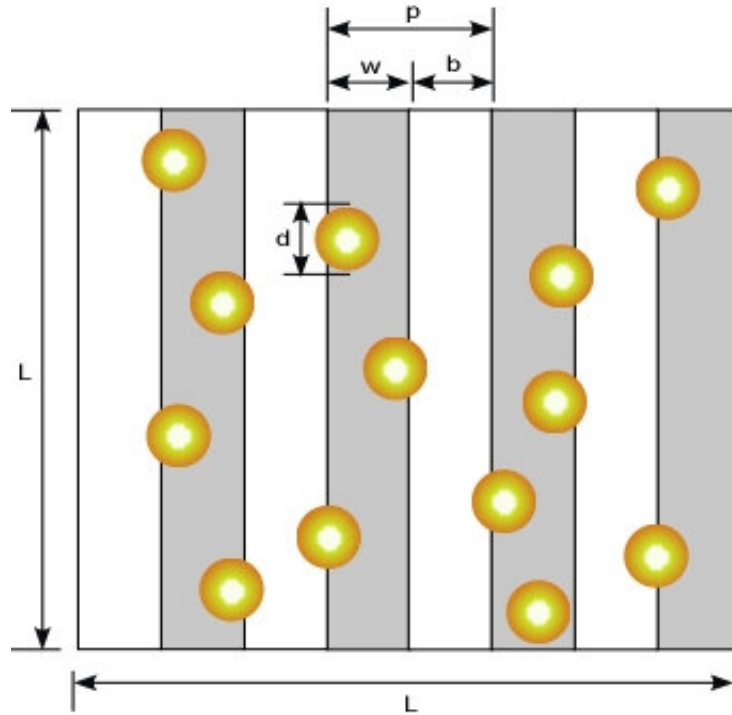


Figure 4.1: Schematic representation of the modeled surface charge heterogeneity. The square collector of height L consists of rectangular stripes with alternate regions that are favourable (gray) and unfavourable (white) to deposition of widths w and b respectively. The total width of a favourable and unfavourable stripe gives the pitch, p . The deposited spherical particles of diameter $d = 2a_p$ have their centers constrained to lie within the favourable stripes.

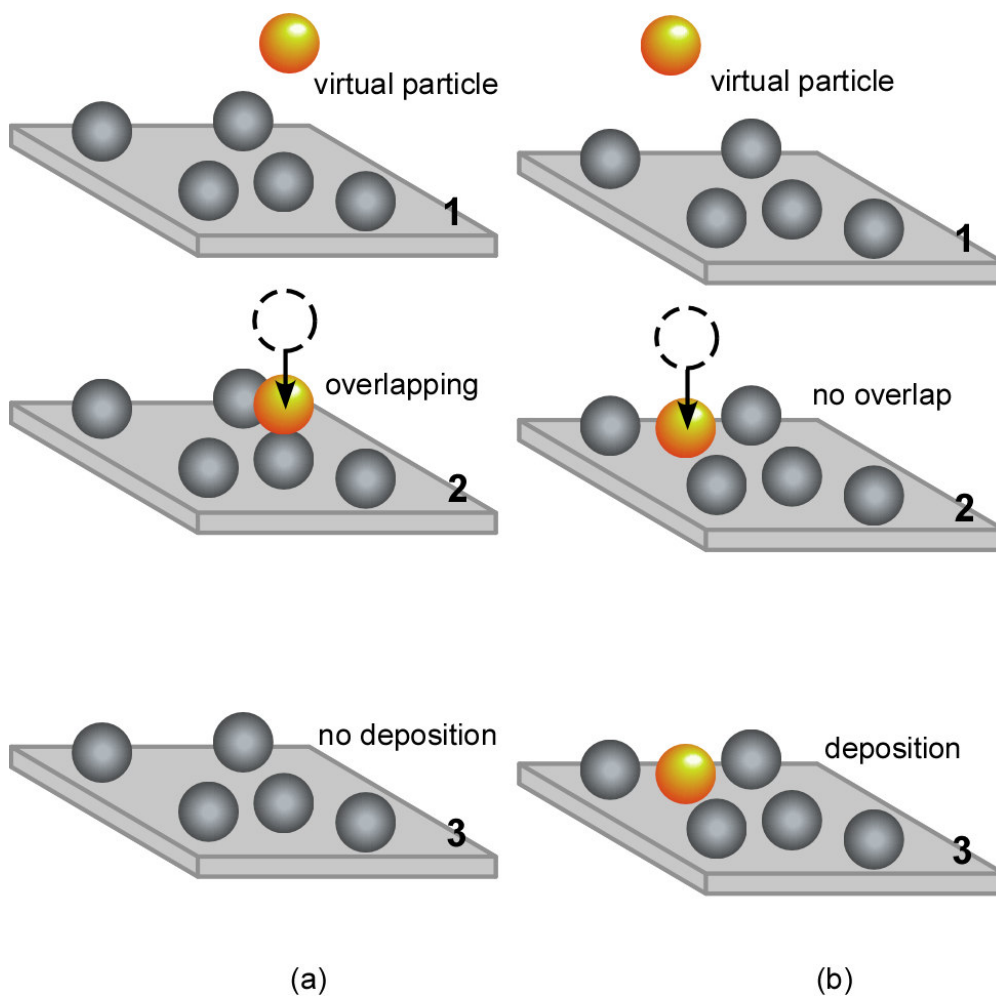


Figure 4.2: A schematic representation of the standard RSA method of simulation: (a) A random virtual particle fails to deposit due to overlapping with previously deposited particle. (b) A successful deposition has occurred at a vacant site [102].

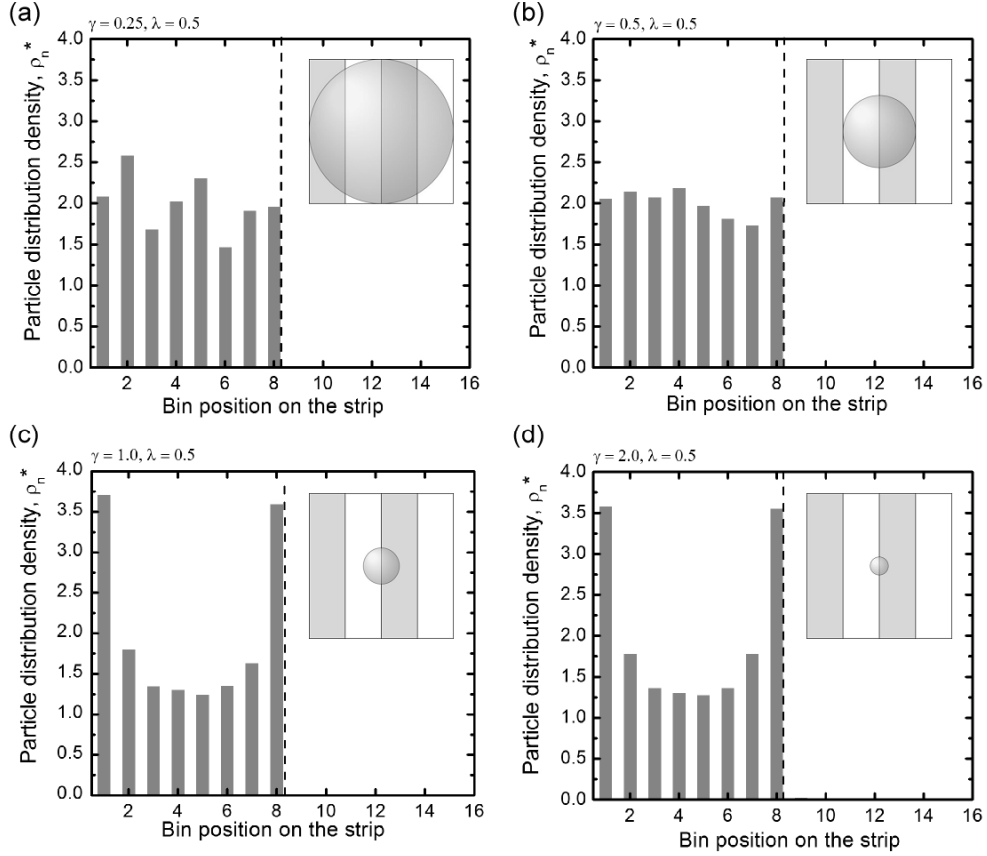


Figure 4.3: Particle distribution histograms for simulation results obtained by varying width to diameter ratios (a) $\gamma = 0.25$, (b) $\gamma = 0.5$, (c) $\gamma = 1.0$ and (d) $\gamma = 2.0$. Particles of diameter d (varying from 0.05 to 0.00625) were deposited on a scaled square area of 1.0 with $\lambda = w/p = 0.5$ (where, $w = b = 0.0125$). Each stripe pair (composed of half favourable and half unfavourable region) has been divided up into 16 bins. The dotted line represents the boundary between the favourable and unfavourable stripes. The inset diagrams show the relative magnitude of the particle size to the stripe widths and are drawn to scale. The particles (centers) present in each bin are counted and a distribution of deposited particles is obtained over a single pair of stripe. This is repeated over the entire area and the particle count is normalized with the average particle number in each bin and averaged for the total number of stripe pairs (in this case 40 pairs).

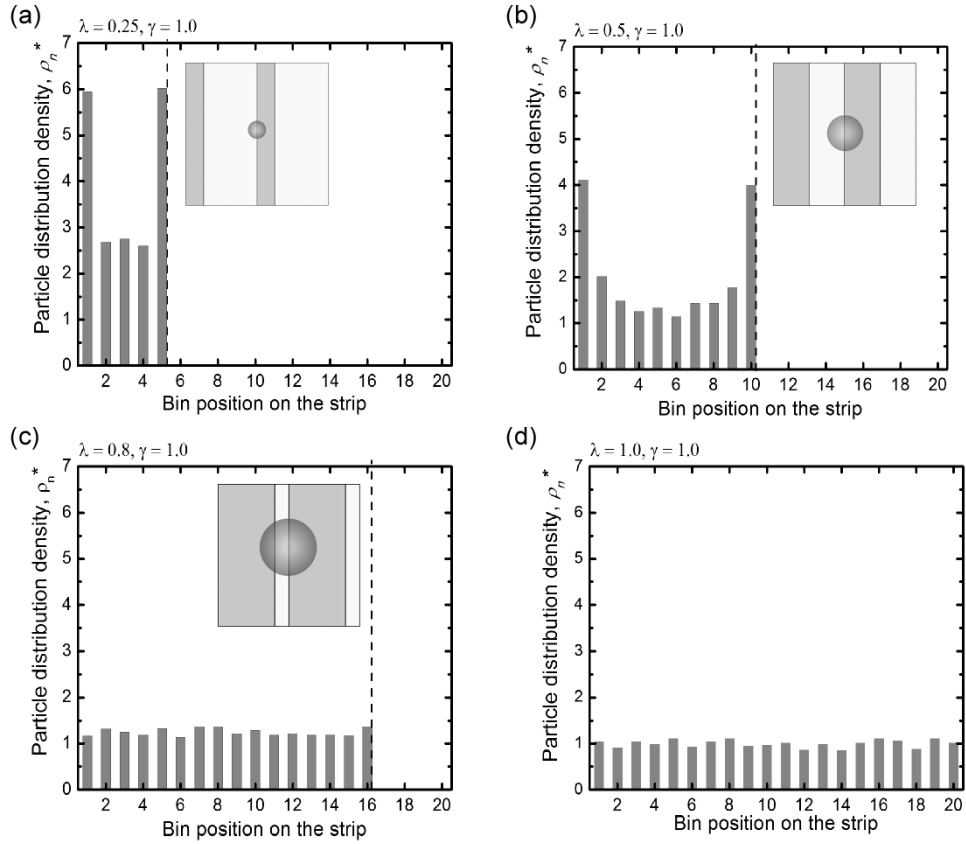


Figure 4.4: Particle density distribution charts obtained for the simulations results by varying favourable width to pitch ratios (a) $\lambda = 0.25$, (b) $\lambda = 0.5$, (c) $\lambda = 0.8$ and (d) $\lambda = 1.0$. Particles of diameter $d = 0.0125$ were deposited on a scaled square area of 1.0 with $\gamma = w/d = 1.0$ (where, $w = 0.0125$ and b is varying). Each stripe pair has been divided up into 20 bins. The dotted line represents the boundary between the favourable and unfavourable stripe. The inset diagrams show the relative magnitude of the particle to the stripes and are drawn to scale. The analysis procedure is the same as described in Fig. 4.3.

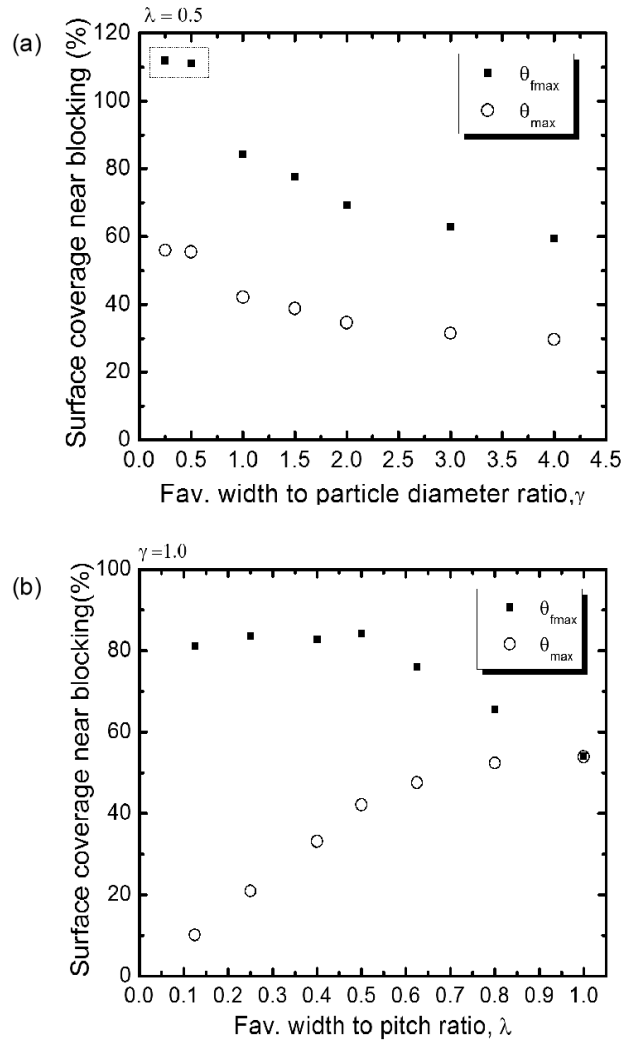


Figure 4.5: Near-blocking surface coverage calculated over the total favourable available area (θ_{fmax} in square “■”) and the total collector area (θ_{max} in circles “o”) for varying (a) γ values and (b) λ values.

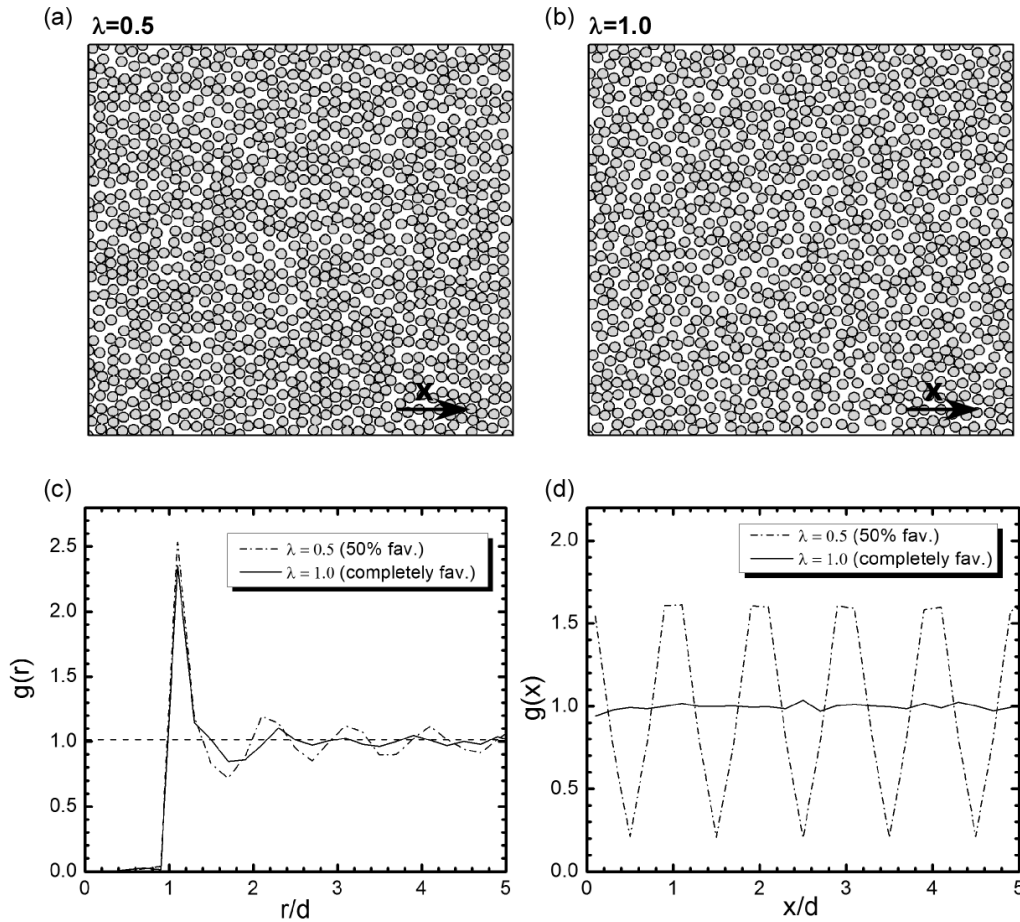


Figure 4.6: (a) Distribution of adsorbed particles generated in the RSA simulation by depositing on a striped surface with a 50% favourable area ($\lambda = 0.5$) by spheres (disks) of diameter that is twice the size of the width of a favourable stripe ($\gamma = 0.5$) and coverage is $\theta = 0.551$. (b) Distribution of the same sized particles as in (a) deposited onto a homogeneously favourable collector ($\lambda = 1.0$) with $\theta = 0.527$. (c) Radial pair distribution functions and (d) directional distribution functions plotted for the cases shown in (a) and (b). Both the plots are shown over a scaled distance of 5 particle diameters with the dotted line representing the data for the striped surface ($\lambda = 0.5$) and the solid line representing the homogeneous surface ($\lambda = 1.0$).

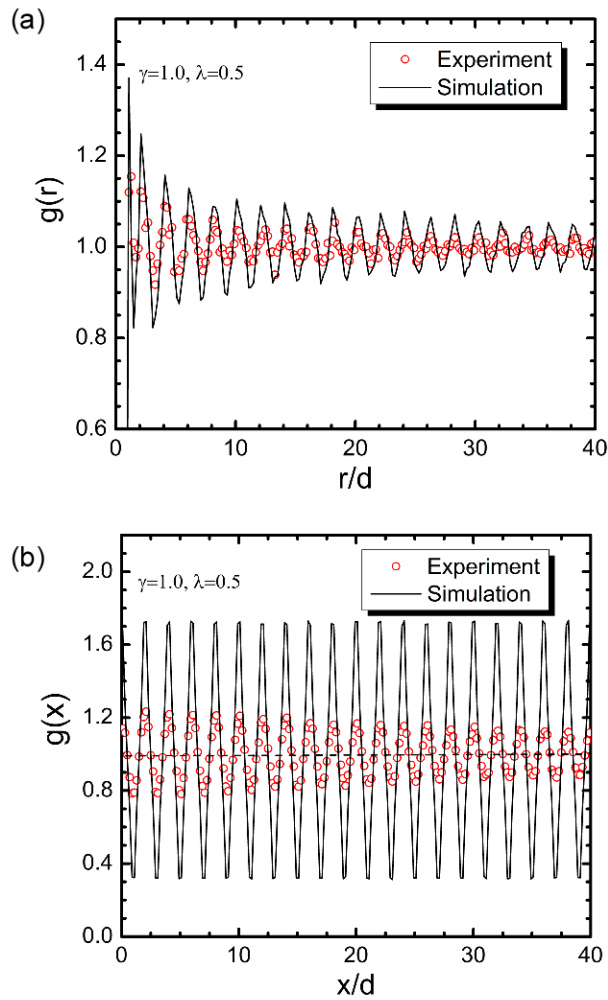


Figure 4.7: (a) Comparison of the radial distribution functions obtained for $\gamma = 1.0$ and $\lambda = 0.5$ with a total coverage of $\theta \approx 0.3$; the continuous line shows the simulation results for a 2D hard sphere and the dots shows the experimental results. (b) Comparison of the x -directional distribution function for the same parameters as in (a). All distances are scaled with respect to the particle diameter, d .

CHAPTER 5

ELECTROSTATIC INTERACTIONS BETWEEN A CHARGED PARTICLE AND A PLANAR CHARGE-HETEROGENEOUS SUBSTRATE

5.1 Introduction

In the previous chapter, it was shown how a simple binary probabilistic model based on a Monte Carlo method was able to capture the deposition structure on patterned heterogeneous substrates. In this chapter, the goal is to try and understand deposition behaviour on these substrates in light of the interaction forces that occur between a charged particle placed near a charged heterogeneous substrate.

It is known [41, 54, 242-244] that the asymmetrical distribution of physical and chemical heterogeneity on surfaces gives rise to an unbalanced force on a particle in a direction parallel (lateral) to the surface along with the vertical (or normally directed) ones. When one considers the three-dimensional nature of the interaction forces, it becomes pertinent to explore the influence of lateral forces caused by heterogeneities on colloidal phenomena such as the attraction or repulsion of particles to/from particular regions of a surface, particularly in the limit of low to no shear force (*i.e.* under quiescent conditions), when the particle can move laterally solely under the influence of this lateral force. Lateral (*i.e.*, parallel to the plane of the surface) forces have been mentioned in studies on surface roughness [41, 54], and there are some studies that attempt to quantify these forces on chemically heterogeneous substrates within the framework of DLVO interactions [242-244]. However, most of the studies involving chemical heterogeneity deal with nanometre scaled heterogeneities. A model was therefore created here to study the influence of the electrostatic forces in three dimensions, on a micron

sized charged particle in a stationary fluid as it is positioned close to a heterogeneous surface possessing chemical or charge heterogeneity of comparable size.

The mathematical model for the electrostatic double layer interaction (EDL) between a particle and a patterned charge heterogeneous planar (flat) surface based on the non-linear Poisson-Boltzmann (NLPB) equation is presented in this chapter. Since, no exact analytical solution to the nonlinear Poisson-Boltzmann equations exists except for a simple planar geometry, and numerical solutions [245] as well as approximate analytic expressions [246, 247] are available for only homogenous 2D systems, thus in this work the three dimensional (3D) NLPB equation was solved numerically for a heterogeneous substrate using the finite element method. In order to investigate the role of charge heterogeneity on the particle deposition behaviour (particularly when the heterogeneity is in the same scale as the particle), the charge heterogeneity on the substrate surface has been modeled taking the lead from the experimental work (Chapter 3) and modeled as alternating stripes of microscopic dimensions bearing favourable and unfavourable regions with respect to deposition. A single colloidal particle was then scanned over the substrate held at different separation heights from the substrate surface and the EDL interaction forces calculated. The interaction force is resolved into a normal and a lateral component, and their magnitudes are compared. The interaction forces are finally incorporated in a simple trajectory analysis to understand the particle distribution results obtained in Chapter 4. The work described in this chapter provides insight regarding the three-dimensional nature of colloidal interactions between chemically heterogeneous bodies at close proximity to each other, and leads to a better understanding of the role of such heterogeneities on particle deposition onto a heterogeneous substrate.

5.2 Mathematical Modeling of Electrostatic Interactions

5.2.1 Governing Equation

Most surfaces acquire charge when brought in contact with an aqueous solution, as discussed in Chapter 1. As a consequence, counterions are attracted to the

charged surface while the co-ions are repelled, forming the electric double layer (EDL). The stability of such a system can be affected by the electric potential distribution near the charged surface. The electric potential distribution within the diffuse double layer is given by the Poisson's equation as:

$$\epsilon \nabla^2 \psi = -\rho_f \quad (5.1)$$

Here ψ is the electric potential, ϵ ($=\epsilon_r \epsilon_0$) is the dielectric permittivity of the suspending fluid, where ϵ_r is the dielectric constant and ϵ_0 is the permittivity of vacuum, and ρ_f is the free charge density given by,

$$\rho_f = \sum_{i=1}^N n_i z_i e \quad (5.2)$$

where n_i represents the ionic number concentration of the i^{th} species having valency z_i , and e represents the magnitude of the electronic charge.

According to Boltzmann probability law, the distribution of charged ions in the diffuse layer is given by,

$$n_i = n_{i\infty} \exp \left[-\frac{w_i}{k_B T} \right] \quad (5.3)$$

where w_i ($= z_i e \psi$) represents the work done in bringing an ion i from the bulk solution to a point in the double layer where the potential is ψ , $n_{i\infty}$ is the bulk solution ionic number concentration at the neutral state where $\psi = 0$, k_B is the Boltzmann constant, and T is the absolute temperature. In the above equation energies involved in moving the other ions aside or creating a passage in the solvent ions are ignored. Inserting Eqs. (5.2) and (5.3) into Eq. (5.1) leads to the well-known Poisson-Boltzmann (PB) equation for the distribution of the electric potential within the charged medium:

$$\epsilon \nabla^2 \psi = - \sum_{i=1}^N n_{i\infty} z_i e \exp \left[-\frac{z_i e \psi}{k_B T} \right] \quad (5.4)$$

For symmetric electrolyte ($z_+ = -z_- = z$, $n_{i\infty} = n_\infty$), the PB equation can be written as:

$$\nabla^2 \psi = \frac{2n_\infty z e}{\epsilon} \sinh \left(\frac{ze\psi}{k_B T} \right) \quad (5.5)$$

The above expression is valid within the electrolyte medium, *i.e.*, outside the charged bodies.

Depending on the charging behaviour of the surface immersed in the dielectric, the electrostatic interaction may be calculated assuming constant surface potential, constant charge, or surface charge regulation boundary conditions at the solid liquid interfaces [1]. Constant potential (CP) and constant charge (CC) conditions represent the limiting charging behaviours of the interfaces and provide a lower and upper bound of the interaction, respectively. Usually, most charged interfaces in aqueous media tend to obey some form of intermediary behaviour between the two above mentioned limits-which is called charge regulation. In the present investigation, only CP conditions have been investigated.

The above equations provide a generalized formulation of the electrostatic problem. Solution of the PB equation in a given geometric framework requires recasting Eq. (5.5) in the proper coordinate system and defining the appropriate boundary conditions at all the solid-liquid interfaces. In the following subsection, a description of the geometry of the computation domain and the boundary conditions employed is presented.

5.2.2 Computational Geometry and Boundary Conditions

The schematic of the 3D computational domain $ABCDEFGH$ in the Cartesian coordinate system (with origin located at D) is shown in Figure 5.1a. It encloses the charged spherical particle P of radius a approaching a planar (heterogeneous) surface $ABCD$ immersed in an electrolyte medium. The vertical separation distance (along the z axis) between the surface $ABCD$ and the approaching particle is denoted by h (Fig. 5.1b). The surface charge heterogeneity residing on the plane $ABCD$ is modeled as alternate rectangular stripes of microscopic dimensions bearing opposite charges (similar to what has been created experimentally as discussed in Chapter 3). Each negative and positive stripe has a specific width which is defined as b and w respectively and lie laterally along the y axis. Since the particle is assumed to be negatively charged throughout this study, the negatively charged stripe will therefore act as an unfavourable region while the positively charged stripe will act as a favourable region with respect to deposition. In the present study the stripe width of the negative and positive stripe is held

equal, *i.e.* $b = w$ such that the favourable area fraction λ defined previously as the ratio of the width of favourable stripe, w to the pitch, $p (= w + b)$ is 0.5. The dimensionless size ratio $\gamma (= w/2a)$ ratio gives a measure of the scale of the heterogeneity with respect to the particle size.

In the framework of the Poisson-Boltzmann equation, the potential distribution around a charged spherical particle in a symmetric ($z:z$) electrolyte is given by Eq. (5.5) expressed in Cartesian coordinates as:

$$\frac{\partial^2 \psi}{\partial X^2} + \frac{\partial^2 \psi}{\partial Y^2} + \frac{\partial^2 \psi}{\partial Z^2} = \frac{2n_\infty z e}{\epsilon} \sinh\left(\frac{ze\psi}{k_B T}\right) \quad (\text{outside the sphere}) \quad (5.6)$$

To render the problem independent of actual physical dimensions of the particle or the box, these equations can be non-dimensionalized with respect to the particle radius a and thermal energy $k_B T$ yielding the following form,

$$\bar{\nabla}^2 \Psi = (\kappa a)^2 \sinh(\Psi) \quad (5.7)$$

Here $\Psi (= \frac{ze\psi}{k_B T})$ is the scaled potential, $\bar{\nabla} = a \left(\frac{\partial}{\partial X} \hat{i} + \frac{\partial}{\partial Y} \hat{j} + \frac{\partial}{\partial Z} \hat{k} \right)$ is the vector derivative operator and κ is the inverse Debye screening length which is defined as:

$$\kappa = \sqrt{\frac{2n_\infty e^2 z^2}{\epsilon k_B T}} \quad (5.8)$$

The surface of the charged particle P and the patterned surface $ABCD$ are assigned a constant potential (CP) conditions as:

$$\Psi = \Psi_p \quad (5.9a)$$

$$\Psi = \Psi_s \quad (5.9b)$$

The variation of Ψ_s along the y direction for a heterogeneous substrate consisting of negative and positive stripes can be considered to have a periodic behaviour:

$$\Psi_s = \Psi_{sn} \quad \text{on the negative stripe} \quad (5.10a)$$

$$\Psi_s = \Psi_{sp} \quad \text{on the positive stripe} \quad (5.10b)$$

where Ψ_{sn} and Ψ_{sp} are the substrate surface scaled potentials corresponding to negative and positive stripes, respectively. This equation implies that the substrate surface potential is stepwise in nature, changing instantaneously from Ψ_{sn} and Ψ_{sp} at the boundary between the unfavourable and favourable stripe. In reality, at the boundary of the stripes there should be a smooth transition of the surface potential

as it changes value over the negative stripe Ψ_{sn} , to its value over the positive stripe Ψ_{sp} , while taking a value of zero at the boundary between the charged stripes [248, 249]. Therefore, in order to capture this behaviour, a smoothing function of sigmoidal nature was incorporated in Eq. (5.10) to smoothen out the changes of Ψ_s in the vicinity of the boundaries between the oppositely charged stripes. The parameters of this smoothing function were defined such that it ensured a zero value for Ψ_s at the edge between the negative and positive stripe:

$$\Psi_s(y) = (\Psi_{sn} - \Psi_{sp}) \left\{ \frac{1}{1+e^{-a(y-y_i)}} - \frac{1}{1+e^{-a(y-y_{i+1})}} \right\} - \Psi_{sn} \quad (5.11)$$

where Ψ_{sn} and Ψ_{sp} are the left and right horizontal asymptote parameters respectively and determines the value of the potential to be applied on the stripe; a is the parameter that controls the steepness of the sigmoid curve, while y_i and (y_i+1) are the inflection points (*i.e.* location where the boundary between the two stripes will be situated). The resulting variation in potential by incorporating Eq. (5.11) for a heterogeneous surface containing oppositely charged stripes of scaled potential Ψ_s ($= +1, -1$) is shown in Figure 5.2, which depicts the variation of Ψ_s in the y direction (along the width of the substrate). Using this type of smoothing function for Ψ_s provides a better estimation of the EDL force between a particle and a heterogeneous substrate consisting of alternate negative and positive bands compared to the stepwise variation of Ψ_s [249].

On the sidewalls $AEFB$, $BFGC$, $DHGC$ and $AEHD$ of the outer domain of the computational box in Fig. 5.1a, symmetry boundary (zero charge) condition is applied:

$$\hat{\mathbf{n}} \cdot \nabla \Psi = 0 \quad (5.12)$$

Here, $\hat{\mathbf{n}}$ represents the unit normal to the surface pointing toward the electrolyte medium. This boundary condition is applicable at the midplane of the stripe positioned at the end of the computation box.

A ground boundary condition is assigned on the top of the domain,

$$\Psi = 0 \quad (5.13)$$

To maintain the overall electro neutrality of the substrate, it was ascertained that the substrate always contained the same number of positive and negative stripes.

It is apparent that Eqs. (5.12) and (5.13) do not represent the true boundary condition for the outer walls and the top surface of the computational domain. In the numerical solution, an appropriate measure must be taken to ensure that these artificial boundary conditions do not influence the accuracy of the solution by placing these boundaries sufficiently far away from the particles and the plate. This requirement dictated the choice for the linear dimensions of the computational box. The particle was usually positioned near the center of the box and traversed a small region along the y direction (*i.e.* from the center of a negative stripe to the center of a positive stripe). Thus, it was found that by making the box dimensions at least 10 times the particle radius ensured minimal effect of the box boundaries on the calculations.

5.2.3 Calculation of Interaction Force

Once the potential distribution is numerically obtained by solving the PB equation, the electrostatic force experienced by the spherical particle can be calculated by integrating the total stress tensor over the particle surface.

$$\mathbf{T}_{ij} = \left(\Pi - \frac{1}{2} \varepsilon \mathbf{E} \cdot \mathbf{E} \right) \mathbf{I} + \varepsilon \mathbf{E} \mathbf{E} \quad (5.14)$$

The stress tensor is comprised of an isotropic osmotic stress contribution and the Maxwell stresses arising from the electrostatic field. Combining these, the electrostatic force on the approaching particle is expressed as [1]:

$$\mathbf{F} = \iint_S \mathbf{T}_{ij} \cdot \hat{\mathbf{n}} dS = \iint_S \left[\left(\Pi - \frac{1}{2} \varepsilon \mathbf{E} \cdot \mathbf{E} \right) \mathbf{I} + \varepsilon \mathbf{E} \mathbf{E} \right] \cdot \hat{\mathbf{n}} dS \quad (5.15)$$

where the subscript S represents integration over the closed particle surface. Here \mathbf{F} is the force acting on the approaching particle, \mathbf{T}_{ij} is the electrostatic stress tensor, $\mathbf{E} (= -\nabla\psi)$ is the electrostatic field vector, $\Pi = 2n_{\infty}k_B T [\cosh(\Psi) - 1]$ is the osmotic pressure difference between the electrolyte at the particle surface and the bulk electrolyte, $\hat{\mathbf{n}}$ is the unit outward surface normal, and \mathbf{I} represents the identity tensor. The force acting on the approaching particle along the lateral (y) direction and the normal (z) direction can be determined from the total force \mathbf{F} and can be written explicitly as

$$\begin{aligned}
F_y &= \mathbf{F} \cdot \mathbf{j} \\
&= \varepsilon \left(\frac{k_B T}{zea} \right)^2 \iint_S \left[E_y E_x n_x + E_y E_z n_z + \{(\kappa a)^2\} (\cosh \Psi - 1) + \frac{1}{2} (-E_x^2 + E_y^2 - E_z^2) \right] dS
\end{aligned} \tag{5.16a}$$

$$\begin{aligned}
F_z &= \mathbf{F} \cdot \mathbf{k} \\
&= \varepsilon \left(\frac{k_B T}{zea} \right)^2 \iint_S \left[E_z E_x n_x + E_z E_y n_y + \{(\kappa a)^2\} (\cosh \Psi - 1) + \frac{1}{2} (-E_x^2 - E_y^2 + E_z^2) \right] dS
\end{aligned} \tag{5.16b}$$

where \mathbf{j} and \mathbf{k} are the unit vectors in the positive y and z directions respectively and n_x , n_y , and n_z are the components of the unit surface normal vector $\hat{\mathbf{n}}$ along the x , y , and z directions, respectively. E_x , E_y , and E_z are the components of the electric field vector \mathbf{E} along the x , y , and z directions, respectively. When calculating the force for the constant potential case, the integral of the isotropic osmotic pressure term over a closed surface of constant potential vanishes. This was utilized and the net force was evaluated by excluding the osmotic pressure term from Eq. (5.14). Finally, the force components are presented in their non-dimensional form as:

$$f_y = f_L = \frac{F_y}{\varepsilon} \left(\frac{zea}{k_B T} \right)^2 \tag{5.17a}$$

$$f_z = f_N = \frac{F_z}{\varepsilon} \left(\frac{zea}{k_B T} \right)^2 \tag{5.17b}$$

5.2.4 Trajectory Analysis

To assess the influence of the interaction forces on the equilibrium position of an approaching particle near a heterogeneous substrate, a simplified trajectory analysis was employed. The trajectories of 1 μm radius particles under the influence of spatially varied interaction forces due to a heterogeneous substrate were calculated. The particles are assumed to undergo non-accelerating motion during each time step in the quiescent fluid. The final equilibrium position of the particle is also recorded. The trajectory analysis is derived by applying Newton's second law of motion to a suspended particle in the fluid, given by:

$$m \frac{d\vec{v}}{dt} = \sum_i \vec{F}_i \quad (5.18)$$

where m is the particle mass and $\vec{v}(v_y, v_z)$ is the particle velocity vector. The right hand side of Eq. (5.18) represents the sum of all the forces \vec{F}_i , acting on the particle. In the present study, gravity force, fluid drag, van der Waals, and electrostatic double layer forces were considered as the pertinent forces. Trajectory analysis is often used for the case when Brownian motion can be considered negligible. The Brownian effects can be included in the trajectory analysis, the resulting mathematical analysis is complicated [1, 15, 250]. Hence, the present analysis is not applicable for sub-micrometer particles where Brownian motion contributes significantly to the particle trajectory.

A force balance performed on the forces acting on the particle (see Section 1.1.3 and Fig. 1.1 in Chapter 1) in the normal and lateral direction yields [71]:

In y direction,

$$6\pi\mu_f a K_y \frac{dy}{dt} = F_{L_EDL} \quad (5.19)$$

where the right hand side of the equation represents the lateral EDL force acting on the particle and is obtained from the simulations results. The left hand side of the equation represents the hydrodynamics interaction (fluid drag) and dy/dt represents the rate of lateral displacement of the particle, μ_f is the fluid viscosity and K_y is the modified the drag factor [251]:

$$K_y = -\left(\frac{8}{15}\right) \log z_i + 0.9588 \quad (5.20)$$

where z_i is the initial (or current) separation distance of the particle surface from the substrate).

In z direction,

$$\begin{aligned} 6\pi\mu_f a K_z \frac{dz}{dt} &= F_{N_EDL} + F_{vdw} + F_g \\ &= F_N + \left(-\frac{A_H}{6az_i^2}\right) + \frac{4}{3}\pi a^3(\rho_p - \rho_f)g \end{aligned} \quad (5.21)$$

where the different terms in right hand side of Eq. (5.21) represent normal component electrostatic double layer force, van der Waals and gravity, respectively.

The left hand side of the equation represents the normal hydrodynamic drag component acting on the particle and K_z is the modified drag factor [252]:

$$K_z = \frac{1-0.2z_i \log z_i + 0.9712z_i}{z_i} \quad (5.22)$$

Equations (5.19) and (5.21) are the governing trajectory equations for the particle motion. The values of the relevant constants and parameters used in the above calculations are summarized in Table 5.1.

5.3 Numerical Solution Procedure

5.3.1 Finite Element Method

A finite element (FE) technique was employed to evaluate the electric double layer (EDL) interaction forces experienced by the charged spherical particle in presence of the charge heterogeneous flat plate as the particle approaches the planar surface immersed in an electrolyte domain in this three dimensional non linear Poisson Boltzmann (3D-NLPB) model. The model involved solving the three dimensional non linear Poisson-Boltzmann (NLPB) equation in the Cartesian coordinate system to obtain the potential distribution in the electrolyte domain with the appropriate boundary conditions imposed on the negatively charged particle positioned at the center of the domain above the planar striped surface. Essentially, the particle size (diameter $d = 2a$) was held constant, and the stripe width (therefore the size ratio, $\gamma = w/d$) was varied to investigate the effect of the heterogeneity on the forces. The primary objective of using such a 3D model was to render the substrate chemically heterogeneous in the lateral (y) direction in order to compute the normal forces, F_N (in the z direction) as well as the lateral forces, F_L (in the y direction) arising due to the presence of the heterogeneity. The two components were calculated for each position of the particle as it is scanned from the center of a negative stripe to the center of a positive stripe of the striped surface at each scaled separation height, h/a . The forces were determined for a wide range of κa values which is tantamount to changing the solute concentration, since particle radius was held constant. All these conditions have

been enforced in the constant potential scenario. The operating and physico-chemical properties of the modeled system used in this work are listed in Table 5.1.

The size of the domain is considered to be considerably large with respect to the particle radius to justify the boundary conditions imposed on the outer boundaries of the domain. As mentioned in the previous section, the boundary conditions on the sidewalls are artificial symmetry conditions which may be valid only when these boundaries are placed far enough away from the sphere. To determine the minimum distance between the sphere and surrounding boundaries (namely the sidewalls $AEFB$, $BFGC$, $DHGC$ and $AEHD$ and the top $EFGH$) such that negligible errors arise while computing the forces, simulations were performed by setting different values of the linear dimensions of the computational box. Based on this analysis, the box length (along x axis), width (along y axis), and height (along z axis) was set at least ten times larger than the particle radius a . This proved sufficient to ensure that the artificial symmetry conditions imposed on the sidewalls and the ground boundary condition on the top have negligible effect on the computational results.

The Newton nonlinear method along with a conjugate gradient (CG) iterative solver was used to solve the NLPB equation. The post processing of the data involved the calculation of the interaction forces on the boundary of the spherical particle. The values of the x component of the interaction force was computed and found to be negligible (as expected) since no variations exist in that direction.

5.3.2 Mesh Generation

The computational domain was discretized using tetrahedral, Lagrangian quadratic mesh elements. Mesh size and its distribution were controlled by tuning two important mesh parameters: the ‘maximum element size’ (in the domain and boundaries) and the ‘element growth rate’ (in the domain). The maximum element size, as the name implies, signifies the maximum allowable element size in the domain or the boundary that it is specified for. In a finite element analysis, a small mesh size is necessary for the regions of high potential gradients, *i.e.* regions

where large variation of potential with respect to small distances occurs. This is particularly important because of the non-linear nature of the PB equation where the potential, ψ varies sharply near the charged surfaces. Thus to capture these variations with adequate precision, a low maximum element size value was specified on the particle surface and at the boundaries of two differently charged stripes. A fine mesh size on the particle surface ensured better representation of the curvature and an accurate integration of the stress tensors to obtain the force value. The element growth rate determines the maximum rate at which the elements grow in size from a region containing the smallest elements to a region containing the largest elements. A low element growth rate at the particle surface ensured a very fine mesh in the particle neighbourhood. The mesh size was then gradually increased from the particle surface to the outer (fluid) domain. The regions further away from the particle being of less importance, were subjected to coarser elements in order to reduce the number of elements and thus minimize computational time and effort.

The mesh parameters were varied and the results compared to obtain an optimum value for the parameters for the refinement of the mesh in the computational domain. A mesh sensitivity analysis was performed to obtain an optimum number for the mesh density that would provide the required level of accuracy of the simulation results. For rest of the analysis, it was ensured that the number of elements employed was higher than the optimum number to maintain the consistency of the accuracy of the solution. For the domain size selected, it was found that the number of elements varied between 75,000 and 90,000. By adjusting the maximum element size on the particle surface and defining the appropriate element growth rate, a non-uniform mesh structure is generated with high mesh density around the spherical particle and at the boundary stripes of the alternating potential. The non-uniform mesh configuration employed in the computational domain is shown in Figure 5.3. As can be seen in Fig. 5.3b, the surface of the particle has the highest mesh density compared to the other regions in the computational domain. The element size on the particle surface was chosen to be at least 10 times smaller than the largest element in the domain. A gradual zoom into the

area of interest (near the particle surface), shows how the mesh was refined in that region (Fig. 5.3c).

5.3.3 Validation of Numerical Model

In this subsection, the accuracy of the 3D-NLPB model calculations is investigated by comparing results for the limiting case of the electrostatic force experienced by a charged spherical colloidal particle approaching a uniformly charged planar surface with corresponding results available in the literature. The scaled interaction forces obtained from the 3D-NLPB model were compared with the scaled forces obtained from the well-known Hogg, Healy, and Fuerstenau (HHF) analytical expression [25] for the electrostatic double layer interaction force. Assuming constant surface potential on the particle and the planar substrate and a symmetric ($z:z$) electrolyte solution, the HHF equation for interaction force can be derived from Eq. (1.2) and has the form:

$$f_{HHF} = \pi(\kappa a) \left[\frac{4\Psi_p \Psi_s \exp(-\kappa h)}{1 - \exp(-2\kappa h)} - \frac{(\Psi_p + \Psi_s)^2 \exp(-2\kappa h)}{1 - \exp(-2\kappa h)} \right] \quad (5.23)$$

where $f_{HHF} = \left(\frac{F_{HHF}}{\varepsilon} \left(\frac{ze}{k_B T} \right)^2 \right)$ represents the scaled force, Ψ is the scaled surface potential, and κh is the scaled surface-to-surface separation distance between the particle and the planar surface. The above equation is based on the linearized PB equation, so calculations based on this expression will always overestimate the forces at small separation distances. However the expression can be assumed to estimate accurately the electrostatic double layer interaction between a particle and a homogeneous collector at larger separation distances and low surface potentials. The 3D-NLPB model was also compared with results from a numerical model created by Carnie *et al.* [245] based on the nonlinear Poisson-Boltzmann theory to calculate the interaction between a sphere and a homogenous plate in an infinite medium. The direction of the force calculated by both the above mentioned methods is normal to the substrate surface which by considering the geometry of the present problem implies that the EDL force is comprised of just one component F_z in the vertical z direction. Two values of the scaled particle size

$\kappa a = 1.0$ and 5.0 were investigated, with an equal dimensionless surface potential $\Psi_p = \Psi_s = 1.0$ on the particle and the plate over a range of scaled surface to surface separation distance of $0.1 < \kappa h < 3.0$. Figure 5.4 depicts the comparison of the interaction forces obtained through the three methods under CP conditions. The interaction forces obtained from the 3D-NLPB finite element model agree well with the results obtained from the analytical expression as well as the Carnie model over the entire range of scaled separation distances chosen. The disagreement of the two numerical solutions with the analytically obtained force value at small separation distances is mainly attributable to the overestimation of the force by the HHF expression. For separation distances larger than 1.0 , all three results agree well with each other. It is evident from Fig. 5.4 that the 3D-NLPB model provided identical results to those obtained by the Carnie model. The numerical results from these two techniques were in conformity within 0.5% for $\kappa a = 1$ and within 3% for $\kappa a = 5$ over the studied separation distance $0.1 < \kappa h < 3.0$.

5.3.4 Trajectory Analysis Procedure

The methodology involved in simulating particle trajectories by incorporating the interaction forces is described in this subsection. Figure 5.5 is a flow chart outlining the scheme for the trajectory analysis. With this sequence of steps, the trajectory of a single particle is computed as it translates over a heterogeneously charged surface having a pair of oppositely charged stripes in the presence of no fluid flow. The particle starts off at an initial separation distance z of 200 nm. The initial y (or lateral) position of the particle was chosen randomly (using a random number generator) and also in an ordered manner (consecutively) spaced at regular intervals along the width of the stripe pair. The forces acting on the particle at this position are calculated using the expressions developed earlier in Sections 5.2.3 and 5.2.4. Once the force is computed, the next step is to calculate the velocities as described in Section 5.2.4. The new position of the particle is then obtained from the velocity vector. At this stage, the termination criteria needs to be satisfied for the simulation to end otherwise the previous steps are repeated using the new position of the particle. The simulation is terminated once the

particle reaches a separation height of 10 nm from the surface. The particle is assumed to have stopped moving at this point and considered to be deposited on the substrate and the final y equilibrium position of the particle is noted. No steric interactions have been considered in this analysis. Based on this strategy, a large number of individual particle trajectory simulations are performed and the total number of particles deposited was then tallied. A simulated particle deposition distribution on the substrate determined based on the positions of the particle on a pair of stripes on the heterogeneous substrate (similar to the particle distribution analysis performed in Chapters 3 and 4) was obtained to illustrate the influence of heterogeneity on particle deposition.

5.4 Particle Interaction with Patterned Substrates

5.4.1 Potential Distribution

Potential maps provide a qualitative indication of the interaction forces acting on the particle and the possible effect these forces have for different stripe sizes relative to the particle diameter. Some representative potential distributions near the particle and the heterogeneous surface in the confined electrolyte corresponding to particle surface potential of $\psi_p = -1$ and substrate potentials of $\psi_{sp} = +1$, $\psi_{sn} = -1$ are depicted in Figure 5.6. The coloured maps are slice plots of the potential distribution in the y - z plane placed through the center the particle and in the midplane of the domain. These maps were obtained for different size ratios γ with the particle center positioned at the boundary between the negative and positive stripes and held above the substrate at a scaled separation height of $h/a = 0.03$ for $\kappa a = 1$. For example, if the particle size is held constant, one ends up with different sized heterogeneities for the different γ values while noting that the width of the positive and negative stripes was held equal (*i.e.* the favourable area fraction is always $\lambda = 0.5$) throughout the simulation. On the map, the blue colour represents a negative potential and red represents the positive potential. Noting that the electrostatic field is obtained from the gradient of the potential ($\mathbf{E} = -\nabla\psi$), it can be recognized that any sharp change in colour in the map denotes a potential

gradient signifying a high electric field, which, in turn, implies larger Maxwell stresses (*i.e.* electrostatic forces) to be acting on the particle.

In Figure 5.6a, for the case when $\gamma = 2.0$ (*i.e.* each stripe is twice as large as the particle diameter), the potential distribution in the region adjacent to negative stripe and the negative particle shows the negative potential (in blue) to encompass the two interacting surfaces, signifying slight repulsion between them. In the region of the particle adjacent to the positively charged stripe, the potential is seen to vary sharply at the vicinity of the two oppositely charged surfaces, the region of variation being wedged in between the underside of the negatively charged particle (in blue) and the positively charged substrate surface (in red). This implies that the particle will feel a strong (lateral) attraction towards positive stripe causing it move away from the boundary. A similar effect is observed in the case of $\gamma = 1.0$.

For $\gamma = 0.5$, each stripe is now half the particle diameter, and a distinctly different picture emerges from the previously mentioned two cases. Notably, the particle in this case begins to sense the presence of the neighbouring stripes (two stripes away). There is still a sharp region of variation (as in $\gamma = 2.0$ and $\gamma = 1.0$) near the vicinity of the particle and positive stripe, but the particle now experiences the additional influence of the negative stripe present adjoining the positive one, as is evident by the blue coloured region ensuing from the stripe and linking to that of the particle. Similarly, on the other side of the particle, the neighbouring positive stripe (lying next to the negative stripe adjacent to the particle), also influences the potential distribution near that part of a particle, creating another area of potential variation. This variation is however, is more modest compared to that on the other side, indicating that the force resulting from this potential gradient will not be as strong.

A similar effect is observed when the stripe size is further reduced ($\gamma = 0.25$) such that each stripe is now one quarter of the particle diameter. The difference is this case with the other cases is that the neighbouring stripes now have a stronger influence on the particle as the particle essentially feels two attractive forces acting on both sides of the particle. The magnitudes of the two forces differ (as

also seen in the $\gamma = 0.5$ case), with the force acting towards the positive stripe lying adjacent to the particle being more attractive. This suggests that the boundary has less of an effect on the particle when a particle is much larger than the stripe. Thus a particle positioned at the boundary would experience attractive forces from stripes located on either side of the particle (as it would when placed anywhere on the substrate), pinning the particle in its current position.

5.4.2 Interaction Forces

Based on the above qualitative observations, it can be seen that lateral forces can arise along with normal forces in the presence of heterogeneity. In this subsection, the electrostatic interaction forces acting on the charged particle placed near a heterogeneous surface in an aqueous medium is explored. The net resultant force acting on the particle is resolved into a normal component (in the vertical z direction) and a lateral (*i.e.* parallel to the plane of the surface, in the y direction) component, and their magnitudes are compared. It is worth mentioning here that the component in the x -direction is negligible as there is no heterogeneity in that direction.

Figure 5.7 shows the variations of the normal and lateral components of the net force acting on the particle for different values of γ (different stripe widths) when the particle is held at a scaled separation height of $h/a = 0.03$ at $\kappa a = 1$, similar to the cases seen in Fig. 5.6. The scaled component forces f_N and f_L were calculated (according to Eq. 5.17) for a scaled particle potential of the particle $\Psi_p = -1$ and the negative and positive stripes potentials of $\Psi_{sn} = -1$ and $\Psi_{sp} = 1$, respectively. The x axis on the graphs represents the relative y position of the particle when it is scanned from the center of the negative stripe (as represented by the negative values on the x axis of the graphs) to the center of the positive stripe and is scaled with respect to half the stripe width $w/2$. The boundary is located at the zero on the x axis, as denoted by the dotted line on the graphs. The graphs are accompanied by schematics showing the direction (sign) of the force.

In Fig. 5.7a, representative plots of the normal force as it varies along the stripe with different heterogeneity sizes are shown. When the heterogeneity is compara-

ble in size to the particle, as is in the case of $\gamma = 2.0$ (heterogeneity is twice as large as particle) and $\gamma = 1.0$ (heterogeneity is the same size as the particle), one observes from the graph that with the particle positioned at the center of the negative stripe, the normal force is slightly repulsive (positive value) and gradually transitioning to attraction (negative value) as the particle moves over to the positive stripe. The magnitude of the normal force reaches its maximum value when the particle is above the center of the positive stripe for both cases. As the stripe width decreases and becomes smaller than the particle size ($\gamma < 1.0$), the normal forces are seen to remain predominately attractive over the substrate surface, even over the unfavourable (negatively charged) stripe. This indicates the dominant influence of the favourable (positively charged) stripes. At these γ ratios, the particle surface interacts with greater areas of the neighbouring stripes (*cf.* Figs. 5.6c and 5.6d) implying that the heterogeneous substrate, despite possessing unfavourable patches on its surface, acts more like a favourable one.

In Fig. 5.7b, the graph shows plots of the lateral force on the particle positioned very close to the substrate surface, and how it varies along the width of the pair of unfavourable and favourable stripe for the different γ values. When the particle diameter is comparable to the stripe width ($\gamma = 2.0$ and $\gamma = 1.0$), the lateral forces become significant near the boundary. In both cases, the lateral force is non-existent when the particle is positioned above the center of the negatively charged or positively charged stripe. As the particle is scanned over the unfavourable stripe, it begins to experience an attractive (negative) lateral force which implies the force is towards the positively charged stripe (as shown in the schematic in Fig. 5.7b). The magnitude of this lateral force gradually increases as the particle approaches the edge of the unfavourable stripe, reaching a maximum at the boundary of the two oppositely charged stripes. This so happens because one side of the sphere is repelled while the other side is attracted. Another observation worth mentioning is the particle's relative unawareness of the presence of the neighbouring negative and positive stripe on either side at this position. This is observed in Figs. 5.6a and 5.6b as the confinement of the blue colour around the

particle surface and in between the adjacent negative stripe, implying the interaction will be confined primarily within the stripes lying adjacent to the particle.

As the particle moves away from the boundary and approaches the positive stripe, for both the cases, the lateral force decreases in value. As the stripe width decreases relative to the particle size ($\gamma = 0.5, 0.25$), the variation of the lateral force over the width of the heterogeneous substrate is similar to what was observed for $\gamma = 2.0$ and 1.0 but the overall magnitude of the lateral force is decreased compared to the above two cases ($\gamma = 2.0, 1.0$). It is pertinent to mention here that in the case of a uniformly charged surface, the net lateral force acting on a particle would be zero as they are equally present in all directions and hence the resultant lateral force is zero.

In Figure 5.7c, the force ratio f_L/f_N is obtained by combining the results of Figs. 5.7a and 5.7b using the absolute values (or magnitudes) of the forces and ignoring the sign and plotted over the width of the striped pair. Through these plots, it is possible to get an idea of the influence of the lateral force (relative to the normal force) at specific positions over the substrate surface. Some of the observations made from this figure are listed below:

- At the separation distance $h/a = 0.03$ investigated, for $\gamma = 2.0$ and $\gamma = 1.0$, in both cases the force ratio remains above 1.0 (100%) along the negative stripe for y scaled positions close to the edge of the stripe. This implies that the lateral force acting on a particle becomes comparable to the normal force when the particle is comparable in size to the heterogeneity, at certain positions over the substrate.
- For $\gamma = 0.5$ and 0.25 , the force ratio is below 1.0 for positions near the edge of the negative stripe and drops off quickly for all other positions. From this one can surmise that if the stripes are small enough compared to the particle, the normal forces dominate and the particle will not sense the heterogeneous nature of the substrate as the effect of the lateral forces will be smeared out.
- An upward spike in the force ratio is observed for $\gamma = 2.0$ and $\gamma = 1.0$, (as shown in Fig. 5.7c) at positions $y/a = -0.3$ and $y/a = -0.6$ respectively.

The spike in the plot occurs when the magnitude of the lateral force becomes considerably larger than the normal force. This suggests for these size ratios, there is a significant lateral force acting on the particle positioned near the edge of the unfavourable stripe that could push it laterally from the negatively charged stripe to the more attractive heterogeneous stripe.

- The spike in the force ratio curve for $\gamma = 2.0$ occurs when the particle is positioned closer to the edge of the negative stripe than for the case when $\gamma = 1.0$. This seems to suggest that the effect of substrate heterogeneity is perceived by the particle earlier if the particle is the same size as the heterogeneity.

In Figure 5.8, a closer look is cast upon the variation of the two force components acting on the particle near the substrate where $\gamma = 1.0$ (*i.e.* when the heterogeneous stripe width is equal to the particle diameter) as it is scanned above the charge heterogeneous surface from different separation heights. The scaled component forces f_N and f_L were calculated for $\kappa a = 5$, and plotted against the y scaled position (y/a). Fig. 5.8a represents the variation of normal force. At a scaled separation height of $h/a = 0.2$ (farthest away from the substrate surface), which translates to a separation distance 200 nm for a 1 μm radius particle, the normal force shows little or no change as the particle is scanned from the negatively charged (repulsive) to the positively charged (attractive) stripe. However, as the separation between the negatively charged particle and the substrate is reduced, the particle begins to ‘feel’ the heterogeneous nature of the substrate. For example, at a scaled height of $h/a = 0.03$, *i.e.* when the 1 μm particle is held 30 nm away from the surface, the normal force stays repulsive (implying the particle finds this region of the substrate unfavourable for deposition) as the particle tends to be repelled as it moves along the negative towards the positive stripe until it approaches the boundary between the two stripes. The normal force transitions from repulsion (positive value) to attraction (negative value) even before the particle center reaches the boundary with its magnitude increasing rapidly as the

particle crosses over the edge and moves into the positive stripe, and attaining a maximum value at the center of the favourable (positive) stripe.

The lateral force like its vertical counterpart, also increases with decrease in separation distance (forces are higher at $h/a = 0.03$ than at $h/a = 0.1$), but varies somewhat differently along the width of the heterogeneous substrate. When the particle is positioned at the center of the negative or positive stripe, the particle experiences no lateral forces at all separation distances investigated. When the negatively charged particle begins its scan over the negative stripe, it begins to experience a negative lateral force which implies the force is directed towards the positively charged stripe (as shown in the schematic in Fig. 5.7b). As the particle approaches the edge of the negative stripe, the magnitude of the force increases steadily, attaining a maximum value at the boundary between the two oppositely charged stripes. The magnitude of the force begins to decrease as the particle moves away from the boundary and into the positive stripe, becoming null at the center. This trend was observed for all the separation distances investigated.

The overall magnitude of the lateral force is seen to increase with decreasing separation distances. The force ratio plot shown in Fig. 5.8c shows some interesting features. All the spikes lie within the vicinity of the edge of the negatively charged stripe ($0 > h/a > -0.3$). For higher separation distances (e.g. for $h/a = 0.2, 0.1$), the spike values are higher (implying predominance of the lateral forces at those positions) than the peaks at lower separation distances ($h/a \leq 0.05$), but the peaks are situated closer to the edge compared to the peaks at the lower separation distance. This implies that a particle situated further away from the substrate surface has to be positioned closer to the boundary of the heterogeneity to feel its effects.

Figure 5.9 is a vector plot of the net force acting on the particle under the same conditions as mentioned in Fig. 5.8. The graph illustrates the effect of the charge heterogeneity of the substrate for a particle placed at different separation heights as represented by the resultant EDL force acting on the particle. The plot was obtained using the two components f_N (in the z direction) and f_L (in the y direction) of the net force, noting that the force in the x direction is negligible. The direction

of the arrowhead points to the direction in which the net force is acting on the particle center, while the length of the arrow indicates the relative magnitudes of the forces at the various positions. Please note that the magnitude of the vectors enclosed in the dotted box in Fig. 5.9 have been reduced by four times their magnitude, for ease of representation.

Considering the electrostatic forces to be dominant within the separation height considered, the plot shows that over the positive stripe the particle always experiences a net attractive force directed vertically towards the attractive stripe. Thus a particle approaching the attractive stripe from any position above the stripe will tend to deposit onto a region as dictated by the downward arrows.

On the other hand, when the particle is positioned near center of the unfavourable stripe, it has no affinity to deposit on the negative region, as it feels a net repulsive force pushing it away from the unfavourable surface. If the particle is positioned close to the edge of the negative stripe, the lateral component of the net force on the particle tends to push it towards the boundary (as also seen from the force ratio curve of Fig. 5.8c). However, the position where the particle will deposit is not so obvious from the vector plot. For example, consider the particle to be positioned over the edge at a scaled distance $h/a = 0.10$ away from the substrate. At this separation distance, the particle feels a net force pulling it towards the favourable stripe. If this force is large enough to overcome frictional drag imposed by the surrounding medium, the particle will follow a trajectory towards the positive stripe and the final position will be dictated by the net force balance on the particle. However, these calculations clearly indicate that the lateral forces become comparable to or greater than the normal forces near the boundary for all separation distances considered.

Figure 5.10 investigates the variation of the normal and lateral forces for $\gamma = 1$ for three different values of κa . As mentioned previously, changing the value of κa is tantamount to changing the ionic strength of the aqueous solution in which the particle is immersed. For a fixed particle radius, as κa values are increased, the ionic strength of the solution is increased. For example, for a particle radius of $1 \mu\text{m}$, $\kappa a = 5$ implies the molarity of a (1:1) electrolyte solution to be about 0.002

mM (1 mM = 10^{-3} M) while for $\kappa a = 10$ it is about 0.01 mM. Thus these plots reveal the effects of electrolyte concentration on the interaction forces as the particle approaches a heterogeneous substrate. For both the normal and lateral forces, the force profiles show similar trends as seen thus far (*cf.* Figs. 5.7 and 5.8). For both forces, the overall magnitude of each component force increases with a decrease in κa (that is with a decrease in ionic concentration) along all the positions over the stripe and at all separation distances. Particularly at higher κa values, the magnitude of the lateral forces becomes smaller with increasing separation distances.

5.4.3 Trajectory Analysis-Particle Distribution

The results of the trajectory analysis on a stripe pair of $\lambda = 0.5$ (50% favourable) and $\gamma = 2$ (particle diameter is twice the size of the stripe width) are depicted in Figure 5.11. The κa value used was 15 to emulate the conditions of the experiment performed earlier in Chapter 3. Table 5.2 compares the experimental parameters with the simulation parameters. The plot shows the particle distribution histograms for particles whose initial positions were chosen randomly and also in an ordered manner (consecutively) along the width of the stripe pair. The plots represent the probability of particles depositing along the width of the pair stripe based on a simple consideration of the interactions between the particle and heterogeneous substrate. The distributions were obtained on a 1D heterogeneous substrate based on the y positions of the particles along the width. The x positions along the length of the substrate were not under consideration. In essence these distributions can be compared to those particle distributions obtained in Chapters 3 and 4 from the experimental and simulation data since the distributions represented there also reflect the deposition probability of the particles along the width of the stripes.

The first prominent feature in both plots is that more particles deposit nearer to the edge of the positive stripe while no particles are seen to deposit on the negative stripe. This is similar to what has been observed experimentally (in Chapter

3) and through deposition simulations based on simple binary probability (in Chapter 4). The other feature that stands out is the presence of a denuded zone lying next to the edge of the positively charged stripe. No particles (centers) are seen to deposit in this zone and this is attributed to the high lateral forces acting at the edge of the stripe (as seen from the discussion of the vector plot in Fig. 5.9). Similar experimental observation has been made previously by Ma *et al.* [253] while performing experiments with nanometre sized particles and sub micron sized patterns and the phenomenon was attributed to the magnitude of the electrostatic interaction energy gradient (in a direction parallel to the substrate) in guiding nanoparticles to the surface.

5.5 Conclusions

A three dimensional non linear Poisson Boltzmann (3D-NLPB) model has been implemented to study the effects of chemically induced heterogeneity on a single charged particle when placed close to a substrate containing charge heterogeneous stripes of comparable dimensions. A finite element (FE) technique was employed to evaluate the electric double layer (EDL) interaction forces experienced by the charged spherical particle in presence of the charge heterogeneous flat plate as the particle approaches the planar surface immersed in an electrolyte domain. The model involved solving the 3D NLPB equation in the Cartesian coordinate system to obtain the potential distribution in the electrolyte domain and the forces acting of the charged particle were calculated when positioned at different separation heights above the planar striped surface and for different lateral positions along the width of the substrate. The following is a summary of the salient points inferred from the numerical results:

- Lateral forces arise (along with normal forces) in presence of a potential gradient due to the presence of chemical heterogeneity. In the case of a uniformly charged substrate surface, the net lateral force acting on a particle would be zero as they are equally present in all directions and hence the resultant lateral force is zero. However, near a heterogeneous surface, one side

of the spherical particle is repelled while the other side is attracted. Thus, these forces together result in a net lateral force.

- Lateral forces are significant at close separation distances when the heterogeneity is comparable in size to the particle ($\gamma = 1, 2$). Furthermore as the particle approaches a heterogeneous substrate, particularly near the edge of the unfavourable stripe, there is significant lateral force acting on the particle, pulling it laterally over the surface toward the more attractive heterogeneous stripe. At the boundary, the magnitude of the lateral force reduces with increasing separation distance.
- Normal forces have the highest magnitude at the center of the stripe (minimum energy), while the magnitude of the lateral force is highest at the boundary between the positive and negative stripe, where the substrate's surface potential changes most dramatically. This observation provides evidence of the importance of the magnitude of the electrostatic potential gradient (in a direction parallel to the substrate) in guiding particles to the surface (in absence of a flow field). One can surmise that when the gradient is steep, the lateral force experienced by the negatively charged particles will be stronger and the particles will be guided further away from the edge and channelled towards the central region of the positively charged stripe.
- When the surface is 50% favourable ($\lambda = 0.5$), for $\gamma \leq 1$ (*i.e.* the particle is larger than the heterogeneity), the heterogeneous substrate despite possessing unfavourable patches on its surface, acts more like a favourable one. From this one can surmise that if the stripes are small enough compared to the particle, the normal forces dominate and the particle will not sense the heterogeneous nature of the substrate as the effect of the lateral forces will be smeared out.
- For $\gamma = 1$ and 2, when the particle-substrate separation is greater, the particle has to be situated closer to the boundary of the two oppositely charged heterogeneities in order to feel the maximum effect of the heterogeneity. However, at closer separation distance, the particle senses the heterogeneity when placed further away from the edge for $\gamma = 1$ than compared for $\gamma = 2$.

- Trajectory analysis performed to obtain particle distribution probability over the width of a pair of heterogeneous stripes reveals that more particles have a tendency to deposit near to the edge of the favourable stripe while no particles are seen to deposit on the negative stripe. This is similar to what has been observed experimentally (in Chapter 3) and through deposition simulations based on simple binary probability (in Chapter 4). The other feature that stands out is the presence of a denuded zone near the lying next to the edge of the positively charged stripe. No particles (centers) are seen to deposit in this zone and this is attributed to the lateral forces acting at the edge of the stripe.

Table 5.1 Physical and chemical properties of the system used in the simulations

Property	Value
Particle radius, a	1 μm
κa	1, 5, 10
Size ratio, γ ($= w/2a$)	0.25, 0.5, 1.0, 2.0
Scaled particle potential, ψ_p	+1
Scaled substrate surface potential, ψ_s	-1, +1
Stripe width, ($w = b$)	0.5 - 4 μm
Pitch, p ($= w + b$)	1 - 8 μm
Favourable area fraction, λ ($= w/p$)	0.5
Separation height, h	200 - 20 nm
Particle density, ρ_p	1055 kg/m^3
Fluid density, ρ_f	1000 kg/m^3
Fluid viscosity, μ_f	$1.0 \times 10^{-3} \text{ N.s/m}^2$
Temperature, T	298 K
Boltzmann constant, k_B	$1.38 \times 10^{-23} \text{ J/K}$
Gravitational acceleration, g	9.81 m/s^2
Electronic charge, e	$1.6 \times 10^{-19} \text{ C}$
Dielectric constant, ϵ_r	78.54
Permittivity of vacuum, ϵ_0	$8.85 \times 10^{-12} \text{ C/Vm}$
Valence of ions, z	1
Hamaker constant, A_H	$4 \times 10^{-21} \text{ /J}$

Table 5.2 Comparison of the parameters of the system used in the experiment and trajectory analysis

Property	Experimental	Trajectory Analysis
Particle diameter, d	1 μm	2 μm
Stripe width, ($w = b$)	2 μm	4 μm
Pitch, p ($= w + b$)	4 μm	8 μm
Favourable area fraction, λ ($= w/p$)	0.5	0.5
Size ratio, γ ($= w/d$)	2	2
Solution concentration	0.1 mM	-----
κa	16.45	15

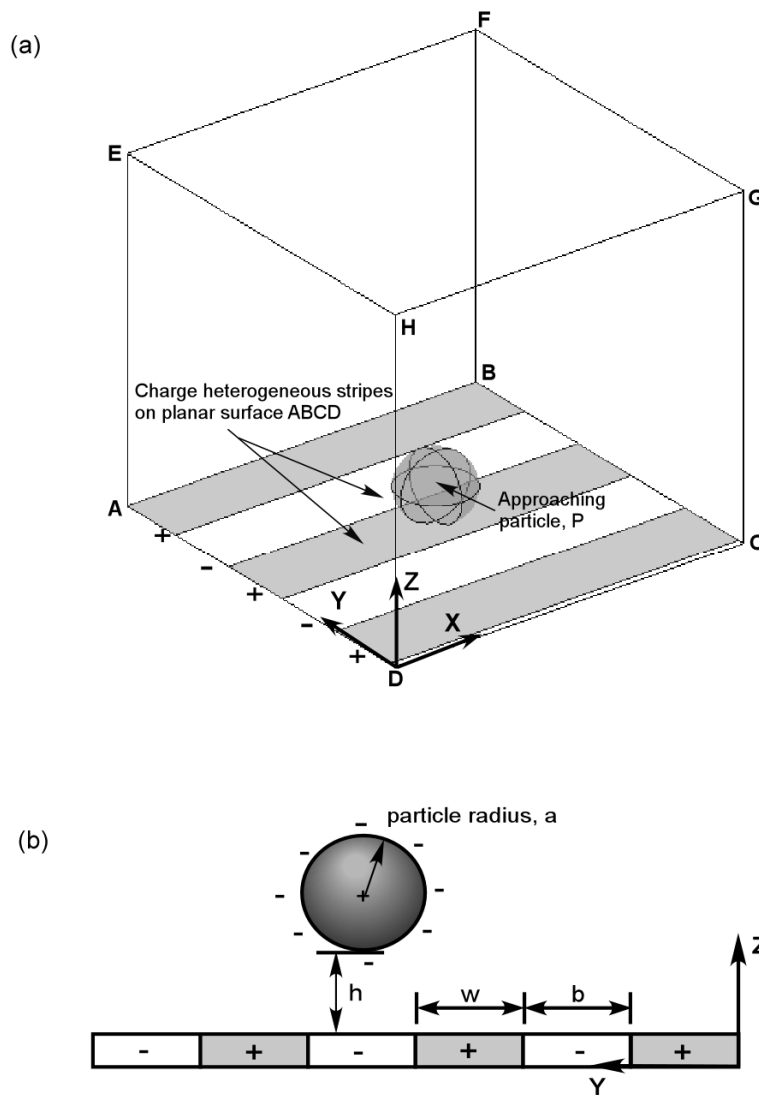


Figure 5.1: (a) Pictorial and (b) schematic representation of the numerical model showing the substrate as a planar surface consists of rectangular stripes of alternating negative (white) and positive (gray) surface potentials with width of b and w , respectively. The particle of radius a , is negatively charged and approaches the substrate from a vertical distance h . In these simulations, the width of the stripes are held equal, *i.e.* $b = w$.

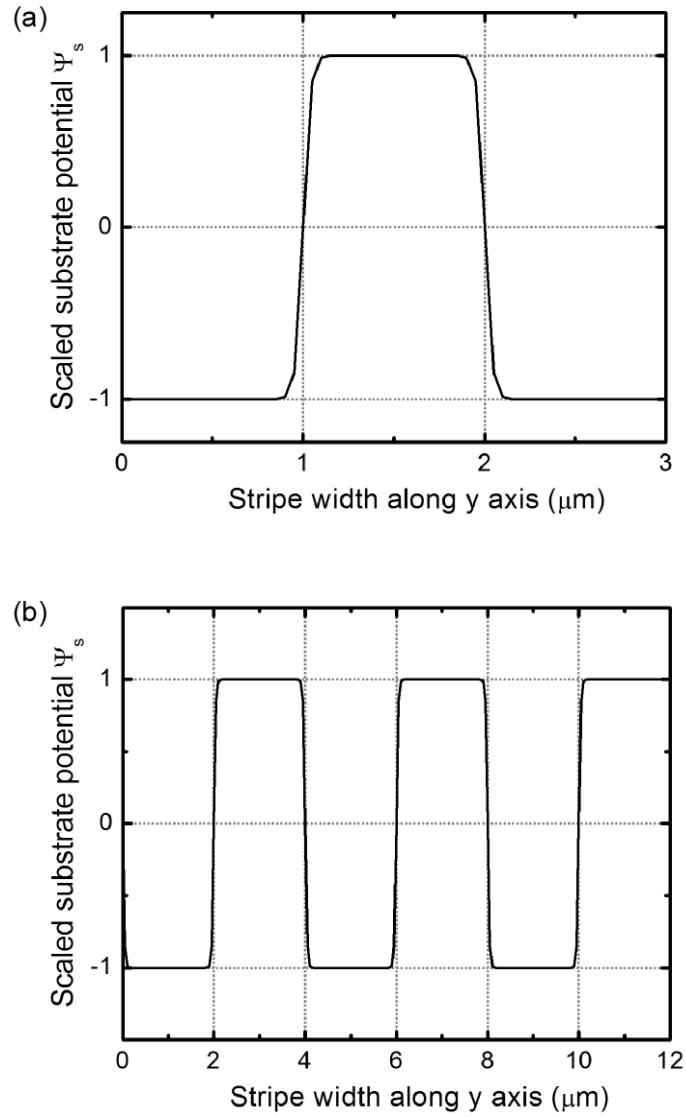


Figure 5.2: Illustration of the smoothing sigmoidal function to represent the variation (with y) of a scaled striped surface potential $\psi_s = (+1,-1)$ along the width of a heterogeneous substrate (a) by employing Eq. (5.11) with the following parameter values: $\Psi_{\text{sn}} = -1$, $\Psi_{\text{sp}} = 1$, $a = 80$, $y_1 = 1$ and $y_2 = 2$, and (b) extended over a substrate with three pairs of oppositely charged stripes of width 2 μm each.

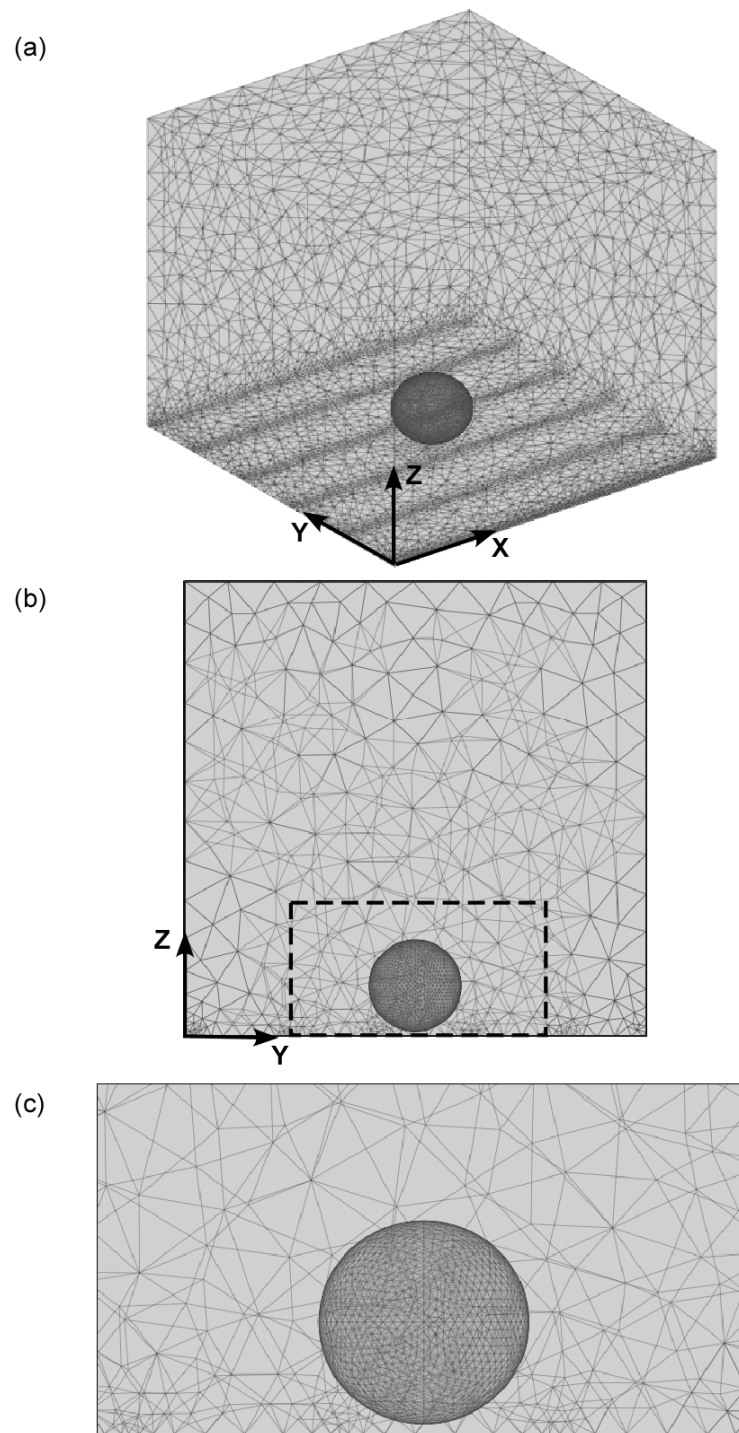


Figure 5.3 Schematics showing mesh generation (a) in the entire computational domain (b) on the y - z plane of the box and (c) on the particle surface.

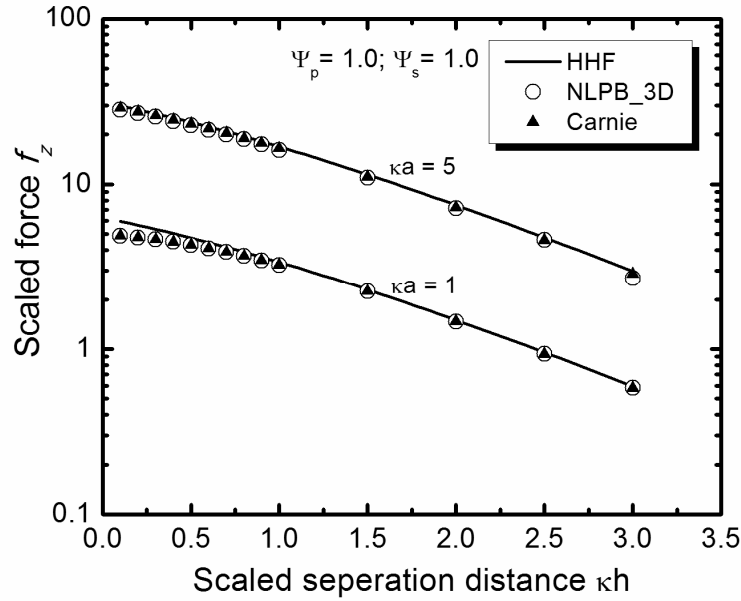


Figure 5.4: Comparison of the electrostatic double layer interaction forces between a charged spherical particle and a planar substrate obtained from the finite element 3D-NLPB model (open symbol, \circ) with the corresponding estimates from Carnie model [245] (solid symbol, \blacktriangle) and the analytical HHF equation [25] (solid line). The variations of the scaled electrostatic force f_z with scaled (surface to surface) separation distances κh are depicted for a scaled surface potential of $\Psi_p = \Psi_s = 1.0$ at constant potential (CP) condition for $\kappa a = 1$ and $\kappa a = 5$.

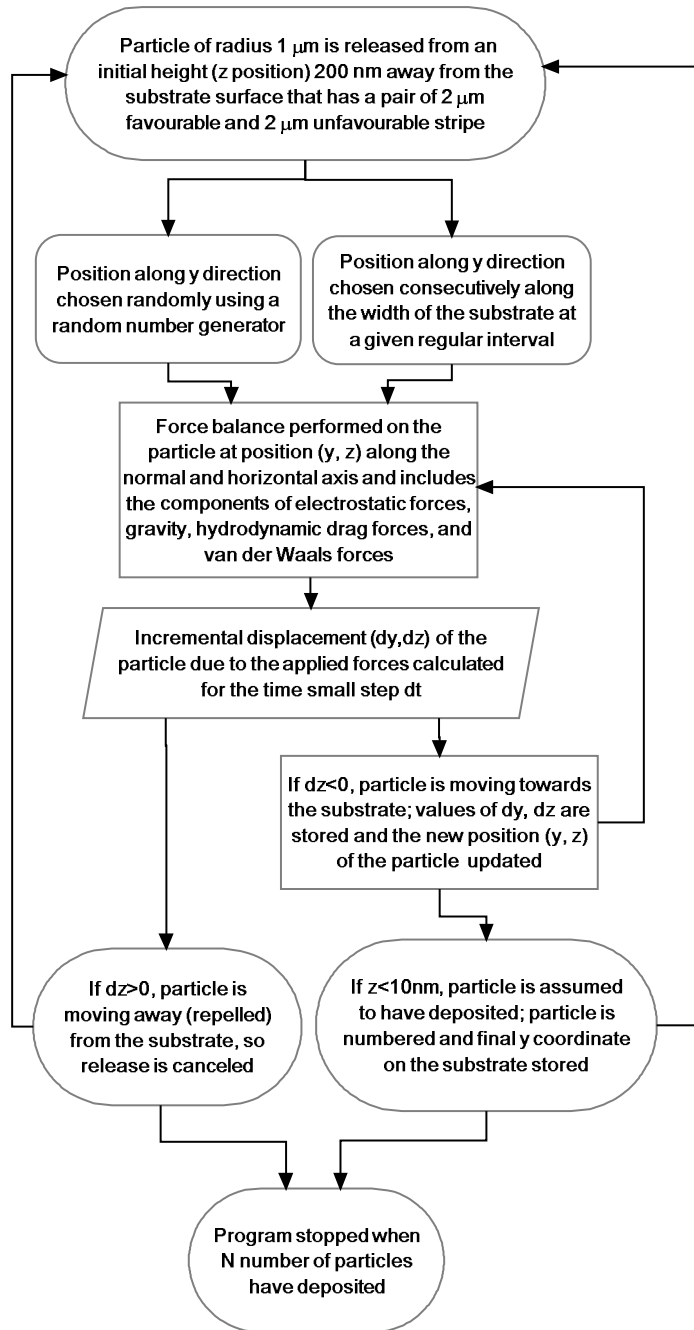


Figure 5.5: Flowchart outlining the scheme used for the trajectory analysis.

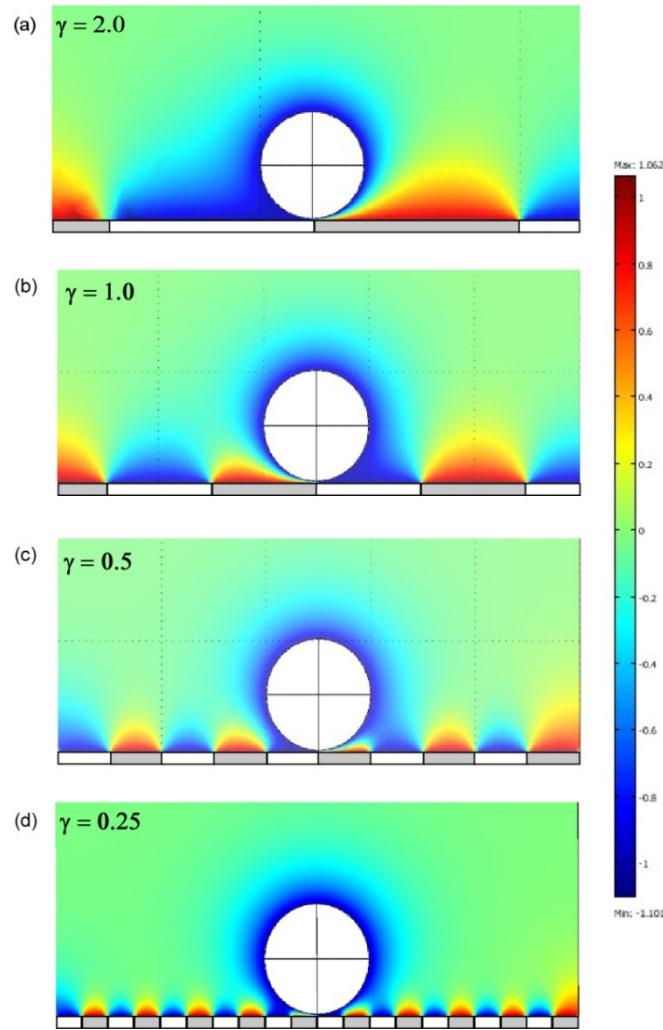


Figure 5.6: Comparison of the potential maps near a negatively charged particle and the charge heterogeneous surface at a separation height of $h/a = 0.03$ and $\kappa a = 1$ for 4 different size ratios γ . Schematic showing the rectangular stripes of alternating negative (white) and positive (gray) surface potentials also accompany each potential map. The particle, in all cases, is positioned above the boundary between a negative and positive stripe. The colour blue represents the negative potential while red represents the positive potential (as shown by the colour bar). A sharp change in colour denotes a higher electric field implying a larger electrostatic force. The scaled surface potential of the particle is $\Psi_p = -1$ and the negative and positive stripes have a scaled potential of $\Psi_{sn} = -1$ and $\Psi_{sp} = 1$, respectively.

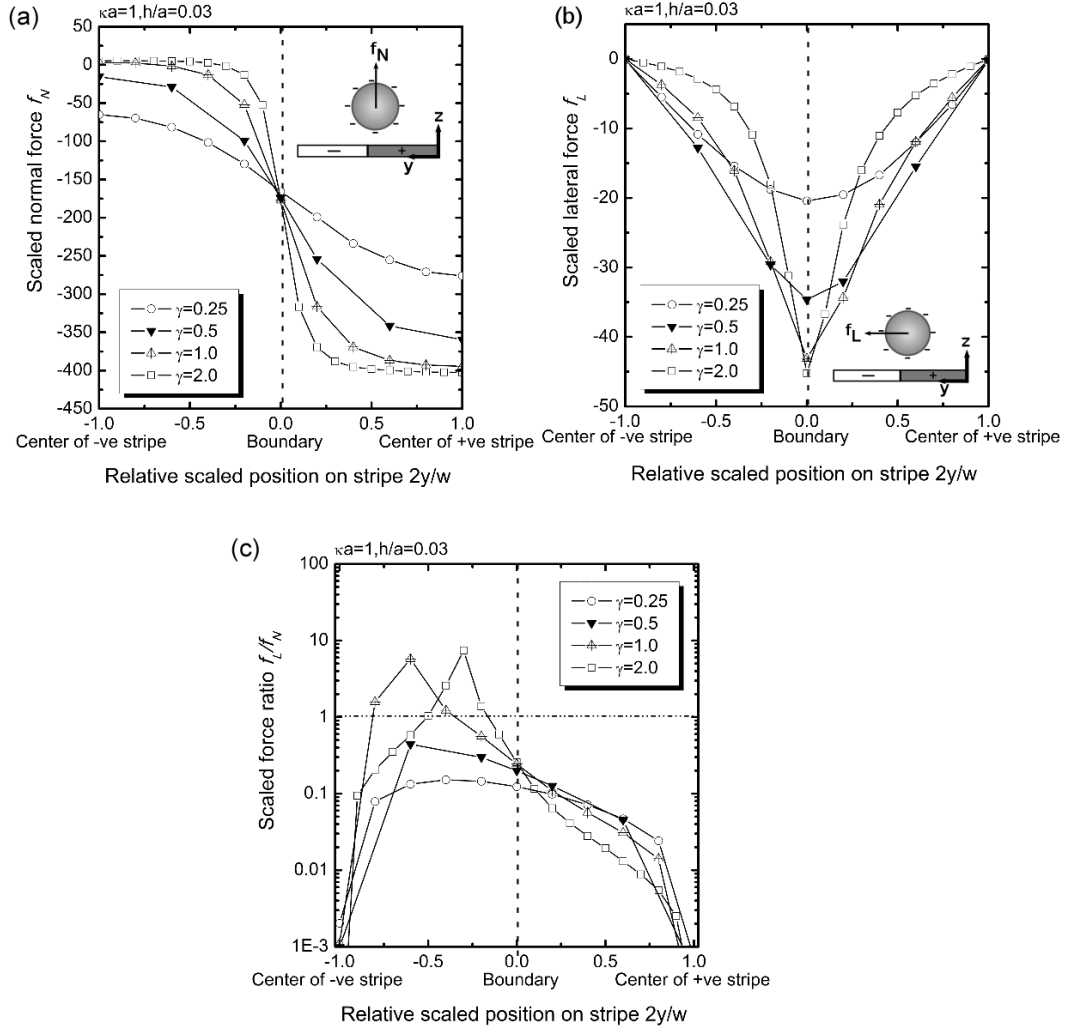


Figure 5.7: Variation of the scaled (a) normal force f_N , (b) lateral force f_L and, (c) force ratio f_L/f_N with different size ratios γ (stripe width to particle diameter ratio) at $\kappa a = 1$ and a scaled separation distance of $h/a = 0.03$. The x axis represents the relative position of the particle above the stripe. The scaled particle potential is $\Psi_p = -1$ and the negative and positive stripes have a constant potential of $\Psi_{sn} = -1$ and $\Psi_{sp} = +1$, respectively. The boundary between the negative and positive stripe is located at $2y/w = 0$ and is indicated by the dotted line.

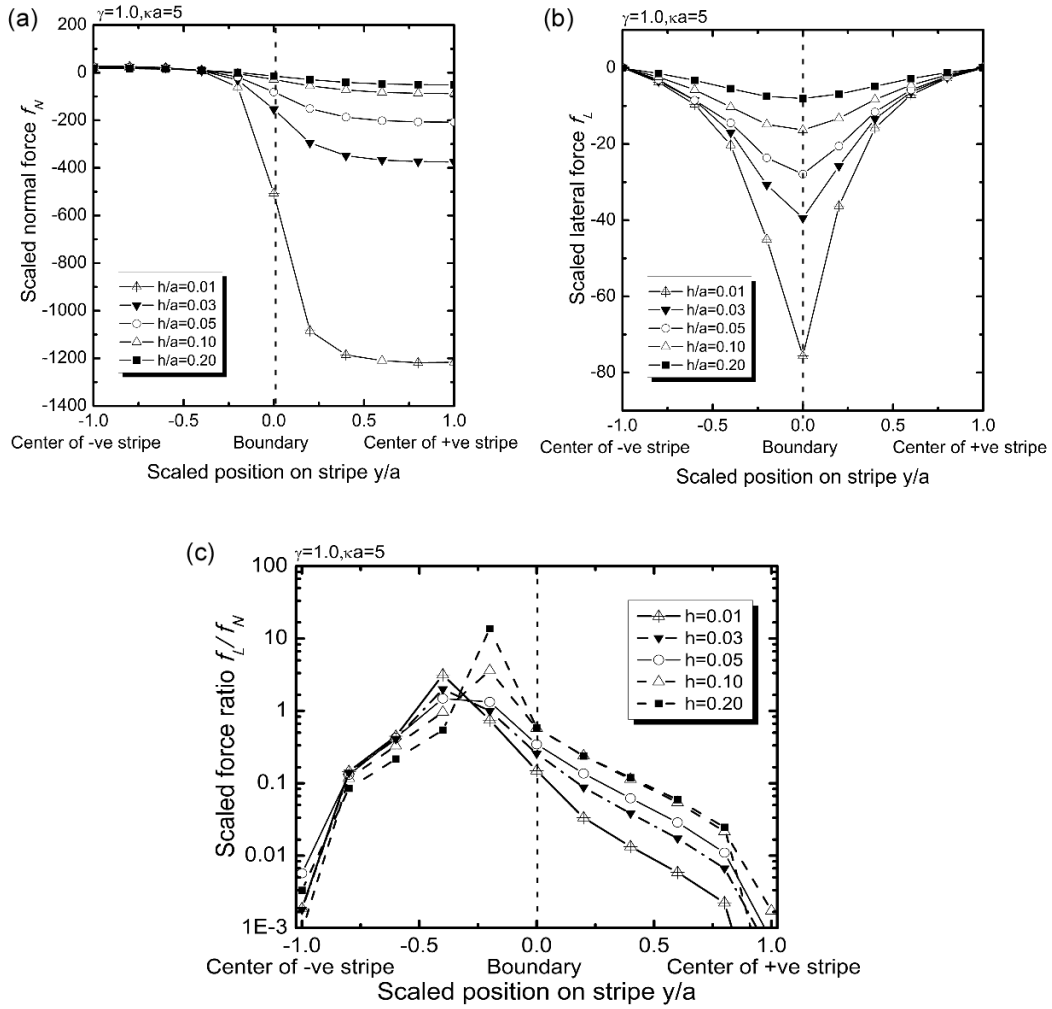


Figure 5.8: Variation of the scaled (a) normal force f_N , and (b) lateral force f_L acting on the particle placed at different scaled y/a positions along the heterogeneous surface for $\kappa a = 5$ and $\gamma = 1.0$. The different scaled separation distance h/a of the particle surface from the substrate surface are represented by the different symbols. The particle has a constant surface potential, $\Psi_p = -1$ and the negative and positive stripes have a constant potential of $\Psi_{sn} = -1$ and $\Psi_{sp} = 1$, respectively. The boundary between the negative and positive stripe is located at $y/a = 0$ as indicated by the dotted line.

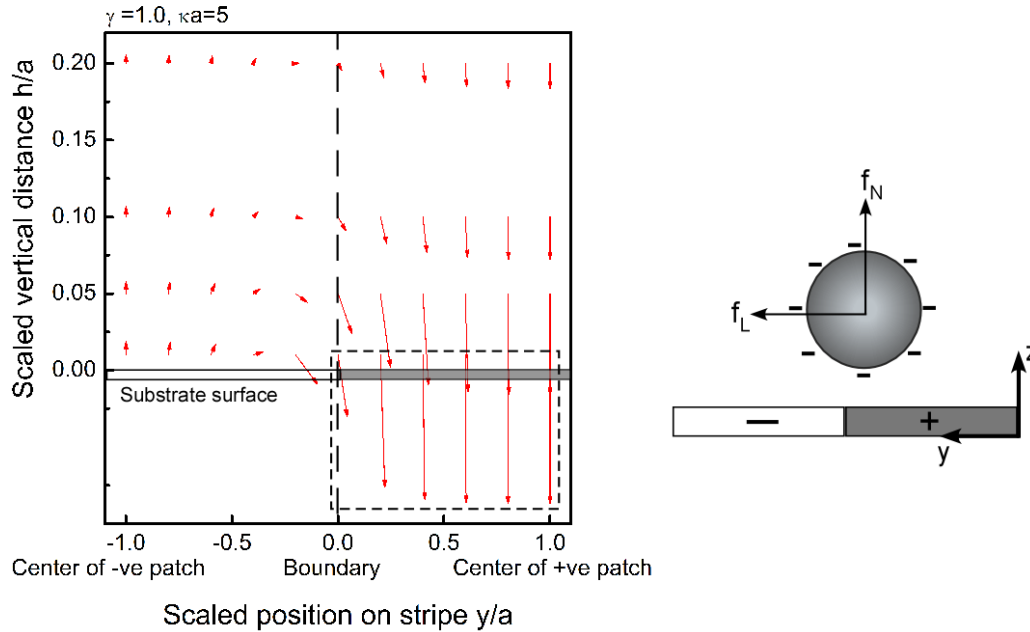


Figure 5.9: Vector plot of the net EDL force acting on the particle at $\kappa a = 5$ when particle center is placed at above different scaled y positions along the width of the charge heterogeneous surface for different scaled separation distances h/a under the same conditions as stated for Fig. 5.8. The ratio of the stripe width to particle diameter γ is 1.0. The direction in which the force is acting is indicated by the arrowhead and the relative magnitude by the arrow body. Please note the magnitude of the vectors enclosed in the dotted box have been reduced by four times their magnitude, for ease of representation. The boundary between the negative and positive stripe is located at $y/a = 0$ as indicated by the dotted line.

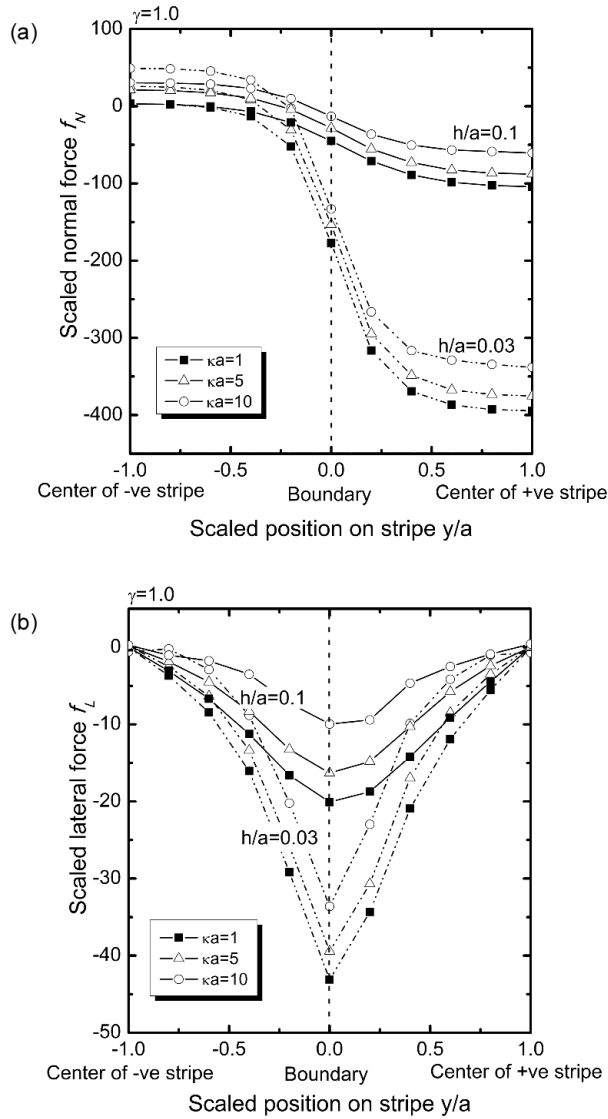


Figure 5.10: Comparison of the (a) normal and (b) lateral forces experienced by the particle for three different κa values (shown with symbols) at two representative scaled separation distances, $h/a = 0.1$ (solid lines) and $h/a = 0.03$ (dotted lines) for $\gamma = 2$. The scaled particle potential is $\Psi_p = -1$ and the negative and positive stripes have a constant potential of $\Psi_{sn} = -1$ and $\Psi_{sp} = 1$, respectively. The boundary between the negative and positive stripe is located at $y/a = 0$ as indicated by the dotted line.

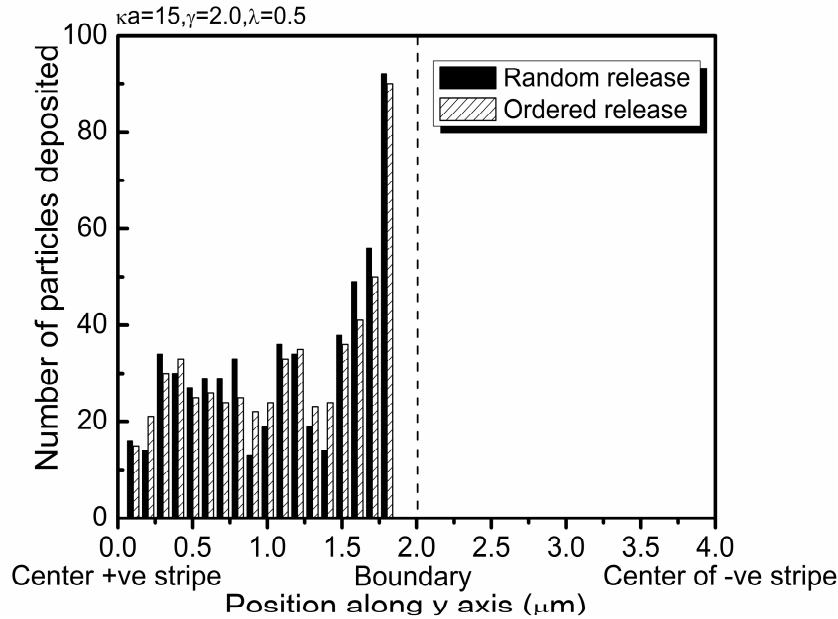


Figure 5.11: Particle distribution histograms for $\gamma = 2.0$ and $\kappa a = 15$ obtained by depositing particles of radius $1 \mu\text{m}$ on a 1.0 with $\lambda = w/p = 0.5$ (where, $w = b = 4 \mu\text{m}$). Each stripe pair composed of half favourable and half unfavourable region which was divided up into 40 bins. The particles (centers) present in each bin are counted and a distribution of deposited particles obtained over the width of the pair of stripes. The solid columns represent the particles whose initial positions were chosen at random and the hatched columns represent the particles that were released consecutively in an ordered manner along the stripe width. The boundary of the two stripes is indicated by the dashed line.

CHAPTER 6

SUMMARY AND RECOMMENDATIONS

6.1 Summary and Concluding Remarks

The aim of this research was to investigate the effect of charge-heterogeneity of a substrate on particle deposition. A literature review performed in this area showed that there are several theoretical studies that report the effect of surface charge heterogeneity on deposition, but there have been very few systematic experimental investigations. This is especially true for the influence of microscopic surface charge heterogeneity on colloidal deposition phenomena, employing large periodic arrays of a repeated pattern and particularly when the heterogeneities are comparable in size to the particles in question. The lack of systematic experimental studies in this area provided the motivation for this work. The study was conducted in two phases:

- I. Initially, an investigation of the initial stages of deposition in a macroscopically planar ‘real’ surface (commercial nanofiltration membranes) was conducted. These surfaces are known to inherently possess physical heterogeneities (or roughness) distributed in a random fashion throughout the membrane surface and were assumed to be otherwise chemically homogeneous. The goal of this phase of the research was to understand the effect of the more dominant physical heterogeneity on deposition and determine whether such a system would be ideal to study the effects of artificially created chemical heterogeneity has on deposition in a practical system.
- II. Next an investigation was conducted on model chemically patterned substrates, artificially created by patterning chemical patches of regular geometries on smooth substrates. Since the distribution and nature of these heterogeneous patches can be accurately known, deposition onto these ideal systems can be studied systematically, leading to considerable insight into

how the deposition behaviour is influenced by the presence of surface charge heterogeneity.

In the first phase of the study, laboratory scale filtration experiments with commercial nanofiltration membrane (NF90) membranes under various operating pressures and ionic concentrations were performed to investigate the role of membrane surface properties on the initial stages of fouling (colloidal deposition). The methodology involved a 'post mortem' analysis of fouled membrane morphologies employing an atomic force microscope (AFM). The major conclusions drawn from this phase of the study are summarized below:

1. There is an enhanced propensity of the particles to deposit on the peaks of the rough membranes as opposed to the valleys. The asperities can act as highly efficient particle capture sites under the combined influence of hydrodynamics and colloidal interactions, particularly when the particles are smaller than the asperities.
2. This enhanced propensity of the particles to deposit on the peaks of the rough membranes as opposed to the valleys may be ascribed to a coupled interplay between the colloidal and near field hydrodynamic interactions between the depositing particles and the protruding asperities. The hydrodynamics of the CFMF system simply assist in increasing the rate of collision of the suspended particles with these peaks, thereby stimulating rapid formation of larger aggregates. The morphology of these deposits clearly indicates the necessity of re-evaluating the present theoretical picture of particle deposition onto rough semi permeable surfaces, particularly when the overall magnitude of the roughness is larger than or comparable to the particle dimensions
3. From a surface energy viewpoint, it might seem that membrane surface is chemically heterogeneous, thereby providing the peaks as attractive sites where the particles can favourably deposit. However, characterizing the chemical heterogeneity of the membrane surface in relation to the topological variation proved to be a difficult task due to the lack of proper resolution of the available characterization techniques.

4. Although studies of particle deposition on naturally occurring heterogeneous substrates (such as filtration membranes) are of practical interest in industrial applications, however, using them to assess the specific roles of surface heterogeneity is not. This is because most 'real world' problems involving deposition are very complex and the systems cannot be described in sufficient detail to enable a complete analysis to be undertaken. The physical and chemical heterogeneities are concurrently present within the interacting bodies, and, are often of different shapes/sizes and randomly distributed over the surfaces. The coexistence of these heterogeneities creates a combined and rather convoluted interaction scenario, while the arbitrary shape/size and random distribution of the heterogeneities renders the task of quantifying these heterogeneities difficult. It, therefore, becomes hard to isolate and assess the effects that each heterogeneous component has on the deposition phenomenon, separately. Thus, such systems do not provide a suitable premise to study effects of chemical heterogeneity in a systematic manner.

In the second phase, the deposition of model colloidal particles onto striped charge heterogeneous planar substrates was studied. This phase of the study was conducted with an experimental and a theoretical component. Experimentally, periodic rectangular striped patterns were developed using microcontact printing on gold substrates. Experimental results were then compared against predictions obtained from a RSA deposition model developed using a Monte Carlo technique. The deposition behaviour observed experimentally was then corroborated in light of the interaction forces that occur between a charged particle placed near a chemically heterogeneous substrate using a finite element technique and a simple trajectory analysis. The major conclusions drawn from this phase of the study are summarized below:

1. The negatively charged particles predominantly deposit on the positively charged stripes and, in some, cases tends to preferentially deposit near the edges of the favourable (positively charged) stripes and this bias can be explained in light of the entropic principle.

2. The enhanced deposition probability at the favourable stripe boundary is subject to modification by the proximity of consecutive favourable stripes (or width of the intervening unfavourable stripes) as well as the particle size relative to the stripe width.
3. If the widths of the unfavourable stripes become comparable to the particle diameter, then the particles deposited on two consecutive favourable stripes can influence the deposition probabilities at the stripe edges.
4. During deposition, the underlying heterogeneity pattern is not revealed by the ordering of the particles on them, particularly when the particle diameter and the width of the favourable stripes are comparable, with the favourable stripes being closely spaced. A considerable variation in the deposit morphology is obtained corresponding to different ratios of γ (favourable stripe width to particle diameter) and λ (favourable stripe width to pitch) of the charge heterogeneous substrate and can be utilized to systematically alter the deposition structure by judiciously changing these ratios.
5. A simple binary probability distribution based Monte Carlo RSA deposition model adequately predicts the deposit structure and radial distributions functions. There is a discrepancy in the magnitudes of the peaks of the distribution functions; the numerical results show consistently larger oscillations compared to the experimental results. This discrepancy is attributed to the simplification of the model where electrostatic interactions between the particles and the substrate have been ignored.
6. The deposition on the favourable fraction of the substrate is enhanced on these heterogeneous surfaces. Deposit morphologies near jamming limits formed on 50% favourable patterned surfaces can be visually identical to those formed on fully favourable surfaces.
7. Lateral forces arise (along with normal forces) in presence of a potential gradient due to the presence of chemical heterogeneity. Lateral forces are significant at close separation distances when the heterogeneity is comparable in size to the particle. The magnitude of the lateral forces reduces drastically as the particle moves further away from the surface. Particle tra-

jectory analysis performed to obtain particle distribution probability over the width of a pair of heterogeneous stripe where the particle is comparable in size to the heterogeneity. The bias towards the edge of the favourable stripe was evident. The other feature that stands out is the presence of a small denuded zone lying next to the edge of the positively charged stripe. No particles (centers) are seen to deposit in this zone and this is attributed to the lateral forces acting at the edge of the stripe.

6.2 Recommendations

The study presented in this work should be considered as an initial step towards developing a systematic methodology to investigate the role of micro-scale charge heterogeneity on particle deposition process. Even though the experimental studies have successfully demonstrated the feasibility of the current technique, a more extensive parametric study (*e.g.* varying ionic strength, using different kinds of particles, *etc.*) is necessary to provide a better understanding of the phenomenon. Based on the experience obtained during this study, a few recommendations are presented below:

1. In this study deposition in a quiescent medium was reported. It is expected that deposition on chemically patterned surfaces in presence of flow can lead to interesting variations of deposit morphologies. It is easy enough to convert the closed cell used in this study into a tangential flow cell by incorporating appropriate ports and an external flow system. Similar data analysis methodology and parametric study can be employed as with the quiescent deposition experiment. Furthermore the micro-patterning and visualization techniques employed in this study could be used to perform an experimental investigation to explore the role of charge heterogeneity on particle deposition inside the impinging jet flow regime and compare results with the patch-wise heterogeneity model.
2. For further exploration into the phenomena associated with microscope heterogeneity in model systems, the next phase in the investigation could be the study of particle deposition near a physically heterogeneous substrate.

This part of the study will include creation of the physical heterogeneity using photolithographic techniques (similar to those outlined in Appendix B) and characterization using AFM. Deposition experiments (including no flow and flow) can be performed following procedures similar to those performed for the substrates with only chemical heterogeneity. A numerical model similar to the one employed for the chemical heterogeneity can also be investigated.

3. The RSA deposition model used in this study can be developed into a more rigorous model by incorporating the actual particle substrate interactions. This may provide a better quantitative agreement between the experimental and theoretical distributions. Furthermore, the model could be modified by simulating the charge heterogeneity as randomly distributed patches over the surface bearing different surface charges.
4. In the experimental investigations in this study, spherical particles were used in a mono-dispersed solution. There has been theoretical work done in studying deposition using different shaped particles (for example, ellipsoidal particles) and there also exists theoretical work involving poly-dispersed particle (for example bi-dispersed) solutions on a homogenous surface. However, there are no experimental works currently present that study these variations, particularly using patterned substrates. It would be straightforward to incorporate these parameter variations in the current experimental setup discussed in this study and observe the effects of variable particle shape and multiple sizes particle has on deposition morphology on heterogeneous substrates.

REFERENCES

1. Masliyah, J.H. and S. Bhattacharjee, *Electrokinetic and colloid transport phenomena*. 2006, Wiley-Interscience: Hoboken, N.J.
2. O'Melia, C.R. and W. Strumm, *Theory of water filtration*. Journal of American Water Works Association, 1967. **59**: p. 1393-1412.
3. Yao, K.M., M.T. Habibian, and C.R. O'Melia, *Water and waste water filtration: Concepts and applications*. Environmental Science & Technology, 1971. **5**(11): p. 1105-1112.
4. Rajagopalan, R. and C. Tien, *Theory of deep bed filtration*. Progress in filtration and separation, ed. R.J. Wakeman. Vol. 1. 1979, Amsterdam: Elsevier. 179-269.
5. Dziomkina, N.V. and G.J. Vancso, *Colloidal crystal assembly on topologically patterned templates*. Soft Matter, 2005. **1**(4): p. 265-279.
6. Ong, Y.L., et al., *Adhesion forces between E. coli bacteria and biomaterial surfaces*. Langmuir, 1999. **15**(8): p. 2719-2725.
7. Burks, G.A., et al., *Macroscopic and nanoscale measurements of the adhesion of bacteria with varying outer layer surface composition*. Langmuir, 2003. **19**(6): p. 2366-2371.
8. Walker, S.L., J.A. Redman, and M. Elimelech, *Role of cell surface Lipopolysaccharides in Escherichia coli K12 adhesion and transport*. Langmuir, 2004. **20**(18): p. 7736-7746.
9. Schwartz, A.M., *The physical chemistry of detergency*. Surface and Colloid Science, ed. E. Matijevic. Vol. 5. 1972, New York; (Chichester): Wiley-Interscience.

10. Hilal, N., et al., *Methods employed for control of fouling in MF and UF membranes: A comprehensive review*. Separation Science and Technology, 2005. **40**(10): p. 1957-2005.
11. Escobar, I.C., et al., *Committee Report: Recent advances and research needs in membrane fouling*. Journal American Water Works Association, 2005. **97**(8): p. 79-89.
12. Chang, I.S., et al., *Membrane fouling in membrane bioreactors for wastewater treatment*. Journal of Environmental Engineering, 2002. **128**(11): p. 1018-1029.
13. Velev, O.D. and A.M. Lenhoff, *Colloidal crystals as templates for porous materials*. Current Opinion in Colloid & Interface Science, 2000. **5**(1-2): p. 56-63.
14. Kooij, E.S., et al., *Ionic strength mediated self-organization of gold nanocrystals: An AFM study*. Langmuir, 2002. **18**(20): p. 7677-7682.
15. Elimelech, M., et al., *Particle deposition and aggregation: Measurement, modelling, and simulation*. 1989, London: Butterworth.
16. Adamczyk, Z., et al., *Kinetics of localized adsorption of colloid particles*. Advances in Colloid and Interface Science, 1994. **48**: p. 151-280.
17. Johnson, C.A. and A.M. Lenhoff, *Adsorption of charged latex particles on mica studied by atomic force microscopy*. Journal of Colloid and Interface Science, 1996. **179**(2): p. 587-599.
18. Semmler, M., et al., *Diffusional deposition of charged latex particles on water-solid interfaces at low ionic strength*. Langmuir, 1998. **14**(18): p. 5127-5132.
19. Adamczyk, Z. and L. Szyk, *Kinetics of irreversible adsorption of latex particles under diffusion-controlled transport*. Langmuir, 2000. **16**(13): p. 5730-5737.

20. Derjaguin, B.V. and L. Landau, *Theory of the stability of strongly charged lyophobic sols and of the adhesion of strongly charged particles in solution of electrolytes*. Acta Physicochimica URSS, 1941. **14**: p. 633-662.
21. Verwey, E.J.W., J.T.G. Overbeek, and K.v. Nes, *Theory of the stability of lyophobic colloids; the interaction of sol particles having an electric double layer*,. 1948, New York: Elsevier Pub. Co.
22. Israelachvili, J.N., *Intermolecular and surface forces*. 1991: Academic Press London.
23. Hunter, R.J. and L.R. White, *Foundations of colloid science*. 1987, Oxford [Oxfordshire]; New York: Clarendon Press ; Oxford University Press.
24. Shaw, D.J., *Introduction to colloid and surface chemistry*. 1980, London; Boston: Butterworths.
25. Hogg, R., T.W. Healy, and D.W. Fuersteneau, *Mutual coagulation of colloidal dispersions*. Transactions of the Faraday Society, 1966. **62**(522P): p. 1638-1651.
26. Ninham, B.W., *On progress in forces since the DLVO theory*. Advances in Colloid and Interface Science, 1999. **83**(1-3): p. 1-17.
27. Kralchevsky, P.A., and K. Nagayama, *Particles at fluids interfaces and membranes attachment of colloid particles and proteins to interfaces and formation of two-dimensional arrays*. 2001, Elsevier: Amsterdam; New York.
28. Israelachvili, J. and H. Wennerstrom, *Role of hydration and water structure in biological and colloidal interactions*. Nature, 1996. **379**(6562): p. 219-225.
29. van Oss, C.J. and R.F. Giese, *Role of the properties and structure of liquid water in colloidal and interfacial systems*. Journal of Dispersion Science and Technology, 2004. **25**(5): p. 631-655.
30. Raviv, U. and J. Klein, *Fluidity of bound hydration layers*. Science, 2002. **297**(5586): p. 1540-1543.

31. Bostrom, M., D.R.M. Williams, and B.W. Ninham, *Specific ion effects: Why DLVO theory fails for biology and colloid systems*. Physical Review Letters, 2001. **87**(16).
32. LaVan, D.A., T. McGuire, and R. Langer, *Small-scale systems for in vivo drug delivery*. Nature Biotechnology, 2003. **21**(10): p. 1184-1191.
33. Dabros, T. and T.G.M. van de Ven, *A direct method for studying particle deposition onto solid-surfaces*. Colloid and Polymer Science, 1983. **261**(8): p. 694-707.
34. van de Ven, T.G.M. and S.J. Kelemen, *Characterizing polymers with an impinging jet*. Journal of Colloid and Interface Science, 1996. **181**(1): p. 118-123.
35. Elimelech, M., *Particle deposition on ideal collectors from dilute flowing suspensions - mathematical formulation, numerical solution, and simulations*. Separations Technology, 1994. **4**(4): p. 186-212.
36. Marshall, J.K. and J.A. Kitchener, *Deposition of colloidal particles on smooth solids*. Journal of Colloid and Interface Science, 1966. **22**(4): p. 342-351.
37. Petsev, D.N. and P.G. Vekilov, *Evidence for non-DLVO hydration interactions in solutions of the protein apoferritin*. Physical Review Letters, 2000. **84**(6): p. 1339-1342.
38. Freitas, A.M. and M.M. Sharma, *Detachment of particles from surfaces: An AFM study*. Journal of Colloid and Interface Science, 2001. **233**(1): p. 73-82.
39. Brant, J.A. and A.E. Childress, *Membrane-colloid interactions: Comparison of extended DLVO predictions with AFM force measurements*. Environmental Engineering Science, 2002. **19**(6): p. 413-427.
40. Ruckenstein, E. and D.C. Prieve, *Rate of deposition of brownian particles under action of london and double-layer forces*. Journal of the Chemical Society-Faraday Transactions II, 1973. **69**(10): p. 1522-1536.

41. Walz, J.Y., *The effect of surface heterogeneities on colloidal forces*. Advances in Colloid and Interface Science, 1998. **74**: p. 119-168.
42. Martines, E., et al., *Superhydrophobicity and superhydrophilicity of regular nanopatterns*. Nano Letters, 2005. **5**(10): p. 2097-2103.
43. Roach, P., N.J. Shirtcliffe, and M.I. Newton, *Progress in superhydrophobic surface development*. Soft Matter, 2008. **4**(2): p. 224-240.
44. Hull, M. and J.A. Kitchener, *Interaction of spherical colloidal particles with planar surfaces*. Transactions of the Faraday Society, 1969. **65**(563P): p. 3093-3104.
45. Bowen, B.D. and N. Epstein, *Fine particle deposition in smooth parallel-plate channels*. Journal of Colloid and Interface Science, 1979. **72**(1): p. 81-97.
46. Elimelech, M. and C.R. O'Melia, *Effect of particle size on collision Efficiency in the deposition of brownian particles with electrostatic energy barriers*. Langmuir, 1990. **6**(6): p. 1153-1163.
47. Hoek, E.M.V., S. Bhattacharjee, and M. Elimelech, *Effect of membrane surface roughness on colloid-membrane DLVO interactions*. Langmuir, 2003. **19**(11): p. 4836-4847.
48. Zhu, X.H. and M. Elimelech, *Colloidal fouling of reverse osmosis membranes: Measurements and fouling mechanisms*. Environmental Science & Technology, 1997. **31**(12): p. 3654-3662.
49. Vrijenhoek, E.M., S. Hong, and M. Elimelech, *Influence of membrane surface properties on initial rate of colloidal fouling of reverse osmosis and nanofiltration membranes*. Journal of Membrane Science, 2001. **188**(1): p. 115-128.
50. Hirose, M., H. Ito, and Y. Kamiyama, *Effect of skin layer surface structures on the flux behaviour of RO membranes*. Journal of Membrane Science, 1996. **121**(2): p. 209-215.

51. Bowen, W.R., T.A. Doneva, and J.A.G. Stoton, *The use of atomic force microscopy to quantify membrane surface electrical properties*. Colloids and Surfaces A-Physicochemical and Engineering Aspects, 2002. **201**(1-3): p. 73-83.
52. Bowen, W.R. and T.A. Doneva, *Atomic force microscopy studies of membranes: Effect of surface roughness on double-layer interactions and particle adhesion*. Journal of Colloid and Interface Science, 2000. **229**(2): p. 544-549.
53. Herman, M.C. and K.D. Papadopoulos, *Effects of asperities on the van der Waals and electric double-layer interactions of 2 parallel flat plates*. Journal of Colloid and Interface Science, 1990. **136**(2): p. 385-392.
54. Czarnecki, J., *The effects of surface inhomogeneities on the interactions in colloidal systems and colloid stability*. Advances in Colloid and Interface Science, 1986. **24**(4): p. 283-319.
55. Martines, E., et al., *DLVO interaction energy between a sphere and a nano-patterned plate*. Colloids and Surfaces A-Physicochemical and Engineering Aspects, 2008. **318**(1-3): p. 45-52.
56. Adamczyk, Z., P. Weronki, and E. Musial, *Colloid particle adsorption at random site (Heterogeneous) surfaces*. Journal of Colloid and Interface Science, 2002. **248**(1): p. 67-75.
57. Bhattacharjee, S., M. Elimelech, and M. Borkovec, *DLVO interaction between colloidal particles: Beyond Derjaguin's approximation*. Croatica Chemica Acta, 1998. **71**(4): p. 883-903.
58. Song, L.F., P.R. Johnson, and M. Elimelech, *Kinetics of colloid deposition onto heterogeneously charged surfaces in porous-media*. Environmental Science & Technology, 1994. **28**(6): p. 1164-1171.
59. Sharma, A., et al., *Nanoscale surface heterogeneities and glass durability*. Journal of Non-Crystalline Solids, 2002. **311**(1): p. 93-98.
60. Gregory, J. and A.J. Wishart, *Deposition of latex particles on alumina fibers*. Colloids and Surfaces, 1980. **1**(3-4): p. 313-334.

61. Vaidyanathan, R. and C. Tien, *Hydrosol deposition in Antigranulocytes media under unfavorable surface conditions*. Chemical Engineering Science, 1991. **46**(4): p. 967-983.
62. Adamczyk, Z., et al., *Particle transfer to solid surfaces*. Advances in Colloid and Interface Science, 1983. **19**(3): p. 183-252.
63. Sjollema, J. and H.J. Busscher, *Deposition of polystyrene particles in a parallel plate flow cell I- The Influence of collector surface properties on the experimental deposition rate*. Colloids and Surfaces, 1990. **47**: p. 323-336.
64. Ridgway, H., et al., *Biofouling of membranes: Membrane preparation characterization and analysis of bacterial adhesion*. 310 ed. Methods in Enzymology. 1999. 463-494.
65. Chambers, L.D., et al., *Modern approaches to marine antifouling coatings*. Surface and Coatings Technology, 2006. **201**(6): p. 3642-3652.
66. Ainslie, K.M., et al., *Attenuation of protein adsorption on static and oscillating magnetostrictive nanowires*. Nano Letters, 2005. **5**(9): p. 1852-1856.
67. Ma, H., C.J. Winslow, and B.E. Logan, *Spectral force analysis using atomic force microscopy reveals the importance of surface heterogeneity in bacterial and colloid adhesion to engineered surfaces*. Colloids and Surfaces B: Biointerfaces, 2008. **62**(2): p. 232-237.
68. Johnson, P.R., N. Sun, and M. Elimelech, *Colloid transport in geochemically heterogeneous porous media: Modeling and measurements*. Environmental Science & Technology, 1996. **30**(11): p. 3284-3293.
69. Elimelech, M., J.Y. Chen, and Z.A. Kuznar, *Particle deposition onto solid surfaces with micropatterned charge heterogeneity: The "hydrodynamic bump" effect*. Langmuir, 2003. **19**(17): p. 6594-6597.
70. Nazemifard, N., J.H. Masliyeh, and S. Bhattacharjee, *Particle deposition onto charge heterogeneous surfaces: Convection-diffusion-migration model*. Langmuir, 2006. **22**(24): p. 9879-9893.

71. Nazemifard, N., J.H. Masliyeh, and S. Bhattacharjee, *Particle deposition onto micropatterned charge heterogeneous substrates: Trajectory analysis*. Journal of Colloid and Interface Science, 2006. **293**(1): p. 1-15.
72. Schaaf, P. and J. Talbot, *Surface exclusion effects in adsorption processes*. Journal of Chemical Physics, 1989. **91**(7): p. 4401-4409.
73. Feder, J., *Random sequential adsorption*. Journal of Theoretical Biology, 1980. **87**(2): p. 237-254.
74. Adamczyk, Z., et al., *Structure and ordering in localized adsorption of particles*. Journal of Colloid and Interface Science, 1990. **140**(1): p. 123-137.
75. Adamczyk, Z. and P. Weronki, *Kinetics of irreversible adsorption of interacting spheroidal particles*. Langmuir, 1995. **11**(11): p. 4400-4410.
76. Adamczyk, Z. and P. Weronki, *Unoriented adsorption of interacting spheroidal particles*. Journal of Colloid and Interface Science, 1997. **189**(2): p. 348-360.
77. Oberholzer, M.R., et al., *2-D and 3-D interactions in random sequential adsorption of charged particles*. Journal of Colloid and Interface Science, 1997. **194**(1): p. 138-153.
78. Jullien, R. and P. Meakin, *Random sequential adsorption with restructuring in 2 dimensions*. Journal of Physics a-Mathematical and General, 1992. **25**(4): p. L189-L194.
79. Choi, H.S., et al., *First layer formation in ballistic deposition of spherical particles - kinetics and structure*. Journal of Chemical Physics, 1993. **99**(11): p. 9296-9303.
80. Tarjus, G., et al., *Restructuring effects in irreversible deposition of spheres on a plane*. Physical Review E, 1994. **49**(4): p. 3239-3252.
81. Schaaf, P., et al., *Fluctuation of the number of adsorbed particles analyzed by a virial expansion - Comparison between experiment and theory*. Journal of Chemical Physics, 1995. **102**(12): p. 5077-5081.

82. Schaaf, P., A. Johner, and J. Talbot, *Asymptotic behavior of particle deposition*. Physical Review Letters, 1991. **66**(12): p. 1603-1605.
83. Senger, B., et al., *Properties of jamming configurations built up by the adsorption of brownian particles onto solid-Surfaces*. Physical Review A, 1991. **44**(10): p. 6926-6928.
84. Senger, B., et al., *Influence of Bulk Diffusion on the Adsorption of Hard-Spheres on a Flat Surface*. Journal of Chemical Physics, 1992. **97**(5): p. 3813-3820.
85. Senger, B., et al., *Effect of the bulk diffusion on the jamming limit configurations for irreversible adsorption*. Europhysics Letters, 1993. **21**(2): p. 135-140.
86. Tovbin, Y.K., *The hierarchy of adsorption models for laterally interacting molecules on heterogeneous surfaces*. Langmuir, 1997. **13**(5): p. 979-989.
87. Ceyrolles, W.J., P. Viot, and J. Talbot, *Kinetics of heterogeneous adsorption: Mean-field theory and simulations*. Langmuir, 2002. **18**(4): p. 1112-1118.
88. Adamczyk, Z., P. Weronki, and E. Musial, *Particle adsorption under irreversible conditions: kinetics and jamming coverage*. Colloids and Surfaces a-Physicochemical and Engineering Aspects, 2002. **208**(1-3): p. 29-40.
89. Adamczyk, Z., et al., *Irreversible adsorption of colloid particles at heterogeneous surfaces*. Applied Surface Science, 2002. **196**(1-4): p. 250-263.
90. Adamczyk, Z., et al., *Irreversible adsorption of particles at random-site surfaces*. Journal of Chemical Physics, 2004. **120**(23): p. 11155-11162.
91. Adamczyk, Z., et al., *Irreversible adsorption of particles on heterogeneous surfaces*. Advances in Colloid and Interface Science, 2005. **118**(1-3): p. 25-42.

92. Faraudo, J., et al., *Deposition kinetics of colloidal particles at an interface: Interplay of diffusion and gravity*. Journal of Chemical Physics, 2003. **119**(21): p. 11420-11428.
93. Adamczyk, Z., B. Siwek, and E. Musial, *Latex particle adsorption at heterogeneous surfaces*. Colloids and Surfaces A-Physicochemical and Engineering Aspects, 2003. **214**(1-3): p. 219-229.
94. Adamczyk, Z., et al., *Particle deposition at electrostatically heterogeneous surfaces*. Colloids and Surfaces A-Physicochemical and Engineering Aspects, 2003. **222**(1-3): p. 15-25.
95. Michna, A., Z. Adamczyk, and M. Zembala, *Deposition of colloid particles on polyelectrolyte multilayers*. Colloids and Surfaces A-Physicochemical and Engineering Aspects, 2007. **302**(1-3): p. 467-472.
96. Adamczyk, Z., M. Nattich, and J. Barbasz, *Deposition of colloid particles at heterogeneous and patterned surfaces*. Advances in Colloid and Interface Science, 2009. **147-148**: p. 2-17.
97. Serizawa, T., S. Kamimura, and M. Akashi, *Electrostatic adsorption of polystyrene particles with different surface charges onto the surface of an ultrathin polymer film*. Colloids and Surfaces A-Physicochemical and Engineering Aspects, 2000. **164**(2-3): p. 237-245.
98. Adamczyk, Z., et al., *Kinetics of latex particle deposition from flowing suspensions*. Journal of Colloid and Interface Science, 1986. **110**(1): p. 188-200.
99. Baloch, M.K. and T.G.M. van de Ven, *Light-scattering from semi dilute dispersions of nonspherical latex particles subjected to an electric-field*. Journal of Colloid and Interface Science, 1990. **135**(2): p. 594-597.
100. Bohmer, M.R., *Effects of polymers on particle adsorption on macroscopic surfaces studied by optical reflectometry*. Journal of Colloid and Interface Science, 1998. **197**(2): p. 251-256.
101. Shin, Y.W., J.E. Roberts, and M.M. Santore, *The relationship between polymer/substrate charge density and charge overcompensation by ad-*

- sorbed polyelectrolyte layers*. Journal of Colloid and Interface Science, 2002. **247**(1): p. 220-230.
102. Kozlova, N. and M.M. Santore, *Manipulation of micrometer-scale adhesion by tuning nanometer-scale surface features*. Langmuir, 2006. **22**(3): p. 1135-1142.
 103. Adamczyk, Z., *Particles at interfaces: Interactions, deposition, structure*. Interface Science and Technology, ed. A. Hubbard. Vol. 9. 2006: Academic Press.
 104. Adamczyk, Z., et al., *Characterization of poly(ethylene imine) layers on mica by the streaming potential and particle deposition methods*. Journal of Colloid and Interface Science, 2007. **313**(1): p. 86-96.
 105. Joscelyne, S. and C. Tragardh, *Kinetics of colloidal deposition and release of polystyrene latex particles in the presence of adsorbed beta-lactoglobulin studied using a flow cell*. Journal of Colloid and Interface Science, 1997. **192**(2): p. 294-305.
 106. Garno, J.C., et al., *Production of periodic arrays of protein nanostructures using particle lithography*. Langmuir, 2002. **18**(21): p. 8186-8192.
 107. Nitta, T. and A. Yamaguchi, *Effects of surface topography on adsorption isotherms of mobile molecules: comparison of patchwise and random surfaces*. Langmuir, 2002. **9**(10): p. 2618-2623.
 108. Adamczyk, Z., et al., *Surface clusters of colloid particles produced by deposition on sites*. Langmuir, 2005. **21**(19): p. 8952-8959.
 109. Adamczyk, Z., P. Weronki, and E. Musial, *Irreversible adsorption of hard spheres at random site (heterogeneous) surfaces*. Journal of Chemical Physics, 2002. **116**(11): p. 4665-4672.
 110. Harreis, H.M., M. Schmidt, and H. Lowen, *Decoration lattices of colloids adsorbed on stripe-patterned substrates*. Physical Review E, 2002. **65**(4).
 111. Adamczyk, Z., J. Barbasz, and M. Zembala, *Particle assembly on surface features (patterned surfaces)*. Langmuir, 2007. **23**(10): p. 5557-5562.

112. Cadilhe, A., N.A.M. Araujo, and V. Privman, *Random sequential adsorption: from continuum to lattice and pre-patterned substrates*. Journal of Physics-Condensed Matter, 2007. **19**(6).
113. Araujo, N.A.M., A. Cadilhe, and V. Privman, *Morphology of fine-particle monolayers deposited on nanopatterned substrates*. Physical Review E (Statistical, Nonlinear, and Soft Matter Physics), 2008. **77**(3): p. 031603-10.
114. Zheng, H.P., M.F. Rubner, and P.T. Hammond, *Particle assembly on patterned "plus/minus" polyelectrolyte surfaces via polymer-on-polymer stamping*. Langmuir, 2002. **18**(11): p. 4505-4510.
115. Jiang, X.P., et al., *Polymer-on-polymer stamping: Universal approaches to chemically patterned surfaces*. Langmuir, 2002. **18**(7): p. 2607-2615.
116. Karakurt, I., P. Leiderer, and J. Boneberg, *Size-dependent self-organization of colloidal particles on chemically patterned surfaces*. Langmuir, 2006. **22**(6): p. 2415-2417.
117. Kruger, C. and U. Jonas, *Synthesis and pH-Selective adsorption of latex particles onto photolithographically patterned silane layers*. Journal of Colloid and Interface Science, 2002. **252**(2): p. 331-338.
118. Michel, R., et al., *Selective molecular assembly patterning: A new approach to micro- and nanochemical patterning of surfaces for biological applications*. Langmuir, 2002. **18**(8): p. 3281-3287.
119. Chen, K.M., et al., *Selective self-organization of colloids on patterned polyelectrolyte templates*. Langmuir, 2000. **16**(20): p. 7825-7834.
120. Fudouzi, H., M. Kobayashi, and N. Shinya, *Assembly of microsized colloidal particles on electrostatic regions patterned through ion beam irradiation*. Langmuir, 2002. **18**(20): p. 7648-7652.
121. Zheng, H.P., et al., *Controlling cell attachment selectively onto biological polymer-colloid templates using polymer-on-polymer stamping*. Langmuir, 2004. **20**(17): p. 7215-7222.

122. Rundqvist, J., J.H. Hoh, and D.B. Haviland, *Directed immobilization of protein-coated nanospheres to nanometer-scale patterns fabricated by electron beam lithography of poly(ethylene glycol) self-assembled monolayers*. Langmuir, 2006. **22**(11): p. 5100-5107.
123. Liang, S., et al., *Site selective micro-patterned rutile TiO₂ film through a seed layer deposition*. Journal of Colloid and Interface Science, 2007. **311**(1): p. 194-202.
124. Betancourt, T. and L. Brannon-Peppas, *Micro- and nanofabrication methods in nanotechnological medical and pharmaceutical devices*. International Journal of Nanomedicine, 2006. **1**(4): p. 483-495.
125. Ozin, G.A., et al., *Nanofabrication by self-assembly*. Materials Today, 2009. **12**(5): p. 12-23.
126. Chase, H.A., *Affinity separations utilizing immobilized monoclonal-antibodies - a new tool for the biochemical engineer*. Chemical Engineering Science, 1984. **39**(7-8): p. 1099-1125.
127. Katz, E., A.F. Buckmann, and I. Willner, *Self-powered enzyme-based biosensors*. Journal of the American Chemical Society, 2001. **123**(43): p. 10752-10753.
128. Howell, S.W., et al., *Patterned protein microarrays for bacterial detection*. Langmuir, 2003. **19**(2): p. 436-439.
129. Mendes, P.M., et al., *Nanostructures from nanoparticles*. Journal of Physics-Condensed Matter, 2003. **15**(42): p. S3047-S3063.
130. Stein, A. and R.C. Schroden, *Colloidal crystal templating of three-dimensionally ordered macroporous solids: materials for photonics and beyond*. Current Opinion in Solid State & Materials Science, 2001. **5**(6): p. 553-564.
131. Lopez, C., *Materials aspects of photonic crystals*. Advanced Materials, 2003. **15**(20): p. 1679-1704.

132. Shipway, A.N., E. Katz, and I. Willner, *Nanoparticle arrays on surfaces for electronic, optical, and sensor applications*. Chemphyschem, 2000. **1**(1): p. 18-52.
133. Holtz, J.H. and S.A. Asher, *Polymerized colloidal crystal hydrogel films as intelligent chemical sensing materials*. Nature, 1997. **389**(6653): p. 829-832.
134. Shafer-Peltier, K.E., et al., *Toward a glucose biosensor based on surface-enhanced Raman scattering*. Journal of the American Chemical Society, 2003. **125**(2): p. 588-593.
135. Gratton, S.E.A., et al., *The pursuit of a scalable nanofabrication platform for use in material and life science applications*. Accounts of Chemical Research, 2008. **41**(12): p. 1685-1695.
136. Luttge, R., *Massively parallel fabrication of repetitive nanostructures: nanolithography for nanoarrays*. Journal of Physics D-Applied Physics, 2009. **42**(12).
137. Maily, D., *Nanofabrication techniques*. European Physical Journal-Special Topics, 2009. **172**: p. 333-342.
138. Clark, P., *Cell Behavior on micropatterned surfaces*. Biosensors & Bioelectronics, 1994. **9**(9-10): p. 657-661.
139. Scotchford, C.A., et al., *Chemically patterned, metal-oxide-based surfaces produced by photolithographic techniques for studying protein- and cell-interactions. II: Protein adsorption and early cell interactions*. Biomaterials, 2003. **24**(7): p. 1147-1158.
140. Wright, J., et al., *Positive and negative tone protein patterning on a photobase generating polymer*. Langmuir, 2003. **19**(2): p. 446-452.
141. Shadnam, M.R., et al., *Direct patterning of self-assembled monolayers on gold using a laser beam*. Langmuir, 2004. **20**(7): p. 2667-2676.

142. Rhinow, D. and N.A. Hampp, *Forming microstructured alkanethiol self-assembled monolayers on gold by laser ablation*. Ieee Transactions on Nanobioscience, 2006. **5**(3): p. 188-192.
143. Chen, J.Y., J.F. Klemic, and M. Elimelech, *Micropatterning microscopic charge heterogeneity on flat surfaces for studying the interaction between colloidal particles and heterogeneously charged surfaces*. Nano Letters, 2002. **2**(4): p. 393-396.
144. Xia, Y.N. and G.M. Whitesides, *Soft lithography*. Annual Review of Materials Science, 1998. **28**: p. 153-184.
145. Aizenberg, J., P.V. Braun, and P. Wiltzius, *Patterned colloidal deposition controlled by electrostatic and capillary forces*. Physical Review Letters, 2000. **84**(13): p. 2997-3000.
146. Fan, F.Q. and K.J. Stebe, *Assembly of colloidal particles by evaporation on surfaces with patterned hydrophobicity*. Langmuir, 2004. **20**(8): p. 3062-3067.
147. Fustin, C.A., et al., *Parameters influencing the templated growth of colloidal crystals on chemically patterned surfaces*. Langmuir, 2004. **20**(21): p. 9114-9123.
148. Kumar, A., H.A. Biebuyck, and G.M. Whitesides, *Patterning self-assembled monolayers - applications in materials science*. Langmuir, 1994. **10**(5): p. 1498-1511.
149. Lee, I., et al., *Controlled cluster size in patterned particle arrays via directed adsorption on confined surfaces*. Advanced Materials, 2002. **14**(8): p. 572-577.
150. Masuda, Y., et al., *Self-assembly patterning of colloidal crystals constructed from opal structure or NaCl structure*. Langmuir, 2004. **20**(13): p. 5588-5592.
151. Srinivasan, C., et al., *Scanning electron microscopy of nanoscale chemical patterns*. ACS Nano, 2007. **1**(3): p. 191-201.

152. Kim, H., et al., *Characterization of mixed self-assembled monolayers for immobilization of streptavidin using chemical force microscopy*. Ultramicroscopy, 2008. **108**(10): p. 1140-1143.
153. Campiglio, P., M. Campione, and A. Sassella, *Kelvin probe force microscopy: Characterization of self-assembled monolayers on metals deposited with dip-pen nanolithography*. Journal of Physical Chemistry C, 2009. **113**(19): p. 8329-8335.
154. Caballero, D., et al., *Atomic force microscopy characterization of a microcontact printed, self-assembled thiol monolayer for use in biosensors*. Analytical Letters, 2006. **39**(8): p. 1721-1734.
155. Marchetto, D., et al., *AFM investigation of tribological properties of nano-patterned silicon surface*. Wear, 2008. **265**(5-6): p. 577-582.
156. Han, J., et al., *Scanning capacitance microscopy for alkylsilane-monolayer-covered Si substrate patterned by scanning probe lithography*. Japanese Journal of Applied Physics Part 1-Regular Papers Brief Communications & Review Papers, 2007. **46**(8B): p. 5621-5625.
157. Hoek, E.M.V. and G.K. Agarwal, *Extended DLVO interactions between spherical particles and rough surfaces*. Journal of Colloid and Interface Science, 2006. **298**(1): p. 50-58.
158. Brant, J.A. and A.E. Childress, *Colloidal adhesion to hydrophilic membrane surfaces*. Journal of Membrane Science, 2004. **241**(2): p. 235-248.
159. Boussu, K., et al., *Characterization of polymeric nanofiltration membranes for systematic analysis of membrane performance*. Journal of Membrane Science, 2006. **278**(1-2): p. 418-427.
160. Freger, V., *Nanoscale heterogeneity of polyamide membranes formed by interfacial polymerization*. Langmuir, 2003. **19**(11): p. 4791-4797.
161. Boussu, K., et al., *Roughness and hydrophobicity studies of nanofiltration membranes using different modes of AFM*. Journal of Colloid and Interface Science, 2005. **286**(2): p. 632-638.

162. Mulder, M., *Basic principles of membrane technology*. 2nd ed. 1996: Kluwer Academic Publishers.
163. Cohen, R.D. and R.F. Probstein, *Colloidal fouling of reverse-osmosis membranes*. Journal of Colloid and Interface Science, 1986. **114**(1): p. 194-207.
164. Bowen, W.R. and F. Jenner, *Dynamic ultrafiltration model for charged colloidal dispersions - a Wigner-Seitz cell approach*. Chemical Engineering Science, 1995. **50**(11): p. 1707-1736.
165. Hong, S., R.S. Faibish, and M. Elimelech, *Kinetics of permeate flux decline in crossflow membrane filtration of colloidal suspensions*. Journal of Colloid and Interface Science, 1997. **196**(2): p. 267-277.
166. Song, L.F., *Flux decline in crossflow microfiltration and ultrafiltration: mechanisms and modeling of membrane fouling*. Journal of Membrane Science, 1998. **139**(2): p. 183-200.
167. Pericet-Camara, R., G. Papastavrou, and M. Borkovec, *Atomic force microscopy study of the adsorption and electrostatic self-organization of poly(amidoamine) dendrimers on mica*. Langmuir, 2004. **20**(8): p. 3264-3270.
168. Bhattacharjee, S., C.H. Ko, and M. Elimelech, *DLVO interaction between rough surfaces*. Langmuir, 1998. **14**(12): p. 3365-3375.
169. Bhattacharjee, S., A.S. Kim, and M. Elimelech, *Concentration polarization of interacting solute particles in cross-flow membrane filtration*. Journal of Colloid and Interface Science, 1999. **212**(1): p. 81-99.
170. Faraudo, J., *New cooperative effects in ballistic deposition of hard disks*. Physical Review Letters, 2002. **89**(27).
171. van de Ven, T.G.M., *Colloidal hydrodynamics*. 1989, London: Academic Press.

172. Bessieres, A., et al., *Investigations of surface properties of polymeric membranes by near field microscopy*. Journal of Membrane Science, 1996. **109**(2): p. 271-284.
173. Bowen, W.R., et al., *Atomic force microscope studies of membranes: Surface pore structures of Cyclopore and Anopore membranes*. Journal of Membrane Science, 1996. **110**(2): p. 233-238.
174. Fritzsche, A.K., et al., *The structure and morphology of the skin of polyethersulfone ultrafiltration membranes - a comparative atomic force microscope and scanning electron microscope study*. Journal of Applied Polymer Science, 1992. **45**(11): p. 1945-1956.
175. Dietz, P., et al., *Surface pore structures of microfiltration and ultrafiltration membranes imaged with the atomic force microscope*. Journal of Membrane Science, 1992. **65**(1-2): p. 101-111.
176. Miwa, T., et al., *Fibrous textured surface of an ultrafiltration membrane delineated by atomic force microscope*. Japanese Journal of Applied Physics Part 2-Letters, 1992. **31**(10B): p. L1495-L1497.
177. Khulbe, K.C., et al., *Surface morphology of homogeneous and asymmetric membranes made from poly(phenylene oxide) by tapping mode atomic force microscope*. Journal of Applied Polymer Science, 1996. **59**(7): p. 1151-1158.
178. Bowen, W.R., A.W. Mohammad, and N. Hilal, *Characterisation of nanofiltration membranes for predictive purposes - Use of salts, uncharged solutes and atomic force microscopy*. Journal of Membrane Science, 1997. **126**(1): p. 91-105.
179. Stamatialis, D.F., C.R. Dias, and M.N. de Pinho, *Atomic force microscopy of dense and asymmetric cellulose-based membranes*. Journal of Membrane Science, 1999. **160**(2): p. 235-242.
180. Singh, S., et al., *Membrane characterization by solute transport and atomic force microscopy*. Journal of Membrane Science, 1998. **142**(1): p. 111-127.

181. Kwak, S.Y., *Relationship of relaxation property to reverse osmosis permeability in aromatic polyamide thin-film-composite membranes*. Polymer, 1999. **40**(23): p. 6361-6368.
182. Dow Chemical Company, T., *Technical Manual Excerpt-Form No. 609-02004-504, Filmtech*. 2007. p. 1-2.
183. Hoek, E.M.V. and M. Elimelech, *Cake-enhanced concentration polarization: A new fouling mechanism for salt-rejecting membranes*. Environmental Science & Technology, 2003. **37**(24): p. 5581-5588.
184. Binnig, G., C.F. Quate, and C. Gerber, *Atomic force microscope*. Physical Review Letters, 1986. **56**(9): p. 930-933.
185. Zhong, Q., et al., *Fractured polymer silica fiber surface studied by tapping mode atomic force microscopy*. Surface Science, 1993. **290**(1-2): p. L688-L692.
186. *Bioscope Instruction Manual, Version 5.12*. 1999: Digital Instruments, Veeco Metrology Group.
187. Cadotte, J.E., *Interfacially synthesized reverse osmosis membrane*. 1981: USA.
188. Cadotte, J.E., et al., *Interfacial synthesis in the preparation of reverse-osmosis membranes*. Journal of Macromolecular Science-Chemistry, 1981. **A15**(5): p. 727-755.
189. Petersen, R.J., *Composite reverse-osmosis and nanofiltration membranes*. Journal of Membrane Science, 1993. **83**(1): p. 81-150.
190. Tang, C.Y.Y., Y.N. Kwon, and J.O. Leckie, *Probing the nano- and micro-scales of reverse osmosis membranes - A comprehensive characterization of physiochemical properties of uncoated and coated membranes by XPS, TEM, ATR-FTIR, and streaming potential measurements*. Journal of Membrane Science, 2007. **287**(1): p. 146-156.
191. Boussu, K., et al., *Physico-chemical characterization of nanofiltration membranes*. ChemPhysChem, 2007. **8**(3): p. 370-379.

192. Cahill, D.G., V. Freger, and S.Y. Kwak, *Microscopy and, microanalysis of reverse-osmosis and nanofiltration membranes*. MRS Bulletin, 2008. **33**(1): p. 27-32.
193. Koo, J.Y., R.J. Petersen, and J.E. Cadotte. *Esca characterization of chlorine-damaged polyamide reverse-osmosis membrane*. in *Polymer Preprints*. 1986: American Chemical Society.
194. Arthur, S.D., *Structure property relationship in a thin-film composite reverse-osmosis membrane*. Journal of Membrane Science, 1989. **46**(2-3): p. 243-260.
195. Bartels, C.R., *A surface science investigation of composite membranes*. Journal of Membrane Science, 1989. **45**(3): p. 225-245.
196. Freger, V., J. Gilron, and S. Belfer, *TFC polyamide membranes modified by grafting of hydrophilic polymers: an FT-IR/AFM/TEM study*. Journal of Membrane Science, 2002. **209**(1): p. 283-292.
197. Malaisamy, R. and M.L. Bruening, *High-flux nanofiltration membranes prepared by adsorption of multilayer polyelectrolyte membranes on polymeric supports*. Langmuir, 2005. **21**(23): p. 10587-10592.
198. Liu, L.-F., et al., *Study on a novel polyamide-urea reverse osmosis composite membrane (ICIC-MPD): I. Preparation and characterization of ICIC-MPD membrane*. Journal of Membrane Science, 2006. **281**(1-2): p. 88-94.
199. Artug, G., et al., *A comprehensive characterization of commercial nanofiltration membranes*. Separation Science and Technology, 2007. **42**(13): p. 2947-2986.
200. Teixeira, M.R., M.J. Rosa, and M. Nyström, *The role of membrane charge on nanofiltration performance*. Journal of Membrane Science, 2005. **265**(1-2): p. 160-166.
201. Bartels, C.R., K.L. Kreuz, and A. Wachtel, *Structure performance relationships of composite membranes - porous support densification*. Journal of Membrane Science, 1987. **32**(2-3): p. 291-312.

202. Freger, V. and S. Srebnik, *Mathematical model of charge and density distributions in interfacial polymerization of thin films*. Journal of Applied Polymer Science, 2003. **88**(5): p. 1162-1169.
203. Brant, J.A., K.M. Johnson, and A.E. Childress, *Characterizing NF and RO membrane surface heterogeneity using chemical force microscopy*. Colloids and Surfaces A-Physicochemical and Engineering Aspects, 2006. **280**(1-3): p. 45-57.
204. Silverstein, R.M., G.C. Bassler, and T.C. Morrill, *Spectrometric identification of organic compounds*. 1981, New York: Wiley.
205. Mondal, S. and S.R. Wickramasinghe, *Produced water treatment by nanofiltration and reverse osmosis membranes*. Journal of Membrane Science, 2008. **322**(1): p. 162-170.
206. Kwon, Y.N., C.Y. Tang, and J.O. Leckie, *Change of chemical composition and hydrogen bonding behavior due to chlorination of crosslinked polyamide membranes*. Journal of Applied Polymer Science, 2008. **108**(4): p. 2061-2066.
207. Xu, P. and J.E. Drewes, *Viability of nanofiltration and ultra-low pressure reverse osmosis membranes for multi-beneficial use of methane produced water*. Separation and Purification Technology, 2006. **52**(1): p. 67-76.
208. Kralchevsky, P.A. and K. Nagayama, *Capillary interactions between particles bound to interfaces, liquid films and biomembranes*. Advances in Colloid and Interface Science, 2000. **85**(2-3): p. 145-192.
209. Guzy, C.J., E.J. Bonano, and E.J. Davis, *The analysis of flow and colloidal particle retention in fibrous porous media*. Journal of Colloid and Interface Science, 1983. **95**(2): p. 523-543.
210. Bhattacharjee, S. and M. Elimelech, *Surface element integration: A novel technique for evaluation of DLVO interaction between a particle and a flat plate*. Journal of Colloid and Interface Science, 1997. **193**(2): p. 273-285.
211. Das, P.K. and S. Bhattacharjee, *Electrostatic double layer force between a sphere and a planar substrate in the presence of previously deposited spherical particles*. Langmuir, 2005. **21**(10): p. 4755-4764.

212. Childress, A.E. and M. Elimelech, *Relating nanofiltration membrane performance to membrane charge (electrokinetic) characteristics*. Environmental Science & Technology, 2000. **34**(17): p. 3710-3716.
213. Ariza, M.J., et al., *Effect of hydration of polyamide membranes on the surface electrokinetic parameters: Surface characterization by X-ray photoelectronic spectroscopy and atomic force microscopy*. Journal of Colloid and Interface Science, 2002. **247**(1): p. 149-158.
214. Brant, J.A., K.M. Johnson, and A.E. Childress, *Examining the electrochemical properties of a nanofiltration membrane with atomic force microscopy*. Journal of Membrane Science, 2006. **276**(1-2): p. 286-294.
215. Love, J.C., et al., *Self-assembled monolayers of thiolates on metals as a form of nanotechnology*. Chemical Reviews, 2005. **105**(4): p. 1103-1169.
216. Ulman, A., *Formation and structure of self-assembled monolayers*. Chemical Reviews, 1996. **96**(4): p. 1533-1554.
217. Tien, J., A. Terfort, and G.M. Whitesides, *Microfabrication through electrostatic self-assembly*. Langmuir, 1997. **13**(20): p. 5349-5355.
218. Michel, B., et al., *Printing meets lithography: Soft approaches to high-resolution printing*. IBM Journal of Research and Development, 2001. **45**(5): p. 697-719.
219. Kokkoli, E. and C.F. Zukoski, *Surface pattern recognition by a colloidal particle*. Langmuir, 2001. **17**(2): p. 369-376.
220. Wilbur, J.L., et al., *Microfabrication by microcontact printing of self-assembled monolayers*. Advanced Materials, 1994. **6**(7-8): p. 600-604.
221. *Electric Force Microscopy (EFM)*, in *Support Note No. 230 Rev. A*. 1996, Digital Instruments: Santa Barbara, CA.
222. Zhu, P.X., et al., *Investigation of apatite deposition onto charged surfaces in aqueous solutions using a quartz-crystal microbalance*. Journal of the American Ceramic Society, 2003. **86**(5): p. 782-790.

223. Cheng, S.S., D.A. Scherson, and C.N. Sukenik, *In situ attenuated total reflectance fourier transform infrared spectroscopy of carboxylate-bearing, siloxane anchored, self-assembled monolayers - a study of carboxylate reactivity and acid-base properties*. Langmuir, 1995. **11**(4): p. 1190-1195.
224. Shyue, J.J. and M.R. De Guire, *Acid-base properties and zeta potentials of self-assembled monolayers obtained via in situ transformations*. Langmuir, 2004. **20**(20): p. 8693-8698.
225. Lichtman, J.W. and J.A. Conchello, *Fluorescence microscopy*. Nature Methods, 2005. **2**(12): p. 910-919.
226. *NI Vision Concepts Manual*. 2005: National Instruments Corporation.
227. Russ., J.C., *The image processing handbook*. 2007, Boca Raton: CRC/Taylor and Francis.
228. Allen, M.P. and D.J. Tildesley, *Computer simulation of liquids*. 1987: Oxford University Press.
229. Onoda, G.Y. and E.G. Liniger, *Experimental determination of the random parking limit in 2 dimensions*. Physical Review A, 1986. **33**(1): p. 715-716.
230. Evans, J.W., *Random and cooperative sequential adsorption*. Reviews of Modern Physics, 1993. **65**(4): p. 1281-1329.
231. Tarjus, G., et al., *New analytical and numerical results on virial coefficients for 2-D hard convex bodies*. Molecular Physics, 1991. **73**(4): p. 773-787.
232. Viot, P., et al., *Random sequential adsorption of anisotropic particles-I: Jamming limit and asymptotic behavior*. Journal of Chemical Physics, 1992. **97**(7): p. 5212-5218.
233. Ricci, S.M., et al., *Random sequential adsorption of anisotropic particles II- Low coverage kinetics*. Journal of Chemical Physics, 1992. **97**(7): p. 5219-5228.

234. Adamczyk, Z. and P. Weronki, *Random sequential adsorption of spheroidal particles: Kinetics and jamming limit*. Journal of Chemical Physics, 1996. **105**(13): p. 5562-5573.
235. Talbot, J. and P. Schaaf, *Random sequential adsorption of mixtures*. Physical Review A, 1989. **40**(1): p. 422-427.
236. Meakin, P. and R. Jullien, *Random sequential adsorption of disks of different sizes*. Physical Review A, 1992. **46**(4): p. 2029-2038.
237. Adamczyk, Z., et al., *Influence of polydispersity on random sequential adsorption of spherical particles*. Journal of Colloid and Interface Science, 1997. **185**(1): p. 236-244.
238. Adamczyk, Z., B. Siwek, and P. Weronki, *Adsorption of colloid particles at partially covered surfaces*. Journal of Colloid and Interface Science, 1997. **195**(1): p. 261-263.
239. Adamczyk, Z. and P. Weronki, *Random sequential adsorption on partially covered surfaces*. Journal of Chemical Physics, 1998. **108**(23): p. 9851-9858.
240. Adamczyk, Z., J. Barbasz, and M. Nattich, *Particle assembly on patterned surfaces bearing circular (Dots) and rectangular (Stripes) surface features*. Langmuir, 2008. **24**(5): p. 1756-1762.
241. Callen, H.B., *Thermodynamics and an introduction to thermostatistics*. 1985, New York: Wiley.
242. Kemps, J.A.L. and S. Bhattacharjee, *Interactions between a solid spherical particle and a chemically heterogeneous planar substrate*. Langmuir, 2005. **21**(25): p. 11710-11721.
243. Duval, J.F.L., F.A.M. Leermakers, and H.P. van Leeuwen, *Electrostatic interactions between double layers: Influence of surface roughness, regulation, and chemical heterogeneities*. Langmuir, 2004. **20**(12): p. 5052-5065.

244. Duffadar, R.D. and J.M. Davis, *Dynamic adhesion behavior of micrometer-scale particles flowing over patchy surfaces with nanoscale electrostatic heterogeneity*. Journal of Colloid and Interface Science, 2008. **326**(1): p. 18-27.
245. Stankovich, J. and S.L. Carnie, *Electrical double layer interaction between dissimilar spherical colloidal particles and between a sphere and a plate: Nonlinear Poisson-Boltzmann theory*. Langmuir, 1996. **12**(6): p. 1453-1461.
246. Ohshima, H., *Surface charge density surface potential relationship for a spherical colloidal particle in a solution of general electrolytes*. Journal of Colloid and Interface Science, 1995. **171**(2): p. 525-527.
247. Ohshima, H., *Electrostatic interaction between a sphere and a planar surface: Generalization of point-charge/surface image interaction to particle/surface image interaction*. Journal of Colloid and Interface Science, 1998. **198**(1): p. 42-52.
248. Molla, S. and S. Bhattacharjee, *Dielectrophoretic levitation in the presence of shear flow: Implications for colloidal fouling of filtration membranes*. Langmuir, 2007. **23**(21): p. 10618-10627.
249. Nazemifard, N., *Particle deposition onto charge heterogeneous surfaces in a radial impinging jet system*, Masters Thesis, 2005, University of Alberta: Edmonton.
250. Adamczyk, Z., *Particle transfer and deposition from flowing colloid suspensions*. Colloids and Surfaces, 1989. **35**(2-4): p. 283-308.
251. Goldman, A.J., R.G. Cox, and H. Brenner, *Slow viscous motion of a sphere parallel to a plane wall-I: Motion through a quiescent fluid*. Chemical Engineering Science, 1967. **22**(4): p. 637-651.
252. Cox, R.G. and H. Brenner, *Slow motion of a sphere through a viscous fluid towards a plane surface-II: Small gap widths including inertial effects*. Chemical Engineering Science, 1967. **22**(12): p. 1753-1777.

253. Ma, L.C., et al., *Electrostatic funneling for precise nanoparticle placement: A route to wafer-scale integration*. Nano Letters, 2007. 7(2): p. 439-445.

APPENDIX A

WORKING PRINCIPLE OF THE ATOMIC FORCE MICROSCOPE (AFM) AND THE FOURIER TRANSFORM INFRA RED (FTIR) SPECTROMETER

A.1 Atomic Force Microscopy

The atomic force microscope (AFM) is a scanning probe microscope which was invented in 1986 by Binnig, Quate and Gerber [184]. Unlike traditional microscopes, the atomic force microscopy (AFM) does not rely on electromagnetic radiation or an electron beam to create an image but uses an opto-mechanical imaging to measure the three dimensional topography as well as the physical properties of a surface with a sharpened probe. The main feature of an AFM instrument is that it can map the topography with microscopic precision (or another surface property) by scanning a sharp probe over a surface. The sharpened probe is positioned close enough to the surface so that it can interact with the force field associated with the surface. Then the probe is scanned across the surface such that the forces between the probe and the surface remain constant. An image of the surface is then reconstructed by monitoring the precise motion of the probe during the scan.

The microscope system consists of probe, a laser a detection system, a piezo-electric scanner and a computer. As a probe the AFM uses a sharp tip that is mounted on the edge of a flexible cantilever which is coated on the back with a reflective layer. When a sample is scanned the interaction forces between the tip and the sample surface cause the cantilever to deflect. Attractive or repulsive forces resulting from interactions between the tip and the surface will cause a

positive or negative bending of the cantilever. The deflection or bending of the cantilever is monitored by an optical system in which a laser reflects off the back of the cantilever onto a split photodiode detector which is a quad-cell Position Sensitive Photo Detector (PSPD) (Figure A.1). In an AFM, either the sample or the tip is moved with extreme precision to make high resolution imaging possible. This positioning is usually done by a piezoelectric scanner, a positioning device which is capable of moving the tip (or the sample) in x -, y -, z - directions with accuracy better than one tenth of a nanometre. There are several operational modes available in the AFM [194]; however brief descriptions of only those methods employed in this work are provided in the following subsections.

A.2 Contact Mode

The contact mode is one of the basic modes of operation of the AFM [186]. In contact mode AFM, the tip which is in perpetual contact with the sample, is attached to the end of a cantilever with a low spring constant. In this mode the scanner gently traces the tip across the sample surface, while the contact forces cause the cantilever to bend. The change in cantilever deflection due to bending is monitored with the quad cell photo detector. The feedback system then maintains a constant deflection between the cantilever and the sample by vertically moving the scanner at each (x,y) data point to maintain a setpoint deflection by adjusting the height of the cantilever to compensate for topographical features. This means that when the tip encounters higher features on the surfaces the piezo moves the tip downwards and when the tip is scanning lower features the piezo element moves the tip upwards. By maintaining a constant cantilever deflection, the force between the tip and the sample remains constant. The force is calculated from Hooke's Law:

$$F = -kx \tag{A.1}$$

where F = Force, k = spring constant and, x = cantilever deflection. Spring constants for the cantilevers usually range from 0.01 to 1.0 N/m, resulting in forces ranging from nN to μ N in an ambient atmosphere. The distance the scanner

moves vertically at each (x,y) data point is stored by the computer resulting in a three-dimensional map of the sample topography.

A.3 Tapping Mode

Tapping mode [186] is ideal for imaging of soft (organic) surfaces or molecular layers that are not firmly attached to the surface. In this mode, the contact time between the tip and the sample is greatly reduced. For imaging in air, a stiff cantilever is physically vibrated vertically near its resonant frequency at a certain distance away from the sample surface by a small piezoelectric element resulting in a large, free air, cantilever amplitude while also scanning the surface laterally. When the probe is brought into the proximity of the sample surface the tip strikes the surface near the bottom of each oscillation such that it begins to make an intermittent or “tapping” contact with the sample, causing a small reduction in the amplitude of the cantilever’s oscillation. As the tip is raster scanned across the sample surface, the cantilever’s oscillation amplitude changes with surface topography. The feedback system, then, maintains the RMS amplitude of oscillations at a setpoint value by adjusting the vertical position of the probe with the piezoelectric scanner. By monitoring the vertical motion of the probe during the scan, a topographical image of the surface is generated.

A.4 Friction or Lateral Force Mode (LFM)

Lateral Force Microscopy (LFM) also called Frictional Force Microscopy (FFM) [186] is a secondary contact AFM mode that detects and maps relative differences in the frictional forces between the probe tip and the sample surface by measuring the lateral deflections of the cantilever as it scans across the sample. In LFM, the scanning is always perpendicular to the long axis of the cantilever. Forces on the cantilever that are parallel to the plane of the sample surface cause twisting of the cantilever around its long axis. The torsion, or twisting, of the cantilever supporting the probe will increase or decrease depending on the frictional characteristics of the surface (greater torsion results from increased friction). This twisting is

measured by the split photodiode (*i.e.* the quad cell PSPD) as shown in Figure A.2. Since the laser detector has four quadrants, it can simultaneously measure and record topographic data and lateral force data. Twisting of the cantilever usually arises from two sources: changes in surface friction and changes in topography. In the first case, the tip may experience greater friction as it traverses some areas, causing the cantilever to twist more. In the second case, the cantilever may twist when it encounters edges of topographical features. To separate one effect from the other, usually three signals are collected simultaneously: the trace and retrace LFM signals, and the AFM height (topography) signal.

A.5 Electrical Force Imaging-Surface Potential Mapping

Surface potential (SP) mapping is performed using a two-pass interleaved technique (Lift Mode) [221]. This measurement is made simultaneously with the topographic scan in the tapping mode using a conducting probe. After each line of the topography scan is completed in the tapping mode, the “Lift Mode” is activated, in which the tip is lifted from the surface and held over the same topography at a constant distance (100 nm) while the feedback loop controlling the vertical piezo is turned off. Instead, a dc bias potential, V_{tip} , and an oscillating potential, $V_{ac}\cos(\omega t)$, are superimposed directly onto the cantilever tip. During scanning, a difference between the dc bias potential applied to the tip and the potential of the surface create a force to act on the tip (and causing it to oscillate) at ω . The amplitude of the force is:

$$F = \frac{dC}{dz} (V_{tip} - V_{sample}) V_{ac} \quad (A.2)$$

Here, $\frac{dC}{dz}$ is the vertical derivative of the tip/sample capacitance. The force on the cantilever depends on the product of the ac drive voltage and the dc voltage difference between the tip and the sample (see Eq. (A.2)). Thus, when the tip and sample are at the same dc voltage, the cantilever will cease to oscillate. The Extender Electronics Module of the AFM uses this fact to determine the effective surface potential on the sample, V_{sample} . The Extender determines the local surface potential by adjusting the dc voltage on the tip, V_{tip} , until the oscillation amplitude

becomes zero. At this point the tip voltage will be the same as the unknown surface potential. Monitoring the dc potential applied to the tip as it is raster scanned across the surface, results in a map of the potential at each point on the surface.

A.6 Fourier Transform Infra Red Spectroscopy

Briefly, a Fourier Transform Infra Red (FTIR) spectrometer [204] obtains infrared spectra by first collecting an interferogram of a sample signal with an interferometer, which measures all of infrared frequencies simultaneously then digitizes the interferogram, performs the Fourier Transform function, and finally outputs the resultant spectrum. The interferometer utilizes a beam splitter to split the incoming infrared beam into two optical beams (see in Figure A.3). One beam is of fixed length and reflects off of a flat mirror which is fixed in place. Another beam of variable length reflects off of a flat mirror which travels a very short distance away from the beam splitter. The two beams reflect off of their respective mirrors and are recombined when they meet together at the beam splitter. The varying distances between the two path lengths of the beams result in a sequence of constructive and destructive interferences and hence variation in intensities. The re-combined signal thus results from the beams “interfering” with each other. Consequently, the re-combined beam gives a resulting signal called interferogram, which has every infrared frequency “encoded” into it. When the interferogram signal is transmitted through or reflected off of the sample surface, the specific frequencies of energy are absorbed by the sample due to the excited vibration of functional groups in the molecules. The infrared signal after the interaction with the sample is uniquely characteristic to the sample. The beam finally arrives at the detector and is measured therein. The detected interferogram cannot be directly interpreted. It has to be “decoded” with a well-known mathematical technique, Fourier Transformation (FT). Fourier transform converts this interferogram from the time domain into one spectral point on the frequency domain. The computer can perform the FT calculation and present an infrared spectrum, which plots absorbance (or transmittance) versus wave number.

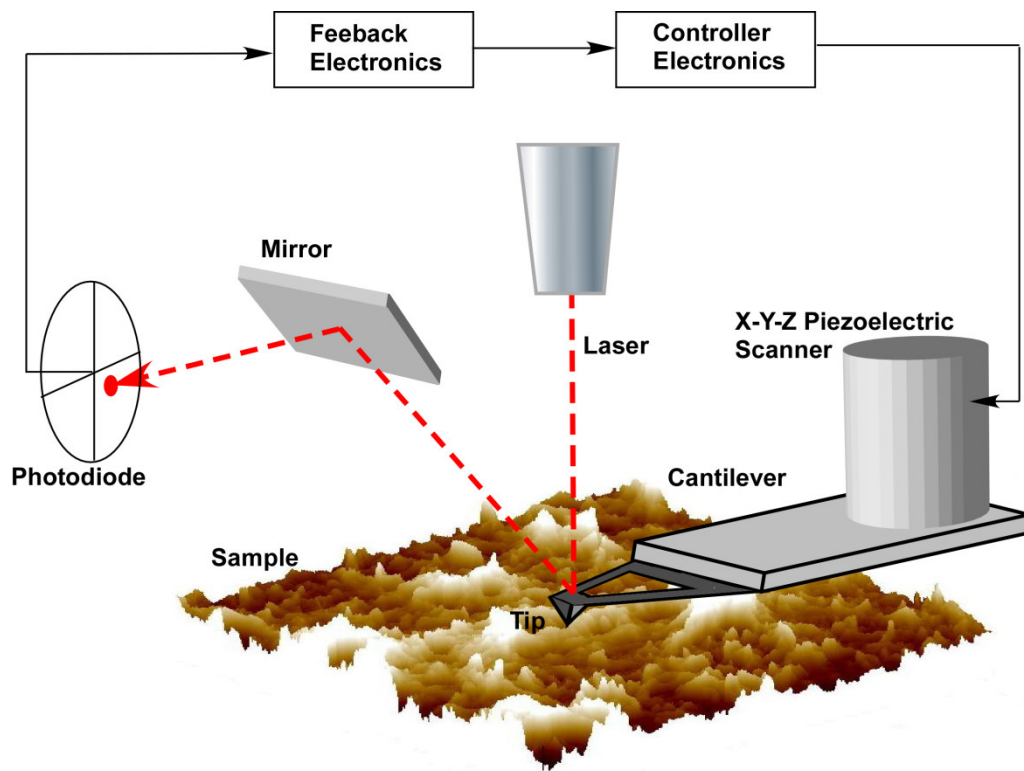


Figure A.1: Schematic showing the principle of an Atomic Force Microscope (AFM).

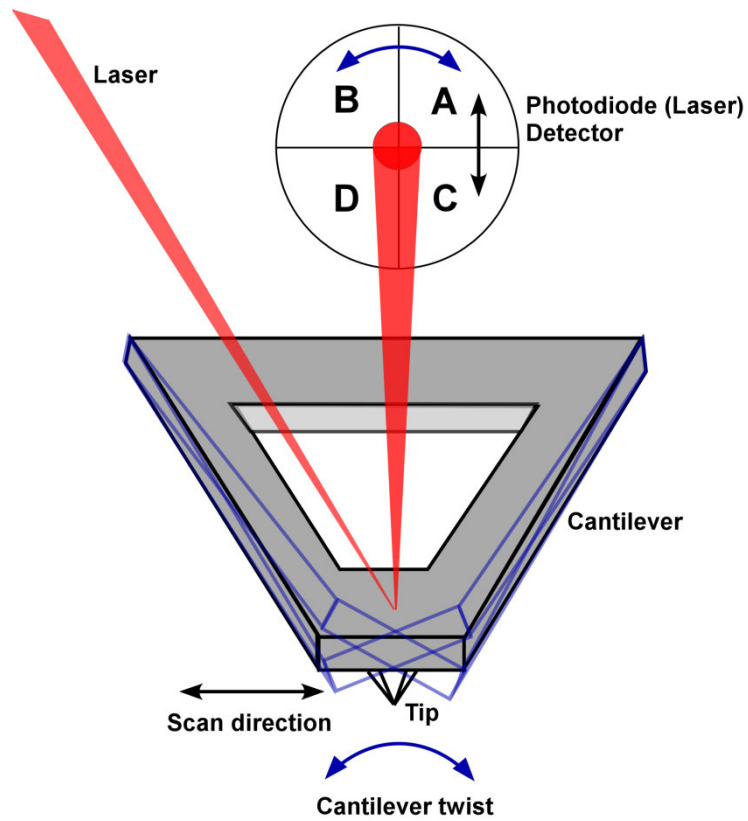


Figure A.2: Scanning and detection with lateral force microscopy. For LFM, the probe is scanned sidewise and the friction signal is calculated as $(A + C) - (B + D)$. The degree of torsion of the cantilever supporting the tip is a relative measure of surface friction caused by the lateral force exerted on the scanning probe. Note that for contact mode, the deflection signal is calculated as laser spot intensity for quadrants $(A + B) - (C + D)$.

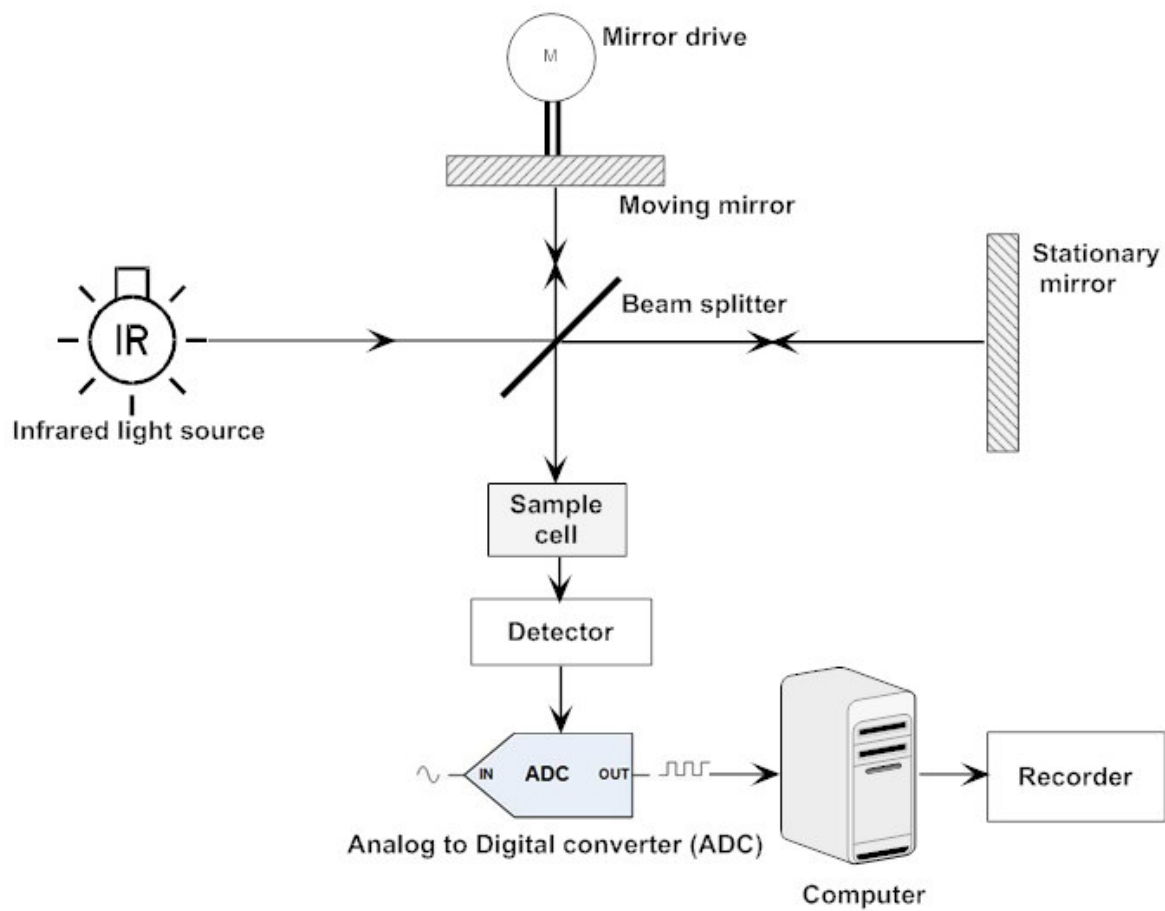


Figure A.3: Schematic illustration of Fourier Transform Infra Red (FTIR) spectrometer system [204].

APPENDIX B

CREATING PDMS STAMPS BY PHOTOLITHOGRAPHY AND CAST MOLDING TECHNIQUE

To fabricate the stamps for the μ CP process conventional photolithography and etching technique was utilized. The flow chart in Figure B.1 summarizes the sequential steps leading to the creation of the stamps. First the desired patterns were designed using CAD software. Next, the design was transferred to a chrome-gold soda lime glass to create a photo mask utilizing a laser mask generator. This photo mask was then used to create the master (mold) on silicon substrates using photolithography and a dry etch process. Finally the Si master was used to cast the stamps by pouring and curing PDMS on them. The entire procedure was carried out at the Nanofabrication (NanoFab) facility at the University of Alberta. The following sections provide more details on the intermediate steps as discussed above and shown in Fig. B.1.

B.1 Design

Designing the pattern on the stamp is the first step after deciding on a manufacturing process. The design of the pattern was created using the L-Edit[®] (MEMSPro, USA). Compared to other design CAD software like AutoCAD and Pro-E, L-Edit is not as user friendly and is cumbersome to use. Although other CAD softwares could have been used to create the design, there were some problems arising when integrating the design file with the mask generator. This was avoided when the file was generated using the NanoFab prescribed software L-Edit.

B.2 Photo Mask Generation

Once the design stage was completed, the outcome of the L-edit program is a file that was compiled for use in the laser pattern generator. The photo mask was produced using a DWL-200 laser mask generator (Heidelberg, Germany). The Heidelberg DWL 200 is a highly precise and accurate instrument using a Krypton-Ion laser to expose at a wavelength of 413 nm. There are generally four steps involved in the creation of the mask: printing, developing, etching and cleaning. The machine prints the patterns by raster scanning blank 5 inch soda lime glass squares (thickness 0.09 inch, Paragon Optical Company, USA) that are coated with chrome and 530 nm of AZ 1518 photo resist. A minimum feature size of 0.7 - 0.8 μm can be attained using the laser mask writer, depending on the geometry of the feature. Once the mask blank has been exposed by the Krypton-Ion laser, photoresist exposed to the laser is chemically altered so that when it was agitated in a developer, that part of the photoresist washed away. This revealed the pattern that was designed in the CAD program. After developing, the mask blank therefore had both the bare chrome and the unexposed photoresist on it. The photoresist acts as a protective layer so that when the mask was placed in chrome etch, only the uncovered chrome was removed. Once the developing and etching was finished, it was necessary to properly clean the mask before using it in lithography. The mask was inspected and the photoresist stripped using acetone and IPA followed by a 30 min dip in a cold piranha bath.

B.3 Photolithography

To create the master mold for the casting process, 4 inch diameter Si wafers (Silicon Valley Microelectronics, USA) were used and the patterns created on them using photolithography and a dry etch process. Figure B.2 is a flow chart outlining the procedures involved in the photolithographic process and the following sections provide a brief description of each step.

B.4 Cleaning

The Si wafer was clean thoroughly to achieve a good adhesion of the SU-8 resist with the wafer. Cleaning was carried out by soaking the Si substrates in freshly prepared Piranha solution which contains 75% H_2SO_4 and 25% H_2O_2 , by volume. The mixing procedure produces a significant amount of heat, raising the temperature of the solution to about 110°C . The substrates were immersed in this hot solution for 15 min. This guarantees that all organic contaminants will be removed. Once removed from the Piranha solution, the substrates were rinsed in copious amount of deionized water and dried in N_2 .

B.5 Thermal (Silicon dioxide) Layer Growth

Next the wafer was placed in a furnace to form a layer of silicon dioxide (SiO_2) before spin coating it with the resist. This “buffer” or “masking” layer of oxide is required for the later deep reactive ion etch (RIE) etching process. The thickness of the layer depends on the depth to which the substrate will be etched. For example, for our Si master, a 200 nm oxide layer is required for a maximum etch depth of up to $2\ \mu\text{m}$ depth of the pattern. The wafers were placed in a furnace for 45 min at 1000°C to obtain a 200 nm thick oxide layer. The substrate was allowed to cool and a thin adhesion promoting layer of HMDS (hexamethyl disilazane) was coated on top to promote good adhesion for the resist since we used does not stick well to SiO_2 . The HMDS reacts with the oxide surface in a process known as silylation, forming a strong bond to the surface. At the same time, free bonds are left which readily react with the photoresist, enhancing the photoresist adhesion.

B.6 Spin Coating Resist and Soft Bake

Spin Coat: The patterning process begins with spinning the photoresist. Photoresist is a polymer sensitive to UV light. It changes its chemical composition once exposed to UV light. The photoresist used in this process was a low viscosity

resist HPR 504. The substrate was placed on a spinning machine and about 5 ml of the resist was dispensed at the center of the wafer and spread at 500 rpm for 10 s. After the initial spreading, the actual spin that coats the resist on the substrate was performed at 4000 rpm for 40 s.

Soft Bake: After spinning, the wafer with the wet HPR 504 layer was then baked on a hot plate to dry and stabilize the film. This pre-exposure bake also makes the surface non-sticking, which prevents it from leaving remains on the photo mask. The duration of baking depends on the type of resist. For glass substrates covered by a thin HPR 504 resist, baking at 110°C for 90 s on a hot plate is recommended. After the bake, the resist was cooled for about 15 min before the exposure step.

B.7 Exposure and Development

Exposure: Once the resist was baked, it was ready for exposure. The exposure process started with setting the mask generated on a mask aligner tool. It was important to ensure that the photo mask was clean before mounting on the machine. Once the mask was mounted, the wafer or Si substrate was placed on the substrate holder by turning the vacuum on. Next the mask was aligned and centered with the Cr side facing towards the Si substrate, which is positioned properly beneath it. After alignment, the substrate was brought into contact with the mask. At this stage it was crucial to ensure that the substrate did not move or change position once contact was made with the mask, otherwise the alignment would have to be performed again. It was also important to ensure that the mask and the substrate were in good contact. Any trapped particle or debris could potentially create a gap between the mask and the substrate. This would let diffused light penetrate under the mask, thereby, causing a deformation of the features or partial exposure of some parts. The exposure time is dictated by the smallest dimension present on the mask. For our design, the exposure time was generally between 2 to 2.5 s.

Development: Developing the photoresist is a chemical process, in which the exposed substrate is immersed in a developer. The developer dissolves the UV exposed parts of the photoresist revealing the bare regions of the Si substrate

while leaving the substrate covered with unexposed photoresist. The standard developer for HPR 504 is the 354 Developer. For slower and more accurate processes involving very small dimensions, water can be added to dilute the developer (up to 50% by volume). The standard development time for the resists mentioned above is 20 to 25 s in 100% of 354 Developer. However, the developing time may vary; depending on the pattern dimensions, temperature, and humidity. For our pattern dimensions, the developer was diluted and the exposure time varied from 15 to 18 s. Finally the wafer was inspected under a microscope to check for the quality of the whole patterning process after developing the resist. The substrate was subsequently rinsed with de-ionized water and blown dry using N_2 .

B.8 Buffered Oxide Etch (BOE)

The next step was to remove the oxide layer from the uncovered regions of Si wafer where the etching action will take place to form the relief pattern or mold. For this purpose, a Buffered Oxide Etch (BOE) was performed with the etching time varying depending on the thickness of the oxide layer. The etching solution contains 10:1 ratio of ammonium bifluoride (NH_4HF_2) and hydrofluoric acid (HF) by volume with an etch rate of 550 Å per minute. The wafer was placed in this solution for about 4 min to remove the oxide layer.

B.9 Dry Etch - BOSCH® Process

In the final step of the master fabrication, an anisotropic etching method was employed for fabricating the relief pattern on the Si master. To achieve anisotropic etching, a Deep Reactive Ion Etch (DRIE) machine using the Bosch® process (named after the German company Robert Bosch that filed the original patent) was employed. This process is used where deep, vertical-walled, high aspect ratio structures with small feature sizes are required. The process cycles between two steps:

Polymer Deposition Phase: In the deposition stage (typically 10 s long), C₄F₈ (octafluoro cyclobutane) gas is introduced in the reactor. The entire surface of the wafer is subsequently coated with Teflon-like polymer formed in the plasma from the C₄F₈ gas.

Etch Phase: In the etch phase (typically 15 s), the C₄F₈ is turned off and SF₆ (sulfur hexafluoride) is let into the chamber. The polymer (on the horizontal surfaces of the wafer) is immediately sputtered away by the SF₆ plasma, and then etches the Si below the polymer. The SF₆ etch occurs only on the horizontal surfaces and not the sidewalls, thus producing an almost vertical wall.

A single process cycle etches trenches from 0.5 to 1 μm at an etch rate of 0.5 to 2.0 μm/min (depending on the etch recipe). The cycle was repeated until the desired structure (depth) has been etched. The system was fully computer controlled in all aspects of the pumping cycles and process control, and can be programmed by the user. A masking layer of 0.6 μm thermal oxide (SiO₂) is usually sufficient for about 200 μm deep etches. In this experiment, one to two BOSCH cycles sufficed to obtain the design etch depth of 0.5 μm and 1 μm with a masking thermal oxide layer of 200 nm.

B.10 Cast Molding

The cast molding process is depicted in Figure B.3. After the master mold was produced, an anti adhesive surface treatment was required before the master could be used to cast the stamps for the μCP process. The surface treatment was needed to favour the release or demolding of the stamp by reducing the surface energy of the Si surface so that the stamp could be removed without tearing or damaging the delicate stamp relief structure. To make the surface anti adhesive, 1H, 1H, 2H, 2H perfluorooctyl trichlorosilane (Aldrich, USA) was used. The substrate and a vial containing a few drops of trichlorosilane were placed in a desiccator under vacuum for 2 h. Trichlorosilane evaporates under vacuum and forms a thin layer of hydrophobic coating on the surface of the master.

Each master (Si wafer) contained up to 25 molds for stamp production arranged in 5 rows within the substrate. The stamps were cast using polydimethyl

siloxane or PDMS which is normally supplied as a two part kit: a liquid silicon rubber base (*i.e.* a vinyl-terminated PDMS) and a catalyst or curing agent (*i.e.* a mixture of a platinum complex and copolymers of methyl hydrosiloxane and dimethyl siloxane). In the casting step, PDMS polymer was made by combining a 10:1 ratio of Sylgard 184 Base and Sylgard 184 Cure (Dow Corning, Midland, MI) and stirring rigorously until they are thoroughly combined. After the mixing, the mixture will be full of air bubbles and requires degassing because the presence of air bubbles can cause unwanted cavities in the stamp structure. Degassing was performed by placing the mixture under vacuum (~22 in Hg vacuum) until the bubbles disappeared. The mixture was then poured in the middle of the wafer over the relief structure on its surface from a low altitude (to minimize the risk of trapped air) and allowed to spread. The master was kept horizontal while the PDMS was being poured to ensure uniformity of the thickness of the stamps formed. The wafer was then baked at 80°C for 2 h causing the PDMS to solidify. Once fully cured, the stamps were removed from the oven and allowed to cool to room temperature. The stamps were then manually stripped off from the master and cut into small individual pieces. The master can be used several times to mold the stamps without compromising the integrity of the stamp structure.

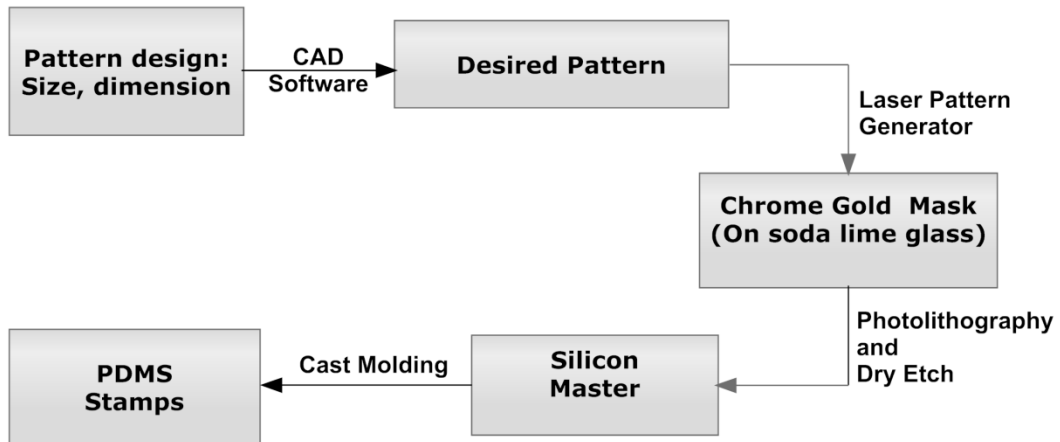


Figure B.1: Flowchart showing the sequence of operations for fabricating PDMS stamps used in the μ CP process.

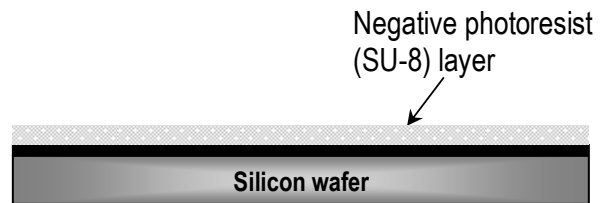
1. Cleaned silicon wafer



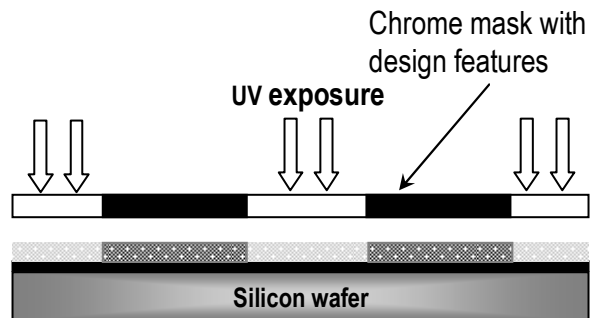
2. Buffer oxide layer growth



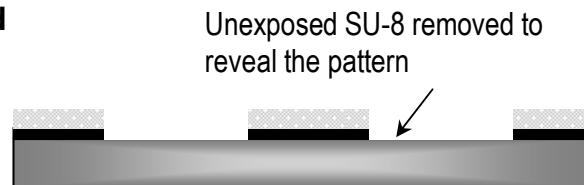
3. Spin coat photoresist



4. Design pattern transfer



5. Develop exposed resist and BOE (Buffered Oxide Etch)



6. Etching the pattern onto the Si wafer by BOSCH Process

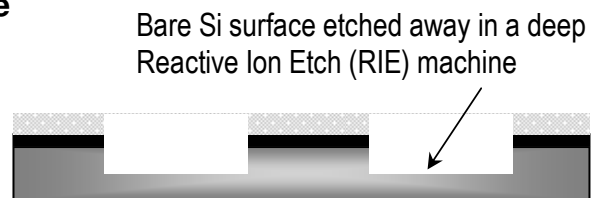
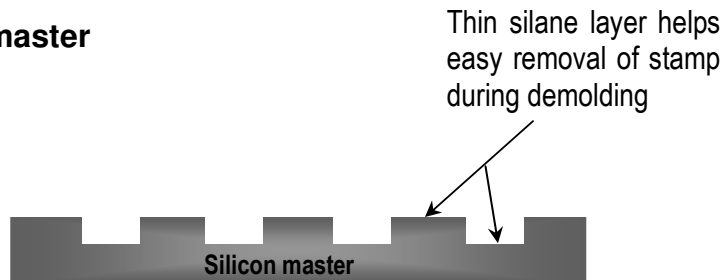
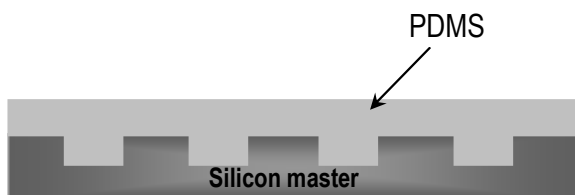


Figure B.2: Summary of the photolithographic process and etching involved in creating the silicon master.

1. Silanized silicon master



2. PDMS poured over master and cured at 80°C



3. Demolding stamp from the master



Figure B.3: Schematic diagram depicting the cast molding process for creating the PDMS stamps